Exciton Transport and Strain Engineering in Atomically Thin Semiconductors

by

Darwin Fernando Cordovilla Leon

A dissertation submitted in partial fulfillment
of the requirements for the degree of
Doctor of Philosophy
(Applied Physics)
in The University of Michigan
2021

Doctoral Committee:

Assistant Professor Parag B. Deotare, Co-chair
Professor Duncan G. Steel, Co-chair
Professor Steven Cundiff
Professor Mackillo Kira
Professor Zetian Mi

Darwin Fernando Cordovilla Leon

dcordovi@umich.edu

ORC iD: 0000-0003-1282-9804

Dedication

To my nieces and nephews: Camila, Emiliano, Gabriel, and Alison. May you make your own way, persist, and always be kind. Los amo.

Acknowledgments

The Eighteenth Century physicist George Christoph Lichtenberg once said: "In each of us there is a little of all of us." I know that to be true because without the little pieces of each of you that I carry with me, I would not be whole: an aspiring scientist, a husband, a son, a brother, an uncle, an immigrant, and more. Without the selfless contributions of many people who have supported me unconditionally throughout this long and demanding journey, I would not be where I am today. First, I would like to thank my family for their unwavering love and support. A special showing of gratitude to my parents, Rosa and Luis, for instilling in me their sense of humility and work ethic; both of these qualities have kept me grounded and have guided me through tough times. My deepest gratitude to my sister Jessica for her unrestricted love, for teaching me to face life with a good sense of humor, and for reminding me to have fun. I could not leave out my brother, Nestor, for protecting me, demonstrating discipline, and for each small detail as you helped raise me. Finally, to all of my other relatives, especially Pato and Patty, I am grateful for all of your encouragement and well wishes.

I owe a lifetime of gratitude to my dearest wife Cesilie and our beloved furbaby, Suca Bella, for their love, encouragement, and patience. Without them in my life, I would not have been able to endure the difficult moments in life, and especially in graduate school. Through thick and thin, they have always been there for me. They have guided me to become a kinder, more thoughtful person, and to find joy in the little things of life. I can't wait to start a new chapter of our life together.

To my American Family, the Keans, I will always be grateful for them for making the best memories together, their kindness, and unwavering support ever since we met during my time as an exchange student in Boise. I also give thanks for my fellow physicist buddies, Thomas Shaw, Jae Choi, and Obinna Uyanna for their friendship, the time we share creating memories, and our recreational conversations about physics and soccer.

Even before I began my undergraduate education, two great women made a huge impact in my life, and I would like to acknowledge them. I feel privileged to have met you and admire you both profoundly, Maria Mercedes Salmon and Bev Fowler. Their guidance and support were pivotal in my transition from high school in Ecuador to college in the United States of America as an Opportunity Funds Program grantee and scholar at the University of Evansville (UE).

Next, I would like to thank my college mentors at UE, Professors Douglas Stamps and Joseph Tipton, for challenging and guiding me to become a rigorous thinker. Their devotion to science, engineering, and teaching instilled in me a curiosity for knowledge and inspired me to pursue a doctoral education. I would like to give special thanks to the late Mr. Craig Tooley, a fellow UE alum, for giving me the opportunity to accomplish one of my childhood dreams and become part of NASA as a summer college intern at Goddard Space Flight Center. Similarly, my deepest gratitude to the MIT Summer Research Program, especially to Monica Orta, Professors Konstantin Turitsyn and Dirk Englund, for giving me the opportunity to spend two summers as an undergraduate researcher at such an elite institution.

At the University of Michigan, I owe a lifetime of gratitude to the Applied Physics program, especially Cindy McNabb and Professor Cagliyan Kurdak, for their consistent encouragement, support, and guidance. To my adviser Professor Parag Deotare, co-authors, and lab mates from the Excitonics and Photonics Laboratory at the University of Michigan, I thank you for giving me the opportunity to learn and develop as a scientist and engineer. The valuable lessons I learned working as part of this team will serve me well as I start a

new chapter in my professional career.

Similarly, I am grateful for my fellow researchers and mentors Aaron Ross, Xi Chen, and Tyler Hill for their valuable mentorship, patience, and kindness both in and out of the laboratory. I also would like to recognize Professors Long Zhang, Hui Deng, and Mack Kira for valuable collaborations, and Professors Steven Cundiff, Zetian Mi and again Professor Mack Kira for serving as my thesis committee. Finally, saving the best for last, I extend an abundance of gratitude to my co-adviser Professor Duncan Steel for his unmatched mentorship and dedication to my personal and professional well-being. You embody kindness and I cherish your company, guidance, and friendship. May it continue into the future.

Lastly, I want to acknowledge financial support from the National Science Foundation Graduate Research Fellowship Program under grant No. DGE 1256260 and the University of Michigan's Rackham Merit Fellowship.

Table of Contents

List of Tables

List of Figures

List of Appendices

Abstract

The explosive energy demand by the communication and information technologies sector in the age of artificial intelligence (AI) calls for increasingly efficient electronics. One promising alternative to the inefficient electron-based information processing paradigm are the electrically neutral, Coulomb-bound electron-hole pairs known as excitons. Unlike electronics, excitonics lack the inherent capacitive delays and the associated energy losses that contribute to electronic hardware's energy inefficiency. While this particular advantage makes excitonics a promising platform for highly efficient communication and information processing hardware, conventional semiconductor materials in their bulk form are highly polarizable and screen out the Coulomb interaction that keeps excitons bound. As a result, excitonic hardware based on conventional semiconductors require cryogenic temperature operation, rendering them impractical for large-scale applications.

Motivated by these challenges, the research in this dissertation broadly focuses on exploring and leveraging the properties of excitons in a new class of two-dimensional (2D) semiconductors known as transition metal dichalcogenides (TMDs). TMD monolayers offer two fundamental advantages over conventional semiconductors. First, the reduced dielectric screening and strong Coulomb interactions stemming from their 2D nature lead to strongly bound excitons with binding energies one order of magnitude higher than that in conventional semiconductors. This property makes excitons in TMD monolayers remarkably stable at room temperature. Second, the band structure of TMD monolayers is highly sensitive to mechanical deformation, enabling the manipulation of excitons via engineered energy

gradients by subjecting the monolayers to non-uniform strain fields.

Specifically, this dissertation centers around three main aspects. First, the physical processes responsible for the deviation of diffusive transport of excitons in TMD monolayers from the conventional Fick's law of diffusion (anomalous diffusion), are investigated. The diffusion of excitons generated in tungsten diselenide (WSe_2) monolayers is studied by monitoring the time evolution of their photoluminescence (PL) intensity distribution. The two mechanisms giving rise to anomalous diffusion in the WSe_2 monolayers are the multi-capture and release of mobile excitons by traps, and the relaxation of the kinetic energy of excitons created non-resonantly. Both of these mechanisms lead to the nonlinear evolution of the mean squared displacement of the exciton distribution, which is a signature of sub-diffusive transport.

Second, the control of the flow of excitons via non-uniform strain in a WSe_2 monolayer is demonstrated by transferring it over a substrate with nanoscale features. The strain field is measured by mapping the PL spectra across the monolayer and calculating the resonance energy shift at the strained area relative to an unstrained point. The control of the flow was verified by exciting a Gaussian distribution of excitons at different points near the strained area of the WSe_2 monolayer, and monitoring the peak of the distribution over time. In all instances, the distribution's peak shifts toward the highest strain point of the monolayer, demonstrating the flow of excitons on demand.

Third, the signatures of quantum coherent effects in the nonlinear absorption spectrum of a molybdenum diselenide ($MoSe_2$) monolayer are identified via continuous-wave coherent optical spectroscopy. The nonlinear absorption spectrum of the $MoSe_2$ monolayer reveals two unique coherent processes: excitation-induced many-body scattering, and population pulsation resonances. These effects can be leveraged to implement coherent control schemes for quantum information applications.

These results represent a steppingstone in the development of hybrid quantum photonic-excitonic devices that meet the energy efficiency demands of the ongoing digital revolution

fueled by the advent of AI.

Chapter 1

Excitonics in the Era of AI

1.1 The unsustainable energy demand of the ICT sector

The growing demand for energy in the age of AI has posed an unprecedented challenge for science and engineering. As the demand for internet connectivity and mobile-phone traffic skyrockets, the information industry could lead to an explosion in energy use. Some of the most alarming forecasts predict that the global electricity use by the information and communication technologies (ICT) sector could range between 20% to 50% by 2030 [77]. Data centers alone currently use more electricity for cooling than the overall national energy consumption of some countries such as Iran, and about 1% of the global electricity demand [77]. Data centers contribute just about 0.3% to global carbon emissions as part of the overall 2% emissions coming from the entire ICT sector. Alarmingly, the electricity use by data centers is expected to increase about 15-fold by 2030 [77] as shown in Figure 1.1.1.

Power dissipation in information-processing systems is a major limitation at many levels. The energy waste of electronic hardware arises from the inherent resistive heating of their electrical components. Electrical interconnects are a particularly growing contributor to energy consumption in integrated circuits as they account for 30% to 50% of power con-

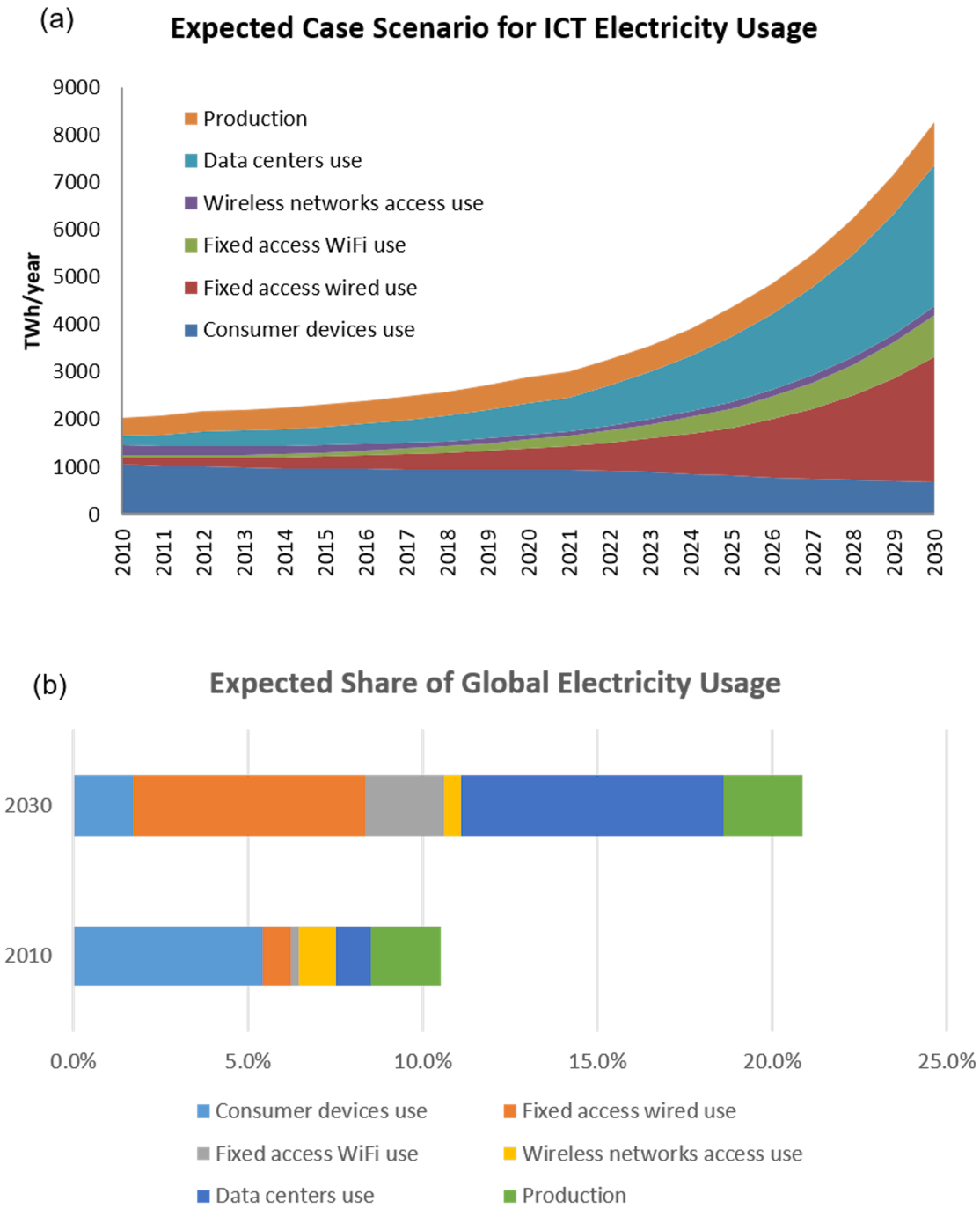

Figure 1.1.1: Expected trends in electricity consumption by the ICT industry sector between 2010 and 2030. (a) Breakdown of electricity consumption by ICT sub-sector and (b) expected share of the global electricity usage between 2010 and 2030. Reproduced with permission from [3].

sumption [114]. In addition, the speed of information processing is limited by the capacitive delays and energy spent in charging the lines (wires) of electrical circuits. Though the operating voltage may not be very large, the energy spent to charge the lines are on the order of [114]

$$E_s > C_l V_r^2 \tag{1.1.1}$$

where C_l is the capacitance of the line, and V_r is the operating voltage. Since the typical capacitance of well-designed electrical lines is about 200 aF/μm, this energy cannot be reduced much further other than by reducing the operating voltage [114]. While the total energy per logic operation is at the femtojoule level even in current silicon CMOS devices, the demand for processing power by the ongoing ICT technology revolution may require operational energies as small as tens of attojoules per bit [115]. Even the adoption of novel materials with remarkably low resistive losses such as graphene are expected to improve the resistive losses and transient delays of electrical interconnects only by a factor of 2-4 [7].

1.2 Alternatives to the current energy-inefficient information processing architecture

1.2.1 Optical interconnects

Optical interconnects naturally arise as an alternative to the inherently lossy electrical interconnects because optical lines do not need to be charged to the operating voltage; only enough energy to charge the photodetector at the receiving end is necessary. This benefit, known as quantum impedance conversion, follows from the photoelectric effect and it removes the distance-dependence of interconnect energy [115]. The relevant energy scale for comparison with electrical interconnects is the optical energy required to discharge the total capacitance of the photodetector and the electrical input that the interconnect is coupled

to. This energy scale is

$$E_p \geq C_d V_r \frac{\hbar\omega}{e} \tag{1.2.1}$$

where the voltage $\hbar\omega/e$ is equivalent to the energy of the photon. The inequality in Eq.1.2.1 accounts for the loss in the optical interconnect and the additional energy cost of the optical output device. Optical interconnects have the potential to be more energy-efficient than their electrical counterparts as long as $C_d\hbar\omega/e < C_l V_r$. Since photon energies are typically much larger relative to the operating voltage V_r, the real energy efficiency advantage of optical interconnects over electrical ones occurs if $C_d \ll C_l$.

While optical interconnects might appear as the most obvious alternative to address the shortcomings of electronic hardware, the size of optical devices is physically constrained by the diffraction limit to the size of the operating wavelength of light, which in turn limits the number of devices that can be integrated on a chip. To minimize these inefficiencies and limitations, the current hybrid optical-electronic information processing architecture relies on electrical components for short-distance information processing and optical interconnects for long-distance communication. However, the additional energy required to convert optical signals into electrical signals and vice-versa, and the packing limitation of optical components make this hybrid architecture inadequate to meet the increasing demands for energy efficiency of the ongoing information and communication technology revolution. Moreover, despite the potential advantages of optical interconnects over electrical ones, the economic cost of integrating optics with electronics on integrated circuits is very high whereas making wires on chips and boards is relatively inexpensive [114]. Being able to make the necessary optical and electronic components in a low-cost process compatible with conventional nano-fabrication technology will be essential for any commercial introduction of optical interconnects.

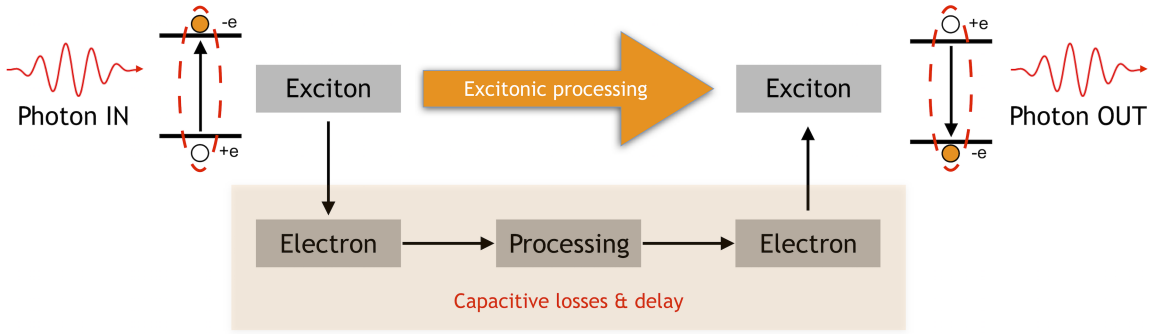

Figure 1.2.1: Schematic illustrating the working principle of excitonic information processing. A photon creates an exciton, which then performs logic operations without dissociating into free carriers, avoiding the capacitive delays and associated energy losses. The exciton finally recombines and emits a photon which then can excite another exciton. Illustration credit: Parag Deotare.

1.2.2 Exciton-based information processing

Another alternative to the shortcomings of the hybrid optical-electrical information processing architecture is to use excitons — Coulomb-bound electron-hole pairs — as the carriers of information instead of either electrons or photons. The mechanism of operation of exciton-based information processing is that when a semiconductor material absorbs a photon, an electron is promoted from the valence band to the conduction band, leaving behind a net positive charge or hole in the valence band. Subsequently, the excited electron can relax back into the valence band, regenerating the photon. In the meantime, Coulomb interactions in the crystal can bind the excited electron and the positive hole together to form an electrically neutral exciton. Most conventional semiconductor materials are highly polarizable and screen out the Coulomb interaction. Therefore, excitons are not typically observed in semiconductors such as silicon, where the electron and holes behave as free carriers [7].

Excitonic information processing eliminates the need to convert optical signals into electrical ones because excitons are formed via the absorption of light, and the logic operations can be carried out by the excitons themselves without the need to dissociate them into individual carriers. An illustration of the operating principle of exciton-based information processing in shown in Fig.1.2.1.

Moreover, exciton-based devices lack the inherent capacitive delays and energy losses arising from charging and discharging of the lines as excitons are electrically neutral quasi-particles. Moreover, their size is only a few unit cells across which is about one to two orders of magnitude smaller than the wavelength of visible light, making the exciton-based architecture fairly compact from the on-chip integration point of view.

While excitonic devices have been proposed and demonstrated in other semiconductor materials in the past, namely in AlAs and GaAs [20], the binding energy that prevents excitons from dissociating into individual carriers in those materials is much lower than room-temperature thermal energy. Such low binding energies require the use of cryogenic equipment to cool down those materials, making excitonics impractical for large-scale operation. Nevertheless, a new class of semiconductor materials known as transition metal dichalcogenide (TMD) monolayers has received significant attention over the past decade due to their remarkably large exciton binding energies. One order of magnitude larger than room-temperature thermal energy, such large binding energies make these materials a very promising platform for developing room-temperature robust excitonic devices.

In addition, their single atomic layer thickness makes TMD monolayers highly sensitive to mechanical deformations. For instance, the optical energy gap can be tuned by applying strain. Such tunability can be leveraged to control the motion of excitons by applying non-uniform strain to create energy gradients that result in the directional flow of excitons towards the regions of lowest energy. In addition, highly localized tensile strain can be used to create quantum dots — nano-structures that confine the motion of excitons in all three spatial dimensions — causing them to effectively behave like atoms. These structures may be used to implement coherent control schemes for quantum information technologies [178].

Both the design of a purely exciton-based information processing architecture as well as the development of novel quantum technologies that leverage the remarkable optical properties of TMD monolayers depend on a thorough understanding of the physical mechanisms that both enable and limit the transport performance and quantum coherence of excitons in

these materials. Similar to conventional electron-based devices, the transport performance of excitons in TMD monolayers is limited primarily by scattering. In the semi-classical limit, Boltzmann transport theory is able to describe the scattering of free excitons with phonons and crystal defects. However, the strong Coulomb interactions in TMD monolayers arising from their reduced dimensionality leads to many-body effects that require higher-level theories to describe effects such as excitation-induced scattering [177, 84]. The work in this thesis revolves around understanding the physical processes that impact the transport and coherence of excitons in TMD monolayers, and leveraging the tunability of their band structure with strain to enable the design of excitonic devices.

1.3 Survey of exciton transport and nonlinear spectroscopy in TMDs

Various efforts to benchmark the excitonic transport properties in TMD monolayers, primarily the exciton diffusivity, have been underway over the past few years [91, 90, 134, 33, 34]. For example, Kumar and colleagues in [91] used a transient absorption spectroscopy technique to study the diffusion of excitons in bulk and monolayer molybdenum diselenide ($MoSe_2$) at room temperature. They used a pump optical beam to generate an exciton density in the material, and after a specific time delay, they measured the reflectivity of the sample while spatially scanning a probe beam. This technique enabled them to indirectly visualize the broadening of the exciton distribution on a picosecond timescale and extract the exciton diffusivity of $MoSe_2$.

Similarly, Kulig and colleagues in [90, 134, 59] measured the diffusion of excitons on a suspended tungsten disulfide monolayer through spatially and temporally-resolved microphotoluminescence imaging at room temperature. In addition to extracting the exciton diffusivity, they observed a peculiar nonlinear behavior of the exciton population characterized by a spatial ring at high excitation densities. This type of nonlinear optical effect

have been linked to the complex band structure of TMD monolayers, and the interaction of non-equilibrium phonons with high-energy excitons [59, 90, 134, 153, 155]. A similar effect was discovered by our lab, and the details of these observations are presented in chapter 5. Other experimental efforts have centered around measuring the diffusivity of excitons in TMD monolayers at various lattice temperatures to isolate the thermally-activated processes that impact the exciton diffusivity. [22, 78, 60, 153].

In addition to measuring the diffusivity of excitons in TMD monolayers, various efforts to demonstrate the control of exciton motion using strain have emerged over the past few years [119, 33, 50, 63, 152]. Both static and dynamic strain have been used to control the flow of excitons. These approaches usually involve applying a local strain gradient with a nanoscale structure, which enables locally and reversibly steering the excitons over micrometer-scale distances [119, 33, 63]. Strain locally modulates the bandgap resulting in an energy gradient that drives the excitons towards the regions of highest strain.

In an analogous approach, the resonance energy of interlayer excitons in TMD heterostructures were tuned locally using electric fields. This approach was utilized to demonstrate an electrically controlled excitonic transistor in a MoS_2-WSe_2 van-der-Waals heterostructure at room temperature [190]. Unucheck and colleagues demonstrated the ability to manipulate the flow of inter-layer excitons by creating electrically re-configurable confining and repulsive potentials in a TMD-based heterostructure.

Beyond their promising potential as a platform for excitonic information processing, TMD monolayers exhibit strong many-body effects that could be leveraged to develop novel quantum technologies that could become part of the quantum internet [207, 5]. While the coherent nonlinear optical spectrum of TMD monolayers has not been investigated extensively, there have been various efforts to characterize the coherent properties of these materials, including dephasing times and many-body interactions, using multi-dimensional coherent optical spectroscopy in the time domain [117, 110, 118, 116]. These efforts have provided insight into exciton resonance broadening mechanisms such exciton-exciton and acoustic phonon

scattering.

In addition, continuous-wave nonlinear spectroscopic studies have reported the observation of remarkably narrow resonances that are typically associated with quantum dots [161]. These resonances have been associated with coherent population pulsation, a phenomenon that arises from the interference of the pump and probe optical fields through the excitation of the medium. Additionally, signatures of coherent many-body effects in the nonlinear optical spectrum of TMD monolayers have also been observed [4, 192, 175]. These effects are linked to Pauli blocking as well as exciton-exciton nonlinearities [177, 46, 80, 81, 79]. However, to the best of our knowledge, the first experimental observations of excitation-induced many-body spectral broadening and shifts in these materials are shown in chapter 6. These effects represent an opportunity to develop novel coherent control schemes based on the many-body states of TMD monolayers.

1.4 Summary of the work in this thesis

Chapter 2 provides an introduction to the physical properties and dynamic effects of excitons that are relevant for the remaining chapters of this thesis. First, the crystal and band structures of TMD monolayers are reviewed. Then, a brief survey of the key factors that impact the mobility and recombination dynamics of excitons is discussed. Lastly, an overview of some of the most intriguing nonlinear effects in both the high and low density limits of these materials is presented.

Chapter 3 describes the experimental technique utilized to image the motion of excitons in TMD monolayers and the physical models used to analyze these imaging data to extract the transport properties of excitons in these materials. In addition, the limitations of these models are discussed at the end of the chapter.

Chapter 4 discusses transport studies of excitons in a non-uniformly strained tungsten diselenide (WSe_2) monolayer. The WSe_2 monolayer was strained with a nanostructured sub-

strate to control the propagation of a Gaussian distribution of excitons. The tunability of the exciton band structure via strain enabled the creation of an effective excitonic potential that resulted in the funneling of excitons towards the high tensile strain points in the monolayer. This chapter also presented evidence of diffusive transport of excitons that deviates from the conventional Fick's law. Such deviation was characterized using the model of anomalous diffusion introduced in chapter 3.

Chapter 5 discusses transport studies of excitons in a hexagonal boron nitride (h-BN) encapsulated tungsten diselenide (WSe_2) monolayer. Similar to the observations in chapter 4, evidence of anomalous diffusion in the h-BN encapsulated WSe_2 monolayer was observed. The origin of such behavior in this sample, however, was traced to the relaxation of the excess kinetic energy of the excitons generated with a non-resonant optical excitation.

Chapter 6 discusses studies of the nonlinear optical response of a hexagonal boron nitride (h-BN) encapsulated molybdenum diselenide ($MoSe_2$) monolayer and the modeling of the macroscopic optical polarization using the master equation to interpret the signatures of many-body effects. The main experimental observations are excitation-induced broadening and shifts of the exciton resonance. While modeling of the full many-body state requires a higher-level theory, the main experimental observations were qualitatively reproduced with the master equation-based model.

Chapter 7 summarizes the work in this thesis, and suggests some future directions.

Chapter 2

Introduction to TMDs

2.1 Introduction

Ever since the discovery of graphene, which led to the Nobel Prize in Physics in 2010 [53, 55, 25], the search for other two-dimensional (2D) materials exhibiting exotic physical properties as a result of their reduced dimensionality and crystal symmetry has become one of the largest endeavors of this decade in the fields of nano-science and engineering. Among this new class of 2D materials are transition metal dichalcogenides (TMDs). TMDs have received ample attention due to their remarkable optical properties, which make them promising candidates for a wide variety of applications in photonics, optoelectronics [106], and valleytronics [162].

TMDs are found naturally occurring in nature as layered and three-dimensional structures, but only the layered crystals, can be cleaved down to single monolayers. Monolayer TMDs are between 6 and 7 angstroms thick, and they comprise of a layer of transition metal atoms, typically molybdenum (Mo) and tungsten (W), packed in a hexagonal plane sandwiched between two planes of chalcogen atoms, typically sulfur (S) and selenium (Se). The bonds among the in-plane atoms are covalent, but their inter-layer interaction is a weak van-der-Waals force that enables the crystal to readily cleave along each layer surface [30]. While they can adopt either a trigonal prismatic or octahedral structures, the most-studied

crystals are the group VI TMDs, which have trigonal prismatic structures, and have out-of-plane mirror symmetry and broken in-plane inversion symmetry [106]. The crystal structure of group VI TMDs is shown in Fig.2.1.1.

2.2 Band structure of TMDs

TMDs are indirect bandgap semiconductors in their bulk form, but their bandgap becomes direct when they are cleaved down to single monolayers [198]. The corresponding band extrema are located at the K and K' points of the hexagonal Brillouin zone, most commonly referred to as the K and K' valleys. The energy degeneracy of the conduction and valence bands at these valleys are split due to spin-orbit coupling (SOC). The splitting at the K point in the valence band is around 0.2 eV for molybdenum-based TMDs, and about 0.4 eV for tungsten-based TMDs [198]. This coupling gives rise to two valence sub-bands and therefore two types of excitons, known as A and B excitons, which involve holes from the upper and lower energy spin states, respectively. SOC is also responsible for the locking of the spin and valley degrees of freedom: the spin-up state at the K valley is degenerate with the spin-down state at the K' valley as shown in Fig.2.2.1. Although to a smaller extent, the conduction band minima are also split, and depending on the metal atom, the splitting has a different sign: negative for molybdenum-based TMDs, and positive for tungsten-based TMDs as shown in Fig.2.2.1. As a result, and in marked contrast to typical GaAs quantum wells, the spin degeneracy of both conduction and valence bands at the K and K' points of TMDs is fully lifted [198]. Moreover, the conduction band splitting results in an energy separation between the spin-allowed or optically bright transitions and the the spin-forbidden or optically dark transitions as shown in Fig.2.2.1.

The broken inversion symmetry of TMD monolayers results in finite Berry curvatures and orbital magnetic moments of opposite sign at the K and K' valleys, which give rise to unique valley-dependent chiral optical selection rules. The absorption of left or right

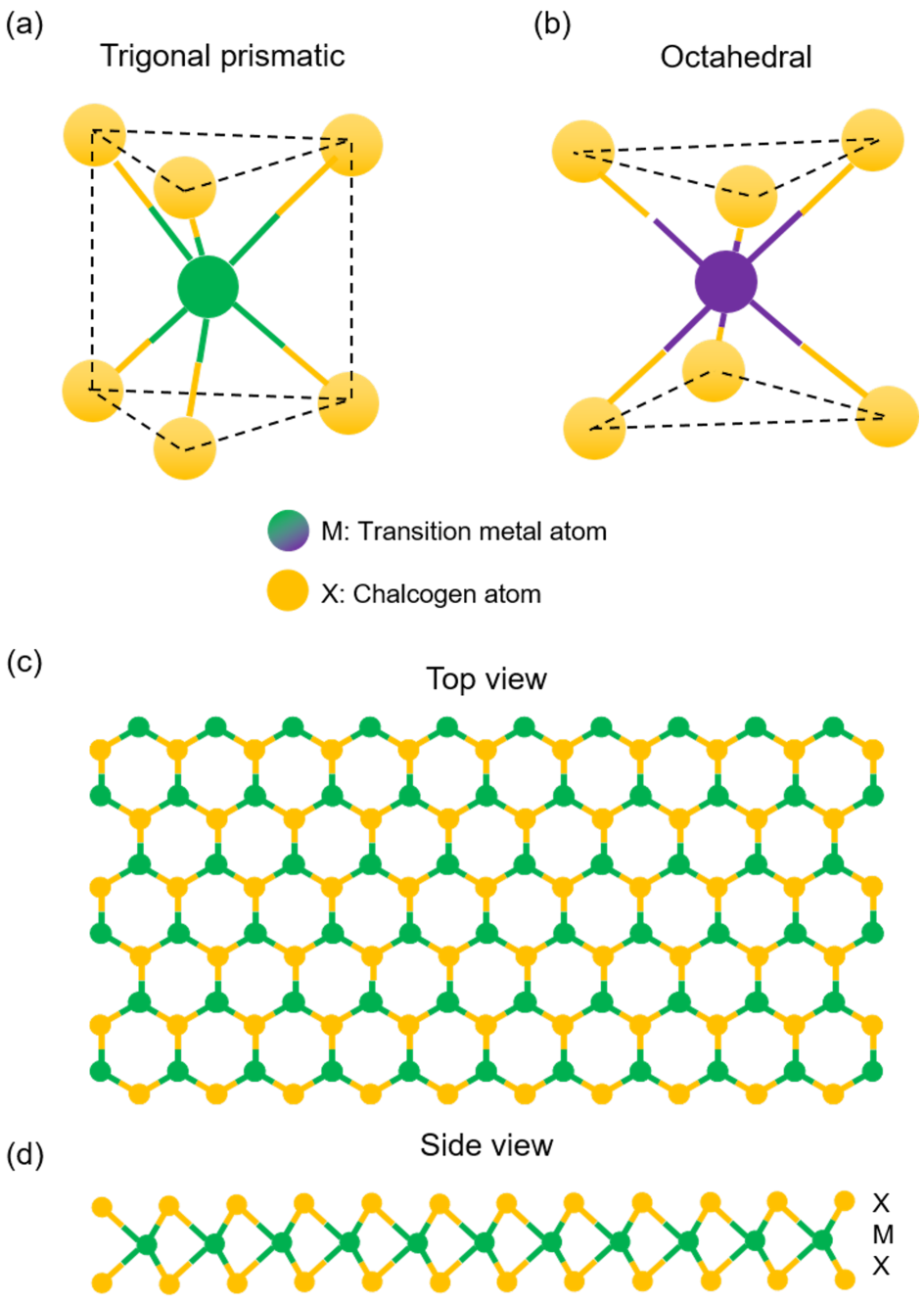

Figure 2.1.1: Crystal structure of TMD monolayers. The local coordination of the metal species can be (a) trigonal prismatic and (b) octahedral. (c) Top and (d) side views of a single layer TMD with trigonal prismatic coordination [87, 30]. Reproduced with permission from [87].

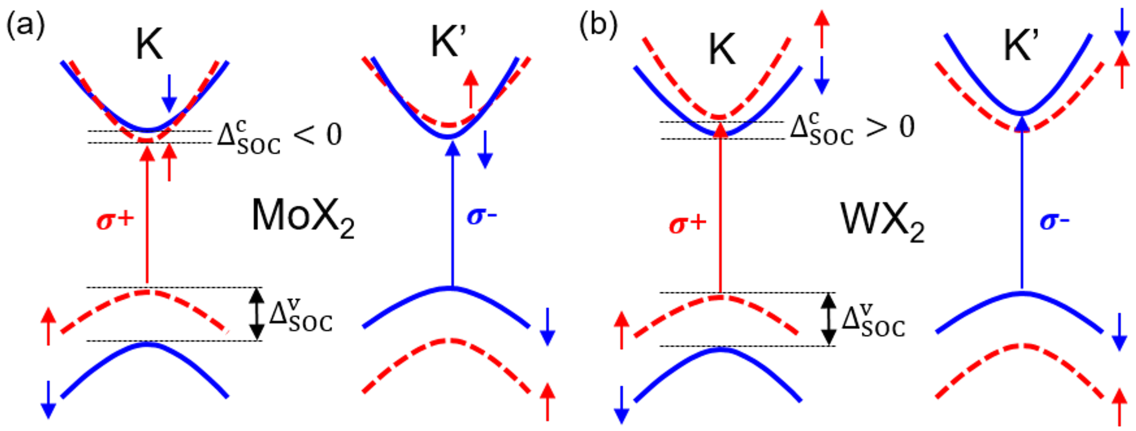

Figure 2.2.1: Schematic illustration of the single-particle band structure of TMD monolayers showing the direct bandgap and the spin-orbit splitting of the conduction and valence bands at the K and K' points of the hexagonal Brillouin zone. The order of the conduction bands is opposite in MoX_2 (a) and WX_2 (b) monolayers. Reproduced with permission from [198].

circularly polarized light transitions are allowed only in a particular valley [106]. As a result, optically generated electrons and holes are both valley and spin polarized, a phenomenon that is referred to as spin-valley locking. Spin-valley locking is the basis for many valleytronics applications of TMD monolayers [162].

The optical spectra of TMD monolayers feature pronounced peaks associated with exciton resonances, which inherit the chiral optical selection rules of the electronic band structure. The exceptionally strong Coulomb interactions in TMD monolayers lead to tightly-bound excitons with binding energies on the order of 500 meV — an order of magnitude higher than conventional semiconductors [118]. In addition, higher-order excitonic quasi-particles such as trions and bi-excitons are typically observed in the optical spectra of TMDs, especially at low temperatures. The bandgap, binding energies, and spin-orbit coupling splitting of the bands of TMDs are summarized in table 2.2.1.

2.2.1 Exciton band structure

In addition to the spin-forbidden states resulting from SOC interactions in TMD monolayers, momentum-forbidden dark states also play a significant role in their optical properties. The

Table 2.2.1: Electronic properties of TMD monolayers [106].

Property	MoS_2	$MoSe_2$	WS_2	WSe_2
Effective mass (m_0)	0.5	0.6	0.4	0.4
Optical gap (eV)	2	1.7	2.1	1.75
Exciton binding energy (eV)	0.55	0.5	0.5	0.45
Conduction band splitting (meV)	-3	-20	30	35
Valence band splitting (meV)	150	180	430	470

relative position of these dark states with respect to the optically accessible bright states has a crucial impact on the emission efficiency of these materials [198]. Besides the typical K and K' valleys, TMDs exhibit two additional conduction band minima at the Λ and Λ' points of the hexagonal Brillouin zone, and one additional valence band maximum at the Γ point of the hexagonal Brillouin zone. Coulomb-bound electron-hole pairs involving electrons and holes located in different valleys can form, resulting in momentum-forbidden dark excitonic states. In addition, excitonic states with the hole located at either the K or Γ points, and the corresponding electron at either the Λ, Λ', K, and K' points can form. All of these states cannot be accessed optically because photons cannot provide the required center-of-mass momentum for the transition to occur. A diagram of optically bright, spin-dark, and momentum-dark exciton states are shown in Fig.2.2.2 and Fig.2.2.3.

2.2.2 Band structure tunability

The band structure of TMDs is highly sensitive to lattice deformations; TMD monolayers are more sensitive to strain than other 2D materials such as graphene [76]. Lattice deformations give rise to different energy shifts for optically bright and dark excitonic states, which can radically change the energy landscape, the efficiency of intervalley scattering, and the influence of each state on the recombination dynamics and transport properties of excitons and charge carriers [152]. Figure 2.2.4 shows a schematic diagram of the effect of strain on the lattice, bandgap energy, and excitonic states [42, 152].

Lattice deformations also lead to changes in effective carrier masses, giving rise to a

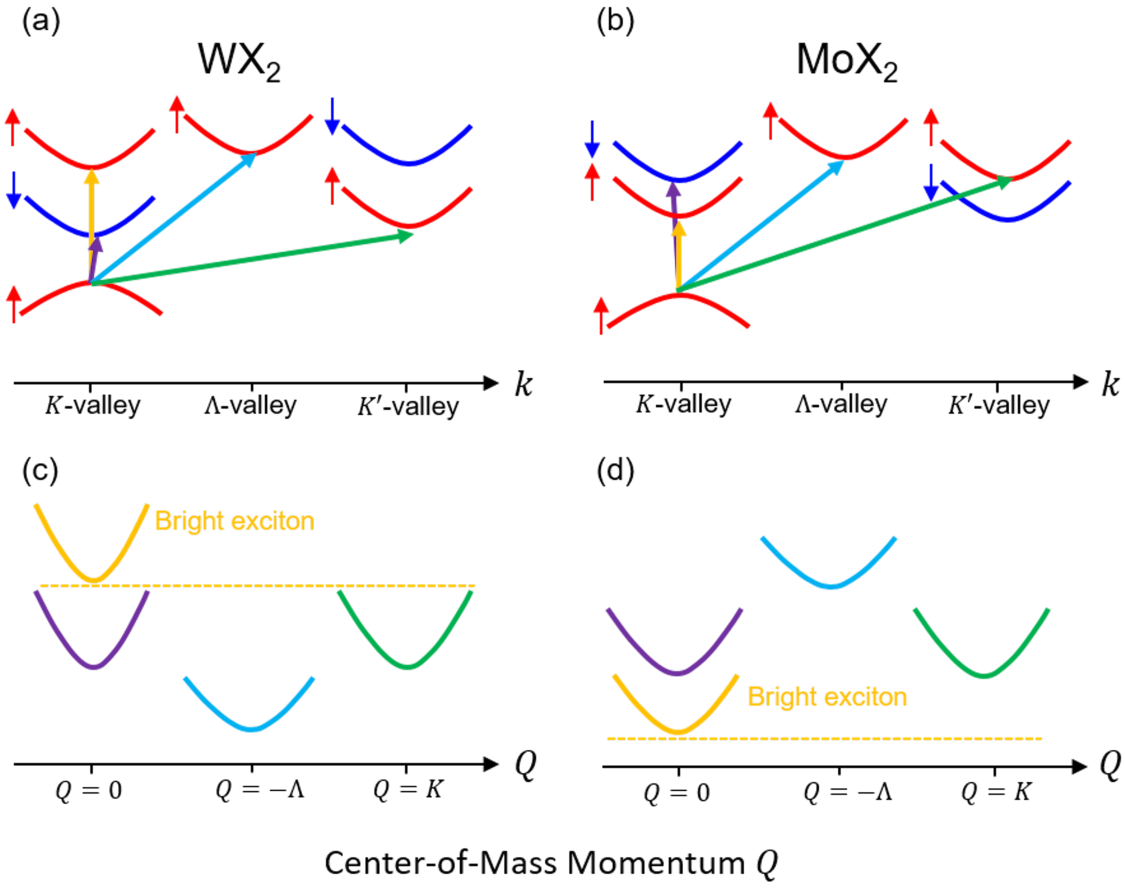

Figure 2.2.2: Electron dispersion around the K, Λ, and K' valleys for (a) tungsten-based (WS_2 and WSe_2) and (b) molybdenum-based TMDs (MoS_2 and $MoSe_2$) with the hole located at the K valley, indicating the optically bright, spin-dark, and momentum-dark transitions. The spin-orbit splitting of the valence bands is not shown since it is a few hundreds of meV, contributing to B excitons. Exciton dispersion of (c) tungsten-based and (d) molybdenum-based TMD monolayers. While in molybdenum-based TMDs, the bright exciton is the energetically lowest-lying state, in tungsten-based TMDs, the dark exciton is the lowest-lying state. Reproduced with permission from [107].

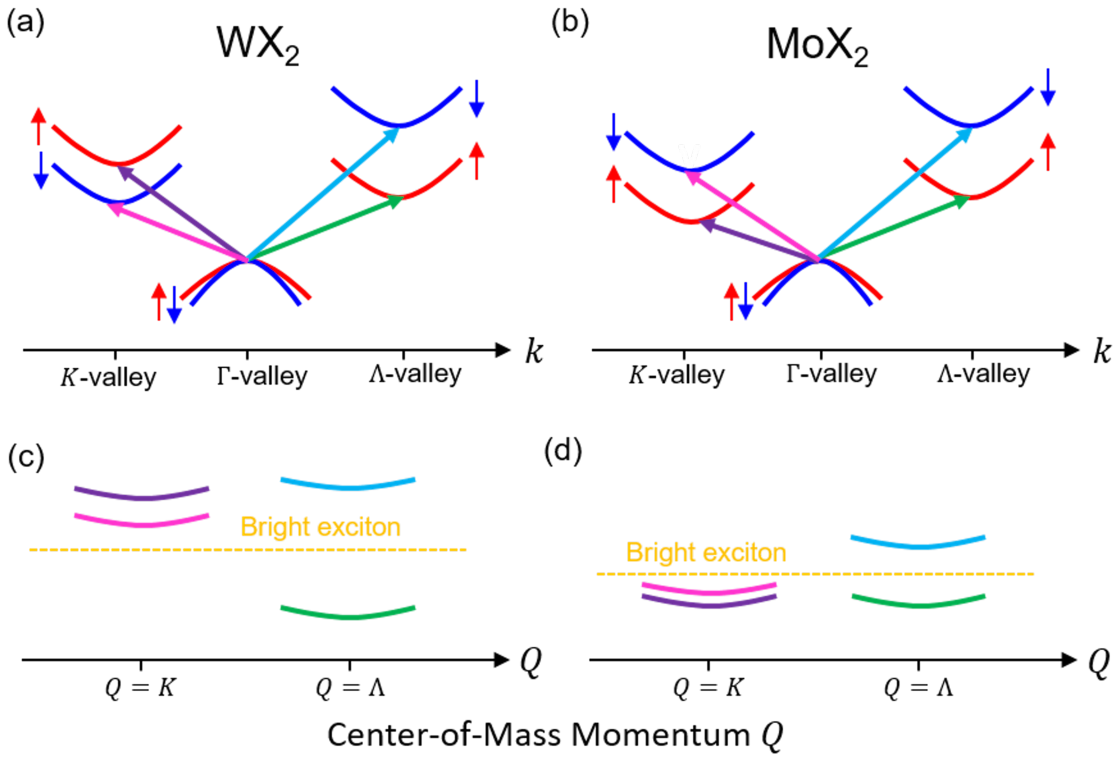

Figure 2.2.3: Electron dispersion around the K, Γ, and Λ valleys for (a) tungsten-based (WS_2 and WSe_2) and (b) molybdenum-based TMDs (MoS_2 and $MoSe_2$) with the hole located at the Γ valley, indicating the spin and momentum-dark transitions. Bright excitons do not appear since there is no direct bandgap at the Γ point. Since the valence band at the Γ point is not spin-orbit split, there is a degenerate momentum-forbidden state for every spin-forbidden state. Exciton dispersion of (c) tungsten-based and (d) molybdenum-based TMD monolayers corresponding to the valleys in (a) and (b). Most of the states in tungsten-based TMD monolayers are above the bright exciton whereas in molybdenum-based TMD monolayers, most states are below the bright exciton. Reproduced with permission from [107].

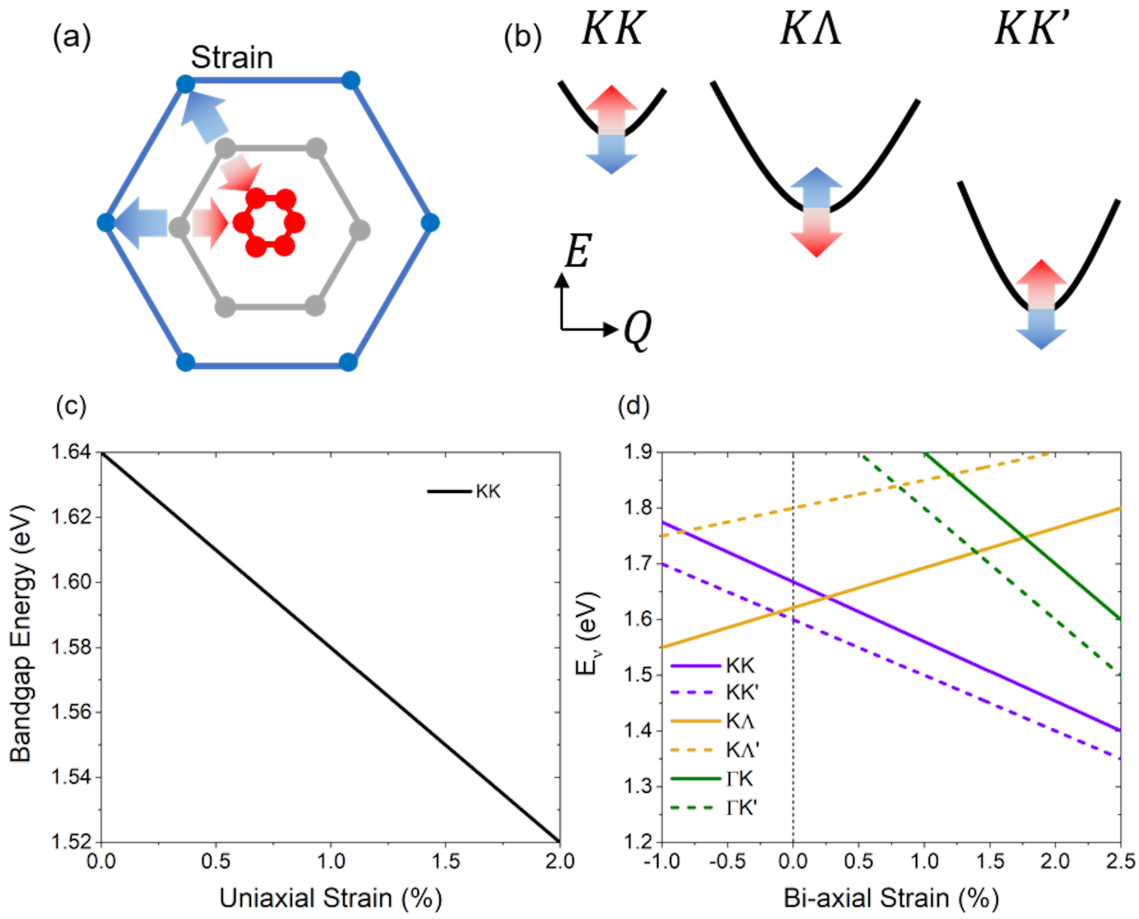

Figure 2.2.4: Strain-dependent exciton band structure of TMD monolayers. (a) At the atomic scale, strain implies lattice deformations, which shift (b) the excitonic band minima, and modify the (c) bandgap energy of the monolayers [42]. (d) Strain-dependent energy shifts of the minima of the optically bright KK, and momentum-dark KK', $K\Lambda^{(\prime)}$, and $\Gamma K^{(\prime)}$ excitons [152]. Reproduced with permission from [152].

reduction in the excitonic binding energy, modifications to the optical selection rules due to strain-induced changes in the crystal symmetry, and radiative broadening of the excitonic resonances due to changes in the lattice structure and in the orbital wavefunctions [48]. Figure 2.2.5 shows a schematic diagram of the effect of uniaxial and biaxial strain on the lattice, conduction band, and excitonic absorption spectrum of TMD monolayers. In the presence of tensile biaxial strain, the atoms are symmetrically pulled apart in both directions, maintaining the hexagonal lattice structure symmetric. In momentum space, the biaxial deformation leads to a decrease of the Brillouin zone. Moreover, due to the larger distance between metal and chalcogen atoms, the orbital function overlap is reduced. In the case of tensile uniaxial strain, however, the hexagonal structure becomes asymmetric both in real and momentum space. Besides the reduced orbital overlap, the atomic orbital functions also become elliptic in the direction of strain. Strain also produces an overall redshift in the exciton absorption peak. The redshift arises from a decrease in the orbital overlap leading to a reduced bandgap, and a decrease in the effective carrier masses, which in turn leads to weaker bound excitons [48].

In addition, tensile strain leads to a direct-to-indirect band gap and a semiconductor-to-metal transition [76]. Such tunability of their band structure makes TMD monolayers an exceptional candidate for optoelectronic and excitonic devices with tunable optical and electronic properties through the introduction of strain. Chapter 4 focuses on the use of strain to control the motion of excitons in TMD monolayers by leveraging the tunability of their band structure to create engineered energy potentials that drive the motion of excitons on demand.

2.2.3 Defect-bound excitons

Besides the variety of optically bright and spin and momentum-dark exciton states, single-photon emission from defect states has also been observed in TMD monolayers [66, 147, 187, 186]. This type of emission originates from excitons that are confined to zero dimensions by

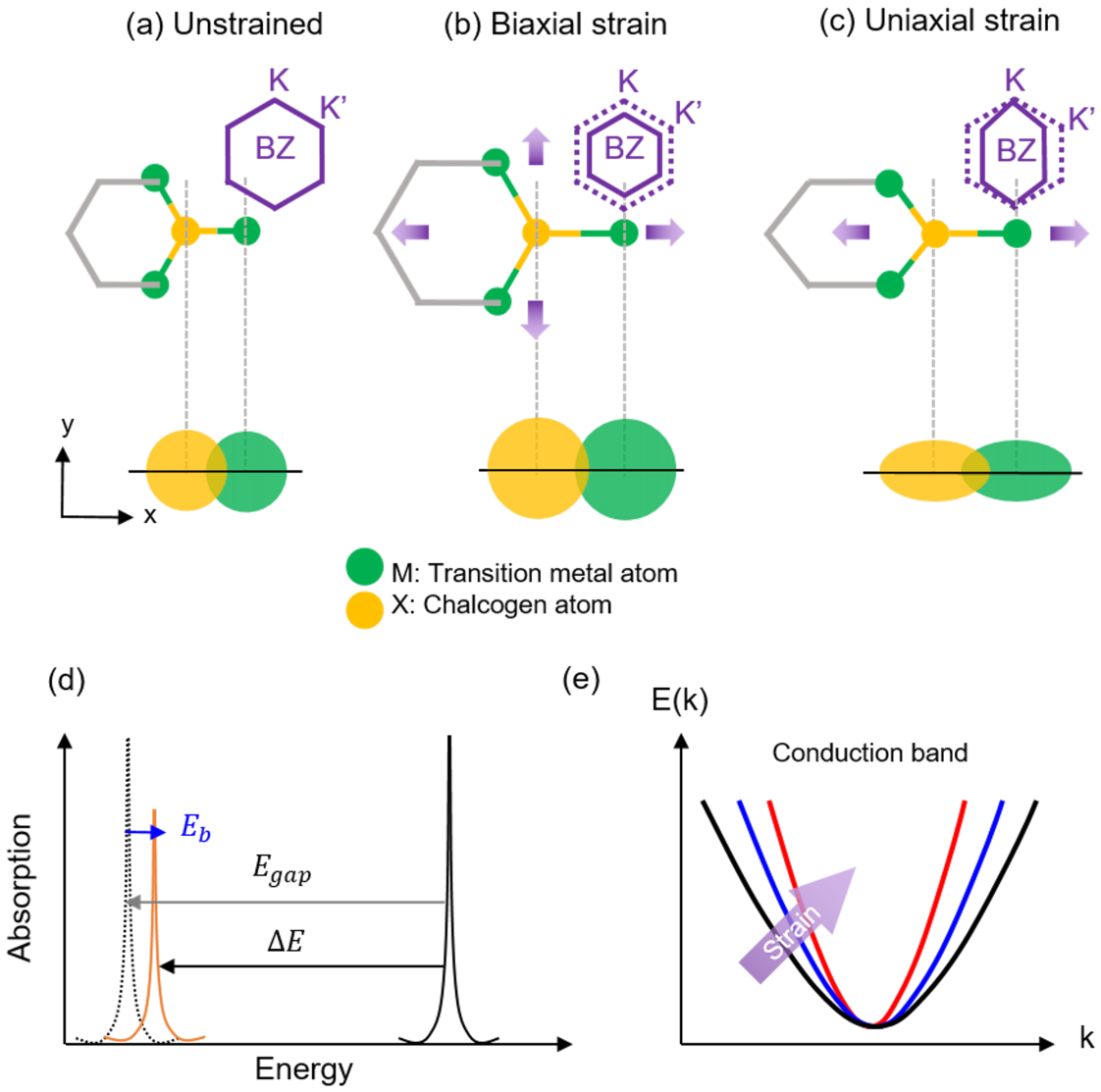

Figure 2.2.5: Effect of strain on binding energy and effective mass. (a)-(c) The upper panels show the hexagonal lattice structure in real space and the corresponding Brillouin zone (BZ) in momentum space for (a) unstrained, (b) bi-axially strained, and (c) uni-axially strained monolayers. The bottom panels show the corresponding orbital functions. (d) Shift in the absorption peak of excitons due to strain. (e) Sketch of the effect of strain on the dispersion of the conduction band at the K point. Reproduced with permission from [48].

a "potential well" generated by a local strain field or a crystal defect [187]. Single-photon emission from defect states in TMD monolayers is particularly relevant to the the development of quantum photonic technologies such as quantum key distribution [100], which rely on the generation of wavelength tunable single photons with reliable quantum correlations.

The tunability of the band structure of TMD monolayers via strain enables the deterministic generation of single-photon emission by locally straining the monolayers. Applying strain to a nanoscale region of a TMD monolayer changes its optical gap and binding energy, hence tuning the emission wavelength of defect-bound excitons localized to the strained area of the monolayer. Moreover, the energy gradient created by the localized strain can drive the "funneling" of free excitons generated by a non-resonant optical excitation toward the point of highest strain where they are subsequently trapped by defects. While there have been many attempts to create quantum dots by confining excitons with localized strain pockets in TMD monolayers, the key role that strain plays in these approaches is to increase the local density of free excitons at the positions of highest strain, thus increasing the probability of excitons to be captured by the defects in the strained area [15]. A diagram of the strain-induced capture of free excitons by defects in strained TMD monolayers is shown in Fig.2.2.6.

2.3 Transport properties and h-BN encapsulation

Much like their optical properties, the transport properties of carriers in TMD monolayers are largely susceptible to intrinsic defects [68, 145, 140, 183, 88]. Some of the major causes of mobility degradation are attributed to intrinsic carrier-phonon scattering and structural defects such as vacancies, grain boundaries, and anti-sites [145, 88]. In addition, scattering with extrinsic defects such as interfacial charges, impurities [56, 95], and substrate phonons[103] further degrade the carrier mobility in monolayer TMDs. Similarly, the transport properties of excitons in TMD monolayers are severely affected by both intrinsic and extrinsic crystal

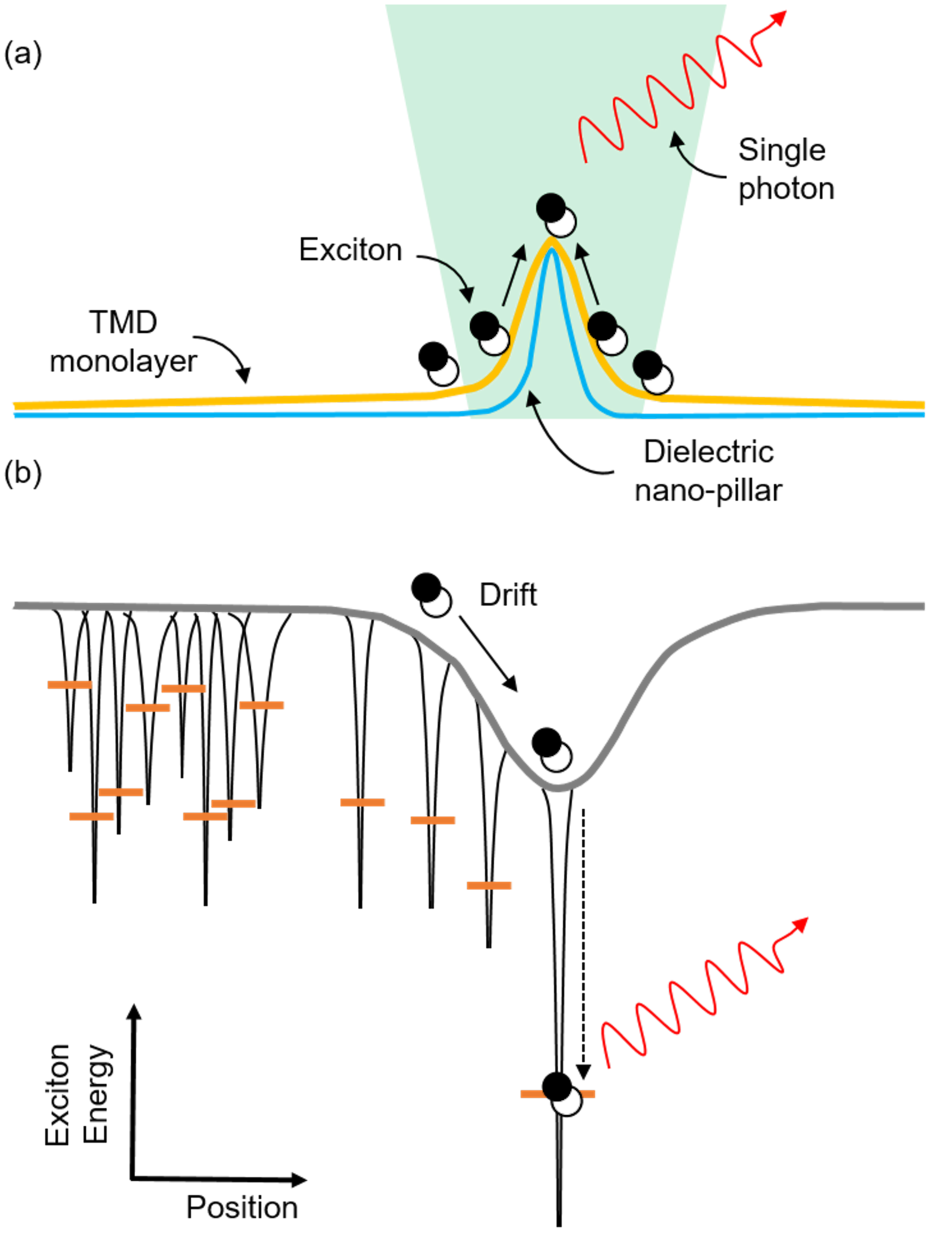

Figure 2.2.6: Schematic of strain-controlled single-photon emission from defects in TMDs. (a) A TMD monolayer is deformed by a nano-pillar to achieve a localized elastic strain perturbation. (b) The strain locally modulates the monolayer's bandgap. Superimposed on this artificial modulation of the exciton energy are randomly distributed localized trap states. Optically created excitons efficiently funnel to an individual strain-tuned localized exciton trap at the nano-pillar center resulting in a single highly efficient quantum emitter. Reproduced with permission from [15].

defects [218].

Their reduced dimensionality makes TMD monolayers particularly susceptible to substrate-related extrinsic defects, which radically influence the energetic disorder and the diffusion properties of excitons [218, 39]. The influence of extrinsic defects is typically mitigated by controlling the fabrication process and carefully isolating the monolayers from the substrate-related defects that lead to energetic disorder. Unfortunately, the standard Si/SiO_2 substrates that are widely used by the 2D materials community are not ideal as they contain charged surface states and impurities [168], surface roughness [131], and surface optical phonons [39] that induce changes in the background doping levels and exciton recombination rates [19]. However, due to its atomically smooth and chemically inert surface, which is relatively free of dangling bonds and charge traps [70], hexagonal boron nitride (h-BN) has become the standard capping material across the 2D materials community. Encapsulation of TMD monolayers with h-BN suppresses exciton-exciton annihilation [70], and reduces the inhomogeneous spectral broadening of their optical spectra [21, 110]. The typical low-temperature emission linewidth of TMD monolayers transferred over standard SiO_2/Si substrates is on the order of 10 meV. This linewidth is dominated by energetic disorder in the local environment as a result of impurities on the substrate's surface or adsorbed during the fabrication process. The key roles of h-BN encapsulation are to protect the sample surface from possible physical and chemical adsorption during experiments, to provide an atomically flat surface for sample exfoliation [108], and to prevent the doping of the monolayer by the SiO_2 substrate [21]. As a result, the linewidth of the low temperature emission spectra narrows down to a few meV, which reflects the intrinsic optical properties of TMD monolayers.

2.4 Recombination dynamics

The non-equilibrium dynamics and transport of excitons in TMD monolayers is dominated to a large extent by dark excitons [17, 107]. While unable to recombine radiatively, these states tend to be sufficiently long-lived that they recombine either through out-of-plane polarized emission [197] or phonon-assisted recombination, resulting in spectral features located energetically below the optically bright excitons [154, 16]. At high temperatures, the emission spectrum is dominated by optically bright excitons at the KK valley. Nevertheless, even at high temperatures, the phonon assisted recombination of momentum-dark excitons leads to an asymmetric emission spectrum [16].

At low temperatures, the emission spectrum acquires multiple indirect recombination peaks below the bright exciton arising from the phonon-assisted recombination of the energetically lowest KK' exciton. The phonon-assisted peaks become only visible at low temperatures because the excitons are forced to undergo an indirect recombination to a virtual state since scattering back to the bright states is energetically unfavorable [16]. A schematic of the phonon-assisted recombination processes that occur in TMD monolayers is shown in Fig.2.4.1.

2.5 High-density nonlinear effects

In addition to playing a key role in the emission spectrum of excitons in TMD monolayers, the efficient coupling of excitons to phonons play a critical role in their spatial and temporal dynamics. At high excitation densities, in particular, signatures of nonlinear optical effects arising from their interaction with non-equilibrium phonons are observed in the spatial dynamics of excitons. For example, the formation of spatial rings in the emission profile as a result of thermal currents of excitons created by the absorption of hot optical phonons has been observed [134, 90]. A sufficiently strong exciton temperature gradient is able to drag ex-

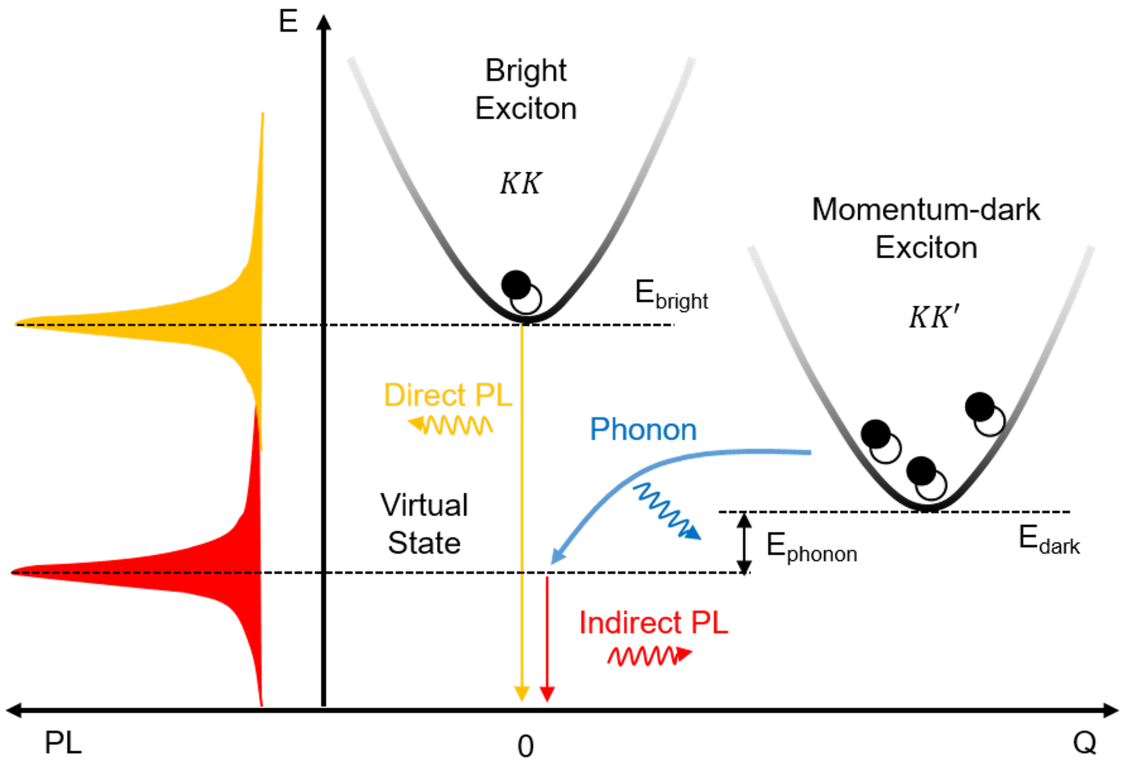

Figure 2.4.1: Sketch of phonon-assisted recombination of momentum-dark excitons in TMD monolayers. Momentum-dark excitons in the KK' valley decay by emitting or absorbing a phonon and subsequently emitting a photon, which contributes to the indirect PL signal. Reproduced with permission from [16].

citons out of the hot region leading to the appearance of spatial rings. Such nonlinear effect is induced by the emission and re-absorption of hot optical phonons and exciton-exciton Auger recombination, which act as a heating mechanism giving rise to strong spatial gradients in exciton temperature [134, 59].

2.6 Coherent many-body effects

Generally, the direct extraction of the full many-body quantum state of solids is challenging because of their overwhelmingly large number of degrees of freedom [177]. Optically excited direct-gap semiconductors such as TMD monolayers are an ideal platform for determining their many-body state because the nonlinear optical properties of the excitonic absorption depend strongly and uniquely on the particular many-body state [177]. Resonant or non-resonant optical excitation of direct-gap semiconductors induces an optical polarization that can be converted into electron-hole pair excitations and possibly into Coulomb-bound excitons. Thus, the actual many-body state contains a mix of polarization, electron-hole plasma, a fraction of excitons, and higher-order correlations [177].

In addition, the intricate band structure of TMD monolayers adds an additional level of complexity to the many-body quantum state due to the numerous channels of inter and intravalley scattering among optically accessible and spin and momentum-dark states. Nevertheless, the signatures of many-body interactions are evidenced uniquely in the nonlinear absorption spectra of these materials, and they include excitation-dependent spectral shifts linewidth and broadening. The control of these many-body quantum states can lead to the development of novel quantum technologies beyond two-level systems such as self-assembled semiconductor quantum dots.

2.7 Summary

This chapter provided an introduction to the most relevant physical properties of transition metal dichalcogenide monolayers for the studies of exciton transport and nonlinear spectroscopy discussed in this dissertation. Particularly, the complex band structure of TMD monolayers and the ability to tune the band structure with strain were discussed. This chapter also highlighted the role of bright, dark, and defect-bound excitonic states as well as h-BN encapsulation on the emission spectra of TMD monolayers. Lastly, a brief descriptions of some of the nonlinear optical effects that are relevant to transport and spectroscopy measurements of TMD monolayers in this thesis were presented.

Chapter 3

Experimental Technique for Exciton Imaging

3.1 Exciton imaging technique

3.1.1 Experimental setup

The transport of excitons in TMD monolayers was studied by measuring the time-resolved photoluminescence (TRPL) intensity of the monolayers using a custom-built confocal microscope similar to the one described in reference [2]. The imaging setup is similar to a laser-scanning confocal microscope, but the PL emission spot is magnified 90-fold using a high-numerical-aperture 60X objective lens, and the 1.5X zoom lens internal to the microscope. An avalanche photodiode detector (APD) with a square active area of 50 μm $\times$ 50 μm is then scanned across the magnified emission spot to obtain a map of the PL intensity as a function of time and position on the sample. A schematic diagram of the setup is shown in Fig.3.1.1.

Generally, the laser excitation source is a diode laser producing pulses of approximately 50 ps in duration, at a repetition rate of 40 MHz, and at a wavelength of 405 nm. The laser is

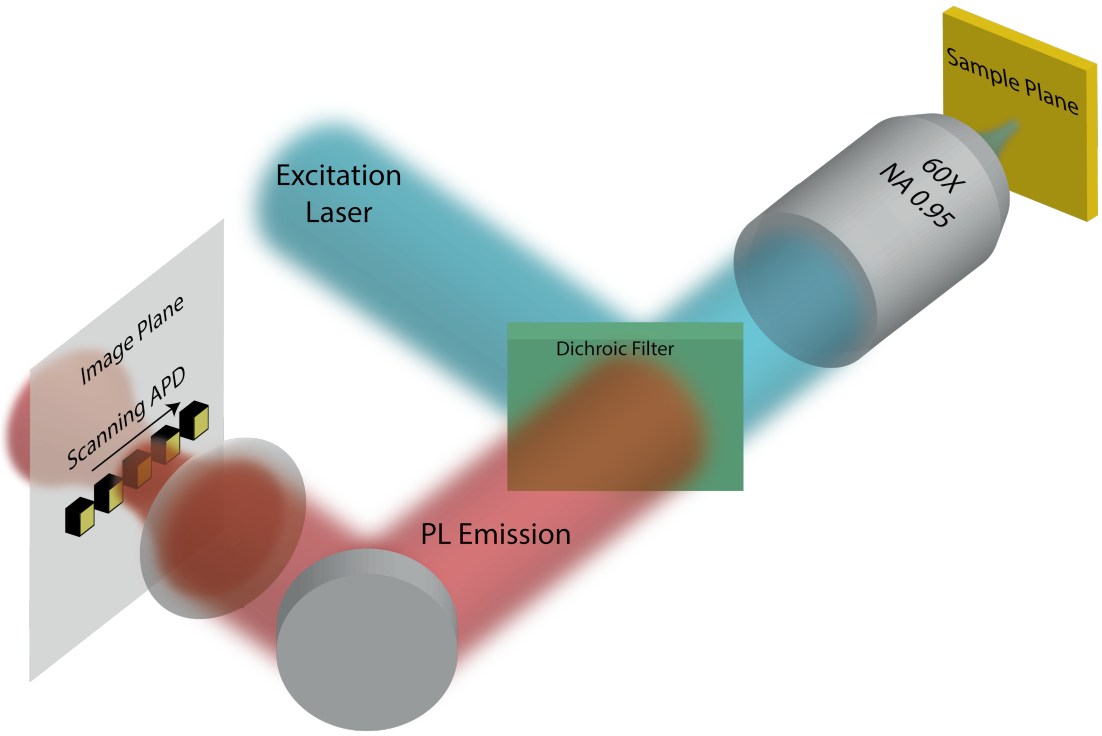

Figure 3.1.1: Experimental setup for exciton imaging in TMD monolayers. A detailed description of the setup is in the text. The illustration is courtesy of Parag Deotare.

coupled into a single-mode optical fiber to produce a beam with a Gaussian intensity profile. The output of the fiber is then collimated and directed into the back of an inverted optical microscope where a long-pass dichroic mirror with a cutoff wavelength of 405 nm reflects the laser into the objective lens (60X, NA=0.95). The objective lens focuses the beam down to a near-diffraction-limited spot with a FWHM of approximately 500 nm as determined from imaging the laser reflection spot.

The sample is mounted above the objective lens on a piezoelectric scanning stage that enables selectively exciting the sample at the position of interest. The scanning capability of the stage is used during measurements only when building PL spectrum raster maps of the sample such as the one shown in Fig.4.2.3. For imaging the motion of excitons, however, the piezoelectric stage is fixed at the position of interest, and it is moved only to excite new positions in the sample between measurements.

The PL emission from the sample is collected by the same objective lens, and the resulting collimated beam passes through the dichroic mirror and is focused by a 1.5X zoom lens down to a region outside of the microscope. The focal plane of this lens is determined by scanning the APD along the optical axis to find the smallest PL spot as determined from the highest PL intensity counts. The APD is mounted on a set of three computer-controlled linear translation stages that enable scanning the APD along the optical axis and the focal plane of the lens.

The output of the APD is connected to a timing module with a resolution of 1 ps (PicoQuant HydraHarp 400), which detects the arrival time of each photon relative to an electrical trigger pulse. This technique, known as time-correlated single photon counting (TCSPC), results in a histogram of photon arrival times which corresponds to the time-dependent rate of photon emission from the sample. The following section provides more details of the TCSPC technique.

Lastly, the APD detector is scanned across the emission spot in either the vertical or horizontal direction, and the TRPL intensity trace is recorded at each detector position

resulting in a map of PL intensity along one axis of the sample as a function of time. The detector is shielded from stray light to reduce the background dark counts.

3.1.2 Time correlated single photon counting

Measuring the time evolution of the photoluminescence of semiconductors, including but not limited to TMD monolayers, is a nontrivial task. Resolving the dynamics of exciton emission from a single-shot excitation cannot be accomplished simply by detecting their PL emission with a photodiode detector and a fast oscilloscope because the typical timescales of the PL dynamics range between tens of picoseconds to a few nanoseconds, and reconstructing the signal would require the detection of at least a few tens of samples per cycle. Such precise temporal resolution is difficult enough to achieve, but on top of that, the emitted light may be simply too weak to create an analog voltage representing the photon flux. In fact, the optical emission may consist of a few photons per excitation cycle, making the discrete nature of the signal itself an obstacle for the analog sampling of the PL evolution.

These problems can be overcome by with a technique known as time-correlated single photon counting or TCSPC, where the data collection is extended over multiple cycles of excitation and emission by using a periodic excitation such as a pulsed laser [196, 128, 11]. TCSPC is based on the repetitive, precisely-timed registration of single photon emission events, relative to the optical excitation pulse, accomplished using a highly-sensitive photodetector such as an APD. Provided that the probability of detecting more than one photon per cycle is low, the histogram of photon arrival times represents the time decay of the PL intensity of the sample that would have been obtained in a single-shot analog recording [196]. The condition of single photon probability is a desirable advantage not only because it can be accomplished simply by attenuating the light intensity at the sample, but also because it prevents unwanted nonlinear optical effects in the sample at higher excitation levels.

Figure 3.1.2 shows a schematic diagram of how the histogram of photon arrival times is recorded over multiple cycles. The APD signal consists of a train of randomly distributed

electrical pulses corresponding to the detection of individual photons. During certain cycles a single photon event is recorded by the APD, but there are also cycles when no photon arrival events are recorded. Over many cycles, however, the histogram reconstructs the evolution of the PL intensity.

Unlike traditional methods of analog signal processing, the timing resolution of TCSPC is not limited by the width of the detector impulse response. Instead, the timing accuracy of TCSPC is determined by the transit time spread of the single photon pulses in the detector, and the trigger accuracy of the electronics [11]. As such, a trigger signal from a sufficiently narrow pulse is desirable.

The high accuracy of TCSPC, and the ability to scan the APD across the emission spot to reconstruct the evolution of the PL intensity at different positions enable the imaging of the exciton density generated by the optical laser excitation with a Gaussian intensity profile. The following section discusses how imaging of the resulting Gaussian PL intensity spot enables the extraction of the transport properties of excitons in TMD monolayers.

3.2 Exciton diffusion analysis

This section discusses the analytical models used to analyze the experimental exciton imaging data to extract the fundamental transport properties of excitons in these materials.

3.2.1 Normal diffusion

The optical laser excitation generates a density of excitons with a Gaussian spatial distribution in the TMD monolayer. Although there are various physical mechanisms that can largely influence the evolution of the initially Gaussian spatial distribution of excitons, such as many-body exciton-exciton and exciton-phonon scattering [59, 90, 134, 34, 153], strain fields [33], or crystal defects [33], as a first approximation, the evolution of the exciton distribution can be modeled using Fick's law of diffusion. The derivation of Fick's law of diffusion

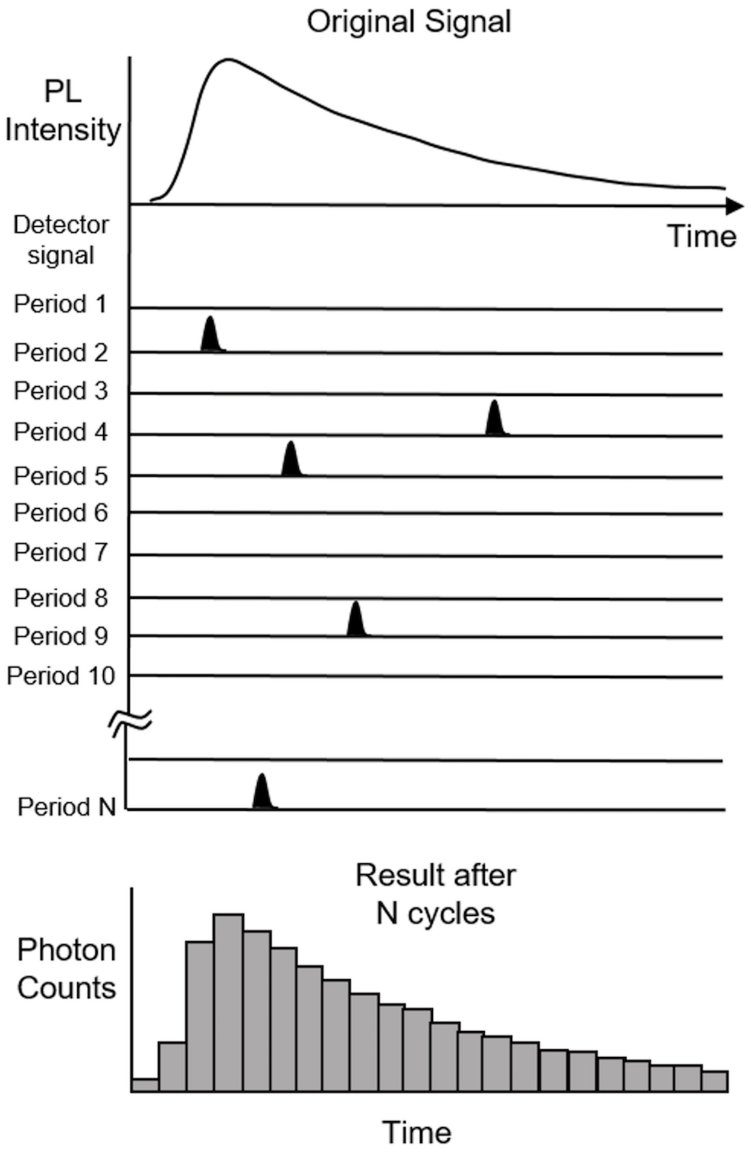

Figure 3.1.2: Diagram illustrating the working principle of time-correlated single photon counting (TCSPC). The detector signal consists of a train of randomly distributed pulses due to the detection of the individual photons. There are many signal periods without photons, but many other signal periods contain one photon pulse. Periods with more than one photon are rare. When a photon is detected, the time of the corresponding detector pulse is measured. After many photons, the histogram of the detection times corresponds to the original time decay of the signal. Reproduced with permission from [11].

is similar to that of the drift, diffusion, and recombination rate equation derived in appendix A. In three spatial dimensions, Fick's law is generally given by

$$\frac{\partial}{\partial t} n\left(\boldsymbol{r}, t\right) = \nabla \cdot \left[D\left(\boldsymbol{r}, n, t\right) \nabla n\left(\boldsymbol{r}, t\right)\right] \tag{3.2.1}$$

where $n\left(\boldsymbol{r}, t\right)$ denotes the exciton density, and $D\left(\boldsymbol{r}, n, t\right)$ is the diffusion coefficient, which in principle, can be spatially, temporally, or density dependent. In the absence of lattice temperature gradients, homogeneous energy bands, and low-density excitation, the diffusion coefficient is constant, and the only factor that drives the evolution of the exciton density is the exciton concentration gradient. Due to the two-dimensional nature of TMD monolayers, the diffusion of excitons is expected to be azimuthally symmetric, and so Eq.3.2.1 further simplifies to a single spatial dimension. Moreover, the APD is typically scanned either along the horizontal or vertical direction of the imaging setup's focal plane, which implies that the evolution of the exciton density is only monitored along either of these directions. Therefore, a simplified form of Fick's law can be solved in Cartesian coordinates to infer the evolution of the exciton density as a result of diffusion. This simplified form of Fick's law is given by

$$\frac{\partial}{\partial t} n\left(x, t\right) = D \frac{\partial^2}{\partial x^2} n\left(x, t\right) \tag{3.2.2}$$

The solution to the one-dimensional diffusion equation Eq.3.2.2 can be found using the so-called Gaussian or heat kernel, where the initial condition is convolved with the heat kernel as [58]

$$
\begin{aligned}
n(x,t) &= \int_{-\infty}^{\infty} dyn(y,0)\frac{1}{\sqrt{4\pi Dt}}\exp\left[-\frac{(x-y)^2}{4Dt}\right] \\
&= \int_{-\infty}^{\infty} dyn(y,0)S(x-y,t) \\
&= [n(0)*S](x,t)
\end{aligned} \tag{3.2.3}
$$

where the heat kernel $S(x,t)$ is defined as

$$
S(x,t) = \frac{1}{\sqrt{4\pi Dt}}\exp\left(-\frac{x^2}{4Dt}\right) \tag{3.2.4}
$$

If n_0 excitons are initially photo-generated and spatially distributed in a Gaussian distribution centered at the origin, and with standard deviation $\sigma(0)$, the initial exciton distribution can be represented as

$$
n(x,0) = \frac{n_0}{\sqrt{2\pi\sigma^2(0)}}\exp\left[-\frac{x^2}{2\sigma^2(0)}\right] \tag{3.2.5}
$$

The exciton distribution at arbitrary time t given by Eq.3.2.3 can be calculated using the property of convolution of two Gaussian functions. The convolution of two Gaussians A and B with variances σ_A^2 and σ_B^2, and centered at x_A and x_B, is equal to a Gaussian with variance $\sigma_A^2+\sigma_B^2$ and centered at x_A+x_B as [208]

$$
\begin{aligned}
[A * B](x) &= \int_{-\infty}^{\infty} dy A(y) B(x-y) \\
&= \int_{-\infty}^{\infty} dy \left\{ \frac{1}{\sqrt{2\pi\sigma_A^2}} \exp\left[-\frac{(y-x_A)^2}{2\sigma_A^2} \right] \right\} \left\{ \frac{1}{\sqrt{2\pi\sigma_B^2}} \exp\left[-\frac{(x-y-x_B)^2}{2\sigma_B^2} \right] \right\} \\
&= \frac{1}{\sqrt{2\pi(\sigma_A^2+\sigma_B^2)}} \exp\left\{ -\frac{[x-(x_A+x_B)]^2}{2(\sigma_A^2+\sigma_B^2)} \right\} \qquad (3.2.6)
\end{aligned}
$$

Accordingly, applying the property for the convolution of Gaussians Eq.3.2.6 to Eq.3.2.3 yields

$$
\begin{aligned}
n(x,t) &= [n(0) * S](x,t) \\
&= \int_{-\infty}^{\infty} dy n(y,0) S(x-y,t) \\
&= n_0 \int_{-\infty}^{\infty} dy \left\{ \frac{1}{\sqrt{2\pi\sigma^2(0)}} \exp\left[-\frac{y^2}{2\sigma^2(0)} \right] \right\} \left\{ \frac{1}{\sqrt{4\pi Dt}} \exp\left[-\frac{(x-y)^2}{4Dt} \right] \right\} \\
&= \frac{n_0}{\sqrt{2\pi[\sigma^2(0)+2Dt]}} \exp\left\{ -\frac{x^2}{2[\sigma^2(0)+2Dt]} \right\} \qquad (3.2.7)
\end{aligned}
$$

This result implies that the initially Gaussian distribution of excitons will preserve its Gaussian shape, but its variance will evolve linearly in time according to

$$
\sigma^2(t) = \sigma^2(0) + 2Dt \qquad (3.2.8)
$$

and as illustrated in Fig.3.2.1. For convenience, however, it is customary to plot the change in variance (CIV) given by

$$
\begin{aligned}
\Delta\sigma^2(t) &= \sigma^2(t) - \sigma^2(0) \\
&= 2Dt \qquad (3.2.9)
\end{aligned}
$$

because the CIV is independent of the initial width of the Gaussian distribution, which may vary between data sets as a result of variations in experimental conditions, and it is directly proportional to the diffusivity of the excitons in the material. As such, the CIV is a quantity that reports on the fundamental transport properties of excitons in the material, and it is independent of the experimental conditions.

It is worth mentioning that in the literature the CIV is often incorrectly referred to as the mean squared displacement (MSD). However, the MSD and the CIV are technically two different quantities. The MSD of an arbitrary Gaussian distribution defined as

$$\begin{aligned} MSD\left(t\right) &\equiv \left\langle \left|x\left(t\right)-x\left(0\right)\right|^{2}\right\rangle \\ &= \left\langle x^{2}\left(t\right)\right\rangle +x^{2}\left(0\right)-2x\left(0\right)\left\langle x\left(t\right)\right\rangle \end{aligned} \tag{3.2.10}$$

is equivalent to the second cumulant of the distribution $\Delta\left\langle x^{2}\left(t\right)\right\rangle$, also known as variance $\sigma^{2}\left(t\right)$ and defined as

$$\begin{aligned} \sigma^{2}\left(t\right) &\equiv \Delta\left\langle x^{2}\left(t\right)\right\rangle \\ &= \left\langle x^{2}\left(t\right)\right\rangle -\left\langle x\left(t\right)\right\rangle ^{2} \end{aligned} \tag{3.2.11}$$

only if the the mean of the distribution does not change with time, i.e. $\left\langle x\left(t\right)\right\rangle =x\left(0\right)$. That is to say, the MSD is equal to

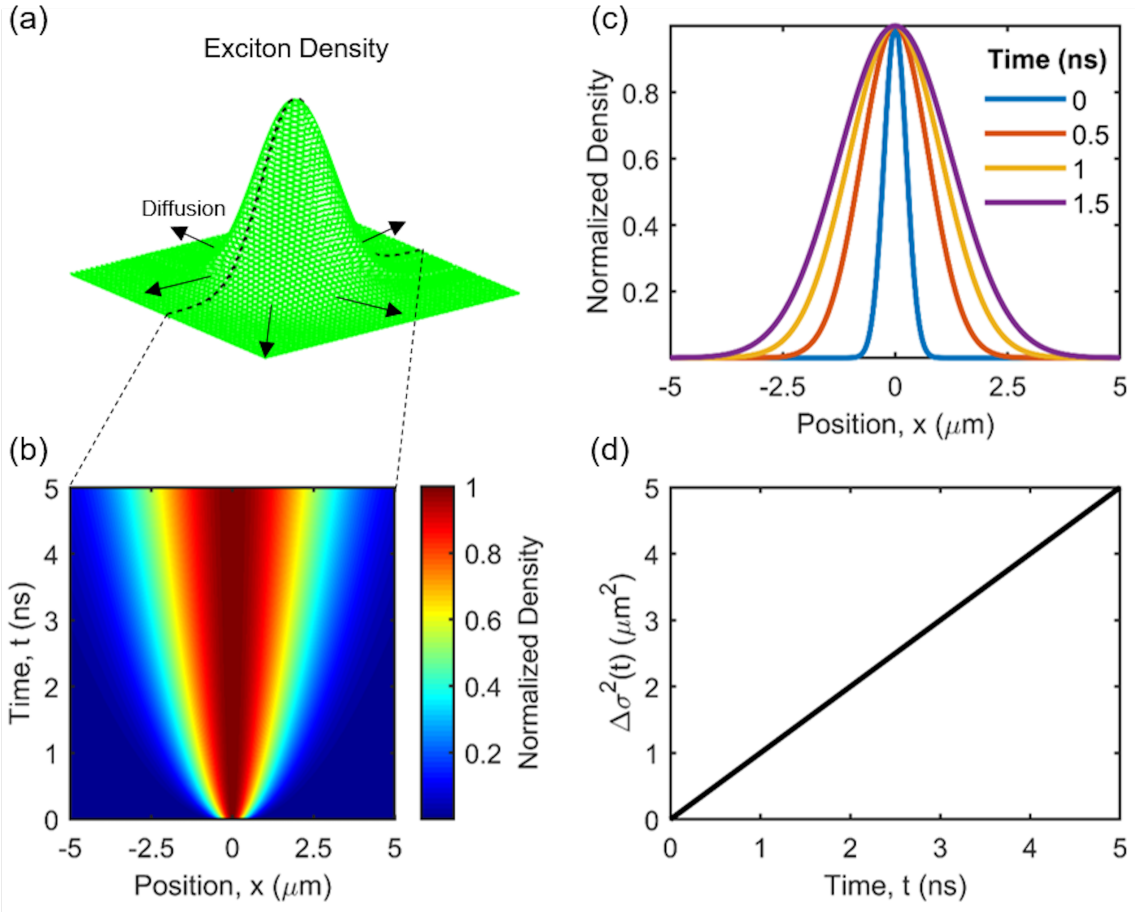

Figure 3.2.1: Calculated diffusion of a Gaussian distribution. (a) Schematic illustration of a Gaussian ditribution of excitons at generated at $t = 0$ by an optical excitation. (b) Map of the normalized exciton distribution as a function of time emphasizing the broadening of the distribution as a result of the diffusion of excitons. (c) Cross-sections of theu time resolved map shwon in (b) comparing the exciton distribution at different times. (d) Change in variance of the Gaussian distribution as a function of time. The linear evolution of the CIV is predicted by Fick's law as given by Eq.3.2.9.

$$
\begin{aligned}
MSD\left(t\right) &= \left\langle x^2\left(t\right)\right\rangle + x^2\left(0\right) - 2x\left(0\right)\left\langle x\left(t\right)\right\rangle \\
&= \left\langle x^2\left(t\right)\right\rangle + x^2\left(0\right) - 2x^2\left(0\right) \\
&= \left\langle x^2\left(t\right)\right\rangle - x^2\left(0\right) \\
&= \left\langle x^2\left(t\right)\right\rangle - \left\langle x\left(t\right)\right\rangle^2 \\
&= \sigma^2\left(t\right) \qquad (3.2.12)
\end{aligned}
$$

which is not the same as the CIV. Substituting the result from Fick's law of diffusion of a Gaussian distribution of excitons given by Eq.3.2.8 into Eq.3.2.12, it is clear that the MSD is

$$
\begin{aligned}
MSD\left(t\right) &= \sigma^2\left(t\right) \\
&= \sigma^2\left(0\right) + \Delta\sigma^2\left(t\right) \\
&= \sigma^2\left(0\right) + 2Dt \qquad (3.2.13)
\end{aligned}
$$

3.2.2 Anomalous diffusion

Anomalous diffusion is a type of transport that is found virtually everywhere in nature, but particularly in energetically disordered, non-crystalline materials such as fractured or porous rocks, diluted magnetic systems, silica aerogels, glassy ionic conductors, and disordered semiconductors [64]. Specifically, anomalous diffusion refers to the deviation of the diffusion of a system from the evolution predicted by Fick's law. The main characteristic feature of anomalous diffusion is the nonlinear evolution of the CIV and the resulting time-dependence of the diffusion coefficient. In the literature, anomalous diffusion is often described by a nonlinear CIV with a power-law function of the form

$$\Delta\sigma^2(t) = \Phi t^{\alpha} \tag{3.2.14}$$

where Φ and α are known as the transport factor and anomalous coefficient, respectively. The diffusion coefficient is similarly described by

$$\begin{aligned} D(t) &= \frac{1}{2}\frac{d}{dt}\Delta\sigma^2(t) \\ &= \frac{\alpha}{2}\Phi t^{\alpha-1} \end{aligned} \tag{3.2.15}$$

and for the particular case of Fick's law diffusion or normal diffusion, $\alpha = 1$ and $D = \Phi/2$.

While descriptive of the evolution of the CIV, the anomalous diffusion model given by Eq.3.2.14 does not provide any insight about the physical mechanisms giving rise to the anomalous behavior. In semiconductor crystals, anomalous diffusion is linked to energetic disorder caused by impurities that give rise to low-lying energy states that tend to trap mobile carriers or excitons. The amount of time that the mobile carriers or excitons remain trapped depends on the details of the distribution of trap states. For instance, if the distribution is deep or has a non-vanishing deep-energy tail relative to the band of mobile or delocalized states, the transport slows down due to the multi-trap-and-release events that mobile excitons or carriers might undergo between free flights. As a result, the evolution of the MSD becomes nonlinear and the diffusion coefficient becomes time dependent [163, 195, 105, 166, 74, 122].

Unlike the hopping models of exciton transport in organic semiconductors and colloidal quantum dots, where the transport of excitons is modeled as the scattering of localized states between adjacent molecular sites or dots with transition energies distributed randomly in a Lévy or Gaussian distribution, the transport of excitons in energetically-disordered TMD monolayers is more suitably described as the multiple trapping-and-release (MTR) of extended excitons by regions of energetic disorder in the crystal, but the motion or "free

flights" occurs in the free exciton bands [136, 105, 166, 14, 167, 185]. In the limit of high energetic disorder, however, the MTR band transport of extended excitons mathematically resembles the hopping transport of localized excitons because the time of flight is shorter than the time the excitons remain trapped [105].

A particularly instructive type of trap distribution is the exponential distribution or Urbach tail of trap states commonly used to describe the anomalous diffusion of carriers and excitons in semiconductors with energetic disorder [45, 191, 219]. Such exponential density of traps states has the form

$$g(E) = \frac{N_t}{E_t} \exp\left(-\frac{E}{E_t}\right) \tag{3.2.16}$$

where N_t is the total density of traps, E is the energy relative to the mobile carrier or exciton band edge, and E_t is the effective trap depth. If the escape from the traps is assumed to be a thermally activated process, the rate of escape can be modeled as

$$W(E) = W_0 \exp\left(-\frac{E}{k_B T}\right) \tag{3.2.17}$$

where W_0 is the attempt-to-escape rate (e.g. via phonon scattering), E is the energy of the trap state relative to the free carrier or exciton band edge, k_B is Boltzmann's constant, and T is temperature. Since the energy of the trap states is distributed according to Eq.3.2.16, the distribution of escape rates associated with the exponential density of trap states is given by [105]

$$P(W) = \int_0^\infty dE \delta\left[W - W(E)\right] g(E) \tag{3.2.18}$$

Assuming that the escape rate is constant, and the attempts to escape the traps are independent of each other, the probability for a carrier or exciton to escape the trap after some time t of being trapped is given by [105]

$$P_{escape}(t) = \int_0^t d\tau \int_0^\infty dW W P(W) \exp(-W\tau) \tag{3.2.19}$$

Similarly, the probability for a carrier or exciton to still be trapped at time t after its capture is simply

$$\begin{aligned} \Pi(t) &= 1 - P_{escape}(t) \\ &= 1 - \int_0^t d\tau \int_0^\infty dW W P(W) \exp(-W\tau) \end{aligned} \tag{3.2.20}$$

Therefore, if all the excitons or carriers are initially free, the number of trapped particles at time t is the sum of particles that have been captured within a time interval $d\tau$ around $\tau < t$ and which are still trapped after a dwell time of $t - \tau$ as [105]

$$\begin{aligned} n_t(t) &= \int_0^t d\tau \omega_0 n_f(\tau) \Pi(t-\tau) \\ &= \omega_0 [n_f * \Pi](t) \end{aligned} \tag{3.2.21}$$

where $n_{f,t}$ represents the density of free or mobile (trapped) excitons and ω_0 is their capture rate. Although the capture rate depends on the density of unoccupied traps, i.e. $N_t - n_t$, it can be approximated to be proportional to the total density of traps as

$$\omega_0 \approx v \sigma_c N_t \tag{3.2.22}$$

where v and σ_c are the thermal velocity of the mobile excitons and the capture cross-section, respectively.

The MTR model describes the anomalous diffusion of excitons in an energetically disordered semiconductor by defining the effective time-dependent diffusivity $D_{\text{eff}}(t)$ as

$$D_{\text{eff}}(t) = \eta(t) D_{\text{free}} \tag{3.2.23}$$

where D_{free} is the scattering-limited free exciton diffusion coefficient, which is the same diffusion coefficient from Fick's law in Eq.3.2.2, and $\eta(t)$ is the fraction of excitons that become trapped relative to the total density of excitons

$$\eta(t) \equiv \frac{n_t(t)}{n_t(t) + n_f(t)} \tag{3.2.24}$$

With this definition of the effective diffusivity, it is clear that the in the limit of high energetic disorder, when the majority of excitons become trapped, the effective diffusivity approaches zero. While both trapping (escaping) and recombination of mobile (trapped) excitons affect the total population of excitons at any given time, trapping alone is sufficient to explain the origin of the anomalous diffusion of excitons in semiconductors with significant energetic disorder. After evaluating the convolution integral given by Eq.3.2.21and substituting the result into Eq.3.2.24, the fraction of trapped excitons becomes [105]

$$\eta(t) = \sum_{k=0}^{\infty} \frac{(-1)^k}{\Gamma[1 + k(1-\alpha)]} \left(\frac{t}{\theta}\right)^{k(1-\alpha)} \tag{3.2.25}$$

where the parameters α and θ are respectively defined as

$$\alpha = \frac{k_B T}{E_t} \tag{3.2.26}$$

$$\theta = \left[\frac{W_0^{\alpha}}{\omega_0 \Gamma(1+\alpha)\Gamma(1-\alpha)}\right]^{\frac{1}{1-\alpha}} \tag{3.2.27}$$

and $\Gamma(x)$ is the complete gamma function. The parameter θ controls the dynamics of trapping as it depends non-trivially on both the capture and escape rates; it can be interpreted

as the approximate time the mobile excitons remain trapped. Moreover, as defined, the parameter α can take values between 0 and 1. If the effective diffusivity is written explicitly using Eq.3.2.23

$$D_{\text{eff}}(t) = D_{\text{free}} \sum_{k=0}^{\infty} \frac{(-1)^k}{\Gamma[1+k(1-\alpha)]} \left(\frac{t}{\theta}\right)^{k(1-\alpha)} \tag{3.2.28}$$

The CIV can be calculated from Eq.3.2.15 by integrating Eq.3.2.28 as

$$\begin{aligned} \Delta\sigma^2(t) &= 2\int_0^t d\tau D_{\text{eff}}(\tau) \\ &= 2D_{\text{free}} \sum_{k=0}^{\infty} \frac{(-1)^k}{\Gamma[1+k(1-\alpha)]\,\theta^{k(1-\alpha)}} \int_0^t d\tau \tau^{k(1-\alpha)} \\ &= 2\theta D_{\text{free}} \sum_{k=0}^{\infty} \frac{(-1)^k}{\Gamma[1+k(1-\alpha)][k(1-\alpha)+1]} \left(\frac{t}{\theta}\right)^{k(1-\alpha)+1} \end{aligned} \tag{3.2.29}$$

In the limit of $t \gg \theta$, the fraction of trapped excitons converges to

$$\eta(t) \approx \frac{1}{\Gamma(\alpha)} \left(\frac{t}{\theta}\right)^{\alpha-1} \tag{3.2.30}$$

In this limit, the time that mobile excitons spend in the band of extended states is assumed to be so small as to almost vanish (i.e. instantaneous trapping and re-trapping) [105, 43, 132]. Moreover, if the effective diffusivity in this limit is also written explicitly using Eq.3.2.23

$$D_{\text{eff}}(t) \approx \frac{D_{\text{free}}}{\Gamma(\alpha)} \left(\frac{t}{\theta}\right)^{\alpha-1} \tag{3.2.31}$$

the resemblance to the effective diffusivity of the anomalous diffusion model given by Eq.3.2.15 is unambiguously clear. In fact, the transport factor is identified to be

$$\Phi \approx \frac{2D_{\text{free}}}{\alpha\Gamma(\alpha)\,\theta^{\alpha-1}} \tag{3.2.32}$$

and the anomalous coefficient is simply given by Eq.3.2.26 and it is a measure of the depth of the traps relative to the thermal energy scale k_BT. Interestingly, in the case of normal diffusion $\alpha = 1$, the transport factor given by Eq.3.2.32 takes the expected form of $\Phi = 2D_{\text{free}}$. For completeness, the CIV in this limit can be calculated from Eq.3.2.15 as

$$\begin{aligned}
\Delta\sigma^2(t) &= 2\int_0^t d\tau D_{\text{eff}}(\tau) \\
&\approx \frac{2D_{\text{free}}}{\Gamma(\alpha)\,\theta^{\alpha-1}}\int_0^t d\tau\,(\tau)^{\alpha-1} \\
&\approx \frac{2D_{\text{free}}}{\alpha\Gamma(\alpha)\,\theta^{\alpha-1}}t^{\alpha}
\end{aligned} \tag{3.2.33}$$

where the resemblance of Eq.3.2.33 to the power-law form of the CIV given by Eq.3.2.14 is unambiguously clear.

Figure 3.2.2 shows plots of the anomalous diffusion coefficient and CIV given by the MTR model for an exponential distribution of traps. For convenience, these expressions are plotted in terms of unit-less quantities as in Eq.3.2.30 and as $\Delta\sigma^2(t)/(D_{\text{free}}\theta)$.

While most of the experimental exciton imaging data shown in the following chapters was analyzed using the results from Fick's law of diffusion, namely Eq.3.2.7 and Eq.3.2.9, the anomalous diffusion model was used to analyze and interpret some of the data in chapter 4 where the origin of anomalous diffusion in a TMD monolayer arises from energetic disorder in the material. In contrast, chapter 5 discusses a physical mechanism that gives rise to anomalous diffusion in a TMD monolayer with reduced energetic disorder. In such case, the the physical process that gives rise to the anomalous diffusive behavior is the relaxation of kinetic energy of excitons generated with a high photon energy optical excitation.

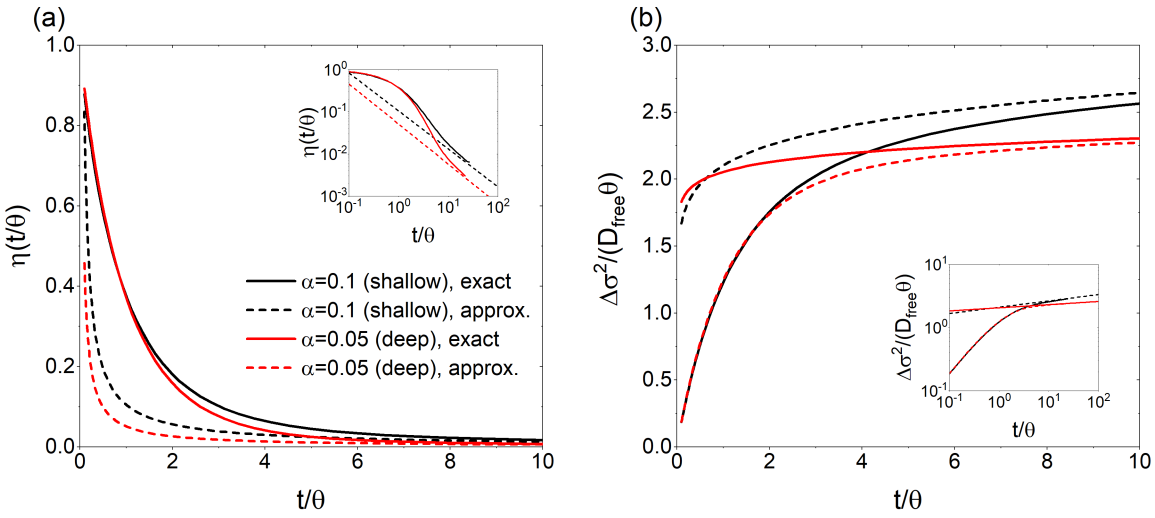

Figure 3.2.2: Anomalous diffusion coefficient and CIV with the MTR model for an exponential density of traps. (a) Anomalous diffusion coefficient, expressed as the fraction of mobile excitons according to Eq.3.2.23, and (b) normalized CIV obtained with the multi-trap-and-release (MTR) model for an exponential density of traps. The solid lines represent the exact forms of the fraction of mobile excitons, i.e. Eq.3.2.25 in (a) and Eq.3.2.29 in (b), and the dashed lines represent the approximate their approximate form in the limit $t \gg \theta$, i.e. Eq.3.2.31 in (a) and Eq.3.2.33 in (b). The insets show the same quantities in log-log scale to emphasize the fact that the exact expressions converge to the approximate forms in the limit of $t \gg \theta$. The x-axis corresponds to normalized time in units of the parameter θ defined in Eq.3.2.27. The legend in (a) is also applicable to (b).

3.3 Summary

This chapter discussed the experimental technique used to image the motion of excitons in TMD monolayers, and the analytical models used to analyze the experimental data to extract the fundamental transport properties of excitons in these materials. Specifically, a detailed description of the experimental setup for exciton imaging was discussed, emphasizing the time-correlated single photon counting technique that enables the resolution of exciton dynamics with picosecond time resolution. Then, two main models of diffusion were discussed, namely Fick's law of diffusion and the power-law model of anomalous diffusion. Fick's law model of diffusion served as the baseline for the identification of interesting dynamic effects that are ubiquitous in transport studies of excitons in TMD monolayers. This chapter concluded by discussing a particularly instructive scenario that gives rise to anomalous diffusive transport in energetically disorder semiconductors. This model discussed the transport of mobile excitons interrupted by the multi-trap-and-release by defect states with an exponential energy distribution with respect to the mobile exciton band edge.

Chapter 4

Strain Control of Exciton Transport in TMDs

4.1 Introduction

Strain engineering of the optical and electronic properties of two-dimensional materials (2D), such as transition metal di-chalcogenide (TMD) monolayers, is a strategy that has been utilized extensively over the past few years due to the remarkable resilience of 2D materials to mechanical deformation [89, 37, 151, 35, 109, 83, 23, 29]. In addition, the exceptional room-temperature stability of excitons in TMD monolayers, as a result of the strong Coulomb interaction, has positioned these materials as outstanding candidates for excitonic device applications [20].

While various devices leveraging the unique optical and electronic properties of TMD monolayers have been demonstrated in recent years, they usually rely on a bias to dissociate the excitons, and drive the individual charge carriers towards an electrical contact for detection [188, 222, 213, 41, 139, 101, 158, 141, 8, 209]. In contrast, purely excitonic devices rely on the large binding energy [220, 189, 65, 184] and highly-tunable band structure [30, 28] of TMD monolayers to control the propagation of excitons at room temperature without

dissociating them to collect the charge carriers separately. Therefore, it is critical for the transport properties of excitons in monolayer TMDs to be well characterized, and enable the design of next-generation excitonic devices.

The transport of excitons under non-uniform strain fields in TMD monolayers is particularly relevant to the design of excitonic devices because of the large tunability of their optical bandgap and exciton resonance energy via mechanical deformation, and the resulting ability to manipulate the propagation of excitons with spatially modulated strain fields. Several studies exploring the effect of in-plane strain on the band structure of TMD monolayers have shown that their direct optical bandgap and exciton resonance energy vary linearly with small strain levels as shown in Fig.2.2.4 [102, 76, 32, 42, 152].

The high sensitivity of TMDs to strain can enable the engineering of excitonic potentials by spatially modulating their resonance energy with non-uniform strain. Such modulation can result in the "funneling" of excitons in the direction of the strain gradient [49]. As a result, the direction and speed of propagation of excitons in TMD monolayers can be controlled by engineering a strain field to have a gradient in the direction of target motion as illustrated in Fig.4.1.1.

While previous studies of exciton transport in TMD monolayers have sought to characterize the diffusion of excitons in bulk and monolayer TMDs [91, 90, 22], their combined drift and diffusion under non-uniform strain fields have not been studied extensively in these materials. This chapter demonstrates the control of the propagation of excitons under the strain gradient created in the WSe_2 monolayer by transferring it over a nanostructured substrate. Both the drift and diffusion of excitons in the WSe_2 monolayer are quantified, and a model that reproduces the experimental results reasonably well is presented. This chapter is based on published work that can be found in reference [33]

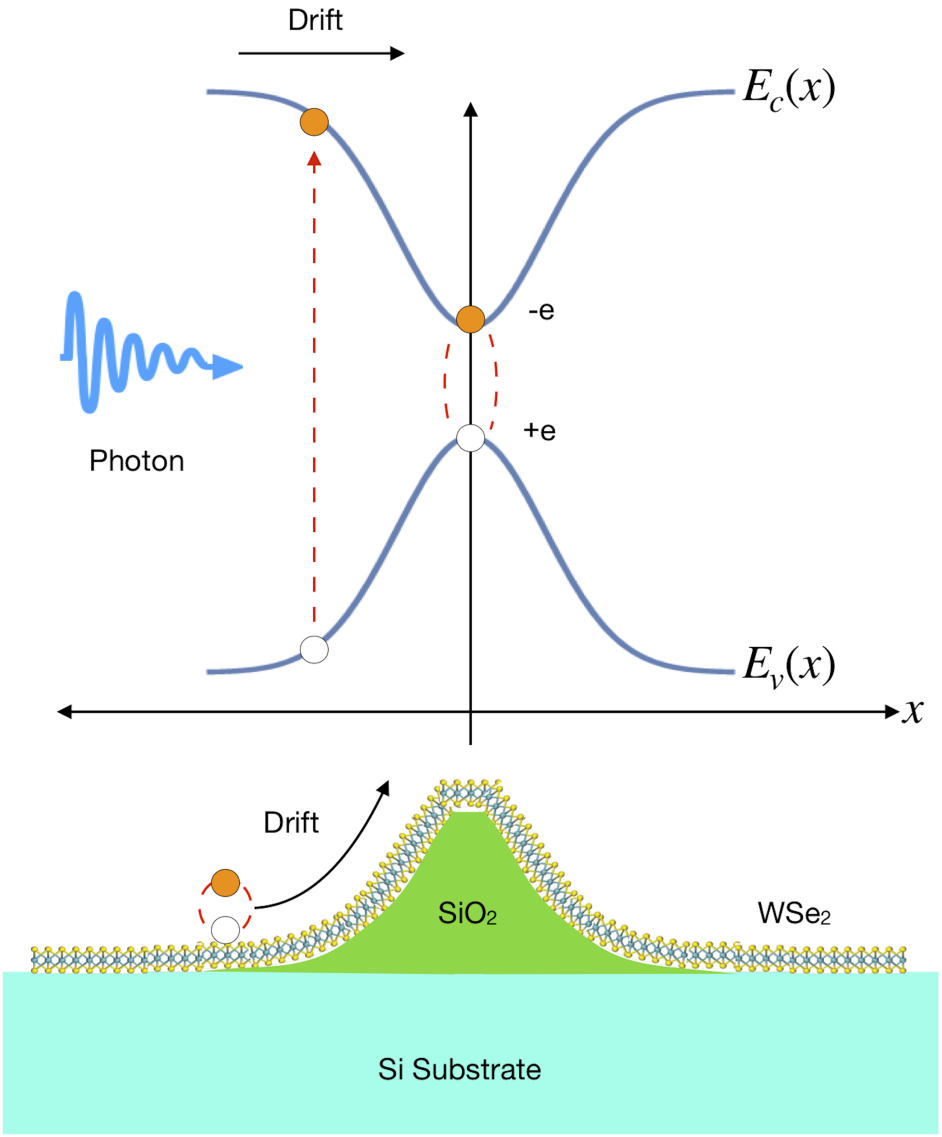

Figure 4.1.1: Illustration of exciton funneling. A WSe_2 monolayer is transferred over a Si substrate with SiO_2 nano-pillars. The nano-pillars create a strain field that modulates the bandgap and the exciton energy leading to an effective force that pushes the photo-generated excitons towards the highest strain point at the top of the pillar.

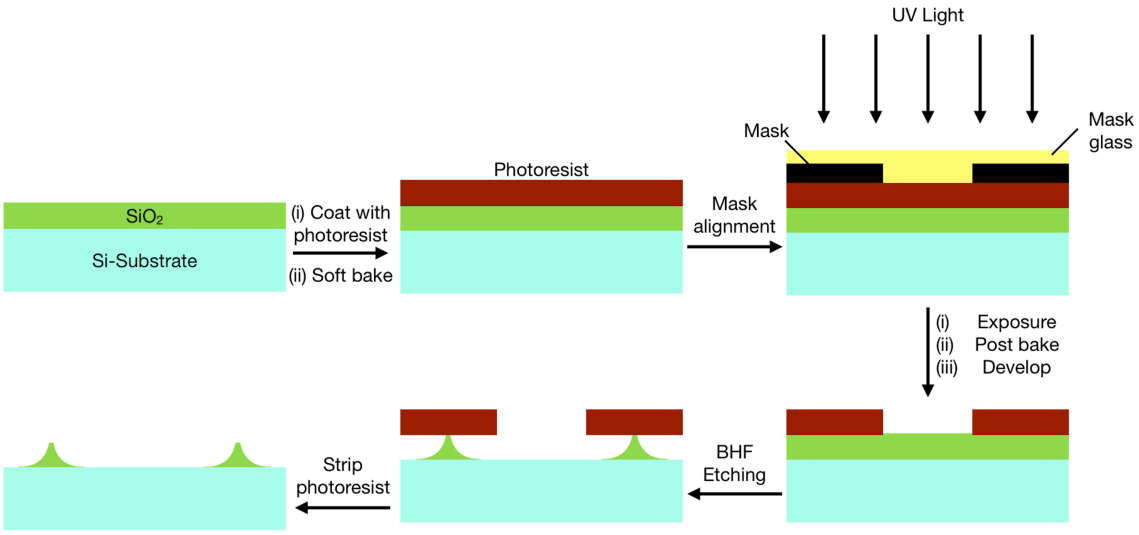

Figure 4.2.1: Procedure to fabricate the nanostructured substrate used to strain the WSe_2 monolayer. The details are in the text. Reproduced with permission from [33].

4.2 Experimental results

This section discusses the fabrication of the nanostructured substrate, and the experimental results of the control of exciton propagation in the WSe_2 monolayer with strain.

4.2.1 Sample fabrication

Monolayer WSe_2 samples were prepared via mechanical exfoliation [127, 24], and then transferred over standard silicon di-oxide (SiO_2) nano-pillars on a silicon (Si) substrate. A schematic diagram of the nano-fabrication process is shown in Fig.4.2.1. The substrate was a standard SiO_2-on-Si substrate with a low p-type doping concentration (resistivity of 10 Ωcm), and with a 300 nm thick oxide layer. The features on the substrate were patterned with a standard optical lithography process on a projection lithography tool. After lithography, the exposed oxide was etched with buffered oxide etch (BHF) for 2 minutes to create pillars with sharp tips, which were intended to produce a circularly symmetric strain field on the WSe_2 monolayers. After the etching step, the Si substrate was rid of the SiO_2 layer except for the SiO_2 pillars.

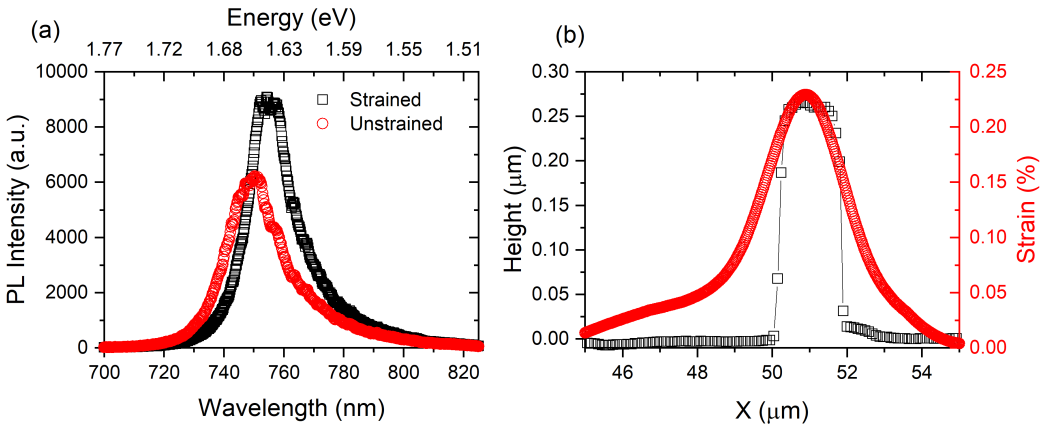

Figure 4.2.2: Typical PL spectra of the WSe_2 monolayer at room temperature and AFM cross-section of the SiO_2 nano-pillar. (a) Typical strained and unstrained PL spectra of the WSe_2 monolayer at room temperature. The excitation was a 532 nm, CW diode laser. (b) AFM cross-section of the SiO_2 nano-pillar indicating its dimensions as well as the approximate strain profile created around the pillar.

4.2.2 Strain mapping

The strain field created in the WSe_2 monolayer by the nano-pillars was mapped by measuring the photoluminescence (PL) spectra of the monolayer locally across the area strained by the SiO_2 pillar. For reference, Fig.4.2.2(a) shows the typical strained and unstrained PL spectra at room temperature of the WSe_2 monolayer, and Fig.4.2.2(b) shows a cross-section of an atomic force microscope (AFM) image of the substrate indicating the approximate height and width of the SiO_2 nano-pillar to be 250 nm and 1.5 μm, respectively.

Figure 4.2.3(a) shows an optical image of the monolayer transferred over a SiO_2 pillar on the Si substrate and Fig.4.2.3(b) shows the monolayer's spectrally-integrated PL spectra from the area enclosed by the square on the optical image. The PL spectra were integrated between 622 nm and 881 nm because the peak intensity of WSe_2 is typically found at around 750 nm as shown in Fig.4.2.2(a). The integrated spectra were also normalized with respect to the maximum integrated intensity within the enclosed area to emphasize the effect of the pillar.

The direct bandgap and exciton resonance energy of TMD monolayers are expected

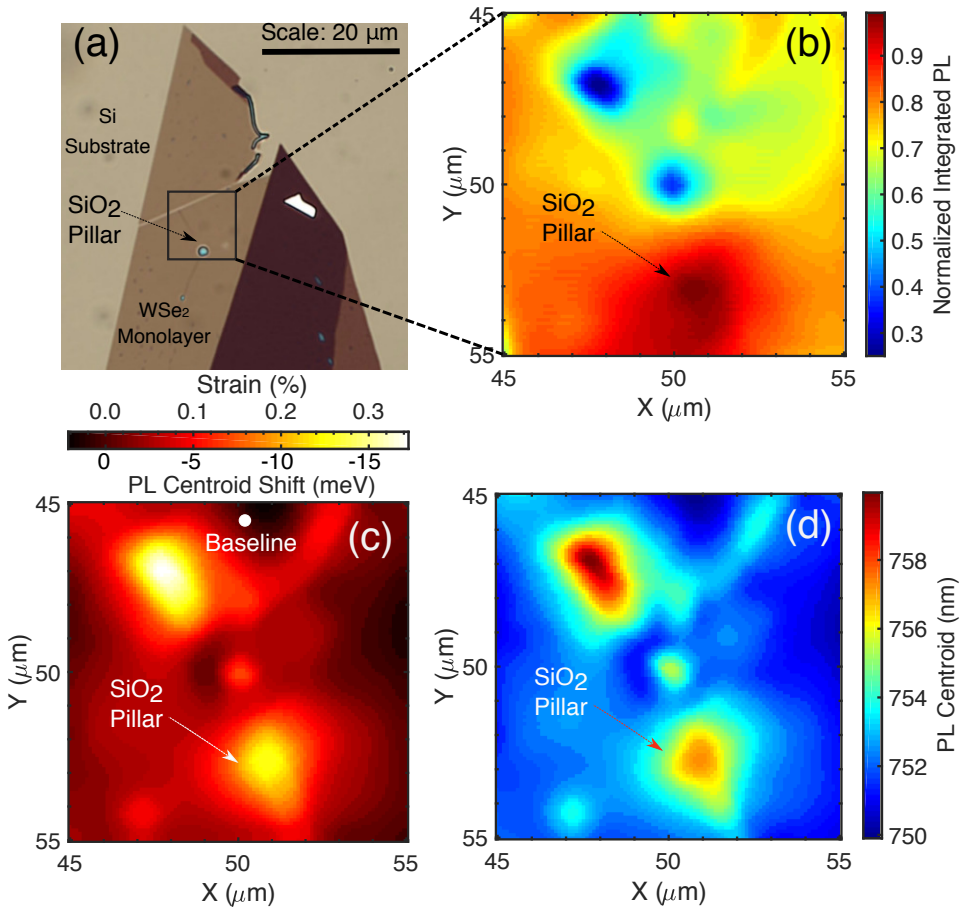

Figure 4.2.3: Mapping of strain field in the WSe_2 monolayer. (a) Optical image of the WSe_2 monolayer transferred over a 1.5 μm diameter, 250 nm tall SiO_2 pillar on a Si substrate. (b) Normalized integrated PL intensity of the WSe_2 monolayers strained by the SiO_2 pillar. The monolayer's scanned area is enclosed by the square shown in (a). The local PL spectra were integrated between 622 nm and 881 nm and they were normalized with respect to the maximum integrated PL intensity within the enclosed area. (c) Energy shift and strain map of the WSe_2 monolayer. The white dot on the strain map indicates the location of the baseline spectrum where the monolayer is assumed to be unstrained. The sensitivity to biaxial strain of the WSe_2 monolayer's bandgap was obtained from [42]. (d) Local PL centroid map. The excitation laser was a 532 nm, CW diode laser. Reproduced with permission from [33].

to decrease (increase) linearly with tensile (compressive) strain [42, 152] which should be evidenced by a red (blue) shift in their PL spectrum's peak energy or centroid. Moreover, an enhancement of the PL intensity at high strain points is expected due to the funneling of excitons towards the low energy, strained regions of the monolayer. Such an enhancement in the WSe_2 monolayer's local PL intensity is observed in Fig.4.2.3(b) around the SiO_2 pillar, which is consistent with the funneling of excitons towards the points of highest tensile strain.

The additional high strain points present on the strain map shown in Fig.4.2.3(c) could be the result of substrate roughness[27] or polymer residue trapped between the monolayer and the substrate during the fabrication process [156]. Figure 4.2.4 shows atomic force microscope (AFM) images of the sample where the topography of the pillar and the rest of the substrate can be observed. The AFM topography image's color scale was set to the height range of 0 nm-60 nm to easily visualize the features that are much smaller than the SiO_2 pillar, and thus appears saturated. The white boxes on the AFM images enclose approximately the same area that was scanned in the spatially-resolved PL maps from which the strain on the WSe_2 monolayer was estimated. The optical image of the WSe_2 monolayer on the SiO_2/Si substrate, and the energy shift/strain map shown in Fig.4.2.3 are also shown in Fig.4.2.4 for reference. The features on the strain map and AFM images labeled as 1, 2, and 3 serve as a guide for the eye, and correspond to the unknown high-strain spots on the strain map.

As shown in these images, in addition to the SiO_2 nano-pillar, there are a number of protrusions on the Si substrate that could have resulted from the sample fabrication process (polymer residue) and could have led to doping of the WSe_2 monolayer. Defects introduced by the fabrication process could be responsible for the asymmetric broadening of the exciton resonance and the quenching of the PL intensity at the locations of these protrusions. The asymmetric broadening of the PL spectra could lead to an effective red shift in the centroid of the PL spectra, which could then be misinterpreted as strain. Although these residual polymer pockets are difficult to eliminate completely, their density can be reduced

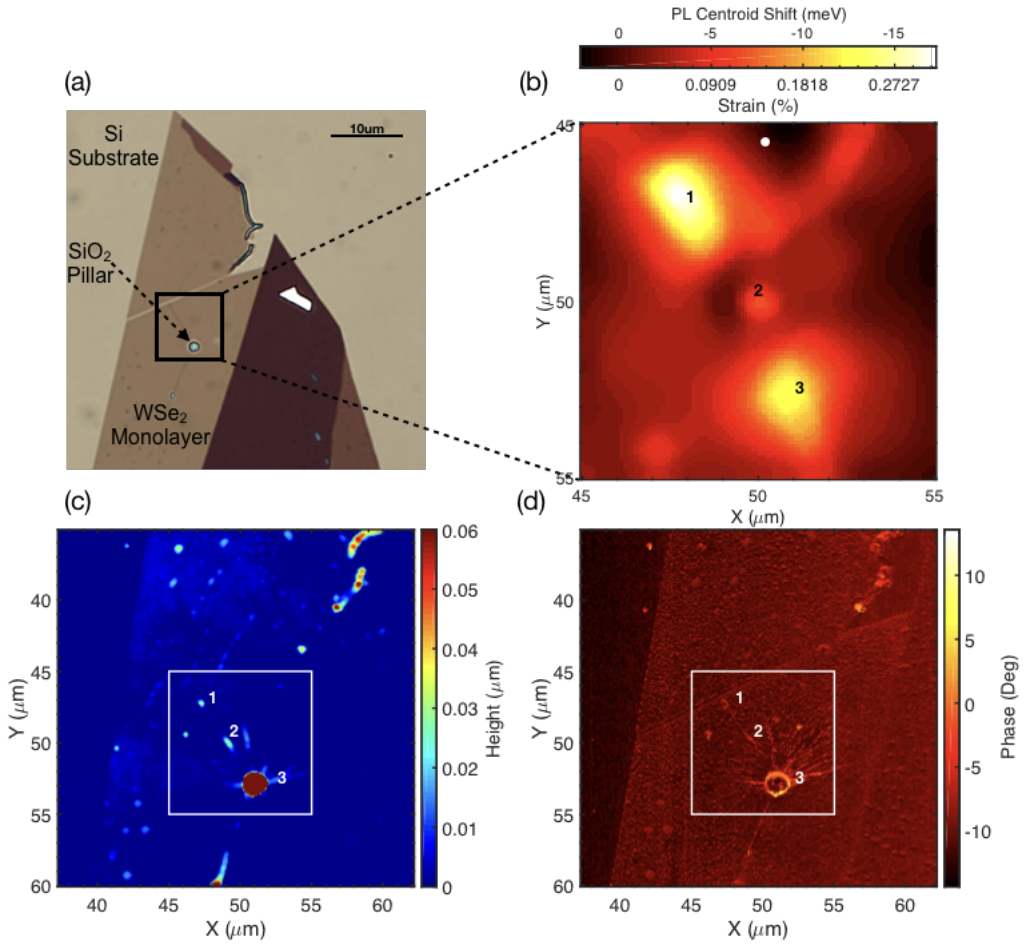

Figure 4.2.4: Atomic force microscope images of the WSe_2 monolayer on a SiO_2 pillar. (a) Optical microscope image and (b) energy shift/strain map of the WSe_2 monolayer also shown in Fig.4.2.3. (c) Atomic force microscope topography and (d) phase images of the WSe_2 monolayer. The white square boxes enclose the area that was scanned in the spatially-resolved strain map shown in (b). The features labeled as 1, 2, and 3 on the AFM images correspond to the features on the energy shift/strain map that appear as high tensile strain points. The color scale of the AFM's topography image (c) was set to the range 0 nm-60 nm to identify the features that are much shorter than the pillar. Therefore, the pillar appears saturated in that scale range, but it was measured to be approximately 250 nm tall and 1.5 μm in diameter as shown in the slice of the AFM topography image in Fig.4.2.2(b). Reproduced with permission from [33].

by controlling the fabrication process.

The strain field in the WSe_2 monolayer was estimated by calculating the shift in the centroid of the local PL spectra with respect to an unstrained point on the monolayer. The spectral shifts were converted to energy shifts and strain using the sensitivity of the WSe_2 monolayer's direct bandgap to strain (-55 meV/%) from reference [42]. Figure4.2.3(c) shows the WSe_2 monolayer's energy shift as a result of the applied strain. The white dot indicates the location of the unstrained PL spectrum used as baseline. While the strain values obtained from calculating the shift in exciton peak wavelength and the centroid of the spectrum are slightly different, this difference remains nearly unchanged throughout the monolayer. Figure 4.2.5 shows a cross-section of the strain map of Fig.4.2.3 at the coordinate $y = 52.7$ μm where the strain was estimated from the shift in the PL spectra's centroid and compare it with the strain obtained from the shift in the exciton peak wavelength. While the centroid and exciton peak shifts led to strain profiles slightly offset from each other, their strain gradients lie virtually on top of each other. Since the strain gradient is what leads to the drift of excitons towards the high tensile strain regions of the WSe_2 monolayer, either the total PL spectra's centroid or exciton peak shifts could be used to estimate the strain gradient. However, it is convenient to estimate the strain in the WSe_2 monolayer with the centroid-based method because the measurements were performed at room temperature, and the contributions from excitons and trions to the spectral shifts are experimentally challenging to separate at this temperature.

While the strain field in the WSe_2 monolayer could also be estimated from the AFM topography image by calculating the change in size of a differential element of the Si substrate's surface with respect to a flat counterpart, this calculation would over-estimate the strain in the monolayer because the monolayer does not necessarily conform to the shape of the nanopillar on the substrate. Therefore, the most accurate way to estimate the strain field in the WSe_2 monolayer is by measuring the PL spectra across the monolayer and calculating the spectral shifts, which can then be converted into strain.

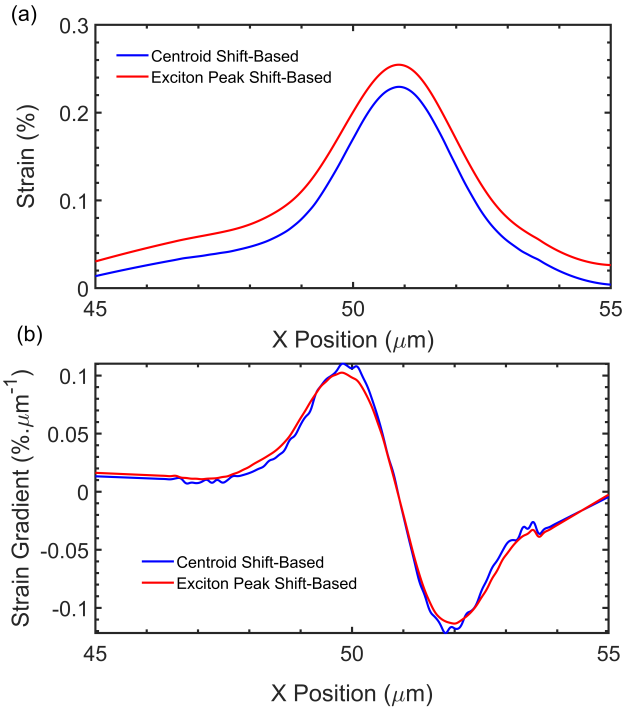

Figure 4.2.5: Comparison of centroid vs peak wavelength shift based strain (a). The strain profiles obtained with these two methods are slightly offset from each other. However, the offset is virtually unchanged across the spatial range shown in the plot. (b) Strain gradient obtained from the strain profiles in (a). Both methods yield virtually identical strain gradients. Since the strain gradient is what is responsible for the drift of excitons, either peak-based or centroid-based strain mapping method is acceptable.

4.2.3 Transport measurements

The transport of excitons on an unstrained section of the WSe_2 monolayer was studied first to have a baseline for the transport of excitons on the strained portion of the monolayer. A map of the time-dependent exciton density as a function of position was constructed using the imaging technique discussed in chapter 3. With this technique, the spatial information is obtained by scanning an avalanche photodiode detector (APD) across the PL emission spot, and the temporal information is obtained via time-correlated single photon counting. Figure 4.2.6(b) shows the exciton PL intensity as a function of time and position where the excitation was fixed at an unstrained point of the monolayer as indicated by the cross mark on Fig.4.2.6(a). The normalized exciton PL intensity was fitted with Gaussian functions at each time step to extract the time-dependent change in variance (CIV), which is proportional to the mean squared displacement (MSD) of the spatial exciton distribution.

Fick's law of diffusion predicts that the evolution of the change in variance of a Gaussian spatial distribution of excitons evolves linearly with time according to $\Delta\sigma^2(t) \equiv \sigma^2(t) - \sigma^2(0) = 2Dt$, where $\sigma^2(t)$ represents the time-dependent variance of the distribution, D is the diffusion coefficient or diffusivity, and t is time. However, when excitons diffuse in an energetically disordered environment, or if they are photo-generated with a non-resonant, high-density optical field that creates excitons with excess kinetic energy [34], the CIV does not increase linearly with time, and the diffusivity becomes time-varying. Such deviation from Fick's law is known as anomalous diffusion, and it is not unique to excitons, c.f. [12, 64, 138].

For the particular case of excitons generated with high excess kinetic energy, the nonlinear evolution of the CIV and the corresponding time-dependence of the diffusion coefficient are linked to the relaxation of their excess energy. This kinetic process is discussed in more detail in chapter 5.

Similarly, for the case of excitons propagating in an energetically disordered environment,

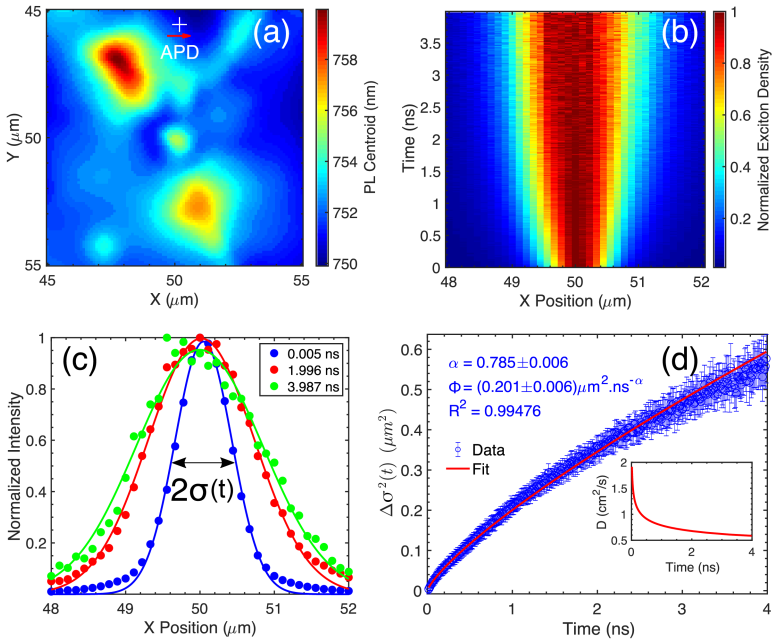

Figure 4.2.6: Transport of excitons in the unstrained WSe_2 monolayer. (a) Local PL centroid map showing the point of excitation on the WSe_2 monolayer indicated by the plus (+) sign marker. (b) Normalized exciton PL Intensity as a function of position and time obtained by scanning an avalanche photodiode detector (APD) across the PL emission spot, and counting the photons using time-correlated single photon counting (TCSPC). (c) Time slices of the normalized exciton density fitted with Gaussian functions showing the broadening of the PL intensity profile; $\sigma(t)$ denotes the time-dependent standard deviation of the Gaussian spatial distribution. (d) Change in variance (CIV) of the exciton density as a function of time showing sub-diffusive transport in the unstrained portion WSe_2 monolayer, which is evidenced by the anomalous coefficient $\alpha < 1$, and resulting in the time-varying diffusion coefficient shown in the inset. The CIV is defined as $\Delta\sigma^2(t) = \sigma^2(t) - \sigma^2(0)$. The error bars represent the fitting error when fitting the measured PL intensity with Gaussian functions. Reproduced with permission from [33].

anomalous diffusion arises from the capture of mobile excitons by trap sites that localize them either temporarily or until recombination occurs. The amount of time that the excitons remain trapped depends on the details of the energy distribution of trap states. If the peak of the energy distribution of traps is below the exciton energy, or if the distribution has a non-vanishing deep-level tail of states that might localize the excitons for extended periods of time, the propagation of mobile excitons slows down due to the multi-trap-and-escape events they undergo in between free flights. Consequently, the CIV becomes nonlinear and the effective diffusivity becomes time-varying [163, 195, 105, 166, 74, 122].

As discussed in chapter 3, anomalous diffusion is better described by a power law model where the chance in variance of the spatial distribution is given by

$$\Delta\sigma^2(t) = \Phi t^{\alpha}, \tag{4.2.1}$$

where Φ and α are known as the transport factor and anomalous coefficient, respectively [211, 12, 64, 112, 229]. Correspondingly, the time-dependent diffusivity is defined as [211]

$$D(t) = \frac{1}{2}\frac{\partial}{\partial t}\left[\Delta\sigma^2(t)\right] = \frac{\alpha}{2}\Phi t^{\alpha-1} \tag{4.2.2}$$

Fitting the experimental CIV data shown in Fig.4.2.6(d) with Eq.4.2.1 evidenced a sub-diffusive transport regime for the excitons on the unstrained portion of the WSe_2 monolayer, and it is characterized by an anomalous coefficient $\alpha = 0.785$ and a diffusion coefficient varying between 1.8 cm^2s^{-1} and 0.6 cm^2s^{-1}. The peak of the Gaussian spatial distribution of excitons in the portion of the unstrained monolayer is virtually immobile, which is consistent with the absence of strain gradients that are expected to shift the peak position of the spatial distribution in the direction of the strain gradient.

On the other hand, when the excitation was positioned at a strained point of the mono-

layer near the SiO_2 pillar, the peak of the Gaussian spatial distribution of excitons did not remain immobile. Specifically, when the excitation was positioned just above the high tensile strain point on top of the pillar, and the PL emission spot was monitored by moving the APD from top to bottom, the peak of the spatial Gaussian distribution of excitons shifted down towards the high tensile strain point on the monolayer as shown in Fig.4.2.7(b). Similarly, when the excitation was positioned just to the left of the high tensile strain point on top of the pillar, and the PL emission spot was monitored by scanning the APD from left to right, the peak of the spatial Gaussian distribution of excitons shifted to the right towards the high tensile strain point as shown in Fig4.2.7.(c). The peak of the spatial Gaussian distribution is expected to shift as a result of the strain gradient in the monolayer.

Figure 4.2.7(d) shows the PL spectra measured at three different positions along the x-axis near the SiO_2 pillar.

The PL spectra measured at the positions labeled as X_1, X_2, andX_3 were fitted with two Gaussian functions to identify the relative change in exciton and trion intensities, and the spectral shifts as the strain on the monolayer increased going from position X_1(near the SiO_2 pillar) to position X_3 (on top of the pillar). The fits were normalized with respect to the PL peak intensity at position X_3 to precisely identify the relative increase in exciton and trion PL intensities. These fits are shown in Fig.4.2.8.

From these fits it is clear that although the relative increase in the PL intensity at position X_3 compared to position X_1 corresponds primarily to an increase in the exciton peak intensity (from 60% to 70%), there is an increase in the trion peak intensity (from 25% to 30%). This increase in the trion peak intensity may be the consequence of a doping difference between the Si substrate and the SiO_2 nano-pillar. Alternatively, the trion population may have increased as a result of the accumulation of free electrons at the local conduction band minimum created by the strain profile; the accumulation of free electrons can increase the probability of neutral exciton-to-trion conversion in the region of highest strain [63]. Either of these possibilities could have have resulted in a centroid shift of the local PL spectra that

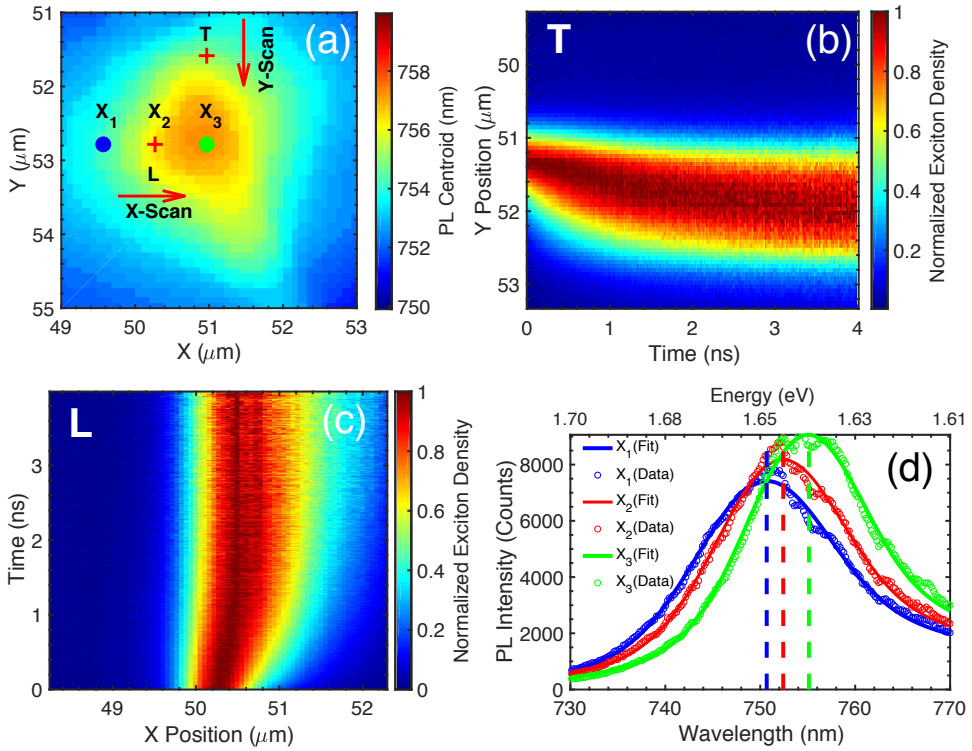

Figure 4.2.7: Transport of excitons in the strained portion of the WSe_2 monolayer. (a) PL centroid map of the WSe_2 monolayer zoomed in around the SiO_2 pillar and showing the excitation positions indicated by the plus (+) sign markers. (b) Normalized PL intensity as a function of position and time when the excitation was placed above the pillar, and the APD was scanned along the vertical direction from top to bottom. (c) Normalized PL intensity as a function of position and time when the excitation was placed to the left of the pillar and the APD was scanned along the horizontal direction from left to right. (d) PL spectra of the WSe_2 monolayer measured at the positions labeled by X_1 (blue), X_2 (red), and X_3 (green) in (a). The dashed vertical lines indicate the peak wavelength of each PL spectrum. The tensile strain caused by the SiO_2 pillar is evidenced by the red shifted PL spectra and the enhancement of the PL peak intensity as the strain increases. The PL spectra were fit with two Gaussian functions as the PL spectrum of the WSe_2 monolayer typically shows exciton and trion peaks. The excitation used for these measurements was a 405 nm pulsed laser with 200 nW average power, a pulse repetition rate of 40 MHz, and a beam diameter of approximately 500 nm. The estimated excitation fluence was 2.5 $\mu J cm^{-2}$. Reproduced with permission from [33].

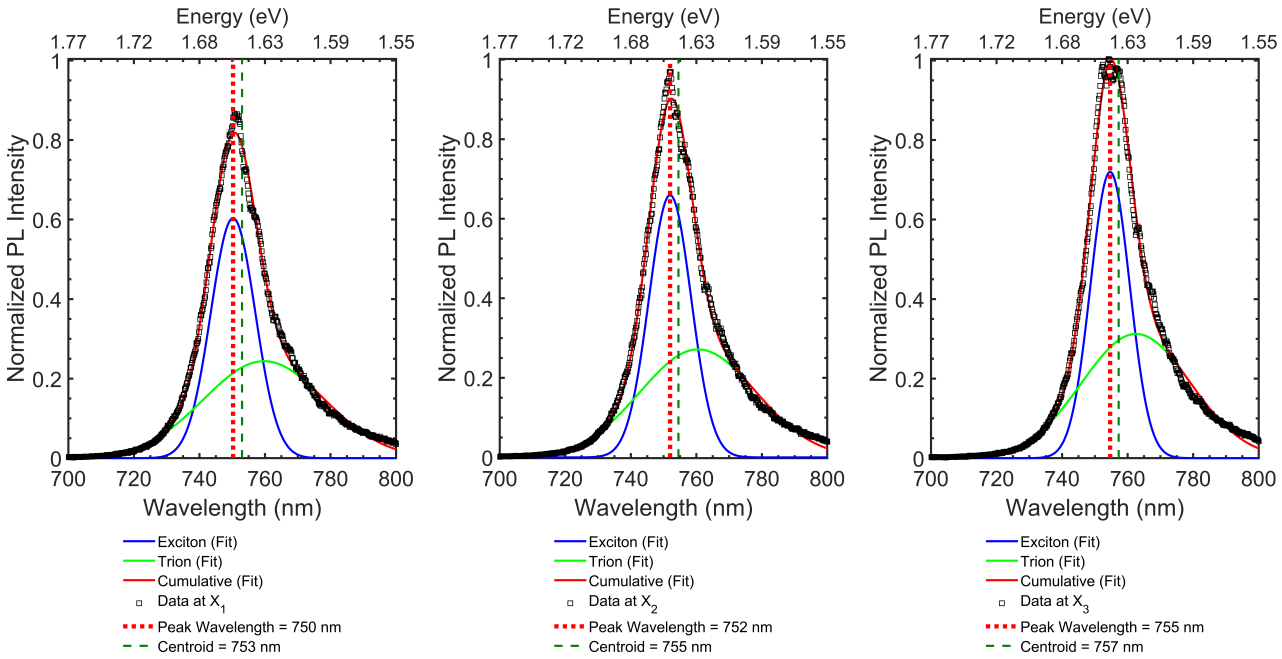

Figure 4.2.8: Fits to PL spectra of strained WSe_2 monolayer. PL spectra corresponding to the positions on the WSe_2 monolayer labeled as X_1, X_2, andX_3 in Fig.4.2.7(a). Each PL spectrum was fit with two Gaussian functions to identify the contributions from excitons and trions to the overall PL intensity. The raw PL intensity data and curve fits from all three positions were normalized with respect to the peak intensity of the PL spectrum at X_3, which corresponds to the top of the pillar, to identify the relative increase in PL intensity going from near the pillar at X_1 to on top of the pillar at X_3. Both the spectra's peak wavelengths and centroid have been labeled to identify the spectral shifts as a result of the strain on the WSe_2 monolayer. Reproduced with permission from [33].

could be misinterpreted as a strain-induced exciton peak wavelength shift. Nevertheless, by comparing the exciton peaks with the PL spectra's centroid, it is clear that the difference between exciton peaks and PL spectra's centroid remains nearly unchanged between position X_1 and position X_3. That is, the shift observed in the PL spectra's centroid correlates with the shift of the exciton peak wavelength. As a result, it can be concluded that the strain caused by SiO_2 nano-pillar is responsible for the increase in the exciton PL peak intensity. Similarly, the red shifts in the PL spectra at the high tensile strain regions result predominantly from the strain in the monolayer while doping and trion drift appear as secondary effects.

It is worth pointing out that since the population of trions relative to the population of excitons in the WSe_2 monolayer is not negligible as shown in Fig.4.2.8, the evolution of the exciton PL spectrum could be influenced by trions. Unfortunately, the time evolution of the WSe_2 monolayer's spectrum was not available, and therefore the evolution of the exciton and trion peaks could not be monitored separately. Furthermore, at room temperature, the spectral overlap between the exciton and trion peaks is too large to filter out the trion contribution in the TRPL measurements. Therefore, the only information that could be extracted from the spatially and temporally-resolved PL intensity maps, such as that in Fig.4.2.7(c), were the PL decay rates. These TRPL measurements typically follow a bi-exponential decay, which is consistent with other reports of TRPL measurements in TMDs where exciton-phonon scattering into dark exciton or trap states leads to a delayed exciton recombination in addition to the fast recombination of bright excitons, cf. references [118, 99, 221]. Figure 4.2.9 shows the spatially integrated, time-resolved PL intensity of Fig.4.2.7(c) and it was fitted with a bi-exponential function. The time-resolved data was normalized to the spatially integrated peak intensity.

It is possible that optically-generated heating of the WSe_2 monolayer could also lead to exciton drift towards the regions of highest temperature in the WSe_2 monolayer due to the temperature modulation of the monolayer's exciton resonance energy. Since the

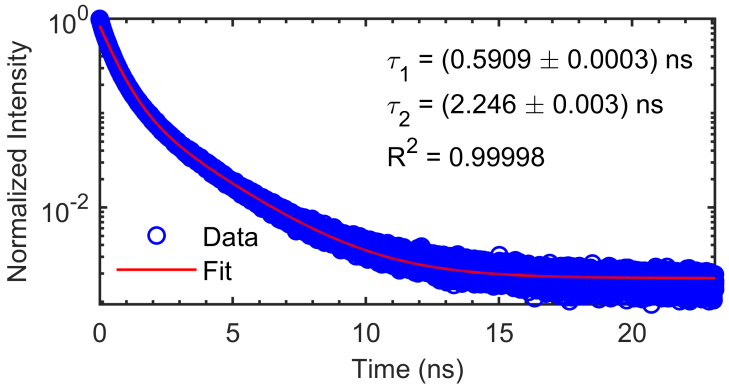

Figure 4.2.9: Time-resolved PL intensity of the strained WSe_2 monolayer. The data corresponds to the spatially integrated, time-resolved PL intensity of Fig.4.2.7(c). The time-resolved data was normalized to the spatially integrated peak intensity. This data was fitted with a bi-exponential function, and the resulting decay times are approximately 0.6 ns and 2.25 ns. Reproduced with permission from [33].

bandgap of semiconductors typically shrinks with increasing temperature, the excitons would be expected to drift towards the regions of highest temperature in the WSe_2 monolayer. As illustrated in the diagram of Fig.4.2.10, the excitons would be expected to drift due to in-plane temperature gradients in the WSe_2 monolayer as a result of two main processes: 1) the heat generated on the monolayer due to the non-resonant optical excitation, and 2) due to the different thermal conductivities of the Si substrate and the SiO_2 nano-pillar that would result in different temperatures at the boundaries between Si/WSe_2 and SiO_2/WSe_2.

An optical beam with a Gaussian intensity distribution should create an identical Gaussian temperature profile on the monolayer, which in turn should cause the drift of excitons towards the center of the excitation spot (away from the nano-pillar) where the intensity is the highest. Furthermore, since the thermal conductivity of Si is higher than the thermal conductivity of SiO_2, the temperature of the monolayer at the Si substrate/WSe_2 interface would be higher than the temperature at the SiO_2/WSe_2 interface (assuming negligible absorption of SiO_2 at the excitation wavelength of 405 nm). This effect would be dramatically increased by the Gaussian profile of the excitation beam. In either scenario, the temperature at the boundary between the monolayer and the nano-pillar would be lower than the temperature at the boundary between the monolayer and the Si substrate, and a drift of

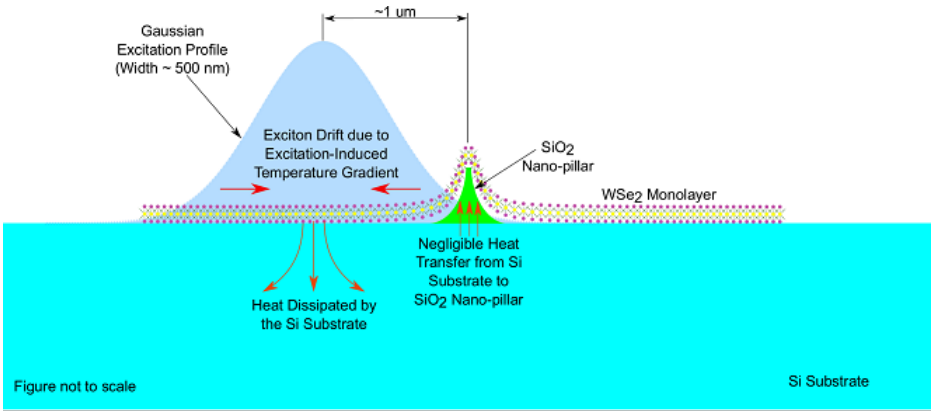

Figure 4.2.10: Diagram of the possible optically-generated heating of the WSe_2 monolayer leading to exciton drift. The figure is not drawn to scale. Reproduced with permission from [33].

excitons away from the SiO_2 pillar (instead of the observed drift of excitons towards the pillar) would be expected.

Lastly, when excitons were observed to drift towards the top of the SiO_2 nano-pillar, the peak of the excitation beam was positioned at a distance of approximately 1 μm from the top of the nano-pillar whereas the excitation beam width was approximately 500 nm. Hence, only the tail of the beam would have excited the WSe_2 monolayer sitting on top of the SiO_2 nano-pillar, generating a negligible amount of heat. Therefore, it can be reasonably concluded that the observed exciton drift towards the nano-pillar is caused by the strain gradient in the WSe_2 monolayer and not by temperature gradients caused by the optical excitation.

4.3 Modeling of exciton drift

To explain the apparent drift of excitons in the WSe_2 monolayer, a model that encompasses the drift, diffusion, and recombination of excitons was developed from Boltzmann's transport theory with the relaxation time approximation, and assuming a uniform exciton mobility [51, 18, 176]. The resulting differential equation describing the exciton dynamics is given by

$$\frac{\partial}{\partial t}n\left(x,t\right) = -\frac{n\left(x,t\right)}{\tau}+D\left(t\right)\left[\frac{\partial^{2}}{\partial x^{2}}n\left(x,t\right)\right]+\mu_{\epsilon}\frac{\partial}{\partial x}\left[n\left(x,t\right)\frac{\partial}{\partial x}\epsilon\left(x\right)\right] \quad (4.3.1)$$

where the first, second, and third terms in the right-hand side of the equal sign of Eq.4.3.1 represent the relaxation of the exciton density denoted by $n\left(x,t\right)$ with relaxation time constant τ, the diffusion of the exciton density with the time-varying diffusion coefficient $D\left(t\right)$, and the drift of the exciton density with strain mobility μ_{ϵ} due to the strain gradient $\frac{\partial}{\partial x}\epsilon\left(x\right)$,respectively. The strain mobility is defined as

$$\mu_{\epsilon}\equiv\left|\mu\frac{\partial E_{g}}{\partial\epsilon}\right|=\left|\frac{v_{d}}{\frac{\partial}{\partial x}\epsilon\left(x\right)}\right| \quad (4.3.2)$$

where $\partial E_g/\partial\epsilon$ is the sensitivity of the WSe_2 monolayer's bandgap to strain, v_d represents the density's drift velocity as a result of the strain gradient, and μ is the conventional mobility, which is defined as [216, 60, 210]

$$\mu = \frac{\left\langle\tau_{k}\right\rangle}{M} \quad (4.3.3)$$

where $\langle\tau_k\rangle$ is the ensemble-averaged scattering time, and M is the exciton translational mass. The units of the strain mobility are length squared per unit time and per percent strain, typically expressed in $cm^{2}s^{-1}\%^{-1}$. More details of the derivation of Eq.4.3.1 from the Boltzmann transport equation can be found in appendix A.

The strain mobility is not necessarily uniform throughout the WSe_2 monolayer because the non-uniform strain field modifies the monolayer's band structure, which in turn changes the exciton translational mass and the average exciton scattering time [44]. Such non-uniformity was observed after extracting the drift velocity from the measurements of the exciton PL intensity as a function of position and time. Specifically, the shift of the Gaussian

spatial distribution's peak as a function of time, which essentially represents the drift velocity of the exciton distribution due to the applied strain gradient, was calculated. Figure 4.3.1 shows the exciton PL intensity's peak position as a function of time when the excitation was placed just to the left of the high tensile strain point on top of the SiO_2 pillar [L in Fig.4.3.1(a)], and the mobility resulting from the local strain experienced by the exciton distribution's peak. As expected, the distribution's peak followed the direction of the strain gradient and moved towards the position of highest tensile strain. With the approximate local strain profile shown in Fig.4.3.1(a), the exciton distribution appeared to reach drift velocities as large as 250 ms^{-1} and drift distances as large as 500 nm.

Both the local strain as a function of position, and the exciton distribution's peak position as a function of time were fit with second-order polynomials to obtain smooth strain gradient, drift velocity, and mobility curves. As predicted, the resulting strain mobility appears to be non-uniform over the range where the distribution's peak moved. However, assuming that such variation is negligible, the model given by Eq.4.3.1, where the mobility is assumed to be uniform, may still be used to qualitatively explain the experimental observations. A simulation of the exciton distribution under an experimentally obtained strain profile along one spatial dimension and time is shown in Fig.4.3.1(e). The inputs to the numerical solver were the experimentally-obtained exciton PL intensity distribution at $t = 0$ as the initial condition, and the experimentally obtained parameters $D(t)$, $\epsilon(x)$, and μ_ϵ, where the strain mobility was averaged over the spatial range where the exciton distribution's peak moved. As expected, the numerical exciton distribution's peak shifted toward the high tensile strain point on top of the SiO_2 pillar. While the experimental exciton distribution appeared to become slightly asymmetric at later times, probably as the result of variations in the local strain field from features that can be observed on the AFM phase image of Fig.4.2.4(d) but the diffraction-limited imaging technique is unable to resolve, the numerical and experimental peak position are in reasonable agreement as illustrated in Fig.4.3.1(d). This reasonable agreement indicates that the drift, diffusion, and recombination model described by Eq.4.3.1

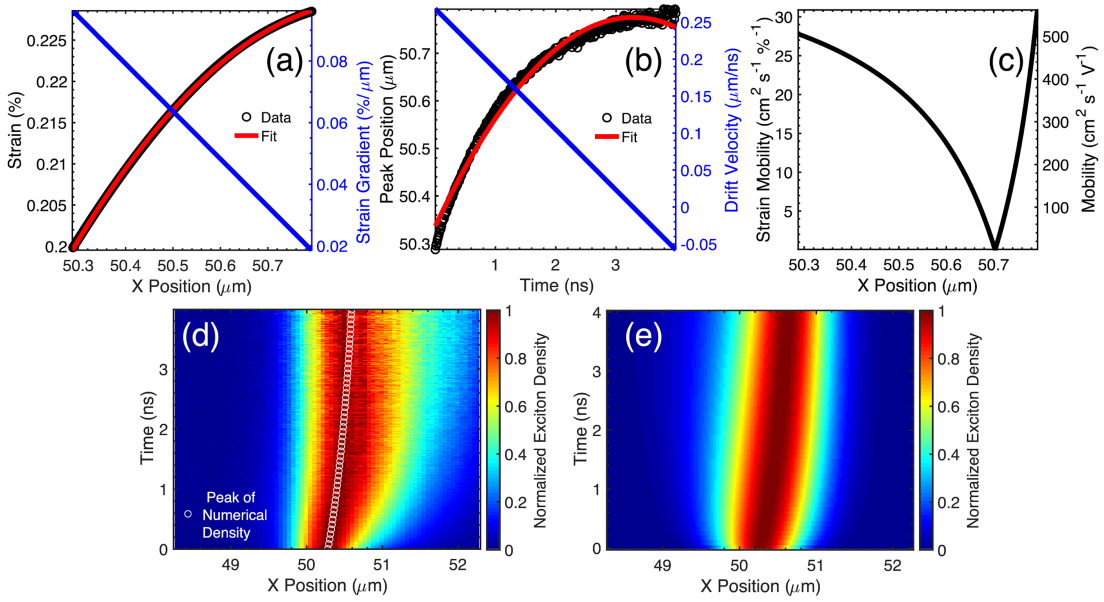

Figure 4.3.1: Strain mobility of the strained WSe_2 monolayer. (a) Local strain profile and strain gradient experienced by the exciton density's peak of the WSe_2 monolayer when the excitation was positioned just to the left of the pillar [L position in Fig.4.2.6(a)], and the APD was scanned along the horizontal direction from left to right. (b) Exciton density's peak position and drift velocity as a function of time. Both the experimental strain and density's peak position were fit with second-order polynomials to calculate smooth strain gradient and drift velocity curves, respectively. (c) Mobility obtained from experimental drift velocity and local strain gradient. Two different units for mobility are shown to compare the strain mobility to the traditional mobility of charge carriers. (d) and (e) Experimental and numerical normalized exciton densities as a function of position and time. The peak of the numerical exciton density is overlain on top of the experimental density for comparison. The parameters used in the numerical solution are $\alpha = 0.66$, $\Gamma = 0.17, \tau = 0.73\,\text{ns}, \mu_\epsilon = 18\,cm^2 s^{-1}\%^{-1}$, and $\partial E_g/\partial\epsilon = -55\ meV\%^{-1}$. Reproduced with permission from [33].

is able to replicate the main feature of the experimental observations.

4.4 Summary and conclusion

This chapter discussed measurements of the motion of a Gaussian spatial distribution of excitons in a non-uniformly strained WSe_2 monolayer. These measurements demonstrate that the propagation of excitons in the monolayer can be controlled via strain gradients at room temperature. The sensitivity of monolayer WSe_2's exciton resonance energy to strain enabled the creation of local strain gradients that resulted in the directional drift of exciton densities towards high-tensile strain points. Furthermore, the large susceptibility of WSe_2 monolayers to disorder led to anomalous diffusive transport with a time-varying diffusion coefficient. These observations were captured by the proposed drift-diffusion-relaxation model that includes the strain field on the WSe_2 monolayer. These results represent a stepping stone towards the control of the motion of excitons in monolayer TMDs with engineered strain profiles, and they open up the possibility to design novel, room-temperature-stable, excitonic devices that are robust against the capacitive losses and scalability limitations that hinder conventional optoelectronic technologies.

Chapter 5

Hot Excitons in TMD Monolayers

5.1 Introduction

Exciton transport in transition metal dichalcogenide (TMD) monolayers has been under extensive investigation over the past few years [22, 57, 90, 91, 78, 190, 33, 34, 198, 203] due to the prospects of building excitonic devices capable of operating at room temperature [190, 20]. Many of these studies have focused on quantifying the transport properties of excitons in TMD monolayers [22, 90, 91, 33, 97]. However, the origin of various dynamic effects, such as the apparent time-dependence of the exciton diffusivity observed in transport measurements of these materials, still remains elusive [33, 97].

A time-varying diffusivity is typically associated with anomalous diffusive transport of a distribution of particles. Anomalous diffusion is characterized by the nonlinear evolution of the spatial distribution's mean-squared displacement [111, 64, 138, 12]. While numerous processes in nature exhibit anomalous diffusive behavior [136, 137, 195, 123, 149, 146, 163], the physical mechanisms that lead to such phenomena are unique to each particular system. In layered, two-dimensional semiconductors, for example, the reduced dielectric screening enhances many-body interactions, which in turn can radically influence the dynamics of excitons, especially in the high-excitation-density regime [198, 144, 92, 121, 159]. Moreover, the

complex band structure of TMD monolayers, comprising of a variety of spin and momentum dark excitonic states, enables the seamless transition of excitons from initially-bright states into dark states via phonon scattering [46, 169, 107, 155]. The coupling between excitons and phonons are responsible for various kinetic effects observed in transport experiments of TMD monolayers such as the formation of spatial halos [90, 134], the apparent contraction or effective negative diffusion of excitons [153], and the transient diffusivity of excitons [34, 153].

In this chapter, the relaxation kinetics of hot excitons formed by a non-resonant optical excitation in an h-BN encapsulated WSe_2 monolayer, and the role of exciton-exciton Auger scattering on the nonlinear evolution of the CIV of excitons in the monolayer are discussed. Specifically, the effect of excitation density and photon energy on the temperature of the exciton gas are explored via optical measurements of the spatial and temporal evolution of the photoluminescence (PL) intensity distribution of the exciton gas at room temperature. The results of these experiments demonstrate that the initially-fast expansion of the exciton gas is the result of hot exciton transport, and it has a minimal contribution from Auger broadening. Auger broadening refers to the apparent fast expansion of the exciton density that results from the center of the PL intensity profile decaying faster than the edges due to density-dependent, non-radiative Auger recombination [90]. This chapter is based on published work that can be found in reference [34].

5.2 Theoretical background

Typical measurements of exciton transport in TMD monolayers employ optical excitations with photon energies above the optical bandgap of these materials. This type of excitation creates electron-hole pairs with excess kinetic energy that is typically relaxed via ultrafast interaction with phonons [17]. Soon thereafter, due to the strong Coulomb interaction in TMD monolayers, these electron-hole pairs bind to form excitons with high center-of-mass (COM) kinetic energy and momentum [135]. Excitons with high COM kinetic energy have a

high probability to undergo non-radiative recombination, which takes place either due to exciton dissociation, trapping by crystal defects [135, 200, 201], or rapid exciton-exciton Auger scattering [135, 17]. Auger scattering is much more likely to occur in semiconductor systems with reduced dimensionality than in the bulk crystal because the reduced Coulomb screening in low-dimension systems enhances many-body interactions [90, 92, 121, 200, 218, 217, 182]. Depending on the relative values of the recombination and kinetic energy relaxation rates, a fraction of the initially-created hot gas of excitons might completely relax the excess kinetic energy via phonon scattering prior to undergoing recombination [17, 135]. Eventually, the relaxed or cold exciton gas recombines and emits light which can be detected to infer the evolution of the exciton population.

While the high kinetic energy of the electron-hole pairs created by the non-resonant optical excitation might relax down to the bottom of the conduction band via phonon scattering, and form excitons with zero COM momentum, the direct formation of hot excitons via carrier-optical phonon scattering shortly after the non-resonant excitation is another possibility. In principle, these two exciton formation channels are both possible, but the dominant mechanism depends on their relative rates and on the material system. For example, in III-V semiconductors, where excitons have relatively low binding energies, the electron-hole pairs might relax toward the band minima separately, and then bind to form excitons after the energy relaxation process is complete [226]. On the other hand, in materials with much larger exciton binding energies, such as TMD monolayers, the formation of hot excitons via phonon scattering is a much more efficient process, thus dominating over the individual relaxation of electrons and holes[226]. Moreover, due to the strong Coulomb interaction and the presence of a large population of optical phonons at elevated lattice temperatures, excitons in TMD monolayers form very soon after the non-resonant optical excitation of electron-hole pairs . Therefore, the direct formation of hot excitons, following a non-resonant optical excitation, is the more efficient mechanism in TMD monolayers.

The distribution of kinetic energy immediately after the formation of hot excitons is not

necessarily a thermal distribution with a well-defined temperature. Instead, this distribution evolves towards equilibrium via many-body scattering with other excitons and with phonons [135]. After they reach a thermalized distribution, but before they recombine, hot excitons typically lose their remaining excess energy to the lattice also via phonon scattering. In the high-excitation-density regime, however, the relaxation of the excess energy or cooling of hot excitons via phonon scattering is counteracted by the heating of the exciton gas via exciton-exciton Auger scattering [82, 129]. During this type of many-body scattering process, an exciton recombines non-radiatively and transfers its energy to a nearby exciton, which ionizes into hot carriers with excess energy in the order of the bandgap energy. These newly-excited hot carriers also lose their excess energy via phonon scattering and eventually form new excitons with kinetic energy that is higher than the energy of the excitons undergoing Auger scattering. Theses newly-formed, hotter excitons continue to scatter with the remaining colder excitons, thereby increasing the overall gas temperature [82]. A schematic illustration of the exciton formation and Auger heating processes, as well as the timescales of the exciton formation, relaxation, and transport regimes, is shown in Fig.5.2.1

Because of the complex band structure of TMD monolayers, inter-valley scattering into energetically-lower-lying, momentum-indirect, dark states can affect the relaxation dynamics of hot excitons, especially at room temperature [155, 169, 16]. For tungsten-based TMD monolayers, in particular, the relaxation of the excess kinetic energy of hot excitons might occur primarily in a momentum-indirect or dark valley of the TMD monolayer because the lowest-lying excitonic states are usually located in such dark valleys [107]. Nevertheless, at sufficiently-high lattice temperatures, the excitons can scatter back into the momentum-direct, bright states and emit light [16]. At low lattice temperatures, the PL spectrum of TMD monolayers exhibit peaks arising from the phonon-assisted recombination of momentum-dark states [154, 16]. On the other hand, at higher lattice temperatures, the lower-lying, momentum-dark states simply give rise to a strong asymmetric broadening of the bright exciton resonance, especially at the low energy side [16]. Whether the relaxation of

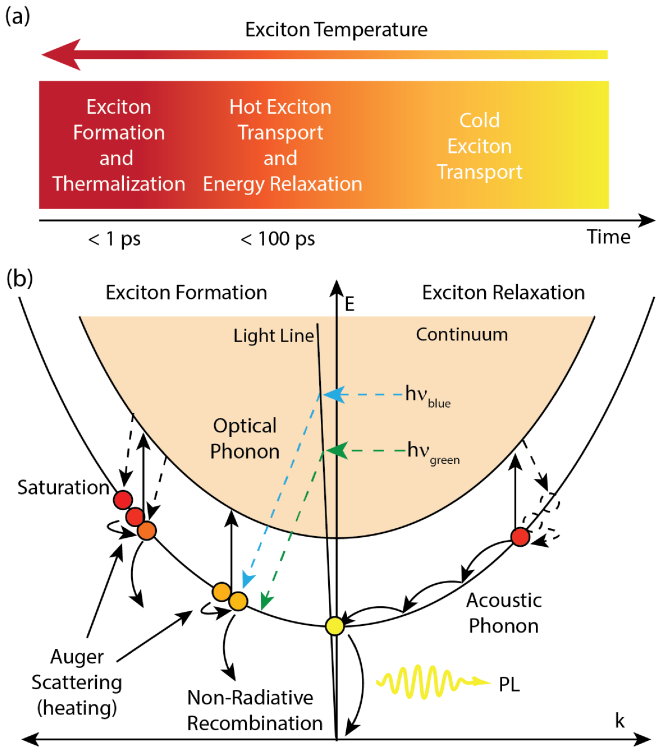

Figure 5.2.1: Schematic illustration of hot exciton dynamics and timescales. (a) Timescales of exciton formation, hot and cold exciton transport regimes, and the evolution of the temperature of the exciton gas. (b) Exciton dispersion relation illustrating the exciton formation, relaxation, and saturation processes. Saturation refers to the balance between the rates of exciton-exciton Auger scattering and exciton-phonon scattering. Reproduced with permission from [34].

the excess kinetic energy occurs in a momentum-dark or momentum-bright valley, evidence of the relaxation process is acquired via the radiative recombination of excitons that couple to the light cone.

Exciton-exciton Auger heating depends strongly on the density of excitons, which implies that this type of heating is most likely to occur at the onset of the relaxation process when the density of the exciton gas is at its highest. While hot excitons relax their kinetic energy, they also propagate and slow down. At the point when the exciton density has decayed enough for Auger scattering to be irrelevant, and the excess kinetic energy of the exciton gas has been relaxed to the lattice via phonon scattering, the remaining cold excitons diffuse at a constant rate. This trend is consistent with the nonlinear evolution of the CIV of excitons observed in transport measurements of TMD monolayers. Namely, the CIV evolves at a fast rate at the beginning of the relaxation process and gradually transitions into a slower constant rate evolution at the end of the relaxation process [33, 34].

The nonlinear CIV evolution implies that the exciton diffusivity is a time-dependent quantity. Such time-dependence can be linked to the evolution of the exciton gas temperature by examining the definition of the exciton diffusivity. In the quasi-classical limit, where the mean free path is much larger than the exciton de Broglie wavelength, the exciton diffusivity has the form [60]

$$D = \frac{k_B T \tau}{M} = k_B T \mu_X \tag{5.2.1}$$

where k_B is the Boltzmann constant, T is the exciton temperature, M is the exciton translational mass, and τ is the exciton momentum relaxation time. The exciton mobility μ_X is defined as

$$\mu_X \equiv \frac{\tau}{M} \tag{5.2.2}$$

The relaxation of the excess kinetic energy can be modeled by defining an effective time-

dependent exciton temperature given by

$$T(t) \equiv T_0 + T^* e^{-t/\tau^*} \tag{5.2.3}$$

where T_0, T^*, and τ^*represent the exciton temperature at the end of the relaxation process (steady state), the initial excess exciton temperature, and the kinetic energy relaxation time constant, respectively. If the excitons relax all of their excess kinetic energy before they recombine, the steady-state temperature T_0 is equal to the lattice temperature T_L, and the kinetic energy relaxation time constant is approximately equal to the exciton lifetime. Substituting the effective time-dependent temperature given by Eq.5.2.3 into the quasi-classical diffusivity expression given by Eq.5.2.1 yields the effective time-dependent diffusivity

$$\begin{aligned} D(t) &= \mu_X k_B \left(T_0 + T^* e^{-t/\tau^*}\right) \\ &= D_0 + D^* e^{-t/\tau^*} \end{aligned} \tag{5.2.4}$$

where D_0 and D^*represent the steady-state diffusivity and the excess diffusivity, respectively, and they are defined as

$$D_0 \equiv \mu_X k_B T_0 \tag{5.2.5}$$

$$D^* \equiv \mu_X k_B T^* \tag{5.2.6}$$

As the excitation density increases, the excess temperature and the excess diffusivity are expected to increase. Similarly, at elevated densities, the excess temperature and diffusivity are expected to saturate due to the balancing effects of Auger heating and phonon cooling

of the exciton gas discussed earlier.

As discussed in more detail in chapter 3, for a dilute gas of cold excitons moving in an energetically homogeneous medium, the MSD of a Gaussian spatial distribution of those excitons can be modeled using Fick's law of diffusion, also known as the diffusion equation. In one dimension, Fick's law of diffusion predicts that the MSD of a Gaussian spatial distribution centered at the origin is equal to its standard deviation, and it evolves linearly with time according to

$$\sigma^2(t) = \sigma^2(0) + 2Dt \tag{5.2.7}$$

where t is time, σ^2 is the variance of the Gaussian spatial distribution, and D is the diffusivity. For convenience, it is customary to plot the CIV of the Gaussian distribution, which is given by

$$\begin{aligned} \Delta\sigma^2(t) &= \sigma^2(t) - \sigma^2(0) \\ &= 2Dt \end{aligned} \tag{5.2.8}$$

and the slope of the CIV curve is proportional to the exciton diffusivity. Although Fick's law of diffusion assumes that the diffusivity is a constant property of the system, for instructive purposes, the evolution of the CIV can be approximated by substituting the effective time-dependent diffusivity from Eq.5.2.4 into Eq.5.2.8 to obtain the nonlinear evolution of the CIV arising from the relaxation of the excess exciton kinetic energy as

$$\Delta\sigma^2(t) = 2t\left(D_0 + D^* e^{-t/\tau^*}\right) \tag{5.2.9}$$

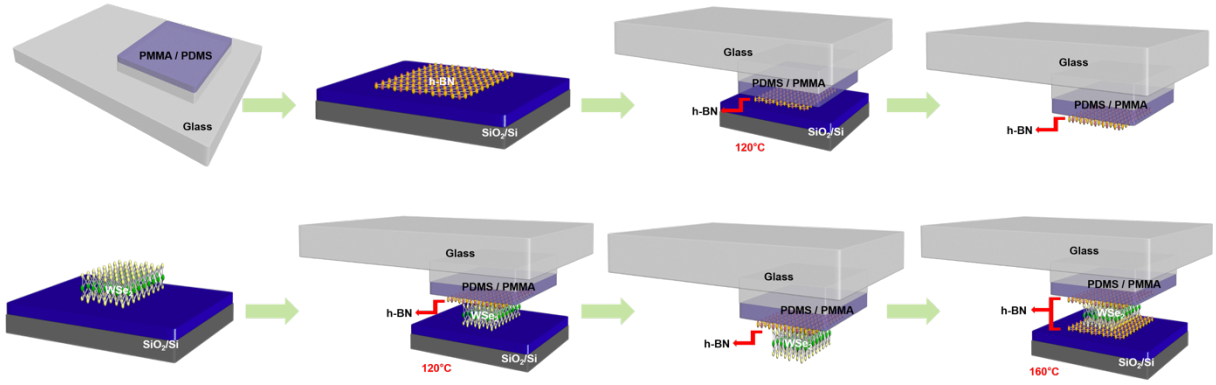

Figure 5.3.1: Procedure to fabricate h-BN encapsulated WSe_2 monolayers. The details of the technique are in the text below. Reproduced with permission from [34].

Fitting the CIV of a Gaussian spatial distribution of excitons in the h-BN encapsulated WSe_2 monolayer with Eq.5.2.9 provides insight into the relaxation kinetics of hot excitons in this type of materials.

5.3 Experimental results

This section discusses the sample fabrication process, and the experiments and analysis of the hot exciton transport measurements in the h-BN encapsulated WSe_2 monolayer.

5.3.1 Sample fabrication

The h-BN encapsulated WSe_2 monolayer sample was prepared by mechanically exfoliating monolayers from a bulk WSe_2 crystal, and then encapsulating them with h-BN using a PMMA/PDMS-assisted transfer process. Figure 5.3.1 shows a diagram detailing these fabrication steps.

First, a thin layer of polymethyl methacrylate (PMMA) was coated onto a thin layer of Polydimethylsiloxane(PDMS) carried by a glass substrate. Then, an h-BN flake was mechanically exfoliated onto a 300 nm thick SiO_2/Si substrate with p-doping, which was prepared in advance by exposing the SiO_2 surface to O2 plasma to turn the SiO_2 surface

into a hydrophilic surface and improve the adhesion of the flakes. Then, the h-BN flake was picked up from the SiO_2/Si substrate by stamping it with the PMMA/PDMS/glass stack while keeping the SiO_2/Si substrate at 120 °C.

Next, a WSe_2 monolayer was mechanically exfoliated onto a separate SiO_2/Si substrate. This WSe_2 monolayer was similarly picked up by the PMMA/PDMS/glass stack, which had already been used to pick up the h-BN flake, while keeping the new SiO_2/Si substrate at 120 °C. Then, the stacked WSe_2/h-BN heterostructure being carried by the PMMA/PDMS/glass stack was stamped onto a separate h-BN flake exfoliated onto another SiO_2/Si substrate while keeping the substrate at 160 °C.

The PMMA residue was removed from the sample by dipping it in an acetone bath for 1 hour followed by a rinse with isopropyl alcohol (IPA) and de-ionized (DI) water. Finally, the sample was annealed at 120 °C in a nitrogen atmosphere for 10 hours to remove the polymer residue, and to stabilize the heterostructure onto the substrate.

5.3.2 Transport measurements

The transport of hot excitons in the h-BN encapsulated WSe_2 monolayer was studied by monitoring its photoluminescence (PL) emission using the imaging technique described in chapter 3. With this technique, a spatially and temporally resolved map of the sample's PL intensity is constructed using an optical pulsed excitation with a diffraction-limited Gaussian intensity profile. The time information is obtained using time-correlated single photon counting, and the spatial information is obtained by scanning an avalanche photodiode detector (APD) across the PL emission spot.

Figure 5.3.2 shows the time evolution of the CIV of a Gaussian spatial distribution of excitons in the h-BN encapsulated WSe_2 monolayer for increasing excitation densities.

The time evolution of the CIV progresses from linear to nonlinear as the excitation density increases. The nonlinear regime, in particular, is characterized by a rapid increase of the CIV at early times, followed by a transition into a slower, constant-rate expansion for timescales

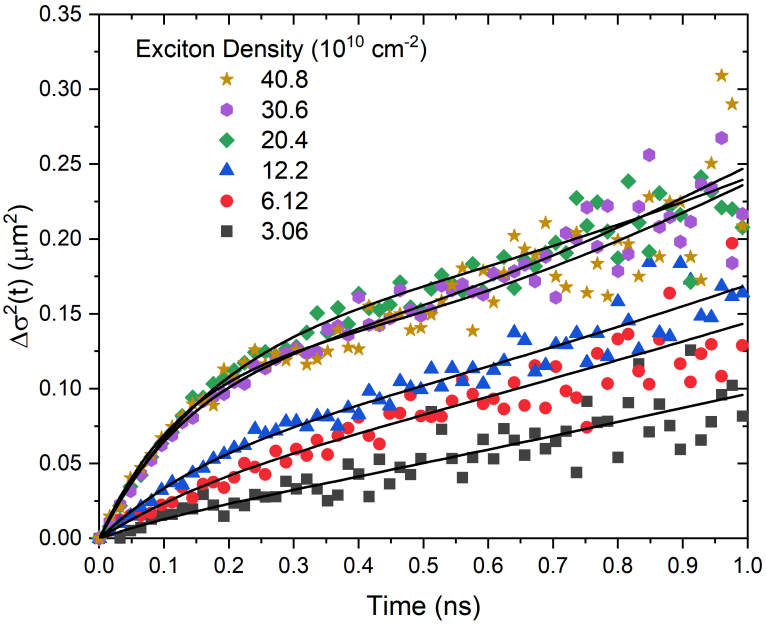

Figure 5.3.2: Evolution of the change in variance of a Gaussian distribution of excitons in an h-BN encapsulated WSe_2 monolayer on a SiO_2/Si substrate for increasing excitation densities. The solid lines represent the kinetic energy relaxation model fit represented by Eq.5.2.4, and the markers are the experimental data. Reproduced with permission from [34].

beyond hundreds of picoseconds. The slope of the CIV curve at early times increases as the excitation density increases, and it saturates at elevated densities. The initial exciton diffusivity, obtained by fitting the CIV curve with the kinetic model given by Eq.5.2.9, ranges between 0.5 cm^2s^{-1} at low excitation densities and 4 cm^2s^{-1} at high excitation densities as shown in Fig.5.3.3.

The apparent anomalous diffusive motion of excitons in the h-BN encapsulated WSe_2 monolayer is a result of the relaxation of the excess kinetic energy of hot excitons formed by the non-resonant optical excitation [82, 129, 36, 228, 215, 225, 130, 226, 223, 125], and partially due to Auger broadening.

Auger broadening refers to the apparent fast expansion of the exciton density that results from the center of the PL intensity profile decaying faster than the edges due to density-dependent, non-radiative Auger recombination [90, 215, 205]. Since the density of excitons at the center of the spot is higher than at the edges, the exciton-exciton Auger recombination rate at the center of the spot is the highest, and it decreases continuously towards the edges

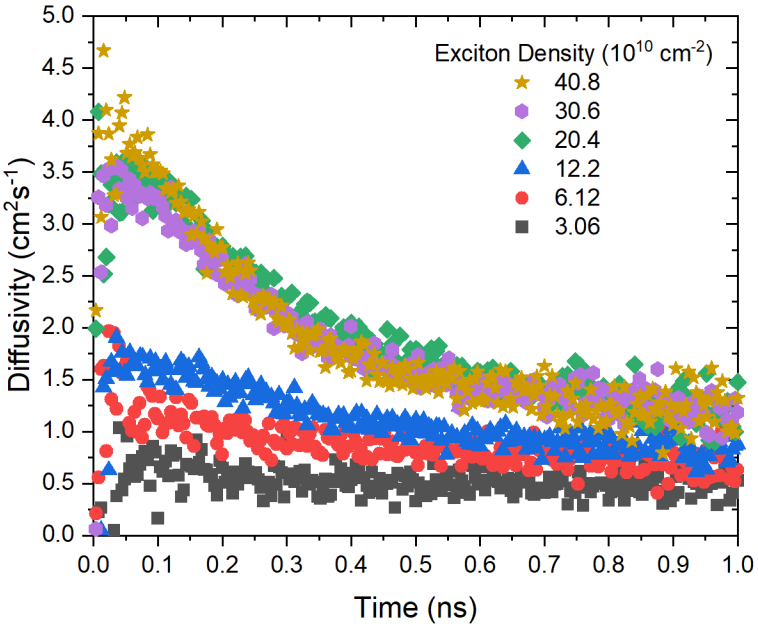

Figure 5.3.3: Time evolution of the diffusivity of the h-BN encapsulated WSe_2 monolayer for various excitation densities. The time-dependent diffusivity was calculated as $\Delta\sigma^2(t)/2t$ where $\Delta\sigma^2(t)$ is the experimental change in variance (CIV). Reproduced with permission from [34].

of the spot. Therefore, this form of non-radiative recombination might misleadingly appear as increasingly-fast exciton diffusion.

To quantify the contribution of Auger broadening to the evolution of the CIV of the exciton distribution, the time evolution of the spatially-integrated exciton density was modeled using the rate equation

$$\frac{\partial n(t)}{\partial t} = -\frac{n(t)}{\tau_r} - \gamma_A n^2(t) \tag{5.3.1}$$

where $n(t)$, τ_r, and γ_A represent the spatially-integrated exciton density or exciton number, recombination time constant or lifetime, and the Auger constant, respectively [218]. A solution to this rate equation is given by [90]

$$n(t) = \frac{n(0)\, e^{-t/\tau_r}}{1 + [n(0)\, \gamma_A \tau_r]\,(1 - e^{-t/\tau_r})} \tag{5.3.2}$$

where $n(0)$ is the exciton number at $t = 0$. Unlike Fick's law of diffusion, the rate equation Eq.5.3.1 does not include the spatial evolution of the exciton density. Nevertheless, the solution to this rate equation can be used to fit the spatially-integrated exciton PL intensity and extract the lifetime and Auger constant. Then, these parameters can be used to estimate the broadening of the exciton density solely due to exciton-exciton Auger recombination by calculating the exciton density locally at each position of the distribution using Eq.5.3.2 as

$$n(x,t) = \frac{n(x,0)\, e^{-t/\tau_r}}{1 + [n(x,0)\, \gamma_A \tau_r]\,(1 - e^{-t/\tau_r})} \tag{5.3.3}$$

where x is the (one-dimensional) spatial coordinate. Moreover, the resulting spatial profile can be fitted with a Gaussian function at each time step and the change in variance purely due to exciton-exciton Auger recombination can be extracted. Lastly, the contribution of Auger broadening to the total CIV can be estimated by breaking it up into components as

$$\Delta\sigma^2 = \Delta\sigma^2_{Hot} + \Delta\sigma^2_A \tag{5.3.4}$$

where $\Delta\sigma^2_{Hot}$ and $\Delta\sigma^2_A$ denote the hot exciton transport and Auger broadening contributions to the total CIV of the exciton distribution.

Figure 5.3.4 shows the time evolution of the spatially-integrated PL intensity of the h-BN encapsulated WSe_2 monolayer for various excitation densities.

The majority of the transport measurements were carried out with an excitation density that falls within the so-called mid-excitation regime [90]. The estimated values for the Auger

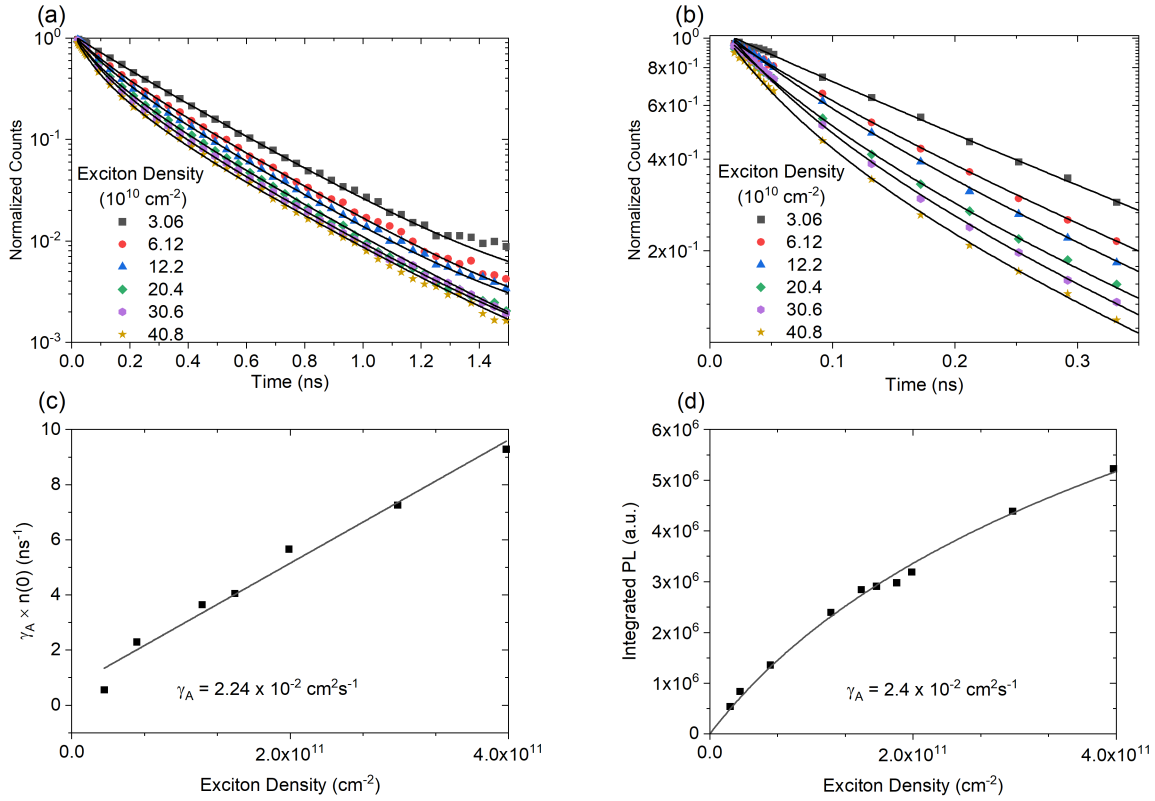

Figure 5.3.4: Time-resolved photoluminescence (TRPL) of the h-BN encapsulated WSe_2 monolayer. (a) TRPL intensity of the h-BN encapsulated WSe_2 monolayer for increasing exciton density. The solid lines represent the fits to the TRPL intensity data (markers) with Eq.5.3.2, and they were obtained assuming 11.5% absorption of the optical excitation at 405 nm [180], and accounting for the optical losses of the experimental apparatus. (b) Initial decay of the TRPL in (a) emphasizing the lack of excitation density-induced saturation if exciton-exciton Auger recombination were the dominant recombination mechanism. (b) Auger constant estimated by fitting the data in (a) with Eq.5.3.2. The y axis represents the product of the initial exciton density, which is denoted by $n\,(0)$, and the Auger constant γ_A. (c) Spatially and time integrated PL intensity for increasing exciton density. The Auger constant was also estimated by fitting the PL intensity with Eq.5.3.5. Reproduced with permission from [34].

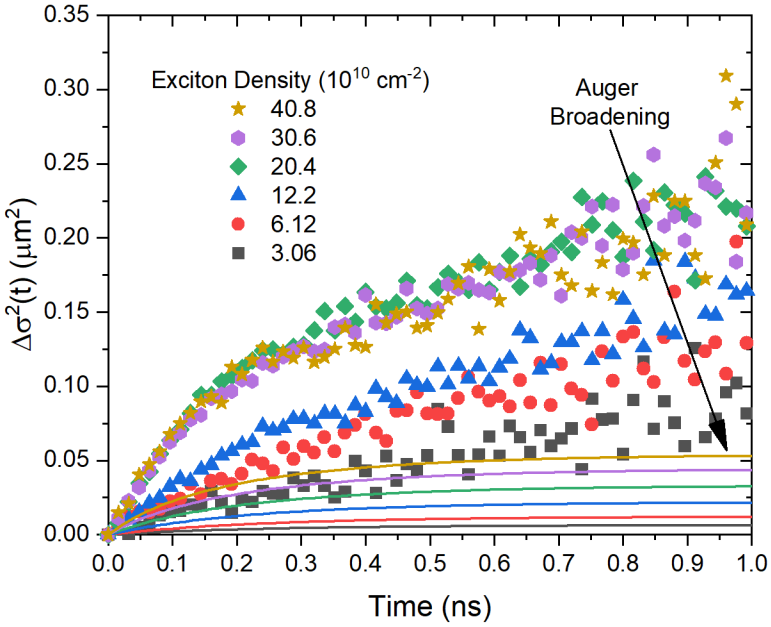

Figure 5.3.5: Contribution of Auger broadening (solid lines) to the change in variance of the Gaussian spatial distribution of excitons in the h-BN encapsulated WSe_2 monolayer for increasing excitation densities (markers). The contribution of Auger broadening to the total CIV is negligible for excitation densities below $4 \times 10^{11} cm^{-2}$. The markers correspond to the data shown in Fig.5.3.2. Reproduced with permission from [34].

constant and exciton lifetime extracted from fitting the the time-resolved PL intensity measurements with Eq.5.3.2 are 0.02 $cm^2 s^{-1}$ and 0.23 ns, respectively, as shown in Fig.5.3.4(c). Based on these values, the contribution of Auger broadening to the CIV is minimal for excitation densities below $(\gamma_A \tau_r)^{-1} = 2 \times 10^{11} cm^{-2}$. To confirm this prediction, the contribution of Auger broadening to the CIV for various excitation densities was calculated as previously discussed, and the results are shown in Fig.5.3.5.

The contribution of Auger broadening to the total CIV is minimal for excitation densities below $4 \times 10^{11} cm^{-2}$. This observation is consistent with other reports of studies where exciton-exciton Auger scattering has been shown to be drastically reduced in h-BN encapsulated TMD monolayers [70]. Most importantly, Auger broadening cannot explain the saturation of the slope of the CIV curves observed in Fig.5.3.2 at excitation densities above $2 \times 10^{11} cm^{-2}$. Because the time-integrated PL intensity shown in Fig.5.3.4(d) continues to rise for excitation densities above this value, it is clear that the exciton-exciton Auger recombination rate is

not higher than the exciton creation rate. Moreover, the Auger constant extracted from the integrated PL intensity using the empirical expression [90]

$$I_{PL} \quad \propto \quad \ln\left[\frac{1+n\left(0\right)\gamma_A\tau_r}{\gamma_A\tau_r}\right] \tag{5.3.5}$$

is consistent with the Auger constant obtained from fitting the TRPL intensity data with Eq.5.3.2 as shown in Fig.5.3.4(c). Therefore, the fast rise of the CIV at early times is caused predominantly by the fast motion of hot excitons whose temperature is higher than the lattice temperature [36, 215, 225, 226, 224]. So, the progression from a fast evolution to a slow evolution of the CIV for a given excitation density can be explained reasonable well as the transition from a hot gas of excitons, which move very fast due to their high kinetic energy, to a cold gas of excitons that move more slowly, after having relaxed their excess kinetic energy.

The fast initial evolution rate of the CIV is proportional to the value of the time-dependent effective diffusivity given by Eq.5.2.4 in the limit as time approaches zero, i.e. $\lim_{t\to 0}\left[D\left(t\right)\right] = D_0 + D^*$. The CIV data shown in Fig.5.3.2 was fitted with the energy relaxation model given by Eq.5.2.9, and the resulting excess diffusivity for various excitation densities is shown in Fig.5.3.6(a).

Following the same trend as the slope of the CIV, the fitted excess diffusivity D^* appears to increase as the excitation density increases, and it also saturates at elevated excitation densities. This saturation is expected to occur due to the balancing effects of Auger heating and phonon cooling of the exciton gas discussed earlier. It is well-known that the rate of carrier and exciton scattering with phonons increases as their kinetic energy increases [148]. Due to strong Coulomb coupling in TMD monolayers, exciton-phonon scattering dominates the energy transfer mechanism that determines the temperature of the exciton gas at elevated excitation densities. Therefore, the observed saturation of the initial slope of the CIV curves

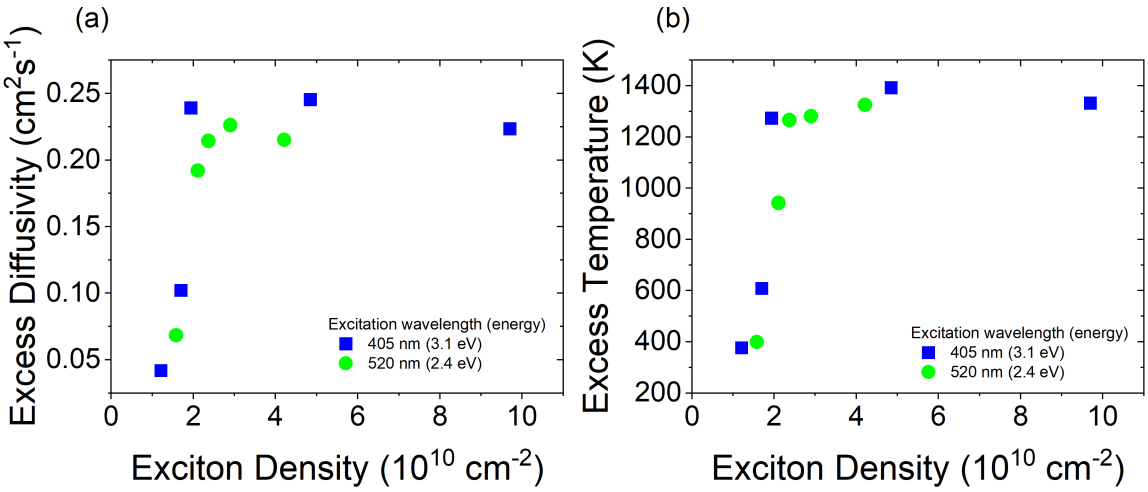

Figure 5.3.6: Excess diffusivity (a) and temperature (b) of excitons in the h-BN encapsulated WSe_2 monolayer for excitations with different photon energies and increasing densities. The excess excess diffusivity was extracted by fitting the CIV curves in Fig.5.3.2 with Eq.5.2.9. The steady-state temperature of the exciton gas was assumed to be equal to the lattice temperature at 300 K, and the resulting relaxation time was equal to 0.26 ns. The saturation of the excess diffusivity and the corresponding excess temperature occur at a higher excitation density for the laser with lower photon energy (2.4 eV) than for the laser with higher photon energy (3.1 eV). Reproduced with permission from [34].

and the extracted excess diffusivity, which is proportional to the exciton gas temperature, is consistent with the balance between exciton-phonon scattering, which removes energy from the exciton gas, and Auger heating, which increases the energy of the exciton gas.

As a reference, the average velocity at which the PL spot corresponding to the data shown in Fig.5.2.7 broadens was compared to the carrier saturation velocities determined by electrical measurements [75]. As shown in Fig.5.3.7, the velocity at which the saturation of the initial slope of the CIV occurs is about two orders of magnitude below the saturation velocity of both electrons and holes in monolayer WSe_2. This result further confirms that hot excitons, and not individual hot carriers, are responsible for the trends observed in the experiments.

To further support the hypothesis that the relaxation of the excess kinetic energy of hot excitons is the responsible mechanism for the nonlinear evolution of the CIV, experiments with an optical excitation with a lower photon energy were carried out on a different h-BN

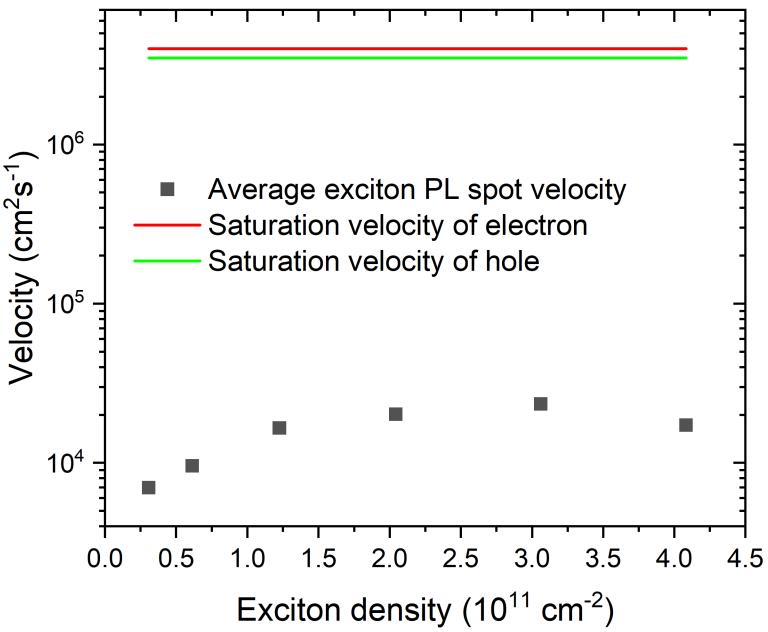

Figure 5.3.7: Comparison of PL spot velocity and electron and hole saturation velocities. The PL spot velocity corresponds to the time-averaged rate of change of the PL spot's standard deviation, i.e. $\left\langle \frac{d\Delta\sigma(t)}{dt} \right\rangle$. The brackets denote time average. The carrier saturation velocities were taken from electrical measurements of reference [75]. Reproduced with permission from [34].

encapsulated WSe_2 monolayer. If the nonlinear evolution of the CIV indeed arises from the relaxation of the excess kinetic energy of a hot exciton gas, and not from Auger broadening, then for lower excitation energies, the saturation of the initially-fast CIV slope and initial excess exciton diffusivity and temperature should occur at higher excitation densities. Such trend is expected because the higher the excitation energy, the higher the excess kinetic energy of the initially-formed hot exciton gas, and the less energy that will be required via Auger heating to reach the saturation temperature. This trend is precisely observed in Fig.5.3.6 where the excess diffusivity and effective temperature of the initially-formed exciton gas is shown for two different excitation energies, 3.1 eV (405 nm) and 2.4 eV (520 nm), for increasing excitation densities. As expected, the excitation density required to reach the saturation excess diffusivity with the lower photon energy excitation (520 nm) is higher than the excitation density required to reach the same saturation diffusivity with the higher photon energy excitation (405 nm). Such correlation between excitation density and photon energy is convincing evidence that the initially-fast motion of the exciton gas stems primarily from the motion of hot excitons created by the non-resonant optical excitation rather than Auger broadening.

5.4 Summary and conclusion

This chapter discussed transport studies of hot excitons in h-BN encapsulated WSe_2 monolayers via spatially and temporally-resolved PL measurements at room temperature. The origin of the apparently anomalous diffusive motion of excitons in h-BN encapsulated WSe_2 monolayers was attributed to hot exciton transport. A correlation between the initial slope of the CIV and the excitation density, which saturates at elevated excitation densities, was identified. This saturation is consistent with the balancing effects of Auger heating and phonon cooling that respectively increase and decrease the temperature of the exciton gas. In addition, it was shown that the excitation density required to reach the saturation point

of the excess diffusivity depends on the excitation's photon energy. That is, a higher photon energy excitation requires a lower excitation density to reach the saturation excess diffusivity. These results offer insights into a process that is ubiquitous in exciton transport studies of TMD monolayers where high-density, non-resonant optical excitation is typically employed. These insights will aid in the design of excitonic devices that exploit the regimes of hot and cold exciton transport.

Chapter 6

Many-Body Effects in TMD Monolayers

6.1 Introduction

Inspired by the possibility of controlling chemical reactions [62, 171, 206], developing increasingly powerful computers [104, 71, 52], and pushing the limits of measurement sensitivity [40], the control of coherent light-matter interactions has been under extensive investigation for several decades. In particular, coherent control in semiconductors has focused on leveraging the strong optical-electric as well as spin-electric coupling that characterize these materials to reduce decoherence and achieve fault-tolerant controllability [214, 193, 181, 142, 178]. Due to their compatibility with traditional III-V semiconductor device fabrication technology and their robust optical response, charge carriers strongly localized in self-assembled semiconductor quantum dots have become the archetypal two-level system in semiconductor materials to investigate coherent light-matter interactions. More recently, the search for coherent nonlinearities beyond Pauli blocking to expand the library of coherent control schemes, has lead to excitons–Coulomb bound electron-hole pairs–as promising quantum excitations with prominent optical nonlinearities [113]. The control of these quantum states inevitably requires the control of many-body effects resulting from their Coulomb interaction with electron-hole plasma and coherent polarizations [177]. While excitonic states in mesoscopic

semiconductor quantum wells have also been studied extensively [93, 164, 9, 84], the small excitonic binding energy in these materials has hindered the coherent manipulation of excitons due to their efficient ionization at room temperature. Recent progress in the fabrication of atomically-thin semiconductors, however, has shifted the focus of the studies of coherent excitonic nonlinearities to TMD monolayers [81, 46, 170, 80, 86, 150, 192, 184, 98, 165].

The optical response of TMD monolayers below the conduction band edge is strongly dominated by excitons as a result of the reduced dielectric screening and strong Coulomb interactions in these atomically-thin semiconductor crystals. These conditions allow for the signatures of excitation-induced many-body effects to be readily accessible in the nonlinear optical spectra of TMD monolayers. Similar to conventional III-V semiconductor quantum wells, the signatures of many-body effects in TMD monolayers include excitation-induced dephasing (EID) and excitation-induced shifts (EIS) arising from a unique mixture of electron-hole plasma, exciton, and polarization effects [177]. Moreover, the complex band structures of TMD monolayers, featuring multiple valleys, enables excitonic nonlinearities mediated by the interaction of optically bright and momentum and spin-dark excitons. While EID and EIS arise primarily from the Coulomb coupling among excitons, electron-hole plasma, and polarizations [177], energy shifts in TMD monolayers have also been attributed to intervalley exciton coupling mediated by the exchange interaction [165].

The spectral signatures of many-body effects in semiconductor quantum wells [177] and in TMD monolayers [46, 81] have been explained theoretically via self-consistent calculations using the semiconductor Bloch equations. However, the main experimental signatures of these effects can be reproduced phenomenologically by modeling the excitons in these materials as an ensemble of two-dimensional, two-level systems or a sheet of dipole emitters (SDE) using the master equation [161]. The following section describes the development of the theoretical model used to interpret the spectral signatures of many-body effects in the nonlinear optical response of TMD monolayers using the master equation.

6.2 Theoretical modeling

While the band structure of TMD monolayers is complex and intervalley coupling has been shown to play a role in the origin of many-body effects in these materials [165, 46], some of the main features present in the nonlinear optical spectrum of TMDs, namely energy shifts and linewidth broadening, can be reproduced reasonably well by modeling one of their optically accessible valleys as a two-level system.

6.2.1 Macroscopic polarization of a two-level system

A TMD monolayer can be modeled as a two-dimensional sheet of dipole emitters (SDE), and the optical response of the system can be expressed through the macroscopic optical polarization given by [10]

$$\begin{aligned} \mathbf{P}(\mathbf{R},t) &= \mathbf{P}(x,y,t)\,\delta(z) \\ &= N_a Tr\left[\hat{\rho}(x,y,t)\,\hat{\mu}\right]\delta(z) \\ &= N_a\left[\rho_{21}(x,y,t)\,\mu_{12}+c.c.\right]\delta(z) \end{aligned} \tag{6.2.1}$$

where $\hat{\rho}$ and $\hat{\mu}$ are the density and dipole moment operators, and N_a represents the aerial density or number of dipoles per unit area. The delta function represents the confinement of the TMD monolayer along the direction of light propagation, and $\mathbf{P}(x,y,t)$ represents the two dimensional, time-dependent, macroscopic polarization. While the in-plane distribution of dipoles strictly depends on the incident laser intensity distribution, the two-dimensional polarization can be assumed to be uniform if the incident field is modeled as a plane wave. In that case, the three-dimensional macroscopic polarization can be recast as

$$\mathbf{P}(z,t) = \mathbf{P}(t)\,\delta(z) \tag{6.2.2}$$

where the uniform two-dimensional polarization is

$$\mathbf{P}(t) = N_a\left[\rho_{21}(t)\,\mu_{12} + c.c.\right] \tag{6.2.3}$$

with positive and negative frequency components defined as

$$\mathbf{P}^{(+)}(t) = N_a\rho_{21}(t)\,\mu_{12}\hat{r}_{12} \tag{6.2.4}$$

$$\mathbf{P}^{(-)}(t) = N_a\rho_{12}(t)\,\mu_{21}\hat{r}_{21} \tag{6.2.5}$$

The evolution of the macroscopic polarization is obtained by solving the Heisenberg equation of motion for the density operator given by

$$\frac{\partial}{\partial t}\hat{\rho} = \left.\frac{\partial}{\partial t}\hat{\rho}\right|_{coh} + \left.\frac{\partial}{\partial t}\hat{\rho}\right|_{incoh} \tag{6.2.6}$$

where the first term in Eq.6.2.6 represents the coherent interaction of the two-level system with the optical field, and the second term represents the dissipation and decoherence of the system. The coherent light-matter interaction term of Eq.6.2.6 is given explicitly by

$$\left.\frac{\partial}{\partial t}\hat{\rho}\right|_{coh} = \frac{1}{i\hbar}[\hat{H},\hat{\rho}] \tag{6.2.7}$$

where

$$\hat{H} = \hat{H}_0 + \hat{V} \tag{6.2.8}$$

is the total Hamiltonian of the system comprising of the internal structure Hamiltonian $\hat{H}_0$ and the interaction with the light field $\hat{V}$. The internal structure Hamiltonian is given by

$$\hat{H}_0 = -\frac{\hbar\omega_{21}}{2}\hat{\sigma}_z \tag{6.2.9}$$

where $\hbar\omega_{21} \equiv \hbar(\omega_2 - \omega_1)$ is the energy difference between the excited and ground states, which is also known as the resonance energy of the two-level system. The factor of $\frac{1}{2}$ in the Hamiltonian comes from the arbitrary assignment of zero energy as the midpoint between the energies of the two states. With this definition, the ground state energy is negative and the excited state energy is positive. The Pauli matrix operator $\hat{\sigma}_z$ is defined in terms of the bra and ket representing the ground state $|1\rangle$ and the excited state $|2\rangle$ of the two-level system as

$$\hat{\sigma}_z = |1\rangle\langle 1| - |2\rangle\langle 2| \doteq \begin{pmatrix} 1 & 0 \\ 0 & -1 \end{pmatrix}$$

The light-matter interaction is described semi-classically by the dipole interaction approximation as

$$\hat{V} \approx -\hat{\mu} \cdot \mathbf{E}(\mathbf{R}, t) \tag{6.2.10}$$

where the dipole moment operator is defined as

$$\hat{\mu} = \mu_{21}\hat{r}_{21}\hat{\sigma}_+ + \mu_{12}\hat{r}_{12}\hat{\sigma}_- \tag{6.2.11}$$

For an arbitrary number N of harmonically oscillating electromagnetic fields of the form

$$\mathbf{E}(\mathbf{R},t)=\frac{1}{2}\sum_{j=1}^{N}\left[\hat{\epsilon}_j\mathcal{E}_j\left(\mathbf{R},t\right)e^{i\mathbf{k}_j\cdot\mathbf{R}-i\omega_j t}+\hat{\epsilon}_j^{*}\mathcal{E}_j^{*}\left(\mathbf{R},t\right)e^{-i\mathbf{k}_j\cdot\mathbf{R}+i\omega_j t}\right] \tag{6.2.12}$$

the interaction part of the Hamiltonian in Eq.6.2.8, within the rotating-wave approximation (RWA), is given by [10]

$$\begin{aligned}\hat{V}_{RWA} &\approx -\hbar\sum_{j=1}^{N}\left[\chi_{R_j}\left(\mathbf{R},t\right)e^{i\mathbf{k}_j\cdot\mathbf{R}-i\omega_j t}\hat{\sigma}_{+}\right.\\ &\left.-\chi_{R_j}^{*}\left(\mathbf{R},t\right)e^{-i\mathbf{k}_j\cdot\mathbf{R}+i\omega_j t}\hat{\sigma}_{-}\right]\end{aligned} \tag{6.2.13}$$

where one half times the Rabi frequency $\chi_{R_j}\left(\mathbf{R},t\right)\equiv\frac{1}{2}\Omega_{R_j}\left(\mathbf{R},t\right)$ is defined as

$$\chi_{R_j}\left(\mathbf{R},t\right)\equiv\left(\hat{r}_{21}\cdot\hat{\epsilon}_j\right)\frac{\mu_{21}\mathcal{E}_j\left(\mathbf{R},t\right)}{2\hbar} \tag{6.2.14}$$

and$\mathcal{E}_j\left(\boldsymbol{R},t\right)$ and $\hat{\epsilon}_j$ represent the amplitude and polarization direction unit vector of each electric field, respectively; $\hat{r}_{12}=\hat{r}_{12}^{*}$ is the unit vector in the direction of the vector dipole operator $\hat{\mu}$. Similarly, the Pauli matrix operators $\hat{\sigma}_{\pm,0}$ are defined as

$$\hat{\sigma}_{-}=\left|1\right\rangle\left\langle 2\right|\doteq\begin{pmatrix}0 & 1\\ 0 & 0\end{pmatrix} \tag{6.2.15}$$

$$\hat{\sigma}_{+}=\left|2\right\rangle\left\langle 1\right|\doteq\begin{pmatrix}0 & 0\\ 1 & 0\end{pmatrix} \tag{6.2.16}$$

$$\hat{\sigma}_0 = \hat{\sigma}_+\hat{\sigma}_- \doteq \begin{pmatrix} 0 & 0 \\ 0 & 1 \end{pmatrix} \tag{6.2.17}$$

The incoherent part of the equation of motion Eq.6.2.6 is given by

$$\frac{\partial}{\partial t}\hat{\rho}\bigg|_{incoh} = -\gamma\left\{\hat{\sigma}_0, \hat{\rho}\right\} + \gamma_{sp}\hat{\sigma}_-\hat{\rho}\hat{\sigma}_+ + 2\Gamma\hat{\sigma}_0\hat{\rho}\hat{\sigma}_0 \tag{6.2.18}$$

where γ, γ_{sp}, and Γ represent the dephasing, spontaneous emission, and pure dephasing rates, respectively; the curly brackets in Eq.6.2.18 denote the anti-commutation relation $\{A, B\} = AB + BA$; the dephasing rate is defined as

$$\gamma = \frac{\gamma_{sp}}{2} + \Gamma \tag{6.2.19}$$

The terms on the right hand side of Eq.6.2.18 are also known as the Lindblad terms and they represent the incoherent or dissipation processes in the system. While the Lindblad terms in the form presented in Eq.6.2.18 are unable to describe certain quantum kinetic aspects of semiconductors such as Coulomb-based quantum memory or many-body effects [85], as a first approximation, the master equation Eq.6.2.6 is often used to model coherent light-matter interactions in semiconductor quantum dots. Substituting the coherent and incoherent equations of motion, Eq.6.2.7 and Eq.6.2.18, into the Heisenberg equation of motion Eq.6.2.6, and enforcing the conditions that the total probability must equal unity $Tr\left[\hat{\rho}\right] = \rho_{11}(t) + \rho_{22}(t) = 1$ and the off-diagonal density matrix elements must be complex conjugates of each other $\rho_{12}(t) = \rho_{21}^*(t)$, the equations of motion for the density operator reduce to

$$\frac{\partial}{\partial t}\rho_{22}(t) = \sum_{j=1}^{N}\left[i\chi_{R_j}(\mathbf{R},t)\,e^{i\mathbf{k}_j\cdot\mathbf{R}-i\omega_j t}\rho_{12}(t) - i\chi^*_{R_j}(\mathbf{R},t)\,e^{-i\mathbf{k}_j\cdot\mathbf{R}+i\omega_j t}\rho_{21}(t)\right] - \gamma_{sp}\rho_{22} \tag{6.2.20}$$

$$\frac{\partial}{\partial t}\rho_{12}(t) = -(\gamma - i\omega_{21})\,\rho_{12}(t) - [1-2\rho_{22}(t)]\,i\sum_{j=1}^{N}\left[\chi^*_{R_j}(\mathbf{R},t)\,e^{-i\mathbf{k}_j\cdot\mathbf{R}+i\omega_j t}\right] \tag{6.2.21}$$

$$\rho_{11}(t) = 1 - \rho_{22}(t) \tag{6.2.22}$$

$$\rho_{21}(t) = \rho^*_{12}(t) \tag{6.2.23}$$

Therefore, the only equations of motion that need to be solved to calculate the macroscopic polarization of the two-level system are Eq.6.2.20 and Eq.6.2.21.

The signatures of many-body effects on the nonlinear optical response of TMD monolayers include excitation-induced shifts and linewidth broadening of the excitonic resonance energy [81, 199]. To account for these effects, the resonance energy and dephasing rate in Eq.6.2.20 and Eq.6.2.21 are corrected by adding the excitation (and therefore population) dependent phenomenological terms $\gamma \to \gamma + \alpha\rho_{22}$ and $\omega_{21} \to \omega_{21} + \beta\rho_{22}$, where α and β are the excitation induced dephasing (EID) rate and excitation-induced shift (EIS), respectively. The addition of these population-dependent phenomenological terms imply that this master equation-based model is no longer descriptive of a single two-level system. Instead, it describes an interacting many-body system (MBS) whose evolution depends not only on the coupling of the system to the optical field but also on the many-body interactions.

The coupling of the MBS to the optical field is greatly simplified by assuming that the light field amplitude is uniform and time-independent, as in the case of continuous-wave

fields. Under such condition, the equations of motion Eq.6.2.20-Eq.6.2.23 simplify to

$$\frac{\partial}{\partial t}\rho_{22}(t) = \sum_{j=1}^{N}\left[i\chi_{R_j}e^{i\mathbf{k}_j\cdot\mathbf{R}-i\omega_j t}\rho_{12}(t) - i\chi_{R_j}^{*}e^{-i\mathbf{k}_j\cdot\mathbf{R}+i\omega_j t}\rho_{21}(t)\right] - \gamma_{sp}\rho_{22} \tag{6.2.24}$$

$$\begin{aligned}\frac{\partial}{\partial t}\rho_{12}(t) &= -(\gamma - i\omega_{21})\rho_{12}(t) - (\alpha - i\beta)\rho_{22}(t)\rho_{12}(t) \\ &\quad -[1-2\rho_{22}(t)]\, i\sum_{j=1}^{N}\left[\chi_{R_j}^{*}e^{-i\mathbf{k}_j\cdot\mathbf{R}+i\omega_j t}\right]\end{aligned} \tag{6.2.25}$$

While these coupled equations could be solved numerically, it is illustrative to solve them using perturbation theory to gain physical insight into the effect of excitation-induced dephasing and resonance energy shifts on the evolution of the density matrix elements and the corresponding macroscopic polarization.

The perturbation solution consists of expanding the density matrix elements in Eq.6.2.24 and Eq.6.2.25 as power series of the form

$$\rho_{uv}(t) = \sum_{n=0}^{\infty}\lambda^n\rho_{uv}^{(n)}(t) \tag{6.2.26}$$

with the assumption that the MBS is initially in the ground state so that

$$\rho_{11}^{(0)} = 1 \tag{6.2.27}$$

$$\rho_{22}^{(0)} = \rho_{12}^{(0)} = \rho_{21}^{(0)} = 0 \tag{6.2.28}$$

After comparing terms of equal perturbation order, a set of uncoupled equations of motion for each perturbation order results for the diagonal density matrix element in

$$
\begin{aligned}
\tfrac{\partial}{\partial t}\rho_{22}^{(0)}(t) &= \gamma_{sp}\rho_{22}^{(0)} \\
\frac{\partial}{\partial t}\rho_{22}^{(1)}(t) &= \sum_{j=1}^{N}\left[i\chi_{R_j}e^{i\mathbf{k}_j\cdot\mathbf{R}-i\omega_j t}\rho_{12}^{(0)} - i\chi_{R_j}^{*}e^{-i\mathbf{k}_j\cdot\mathbf{R}+i\omega_j t}\rho_{21}^{(0)}\right] \\
&\quad -\gamma_{sp}\rho_{22}^{(1)} \\
\frac{\partial}{\partial t}\rho_{22}^{(2)}(t) &= \sum_{j=1}^{N}\left[i\chi_{R_j}e^{i\mathbf{k}_j\cdot\mathbf{R}-i\omega_j t}\rho_{12}^{(1)} - i\chi_{R_j}^{*}e^{-i\mathbf{k}_j\cdot\mathbf{R}+i\omega_j t}\rho_{21}^{(1)}\right] \\
&\quad -\gamma_{sp}\rho_{22}^{(2)} \\
\frac{\partial}{\partial t}\rho_{22}^{(3)}(t) &= \sum_{j=1}^{N}\left[i\chi_{R_j}e^{i\mathbf{k}_j\cdot\mathbf{R}-i\omega_j t}\rho_{12}^{(2)} - i\chi_{R_j}^{*}e^{-i\mathbf{k}_j\cdot\mathbf{R}+i\omega_j t}\rho_{21}^{(2)}\right] \\
&\quad -\gamma_{sp}\rho_{22}^{(3)} \\
&\vdots \quad \vdots \quad \vdots \\
\frac{\partial}{\partial t}\rho_{22}^{(n)}(t) &= \sum_{j=1}^{N}\left[i\chi_{R_j}e^{i\mathbf{k}_j\cdot\mathbf{R}-i\omega_j t}\rho_{12}^{(n-1)} - i\chi_{R_j}^{*}e^{-i\mathbf{k}_j\cdot\mathbf{R}+i\omega_j t}\rho_{21}^{(n-1)}\right] \\
&\quad -\gamma_{sp}\rho_{22}^{(n)}
\end{aligned}
\tag{6.2.29}
$$

and similarly for the off-diagonal density matrix element

$$
\begin{aligned}
\frac{\partial}{\partial t}\rho_{12}^{(0)}(t) &= -(\gamma - i\omega_{21})\,\rho_{12}^{(0)} - (\alpha - i\beta)\,\rho_{22}^{(0)}\rho_{12}^{(0)} \\
\frac{\partial}{\partial t}\rho_{12}^{(1)}(t) &= -(\gamma - i\omega_{21})\,\rho_{12}^{(1)} - (\alpha - i\beta)\sum_{l=0}^{1}\left[\rho_{22}^{(l)}\rho_{12}^{(1-l)}\right] \\
&\quad -\left(1 - 2\rho_{22}^{(0)}\right) i\sum_{j=1}^{N}\chi_{R_j}^{*}e^{-i\mathbf{k}_j\cdot\mathbf{R}+i\omega_j t} \\
\frac{\partial}{\partial t}\rho_{12}^{(2)}(t) &= -(\gamma - i\omega_{21})\,\rho_{12}^{(2)} - (\alpha - i\beta)\sum_{l=0}^{2}\left[\rho_{22}^{(l)}\rho_{12}^{(2-l)}\right] \\
&\quad +2i\rho_{22}^{(1)}\sum_{j=1}^{N}\chi_{R_j}^{*}e^{-i\mathbf{k}_j\cdot\mathbf{R}+i\omega_j t} \\
\frac{\partial}{\partial t}\rho_{12}^{(3)}(t) &= -(\gamma - i\omega_{21})\,\rho_{12}^{(3)} - (\alpha - i\beta)\sum_{l=0}^{3}\left[\rho_{22}^{(l)}\rho_{12}^{(3-l)}\right] \\
&\quad +2i\rho_{22}^{(2)}\sum_{j=1}^{N}\chi_{R_j}^{*}e^{-i\mathbf{k}_j\cdot\mathbf{R}+i\omega_j t} \\
&\vdots \quad \vdots \quad \vdots \\
\frac{\partial}{\partial t}\rho_{12}^{(n)}(t) &= -(\gamma - i\omega_{21})\,\rho_{12}^{(n)} - (\alpha - i\beta)\sum_{l=0}^{n}\left[\rho_{22}^{(l)}\rho_{12}^{(n-l)}\right] \\
&\quad +2i\rho_{22}^{(n-1)}\sum_{j=1}^{N}\chi_{R_j}^{*}e^{-i\mathbf{k}_j\cdot\mathbf{R}+i\omega_j t}
\end{aligned}
\tag{6.2.30}
$$

For crystals that display inversion symmetry, the first non-vanishing nonlinear optical response is the third-order nonlinear macroscopic polarization [13]. This condition implies that the equations of motion that need to be solved to calculate the macroscopic polarization of the MBS system are Eq.6.2.29 up to second order, and Eq.6.2.30 up to third order with the initial conditions given by Eq.6.2.27 and Eq.6.2.28. To obtain the first-order, off-diagonal density matrix element, it is convenient to assume that it has the form

$$\rho_{12}^{(1)}(t) = \sum_{j=1}^{N} \tilde{\rho}_{12_j}^{(1)} e^{-i\mathbf{k}_j \cdot \mathbf{R} + i\omega_j t} \tag{6.2.31}$$

and after substituting Eq.6.2.31 into Eq.6.2.30, the time-independent, first-order off-diagonal density matrix element results in

$$\tilde{\rho}_{12_j}^{(1)} = -\frac{\chi_{R_j}^*}{\delta_j - i\gamma} \tag{6.2.32}$$

where $\delta_j \equiv \omega_j - \omega_{21}$ denotes the detuning of the optical field with respect to the resonance frequency of the MBS. Similarly, the second-order, diagonal density matrix element can be obtained by assuming that it has the form

$$\rho_{22}^{(2)}(t) = \sum_{j,l=1}^{N} \tilde{\rho}_{22_{j,l}}^{(2)} e^{i(\mathbf{k}_j - \mathbf{k}_l)\cdot \mathbf{R} - i(\omega_j - \omega_l)t} + c.c. \tag{6.2.33}$$

and after substituting Eq.6.2.33 into Eq.6.2.29 along with Eq.6.2.31, the second-order diagonal density matrix element becomes

$$\tilde{\rho}_{22_{j,l}}^{(2)} = \frac{1}{(\omega_j - \omega_l) + i\gamma_{sp}} \left(\frac{\chi_{R_j} \chi_{R_j}^*}{\delta_l - i\gamma} \right) \tag{6.2.34}$$

$$\begin{aligned} \rho_{22}^{(2)}(t) &= \sum_{j,l=1}^{N} \frac{\chi_j \chi_l^*}{(\delta_l - i\gamma)(\delta_j + i\gamma)} \left[1 + \frac{2i\Gamma}{(\delta_j - \delta_l) + i\gamma_{sp}} \right] \\ &\quad \times e^{i(\mathbf{k}_j - \mathbf{k}_l)\cdot \mathbf{R} - i(\omega_j - \omega_l)t} \end{aligned} \tag{6.2.35}$$

Lastly, the third-order, off-diagonal density matrix element can be obtained by assuming that it has the form

$$\rho_{12}^{(3)}(t) = \sum_{j,l,m=1}^{N} \tilde{\rho}_{12_{j,l,m}}^{(3)} e^{-i(\mathbf{k}_j - \mathbf{k}_l + \mathbf{k}_m)\cdot\mathbf{R} + i(\omega_j - \omega_l + \omega_m)t} \tag{6.2.36}$$

and after substituting Eq.6.2.36 into Eq.6.2.30 along with Eq.6.2.31 and Eq.6.2.35, the time-independent, third-order, off-diagonal density matrix element becomes

$$\begin{aligned} \tilde{\rho}_{12_{j,l,m}}^{(3)} &= \frac{1}{(\delta_j - \delta_l + \delta_m) - i\gamma}\left(2 - \frac{\beta + i\alpha}{\delta_j - i\gamma}\right)\left[1 + \frac{2i\Gamma}{(\delta_l - \delta_m) + i\gamma_{sp}}\right] \\ &\times \frac{\chi_{R_j}^{*}\chi_{R_l}\chi_{R_m}^{*}}{(\delta_m - i\gamma)(\delta_l + i\gamma)} \end{aligned} \tag{6.2.37}$$

and its complex conjugate is

$$\begin{aligned} \tilde{\rho}_{21_{j,l,m}}^{(3)} &= \left[\tilde{\rho}_{12_{j,l,m}}^{(3)}\right]^{*} \\ &= \frac{1}{(\delta_j - \delta_l + \delta_m) + i\gamma}\left(2 - \frac{\beta - i\alpha}{\delta_j + i\gamma}\right)\left[1 - \frac{2i\Gamma}{(\delta_l - \delta_m) - i\gamma_{sp}}\right] \\ &\times \frac{\chi_{R_j}\chi_{R_l}^{*}\chi_{R_m}}{(\delta_m + i\gamma)(\delta_l - i\gamma)} \end{aligned} \tag{6.2.38}$$

Equation 6.2.36 indicates that there are eight contributions to the third-order, off-diagonal density matrix element when there are two fields ($N = 2$) interacting with the MBS. This case is particularly relevant from a practical point of view because the nonlinear optical response of semiconductor materials is typically measured using a pump-probe technique where two laser fields interact with the system. While the details of this experimental technique are discussed in further detail in the next section, it is worth pointing out that in such experimental scheme, the nonlinear response of interest is the third-order response that is at the same frequency and propagates along the same direction as the probe laser, and is linear in both the probe field's amplitude and pump's intensity. Therefore, the only contributing terms from Eq.6.2.36 that meet these conditions are the pump (P) and probe (pr) field's

time-ordering $(j,l,m)=(P,P,pr)$ and $(j,l,m)=(pr,P,P)$. For the first time-ordering, the third-order, off-diagonal density matrix element is given by

$$\rho^{(3)}_{21_{P,P,pr}}(t)=\tilde{\rho}^{(3)}_{21_{P,P,pr}}e^{i\mathbf{k}_{pr}\cdot\mathbf{R}-i\omega_{pr}t} \tag{6.2.39}$$

$$\tilde{\rho}^{(3)}_{21_{P,P,pr}}=\frac{2\gamma}{\gamma_{sp}}\frac{1}{\delta_{pr}+i\gamma}\left(2-\frac{\beta-i\alpha}{\delta_{pr}+i\gamma}\right)\frac{\chi_{R_P}\chi^{*}_{R_P}\chi_{R_{pr}}}{\delta_P^2+\gamma^2} \tag{6.2.40}$$

and similarly for the second time-ordering, the third-order, off-diagonal density matrix element is given by

$$\rho^{(3)}_{21_{pr,P,P}}(t)=\tilde{\rho}^{(3)}_{21_{pr,P,P}}e^{i\mathbf{k}_{pr}\cdot\mathbf{R}-i\omega_{pr}t} \tag{6.2.41}$$

$$\begin{aligned}\tilde{\rho}^{(3)}_{21_{pr,P,P}} &= \left(2-\frac{\beta-i\alpha}{\delta_P+i\gamma}\right)\left[1+\frac{2i\Gamma}{(\delta_{pr}-\delta_P)+i\gamma_{sp}}\right]\\ &\times \frac{\chi_{R_{pr}}\chi^{*}_{R_P}\chi_{R_P}}{(\delta_{pr}+i\gamma)^2(\delta_P-i\gamma)}\end{aligned} \tag{6.2.42}$$

The total third-order, off-diagonal, density matrix element is the sum of Eq.6.2.39 and Eq.6.2.41

$$\rho^{(3)}_{21}(t)=\tilde{\rho}^{(3)}_{21}e^{i\mathbf{k}_{pr}\cdot\mathbf{R}-i\omega_{pr}t} \tag{6.2.43}$$

$$\begin{aligned}
\tilde{\rho}_{21}^{(3)} &= \tilde{\rho}_{21_{P,P,pr}}^{(3)} + \tilde{\rho}_{21_{pr,P,P}}^{(3)} \\
&= \frac{2\gamma}{\gamma_{sp}} \frac{1}{\delta_{pr} + i\gamma} \left(2 - \frac{\beta - i\alpha}{\delta_{pr} + i\gamma}\right) \frac{\chi_{R_P} \chi_{R_P}^* \chi_{R_{pr}}}{\delta_P^2 + \gamma^2} \\
&+ \left(2 - \frac{\beta - i\alpha}{\delta_P + i\gamma}\right) \left[1 + \frac{2i\Gamma}{(\delta_{pr} - \delta_P) + i\gamma_{sp}}\right] \\
&\times \frac{\chi_{R_{pr}} \chi_{R_P}^* \chi_{R_P}}{(\delta_{pr} + i\gamma)^2 (\delta_P - i\gamma)}
\end{aligned} \tag{6.2.44}$$

Finally, according to the perturbation expansion 6.2.26, the total off-diagonal density matrix element, up to third-order, is approximately given by

$$\rho_{21}(t) \approx \rho_{21}^{(1)}(t) + \rho_{21}^{(3)}(t) \tag{6.2.45}$$

Accordingly, the macroscopic optical polarization can be obtained by substituting Eq.6.2.43-Eq.6.2.45 back into Eq.6.2.1. It is also convenient to explicitly write the positive frequency component of the macroscopic polarization from Eq.6.2.4 as

$$\begin{aligned}
\mathbf{P}^{(+)}(t) &= N_a \left[\rho_{21}^{(1)}(t) + \rho_{21}^{(3)}(t)\right] \mu_{12} \hat{r}_{12} \\
&= \sum_{j=P,pr} N_a \mu_{12} \hat{r}_{12} \left[\tilde{\rho}_{21_j}^{(1)} + \tilde{\rho}_{21_{pr,P,P}}^{(3)} \delta_{j,pr} + \tilde{\rho}_{21_{P,P,pr}}^{(3)} \delta_{j,pr}\right] e^{-i\omega_j t} \\
&= \sum_{j=P,pr} \tilde{\mathbf{P}}_j^{(+)} e^{-i\omega_j t} \\
&= \sum_{j=P,pr} \mathbf{P}_j^{(+)}(t)
\end{aligned} \tag{6.2.46}$$

where the time-independent polarization is defined as

$$\tilde{\mathbf{P}}_j^{(+)} = N_a \mu_{12} \hat{r}_{12} \left\{\tilde{\rho}_{21_j}^{(1)} + \left[\tilde{\rho}_{21_{pr,P,P}}^{(3)} + \tilde{\rho}_{21_{P,P,pr}}^{(3)}\right] \delta_{j,pr}\right\} \tag{6.2.47}$$

6.2.2 Differential absorption of TMD monolayer

The signatures of many-body effects in the nonlinear optical response of TMD monolayers can be probed via non-degenerate, continuous-wave (CW) pump-probe spectroscopy. This type of optical spectroscopy monitors the pump-induced change in the material's absorption of a probe laser. This change in absorption is also referred to as differential absorption, and it is proportional to the imaginary component of the material's nonlinear optical susceptibility [179]. In this technique, the pump laser is fixed on the resonance energy of interest while the probe laser is scanned through the resonance at high energy resolution. At sufficiently low laser intensities, the dominant contribution to the differential absorption signal is the third-order optical susceptibility. Even in such weakly nonlinear regime, many-body effects can strongly influence the nonlinear optical susceptibility of semiconductors–especially TMD monolayers–giving rise to distinct signatures in their differential absorption spectrum. In practice, however, detecting the nonlinear optical response, can be very challenging because of its low signal level. To detect signals at low levels, homodyne detection and a lock-in amplifier can be used to extract the nonlinear optical susceptibility of the material.

The differential absorption of a material can be inferred from the differential transmission, the differential reflection, or both if the sample geometry allows for the simultaneous measurement of both reflection and transmission spectra. In any case, the amplitudes of the CW pump and probe laser beams are modulated at two different frequencies. Lock-in amplifiers referenced to the difference of these modulation frequencies are then used to measure a component of the nonlinear optical response of the material that is oscillating at the difference of the modulation frequencies and propagating along the directions of the transmitted and reflected probe beams as illustrated in 6.3.1. The photocurrent generated in the detectors monitoring the transmitted and reflected probe beams contains various frequency components, but among them, there is one component at the difference of the modulation frequencies of the pump and probe beams [126]. The change in the probe beam's reflection

from ΔR_{pr} and transmission ΔT_{pr} through the material can then be measured to estimate the differential absorption as

$$\Delta A_{pr} \equiv -\Delta T_{pr} - \Delta R_{pr} \tag{6.2.48}$$

The differential absorption ΔA_{pr} can be interpreted as the change in the material's absorption of the probe laser when the pump laser is present, A (pump & probe on), relative to the material's absorption of the probe laser when the pump laser is absent, A (probe on). If the macroscopic polarization generated in the material is approximated as the series expansion in the pump and probe field amplitudes, the third-order, time-independent, macroscopic polarization that is linear in the probe field amplitude $\mathcal{E}_{pr}$ and linear in the pump field intensity $|\mathcal{E}_P|^2$ can be approximated as [13]

$$\tilde{P}^{(3)} \approx \epsilon_0 \chi_e^{(3)} |\mathcal{E}_P|^2 \mathcal{E}_{pr} \tag{6.2.49}$$

In addition, the optical susceptibility can be related to the nonlinear absorption of the material by solving the inhomogeneous wave equation with the macroscopic polarization as the source of electromagnetic radiation to obtain the approximate relation between the nonlinear absorption and the imaginary component of the optical susceptibility [179]

$$A_{NL} = 2\frac{\omega}{c} \sum_n \chi_e^{I,(n)} |\mathcal{E}|^{(n-1)} \tag{6.2.50}$$

where ω, c, and $\chi_e^{I,(n)}$ represent the laser's angular frequency, the speed of light, and the imaginary component of the n-nth order optical susceptibility, respectively.

For the differential absorption spectrum to provide information on the fundamental coherent processes of the material, the strength of the macroscopic polarization must increase linearly with the pump field's intensity and the probe field's amplitude [178, 10]. These

characteristic signatures confirm that the measurements are in the so-called $\chi_e^{(3)}$or weakly nonlinear limit. While the first-order response is the dominant response when only a weak probe field is incident on the material, when both the pump and the probe fields are incident, the dominant nonlinear response that is linearly proportional to the pump's intensity is and the probe's amplitude is the the third-order response due to the time-ordering of the pump and probe fields $(j,l,m) = (P,P,pr)$ and $(j,l,m) = (pr,P,P)$. As a result, the differential absorption of the probe can be approximated using Eq.6.2.50 as

$$\begin{aligned}
\Delta A_{pr} &= A\left(\text{pump on} + \text{probe on}\right) - A\left(\text{pump off} + \text{probe on}\right) \\
&\approx A_{NL}\left(\mathcal{E}_P \mathcal{E}_P^* \mathcal{E}_{pr}\right) - A_{NL}\left(\mathcal{E}_{pr}\right) \\
&\approx 2\frac{\omega}{c}\left[\chi_e^{I,(1)} + \chi_e^{I,(3)}\left|\mathcal{E}_P\right|^2\right] - 2\frac{\omega}{c}\chi_e^{I,(1)} \\
&\approx 2\frac{\omega}{c}\chi_e^{I,(3)}\left|\mathcal{E}_P\right|^2
\end{aligned} \tag{6.2.51}$$

Moreover, the connection between the third-order optical susceptibility, and the density matrix elements of the MBS can be obtained by comparing Eq.6.2.1 with Eq.6.2.49 as

$$\begin{aligned}
\tilde{P}^{(+)} &\approx N_a\left[\tilde{\rho}_{21}^{(1)} + \tilde{\rho}_{21}^{(3)}\right]\mu_{12} \\
\epsilon_0 \chi_e^{(3)}\left|\mathcal{E}_P\right|^2 \mathcal{E}_{pr} &\approx N_a \tilde{\rho}_{21}^{(3)} \mu_{12} \\
\chi_e^{(3)} &\approx \frac{N_a \tilde{\rho}_{21}^{(3)} \mu_{12}}{\epsilon_0\left|\mathcal{E}_P\right|^2 \mathcal{E}_{pr}}
\end{aligned} \tag{6.2.52}$$

Therefore, the imaginary part of the third-order optical susceptibility is proportional to the imaginary component of the third-order, off-diagonal density matrix element

$$\chi_e^{I,(3)} \approx \frac{N_a \mu_{12}}{\epsilon_0\left|\mathcal{E}_P\right|^2 \mathcal{E}_{pr}} \tilde{\rho}_{21}^{I,(3)} \tag{6.2.53}$$

and by substituting Eq.6.2.53 into Eq.6.2.51, the differential absorption spectrum can be

shown to be

$$\Delta A_{pr} \approx \frac{2\omega N_a \mu_{12}}{c\epsilon_0 \mathcal{E}_{pr}} \tilde{\rho}_{21}^{I,(3)} \tag{6.2.54}$$

Accordingly, in the weakly nonlinear or $\chi_e^{(3)}$ limit, measuring the differential absorption of the probe field is equivalent to measuring the third-order optical susceptibility of the material, which in turn is proportional to the third-order, off-diagonal density matrix element.

6.2.3 Multi-layer structure

While the differential absorption spectrum is closely related to the imaginary part of the third-order, off-diagonal density matrix element of the MBS, one of the assumptions that lead to Eq.6.2.54 is that the TMD monolayer is surrounded by vacuum. This assumption greatly simplifies the calculation of the monolayer's differential absorption spectrum, but in practice, the TMD monolayer is encapsulated by h-BN, and is deposited over an NBK7 glass substrate as shown in Fig.6.2.1. These additional dielectric layers can modify the nonlinear absorption spectrum of the TMD monolayer due to changes in the radiative recombination rates [47] and the exciton energy distribution of the material [110]. Therefore, the differential absorption spectrum of the entire dielectric structure should be obtained using a transfer matrix approach.

To obtain the optical transfer matrix for the entire dielectric structure shown in Fig.6.2.1, the fields in each layer are modeled as counter-propagating plane waves. The optical fields are real quantities and can be expressed as a linear combination of complex fields with positive and negative frequency components similar to the field in Eq.6.2.12. For simplicity, and without loss of generality, the transfer matrix calculation can be carried out with the positive frequency fields only. As such, for an electromagnetic field comprising of two lasers, a pump laser and a probe laser, the electric and magnetic fields in each of the layers labeled with the indices $m : 0 - 4$ are given by

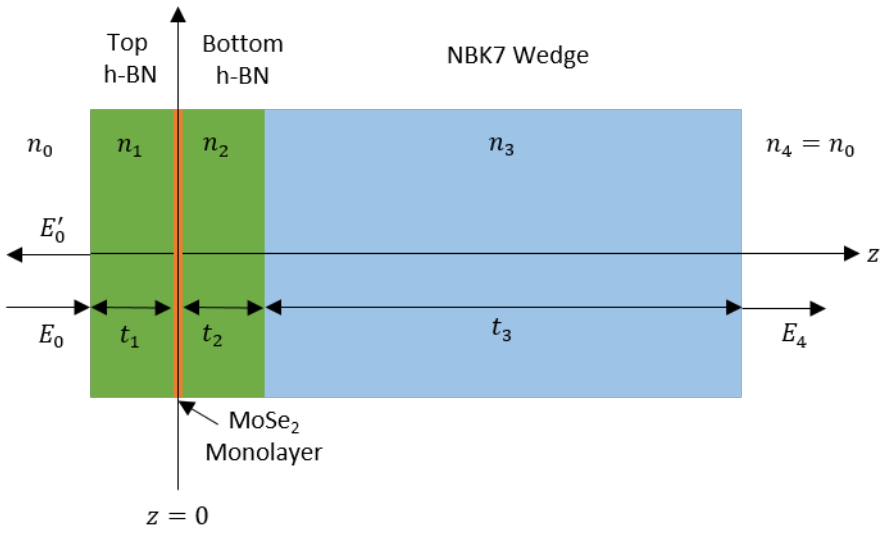

Figure 6.2.1: Diagram of the multi-layer structure. The multi-layer structure comprises of top and bottom h-BN layers surrounding an $MoSe_2$ monolayer. The encapsulated monolayer sits on top of a wedged, AR-coated NBK7 substrate to reduce back reflections and etaloning effects. The incident and transmitted fields are assumed to be in vacuum. The direction of wave propagation is assumed to be along the z axis, which is defined to be perpendicular to the plane of the multi-layer structure. The layers of the structure are labeled 0 through 4 from left to right along the z axis. The $MoSe_2$ monolayer is conveniently positioned at the origin. The thickness of the m-nth layer is labeled by t_m. The transfer matrix of the multi-layer structure is obtained by applying the boundary conditions for the electromagnetic fields at the interfaces of the structure.

$$\begin{bmatrix} \mathbf{E}_m^{(+)}(z,t) \\ \mathbf{H}_m^{(+)}(z,t) \end{bmatrix} = \sum_{j=P,pr} \begin{bmatrix} \mathbf{E}_{m_j}^{(+)}(z,t) \\ \mathbf{H}_{m_j}^{(+)}(z,t) \end{bmatrix} \tag{6.2.55}$$

$$\begin{bmatrix} \mathbf{E}_m^{(+)}(z,t) \\ \mathbf{H}_m^{(+)}(z,t) \end{bmatrix} = \sum_{j=P,pr} \begin{bmatrix} \mathbf{E}_{m_j}^{(+)}(z) \\ \mathbf{H}_{m_j}^{(+)}(z) \end{bmatrix} e^{-i\omega_j t} \tag{6.2.56}$$

where the time-independent terms in the sum of Eq.6.2.55 are specifically given by

$$\begin{bmatrix} \mathbf{E}_{0_j}^{(+)}(z) \\ \mathbf{H}_{0_j}^{(+)}(z) \end{bmatrix} = \frac{1}{2} \begin{bmatrix} \mathbf{E}_{0_j} \\ \mathbf{H}_{0_j} \end{bmatrix} e^{ik_{0_j}(z+t_1)} + \frac{1}{2} \begin{bmatrix} \mathbf{E}'_{0_j} \\ \mathbf{H}'_{0_j} \end{bmatrix} e^{-ik_{0_j}(z+t_1)} \tag{6.2.57}$$

$$\begin{bmatrix} \mathbf{E}_{1_j}^{(+)}(z) \\ \mathbf{H}_{1_j}^{(+)}(z) \end{bmatrix} = \frac{1}{2} \begin{bmatrix} \mathbf{E}_{1_j} \\ \mathbf{H}_{1_j} \end{bmatrix} e^{ik_{1_j}z} + \frac{1}{2} \begin{bmatrix} \mathbf{E}'_{1_j} \\ \mathbf{H}'_{1_j} \end{bmatrix} e^{-ik_{1_j}z} \tag{6.2.58}$$

$$\begin{bmatrix} \mathbf{E}_{2_j}^{(+)}(z) \\ \mathbf{H}_{2_j}^{(+)}(z) \end{bmatrix} = \frac{1}{2} \begin{bmatrix} \mathbf{E}_{2_j} \\ \mathbf{H}_{2_j} \end{bmatrix} e^{ik_{2_j}z} + \frac{1}{2} \begin{bmatrix} \mathbf{E}'_{2_j} \\ \mathbf{H}'_{2_j} \end{bmatrix} e^{-ik_{2_j}z} \tag{6.2.59}$$

$$\begin{bmatrix} \mathbf{E}_{3_j}^{(+)}(z) \\ \mathbf{H}_{3_j}^{(+)}(z) \end{bmatrix} = \frac{1}{2} \begin{bmatrix} \mathbf{E}_{3_j} \\ \mathbf{H}_{3_j} \end{bmatrix} e^{ik_{3_j}(z-t_2)} + \frac{1}{2} \begin{bmatrix} \mathbf{E}'_{3_j} \\ \mathbf{H}'_{3_j} \end{bmatrix} e^{-ik_{3_j}(z-t_2)} \tag{6.2.60}$$

$$\begin{bmatrix} \mathbf{E}_{4_j}^{(+)}(z) \\ \mathbf{H}_{4_j}^{(+)}(z) \end{bmatrix} = \frac{1}{2} \begin{bmatrix} \mathbf{E}_{4_j} \\ \mathbf{H}_{4_j} \end{bmatrix} e^{ik_{4_j}(z-t_2-t_3)} \tag{6.2.61}$$

where t_m denotes the thickness of the m-nth layer along the direction of light propagation defined as the $\hat{z}$ direction; $\begin{bmatrix} \mathbf{E}_{m_j} \\ \mathbf{H}_{m_j} \end{bmatrix}$ and $\begin{bmatrix} \mathbf{E}'_{m_j} \\ \mathbf{H}'_{m_j} \end{bmatrix}$ represent the amplitudes of the j-nth forward and backward propagating electric and magnetic fields in the m-nth layer, respectively; $k_m = n_m k$ is the wavevector in the layer with index of refraction n_m and k is the wavevector in vacuum. Accordingly, the complex reflection and transmission coefficients of the entire multi-layer structure for each field are defined as

$$r_j = \frac{\mathbf{E}'_{0_j}}{\mathbf{E}_{0_j}} \tag{6.2.62}$$

$$t_j = \frac{\mathbf{E}_{4_j}}{\mathbf{E}_{0_j}} \tag{6.2.63}$$

and the real-valued reflection, transmission, and absorption of the j-nth field for the entire structure are defined as [67]

$$R_j = |r_j|^2 \tag{6.2.64}$$

$$T_j = \frac{n_4}{n_0} |t_j|^2 \tag{6.2.65}$$

$$A_j = 1 - R_j - T_j \tag{6.2.66}$$

Similarly, the differential absorption spectrum is defined as the pump-induced change in the structure's probe absorption as in Eq.6.2.48.

To obtain the transfer matrix of the multi-layer structure, expressions for the electric field amplitudes between adjacent layers are obtained by enforcing the boundary conditions for the electric and magnetic fields given by [73]

$$\left[\mathbf{D}_m^{(+)} - \mathbf{D}_{m-1}^{(+)}\right] \cdot \hat{n}_{m,m-1} = \sigma_{m,m-1} \tag{6.2.67}$$

$$\left[\mathbf{E}_m^{(+)} - \mathbf{E}_{m-1}^{(+)}\right] \times \hat{n}_{m,m-1} = 0 \tag{6.2.68}$$

$$\left[\mathbf{B}_m^{(+)} - \mathbf{B}_{m-1}^{(+)}\right] \cdot \hat{n}_{m,m-1} = 0 \tag{6.2.69}$$

$$\left[\mathbf{H}_m^{(+)} - \mathbf{H}_{m-1}^{(+)}\right] \times \hat{n}_{m,m-1} = -\mathbf{K}_{m,m-1} \tag{6.2.70}$$

where $\hat{n}_{m,m-1}$ represents the unit vector normal to the boundary and points from layer $m-1$ to layer m. Since the layers are assumed to be normal to the $\hat{z}$ axis, and the propagation is assumed to be in the positive direction, $\hat{n}_{m,m-1} = \hat{z}$. Moreover, $\sigma_{m,m-1}$ and $\mathbf{K}_{m,m-1}$ denote the surface charge and current densities, respectively, at the interface between adjacent layers. It is convenient to express the boundary conditions for the magnetic field $\mathbf{H}_m^{(+)}$ in terms of the electric field $\mathbf{E}_m^{(+)}$. To that end, the electric field is assumed to be linearly polarized along the $\hat{x}$ direction, and the magnetic field is linearly polarized along the $\hat{y}$ direction. Accordingly, using Faraday's law for non-magnetic media leads to the following relation for the magnetic field in terms of the time-derivative of the electric field

$$\begin{aligned}
\nabla \times \mathbf{E}_m^{(+)}(z,t) &= -\mu_0 \frac{\partial}{\partial t} \mathbf{H}_m^{(+)}(z,t) \\
\frac{\partial}{\partial z} E_{m_j}^{(+)}(z,t) &= -\mu_0 \frac{\partial}{\partial t} H_{m_j}^{(+)}(z,t) \\
H_{m_j}^{(+)}(z,t) &= -\frac{i}{\mu_0 \omega_j} \frac{\partial}{\partial z} E_{m_j}^{(+)}(z,t)
\end{aligned} \tag{6.2.71}$$

With the exception of the interface between the top and bottom h-BN layers, which is the interface where the TMD monolayer is placed, no surface charge or current densities exist in the multi-layer structure. The macroscopic polarization generated in the TMD monolayer by the incident fields induces an oscillating surface current density [85]. Using Eq.6.2.46 and Eq.6.2.44, this surface current density is given by

$$\begin{aligned}
K &= \frac{\partial}{\partial t} P^{(+)}(t) \\
&= \sum_{j=P,pr} -i\omega_j N_a \mu_{12} \left\{ \tilde{\rho}_{21_j}^{(1)} + \left[\tilde{\rho}_{21_{pr,P,P}}^{(3)} + \tilde{\rho}_{21_{P,P,pr}}^{(3)} \right] \delta_{j,pr} \right\} e^{-i\omega_j t} \\
&= \sum_{j=P,pr} \left[\frac{\partial}{\partial t} P_j^{(+)}(t) \right]
\end{aligned} \tag{6.2.72}$$

To obtain a relation for the electric field amplitudes across the interface between the top and bottom h-BN layers, the Rabi frequencies in Eq.6.2.44 need to be written explicitly. To that end, the time-independent, off-diagonal density matrix element in Eq.6.2.44 can be recast as

$$\begin{aligned}\tilde{\rho}_{21}^{(3)} &= \tilde{\rho}_{21_{pr,P,P}}^{(3)} + \tilde{\rho}_{21_{P,P,pr}}^{(3)} \\ &= \xi_{PPpr}\chi_{R_P}\chi_{R_P}^{*}\chi_{R_{pr}} + \xi_{prPP}\chi_{R_{pr}}\chi_{R_P}^{*}\chi_{R_P}\end{aligned} \tag{6.2.73}$$

where

$$\xi_{PPpr} \equiv \frac{2\gamma}{\gamma_{sp}}\frac{1}{\delta_{pr}+i\gamma}\left(2-\frac{\beta-i\alpha}{\delta_{pr}+i\gamma}\right)\frac{1}{\delta_P^2+\gamma^2} \tag{6.2.74}$$

$$\begin{aligned}\xi_{prPP} &\equiv \left(2-\frac{\beta-i\alpha}{\delta_P+i\gamma}\right)\left[1+\frac{2i\Gamma}{(\delta_{pr}-\delta_P)+i\gamma_{sp}}\right] \\ &\times \frac{1}{(\delta_{pr}+i\gamma)^2(\delta_P-i\gamma)}\end{aligned} \tag{6.2.75}$$

and enforcing the boundary condition Eq.6.2.68 at the interface between the top and bottom h-BN layers leads to the Rabi frequency

$$\chi_{R_j} = \left(\frac{\mu_{21}}{2\hbar}\right)\left(E_{1_j}+E'_{1_j}\right) = \left(\frac{\mu_{21}}{2\hbar}\right)\left(E_{2_j}+E'_{2_j}\right) \tag{6.2.76}$$

Finally, enforcing the boundary conditions Eq.6.2.68 and Eq.6.2.70 across all of the boundaries of the multi-layer structure depicted in Fig.6.2.1, and using the auxiliary expressions Eq.6.2.71-Eq.6.2.76, a linear system of equations relating the field amplitudes in the exit layer to the input layer is obtained as

$$\begin{bmatrix} E_{4_j} \\ 0 \end{bmatrix} = \mathbf{M}_j \begin{bmatrix} E_{0_j} \\ E'_{0_j} \end{bmatrix} \tag{6.2.77}$$

where the transfer matrices of each layer are defined as

$$\mathbf{M}_j = \mathbf{M_4}_j \, \mathbf{M_3}_j \left(\mathbf{M_{2_A}}_j + \mathbf{M_{2_B}}_{pr} \, \delta_{j,pr} \right) \mathbf{M_1}_j \tag{6.2.78}$$

$$\mathbf{M_4}_j = \frac{1}{2} \begin{bmatrix} e^{i\kappa_{3_j}} \left(1 + \frac{n_3}{n_4}\right) & e^{-i\kappa_{3_j}} \left(1 - \frac{n_3}{n_4}\right) \\ e^{i\kappa_{3_j}} \left(1 - \frac{n_3}{n_4}\right) & e^{-i\kappa_{3_j}} \left(1 + \frac{n_3}{n_4}\right) \end{bmatrix} \tag{6.2.79}$$

$$\mathbf{M_3}_j = \frac{1}{2} \begin{bmatrix} e^{i\kappa_{2_j}} \left(1 + \frac{n_2}{n_3}\right) & e^{-i\kappa_{2_j}} \left(1 - \frac{n_2}{n_3}\right) \\ e^{i\kappa_{2_j}} \left(1 - \frac{n_2}{n_3}\right) & e^{-i\kappa_{2_j}} \left(1 + \frac{n_2}{n_3}\right) \end{bmatrix} \tag{6.2.80}$$

$$\mathbf{M_{2_A}}_j = \frac{1}{2} \begin{bmatrix} 1 + \frac{n_1}{n_2} - iy_{2_j} \left(x_j - i\right) & 1 - \frac{n_1}{n_2} - iy_{2_j} \left(x_j - i\right) \\ 1 - \frac{n_1}{n_2} + iy_{2_j} \left(x_j - i\right) & 1 + \frac{n_1}{n_2} + iy_{2_j} \left(x_j - i\right) \end{bmatrix} \tag{6.2.81}$$

$$\mathbf{M_{2_B}}_{pr} = \frac{i}{2} y_{2_{pr}} \left(x_{pr}^2 + 1\right) \left(\eta_{PPpr} + \eta_{prPP}\right) f_P f_P^* I_{0_P} \mathbf{g} \tag{6.2.82}$$

$$\mathbf{M_1}_j = \frac{1}{2} \begin{bmatrix} 1 + \frac{n_1}{n_2} - iy_{2_j} \left(x_j - i\right) & 1 - \frac{n_1}{n_2} - iy_{2_j} \left(x_j - i\right) \\ 1 - \frac{n_1}{n_2} + iy_{2_j} \left(x_j - i\right) & 1 + \frac{n_1}{n_2} + iy_{2_j} \left(x_j - i\right) \end{bmatrix} \tag{6.2.83}$$

The following unit-less variables and parameters have been defined to simplify the transfer matrix Eq.6.2.78

$$\kappa_{m_j} \equiv n_m \tau_m \left(x_j + \Lambda_0\right) \tag{6.2.84}$$

$$\tau_m \equiv \frac{\gamma t_m}{c} \tag{6.2.85}$$

$$x_j \equiv \frac{\delta_j}{\gamma} \tag{6.2.86}$$

$$\Lambda_0 \equiv \frac{\omega_{21}}{\gamma} \tag{6.2.87}$$

$$y_{m_j} \equiv \frac{y_j}{n_m} \tag{6.2.88}$$

$$y_j \equiv \zeta \frac{(x_j + \Lambda_0)}{\left(x_j^2 + 1\right)} \tag{6.2.89}$$

$$\zeta \equiv \frac{\mu_0 N_a c \left|\mu_{21}\right|^2}{\hbar} \tag{6.2.90}$$

$$\eta_{j,m,l} \equiv \xi_{j,l,m} \gamma^3 \tag{6.2.91}$$

$$\eta_{PPpr} = \frac{2}{S}\left(\frac{1}{x_{pr} + i}\right)\left(2 - \frac{B - i\Upsilon}{x_{pr} + i}\right)\left(\frac{1}{x_P^2 + 1}\right) \tag{6.2.92}$$

$$\eta_{prPP} = \left(2 - \frac{B - i\Upsilon}{x_p + i}\right)\left[1 + \frac{2iG}{(x_{pr} - x_P) + iS}\right]\left[\frac{1}{\left(x_{pr} + i\right)^2 (x_P - i)}\right] \tag{6.2.93}$$

$$\Upsilon \equiv \frac{\alpha}{\gamma} \tag{6.2.94}$$

$$B \equiv \frac{\beta}{\gamma} \tag{6.2.95}$$

$$G \equiv \frac{\Gamma}{\gamma} \tag{6.2.96}$$

$$S \equiv \frac{\gamma_{sp}}{\gamma} \tag{6.2.97}$$

$$f_P \equiv M_1 (1,1)_P + M_1 (2,1)_P + \left[M_1 (1,2)_P + M_1 (2,2)_P\right] r_P \tag{6.2.98}$$

$$I_{0_P} \equiv |\psi|^2 \left|E_{0_P}\right|^2 \tag{6.2.99}$$

$$|\psi|^2 \equiv \frac{\left|\mu_{21}\right|^2}{4\hbar^2 \gamma^2} \tag{6.2.100}$$

$$\mathbf{g} \equiv \begin{bmatrix} 1 \\ \\ -1 \end{bmatrix} \begin{bmatrix} 1 & 1 \end{bmatrix} \tag{6.2.101}$$

Since the quantity of interest is the pump-induced change in the structure's probe absorption, the probe's reflection and transmission coefficients can be calculated from Eq.6.2.78 as

$$r_j = -\frac{M(2,1)_j}{M(2,2)_j} \tag{6.2.102}$$

$$t_j = M(1,1)_j + M(1,2)_j r_j \tag{6.2.103}$$

and the differential absorption can be calculated using Eq.6.2.66 and with the reflection and transmission coefficients Eq.6.2.102 and Eq.6.2.103, respectively

$$\Delta A_{pr} = A_{pr}(E_{0_P} \neq 0) - A_{pr}(E_{0_P} = 0) \tag{6.2.104}$$

The differential absorption line shapes obtained with Eq.6.2.104 for an illustrative set of parameters are shown in figure 6.2.2.

The details of the calculation of the transfer matrix of the entire dielectric structure can be found on appendix B. The following section discusses the experimental apparatus used to measure the differential absorption of the $MoSe_2$ monolayer sample.

6.3 Experimental apparatus

The experimental apparatus used to measure the nonlinear optical response of the h-BN encapsulated $MoSe_2$ monolayer is illustrated in figure 6.3.1. First, a pair of tunable, high resolution, CW lasers (MSquared Solstis)—the pump and the probe—go through a pair of acousto-optic modulators (Intra Action SWM-502AE3), and the diffracted first order beams are coupled into a pair of single-mode optical fibers. The noise in the paths of the pump and

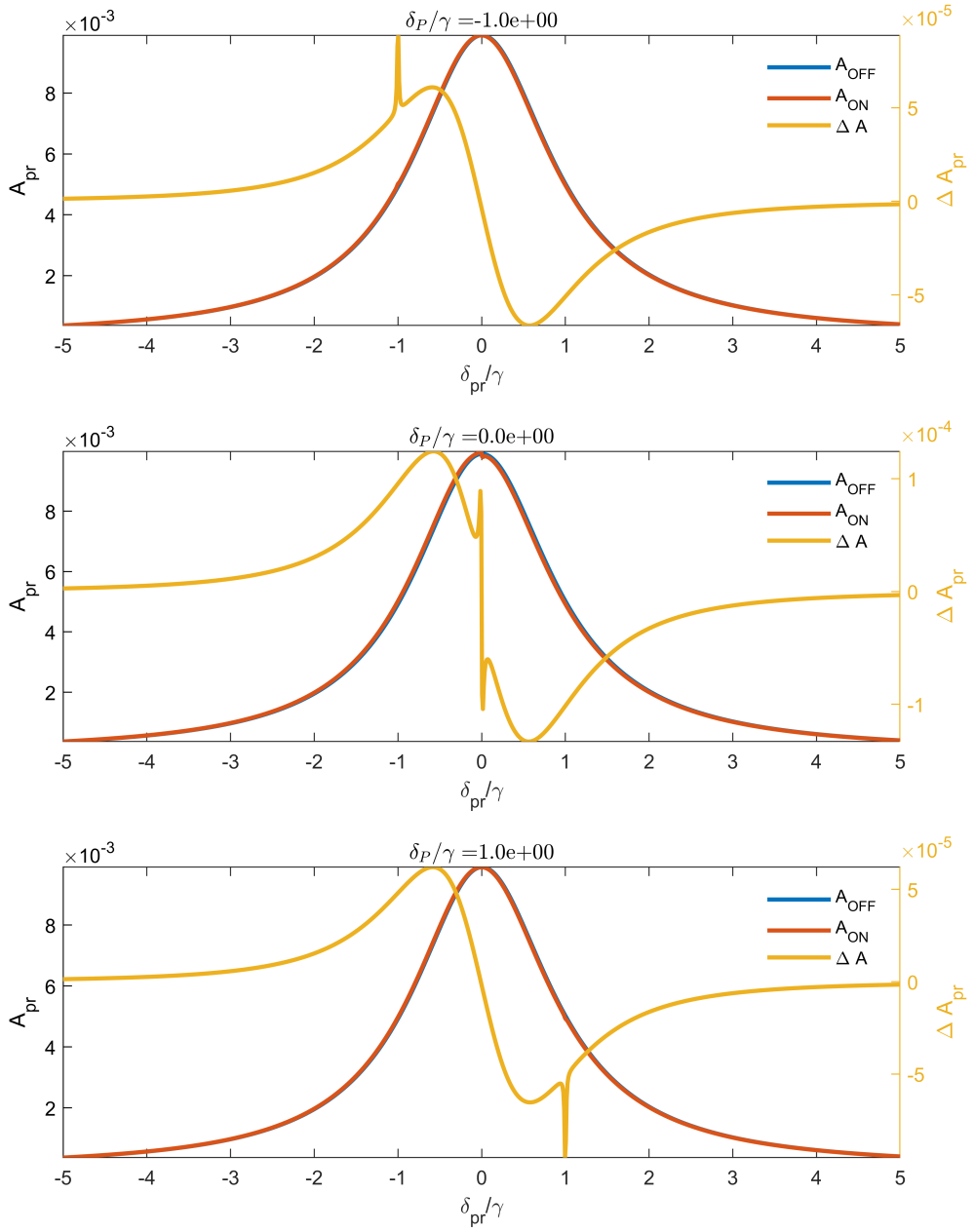

Figure 6.2.2: Calculated differential absorption of the h-BN encapsulated $MoSe_2$ monolayer from master equation-based model. The differential absorption spectra were calculated for three pump detuning values: $\delta_P = -\gamma$ (top), $\delta_P = 0$ (middle), $\delta_P = \gamma$ (bottom). The structure's absorption with pump on and pump off are also shown. The parameters used in these calculations are $n_0 = 1$, $n_1 = 2.6$, $n_2 = 2.6$, $n_3 = 1.5$, $n_4 = 1$, $\tau_1 = 10^{-8}$, $\tau_2 = 10^{-8}$, $\tau_3 = 10^{-4}$, $n_0 = 1$, $\Lambda_0 = 10^2$, $\zeta = 10^{-4}$, $\Upsilon = 1$, $B = -10^2$, $G = 0.995$, $S = 10^{-2}$, and $I_{0_P} = 10^{-6}$. The indices of refraction of h-BN and NBK7 glass were taken from references [94] and [61], respectively.

probe fibers is counteracted by a pair of intensity stabilizers to reduce amplitude noise. These systems consist of a pick-off beam splitter and a photodiode after the fiber outputs. The signals from the photodiodes are sent to a pair of PID controllers (Newport LB1005) where a voltage setpoint that corresponds to a certain optical power at the noise photodetector is chosen. The servo output voltages are sent to the control ports of a pair of voltage-controlled attenuators that increase or decrease the RF modulation signal of the pump and probe beams to reduce the power fluctuations at the noise photodetectors and therefore keep the power of the first order diffracted beams stable. The pump and probe RF modulation signals are generated using a pair of function generators (Keithley 3390), which were set to 70.2 MHz and 70.201 MHz, respectively. The outputs of the function generators are sent to the input ports of the voltage-controlled attenuators, and the output of the attenuators are connected to a pair of RF power amplifiers (Intra Action PA-4) which drive the AOMs. The sync outputs of the function generators are sent to the left and right ports of an RF mixer (Mini-Circuits ZAD-3+) and the mixer's output is sent through a low-pass filter (Thorlabs EF110) with a cut-toff frequency equal to 1 kHz. The 1 kHz signal resulting from mixing is connected to the reference signal ports of two lock-in amplifiers (Signal Recovery 7270) used to monitor the reflection and transmission photodetectors.

After the noise-eating stage, the pump and probe beams are sent through a combination of linear polarizers and half-wave plates. Since most of the measurements discussed in this chapter were performed using either co or cross-circularly polarized light, the pump and probe beams are combined into a beam splitter and then go through a quarter-wave plate to create circularly polarized light. The half-wave plates are then adjusted to generate either co or cross-circularly polarized beams. The pump and probe beams propagate colinearly through the rest of the path and into a closed-cycle cryostat (Attodry 1000) until they are focused down onto the sample using an aspheric lens. Before entering the cryostat, however, the beams go through a beam splitter which is used to pick off part of the beams to monitor the power incident onto the cryostat. The reflected portion of the beams go though the input

window of the cryostat, which is kept at 4 K, a telescope that is used primarily for white light imaging, and a couple of mirrors that steer the beams into the aspheric lens focusing them onto the sample. The sample sits vertically on a sample holder that consists of a 90 degree bracket that is attached to a base plate that rests on a stack of three piezoelectric nano-positioners that move the sample along three axes.

White light from a lamp (Fiber-Lite EEG2823) is coupled into a fiber to produce a clean Gaussian beam. After out-coupling from the fiber, the white light is sent though a long-focal length lens used to focus the white light onto the front focal plane of the aspheric lens inside the cryostat to illuminate the sample uniformly. The white light path is used for imaging only, and it is undone by removing a flip mirror that otherwise blocks the pump and probe lasers paths.

The fraction of the pump and probe beams reflected by the sample is collected with the same aspheric lens used to focus them down onto the sample, and then back-propagate along the incident path. After the beams reach the beam splitter used to monitor the power incident onto the cryostat, they are sent through another beam splitter used to reflect part of the light onto an avalanche photodiode (APD) that is biased using a high-voltage power supply (SRS P5325). Alternatively, the reflected or emitted light is coupled into an optical fiber and sent to a spectrometer if measuring PL. The light transmitted through this last beam splitter is focused onto a color CMOS camera (Thorlabs DCC3260C), which is primarily used for white light imaging. The signal of the reflection APD is then sent to the signal input port of one of the lock-in amplifiers. Lastly, the fraction of the pump and probe beams transmitted through the sample is collected using another aspheric lens mounted behind the sample. The collected light finally reaches a photodiode (DET3630) which is connected to the signal port of the other lock-in amplifier.

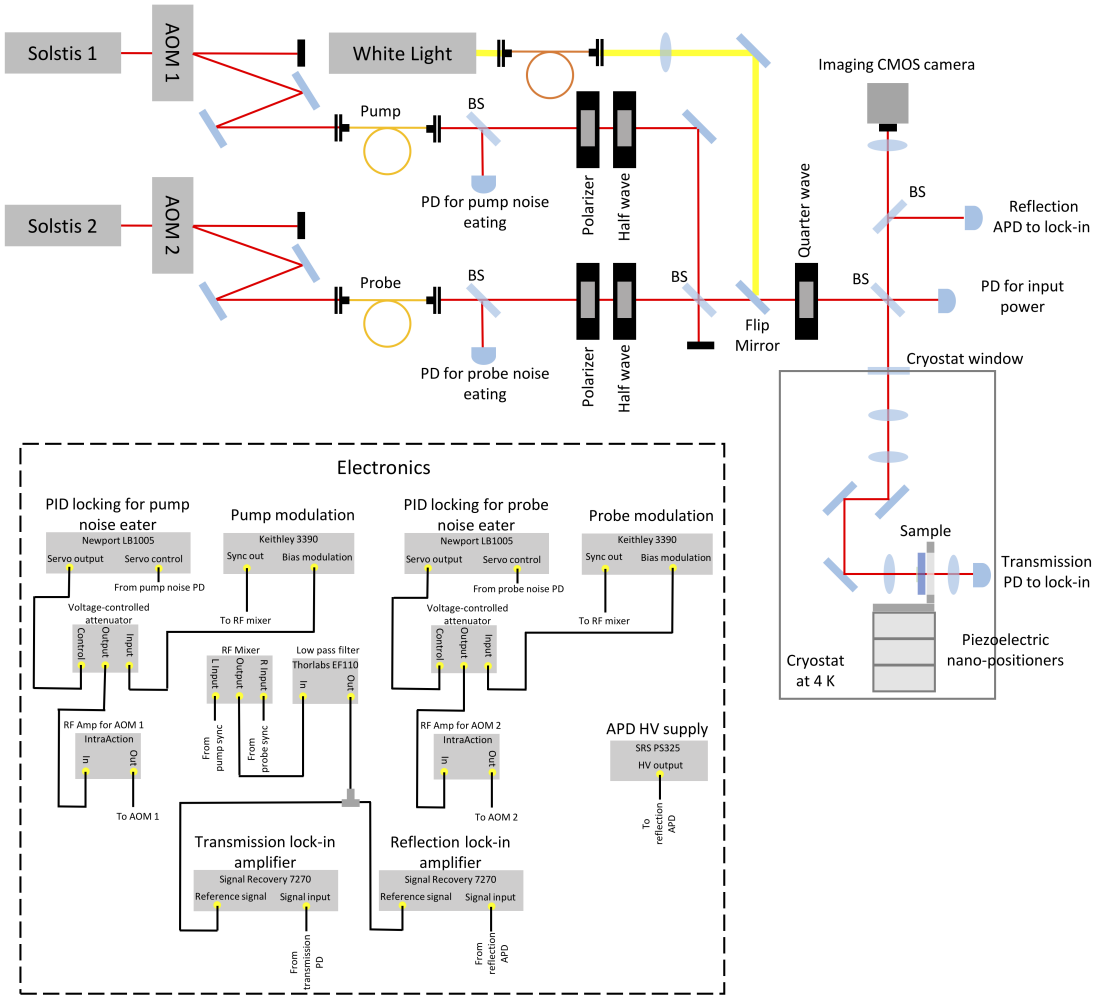

Figure 6.3.1: Schematic of the experimental setup for performing nonlinear optical spectroscopy. Details are in the text. These diagrams were constructed based on diagrams in reference [157].

6.4 Experimental results

This section includes a brief description of the sample preparation and the optical measurements of the h-BN encapsulated $MoSe_2$ monolayer.

6.4.1 Sample preparation

As previously mentioned, the studied sample is an h-BN encapsulated $MoSe_2$ monolayer transferred over a wedged, AR-coated, NBK7 glass substrate. The h-BN and $MoSe_2$ layers were mechanically exfoliated from their bulk crystals and stacked on top of each other using a polymer-based (PMMA) stamp prior to the final transfer of the encapsulated monolayer onto the NBK7 substrate. An electrically-heated mechanical stage was used to assist in the manipulation of the layers. An optical image of the finalized multi-layer structure is shown in figure 6.4.1. The yellow-colored layer corresponds to the bottom h-BN layer and it is in direct contact with the NBK7 substrate, which appears as the dark blue background. The orange-colored layer corresponds to the top h-BN layer, and the white dashed line indicates the outline of the $MoSe_2$ monolayer encapsulated by the h-BN layers.

6.4.2 Linear absorption and photoluminescence measurements

Encapsulation with h-BN has been shown to reduce the inhomogeneous linewidth broadening of TMD monolayers enabling the excitation of nearly pure exciton gasses [110]. To evaluate the quality of the studied sample, the photoluminescence (PL) spectrum was measured with a 633 nm CW laser excitation. The energy of the laser excitation (1.96 eV) is above the low-temperature optical bandgap of the $MoSe_2$ monolayer, which is approximately 1.66 eV. Figure 6.4.2 shows a typical low-temperature PL spectrum of the h-BN encapsulated $MoSe_2$ monolayer where the peaks located at about 1.628 eV and 1.653 eV correspond to the trion and exciton peaks, respectively. The exciton peak was fit reasonably well with a Lorentzian function, and the resulting linewidth is about 3 meV. The high quality of the sample is clearly

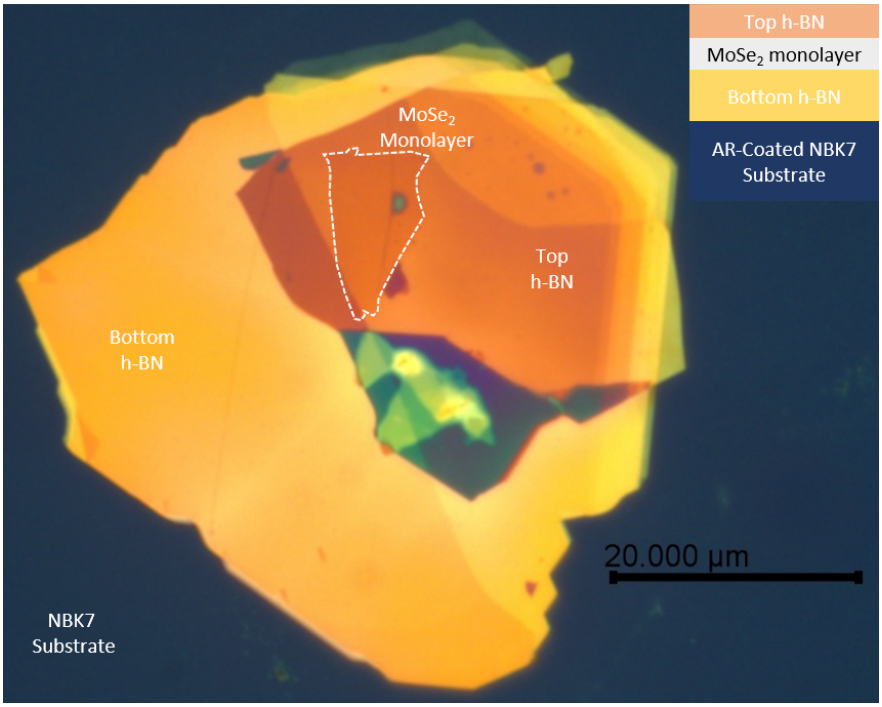

Figure 6.4.1: Optical microscope image of the h-BN encapsulated $MoSe_2$ monolayer. The sample was transferred over a wedged AR-coated NBK7 substrate, which appears as the dark blue background on the image. The outline of the encapsulated $MoSe_2$ monolayer is indicated by the white dashed line. The inset on the top right corner of the optical image is a side-view illustration of the multi-layer structure, but the dimensions are not to scale.

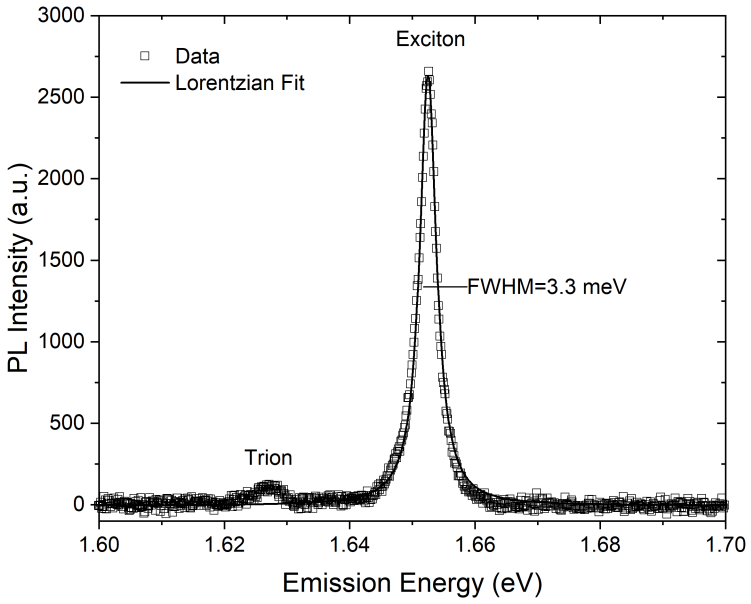

Figure 6.4.2: Photoluminescence spectrum of the h-BN encapsulated $MoSe_2$ monolayer at 4 K. The excitation was a linearly polarized HeNe laser with an energy of 1.96 eV. The PL spectrum of the $MoSe_2$ monolayer shows two peaks: a trion peak at about 1.628 eV and an exciton peak at about 1.653 eV. The exciton peak was fit with a Lorentzian function and the resulting linewidth is about 3.3 meV. A relatively low trion peak and narrow linewidth are both expected results from the encapsulation of the $MoSe_2$ monolayer with h-BN.

illustrated by the reduced inhomogeneous broadening of the exciton peak, and the relatively weaker trion peak indicating low doping levels. Both of these features are expected results from encapsulating the $MoSe_2$ monolayer with h-BN.

While both exciton and trion peaks are typically observed in PL spectra of TMD monolayers, the trion peak is typically much less prominent in absorption measurements. That is one of the reasons why both linear and nonlinear absorption measurements in this work were focused on the exciton resonance. The linear absorption spectrum of the sample was measured using a tunable CW laser excitation that was scanned across the exciton peak observed in the PL spectrum while monitoring the reflection and transmission of the sample. The absolute absorption of the $MoSe_2$ monolayer was estimated by adding together the photocurrent of the detectors monitoring the reflected and transmitted beams when the excitation was incident on a section of the structure that included the $MoSe_2$: $[I_R(E)]_{MoSe_2} + [I_T(E)]_{MoSe_2}$. The sum of these photocurrents was normalized to the relatively featureless sum of the photocur-

rents obtained when the laser was incident on a section of the structure that included the top and bottom h-BN layers but excluded the $MoSe_2$ monolayer: $[I_R(E)]_{hBN} + [I_T(E)]_{hBN}$. The ratio of these sums was subtracted from 1 and the resulting quantity is an estimate of the $MoSe_2$ monolayer's linear absorption. This quantity is summarized by the empirical expression

$$A_{MoSe_2} \approx 1 - \frac{[I_R(E)]_{MoSe_2} + [I_T(E)]_{MoSe_2}}{[I_R(E)]_{hBN} + [I_T(E)]_{hBN}} \tag{6.4.1}$$

where $I_{R,T}(E)$ denote the photon energy-dependent photocurrents of the detectors monitoring the reflected and transmitted laser beams. Figure 6.4.3 shows a typical estimate of MoSe2's absorption obtained with the empirical expression Eq.6.4.1. The estimated peak absorption is about 7%, which is consistent with previous reports of other TMD monolayers [96]. The linear absorption spectrum was also fit reasonably well with a Lorentzian function, and the resulting linewidth is about 8 meV. The absorption spectrum appears asymmetric with respect to the exciton peak and broader than the PL spectrum possibly because of many-body exciton scattering effects. This possibility is discussed in more detail in the following section about nonlinear absorption measurements.

6.4.3 Differential (nonlinear) absorption measurements

The majority of the nonlinear absorption measurements were performed using the pump-probe technique discussed in section 6.2.2, where both differential absorption and differential reflection measurements are made to calculate the differential absorption spectrum. To verify that the measurements probed the sample's nonlinear response in the $\chi_e^{(3)}$ limit, however, only differential transmission measurements were made for various pump and probe power levels because the corresponding differential reflection spectra were not available for this set of measurements. In the absence of the differential reflection spectra, the negative of

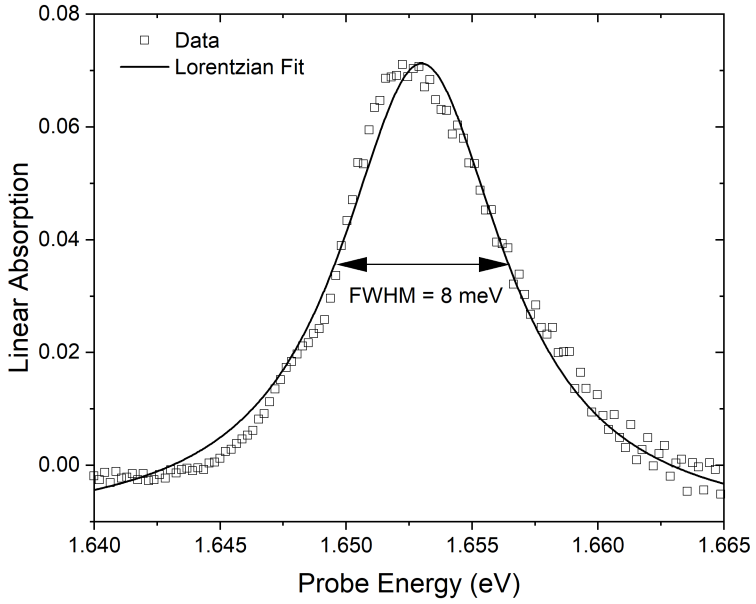

Figure 6.4.3: Linear absorption of the h-BN encapsulated $MoSe_2$ monolayer. The linear absorption of the monolayer was measured using a linearly polarized, tunable, CW laser excitation. The laser was scanned across the energy of the exciton peak observed in the PL spectrum at about 1.653 eV. The linear absorption spectrum was fit with a Lorentzian function, and the resulting linewidth is about 8 meV.

the differential transmission spectrum constitutes an estimate of the sample's differential absorption. Since the main goal of making these power-dependent measurements was to ensure that the spectral features of the nonlinear response, other than the amplitude of the signal, did not change with increasing power, the differential transmission measurements in arbitrary units are an acceptable way to verify that the response is in the $\chi_e^{(3)}$ limit. Figure (6.4.4) shows the negative of the differential transmission spectra of the h-BN encapsulated $MoSe_2$ monolayer for various pump and probe power levels. The spectra display identical features for all the power levels, but their peak-to-peak values begin to increase nonlinearly at the two highest pump and probe power values. Therefore, the remaining nonlinear absorption measurements were performed with a combination of pump and probe powers that fall within the linear regime. That is, the pump was set to 300 μW and the probe was set to 100 μW.

To determine their relative contribution to the differential absorption spectra, both the differential reflection and transmission spectra of the h-BN encapsulated $MoSe_2$ monolayer

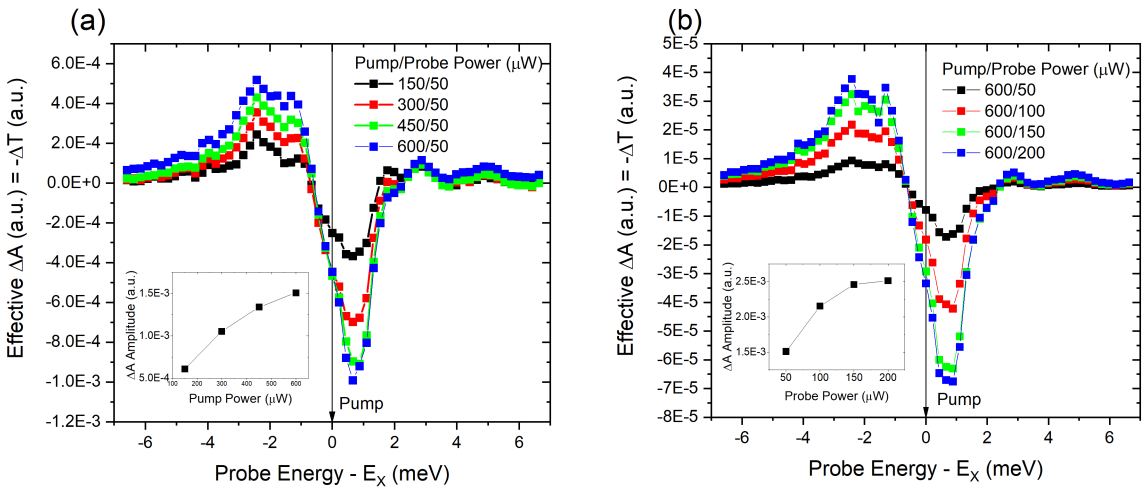

Figure 6.4.4: Effective differential absorption of the h-BN encapsulated $MoSe_2$ monolayer for various pump and probe powers. The $MoSe_2$ monolayer's effective absorption spectra for increasing pump (a) and probe (b) powers were estimated as the negative of the differential transmission spectra. The x-axis corresponds to the energy detuning of the probe with respect to the exciton resonance. The differential reflection spectra were not available for this set of measurements. The insets indicate the peak-to-peak amplitude of the spectra for different power levels. At high pump and probe powers, the peak-to-peak amplitude begins to increase nonlinearly. The main spectral features, however, remain virtually identical for all pump and probe power levels.

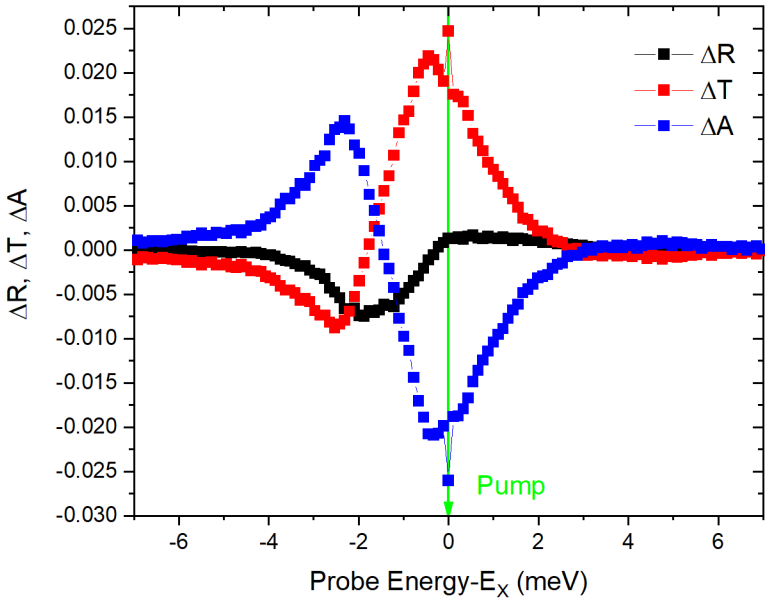

Figure 6.4.5: Typical absolute differential reflection, transmission, and absorption spectra of the h-BN encapsulated $MoSe_2$ monolayer. The absolute differential spectra were obtained by characterizing the optical losses in the measurement apparatus to accurately estimate the amount of probe power reflected from and transmitted through the sample relative to the incident probe power. The pump and probe lasers were co-circularly polarized.

were acquired. These spectra were obtained after calibrating the losses of the optical setup to determine how much power is transmitted and reflected from the sample relative to the power that reaches the sample inside the cryostat. Typical absolute differential reflection, transmission, and absorption spectra for various pump detuning values are shown in Fig.6.4.5.

The reflection, transmission, and absorption spectra shown in Fig.6.4.5 have dispersive line shapes which are asymmetric with respect to the zero crossing. The dispersive shape of these spectra reveals a resonance energy shift whereas the asymmetry with respect to zero crossing indicates a change in the linewidth of the resonance as illustrated in Fig.6.4.6. While the physical mechanisms responsible for these spectral changes are not identified precisely, the master equation model developed in section 5.2 does include a pump-induced shift in the resonance energy (EIS) and a pump-induced increase in the dephasing rate (EIS). These phenomenological terms are sufficient to reproduce the main features of the differential absorption spectra observed in Fig.6.4.5.

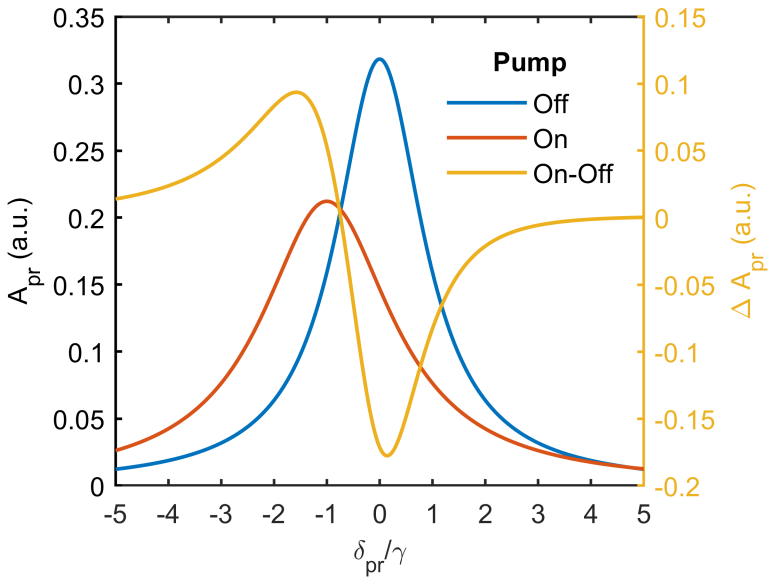

Figure 6.4.6: Illustration of excitation-induced features on the differential absorption spectrum. The dispersive line shape of the differential absorption spectrum arises from the excitation-induced shift of the resonance energy whereas the asymmetry of the spectrum with respect to the zero crossing arises from the excitation-induced broadening of the resonance. The absorption spectra with the pump laser on and off were modeled as Lorentzian functions. With the pump on, the Lorentzian is red shifted one unit and broadened by 50% relative to the Lorentzian with the pump on.

It is plausible that pump-induced changes to the semiconductor lattice might also lead to differential absorption spectra with features identical to those observed in the spectra shown in Fig.6.4.5. Namely, localized optical heating of the $MoSe_2$ lattice with the pump laser could lead to a narrowing of the bandgap, which in turn could appear as a red shift of the resonance energy on the differential absorption spectra. In addition, localized optical heating could lead to a broadening of the resonance due to an increase in exciton-phonon scattering since the phonon population is lattice-temperature dependent. To exclude optical heating as a source of spectral shifts and linewidth broadening, the pump and probe lasers were amplitude modulated at frequencies higher than the inverse of the characteristic thermal time constant of the $MoSe_2$ monolayer. The thermal conduction time constant is a material property that provides information on the ability of the material to conduct heat. Assuming that heat conduction in the direction normal to the TMD monolayer is negligible because of its atomically-thin thickness, and the optically generated heat is primarily dissipated in the in-plane direction, the inverse of the thermal conduction time constant is given by

$$\frac{1}{\tau_{th}} = \frac{k_{th}}{c_M \rho l^2} \tag{6.4.2}$$

where c_M, ρ and k_{th} are the material's specific heat, mass density, and thermal conductivity, respectively. The length scale l corresponds to the distance that heat travels from the high to the low temperature points of the material. For an optical beam with a Gaussian intensity profile, the length scale l can be approximated by the beam radius. The thermal conduction time constant of an $MoSe_2$ monolayer at 4 K with the parameters summarized on table 6.4.1 is 56 ns and its inverse is 18 MHz. This time constant is likely an underestimate since the optically generated heat may actually be dissipated over a length scale of a few beam radii. The modulation frequency of the pump and probe fields were 70.2 MHz and 70.201 MHz, respectively. Because the temperature of the lattice is not able to change at a rate faster than

Table 6.4.1: Thermal conduction properties of monolayer $MoSe_2$ and h-BN at 4 K, and NBK7 glass at room temperature. In-plane heat flow was assumed for $MoSe_2$ while heat flow along the perpendicular direction was assumed for the h-BN and NBK7 layers.

Material	$c_M\left(\frac{J}{KgK}\right)$	$\rho\left(\frac{Kg}{m^{2(3)}}\right)$	$k_{th}\left(\frac{W}{K(m)}\right)$	$l(m)$	$\frac{1}{\tau_{th}}\,(Hz)$
$MoSe_2$ ($\parallel$)	1 [120]	4.46×10^{-6} [173]	2×10^{-9} [120]	5×10^{-6}	18×10^{6}
h-BN ($\perp$)	0.3[174]	2180 [174]	2 [174]	10^{-6}	3.06×10^{9}
NBK7 ($\perp$)	858 [61]	2510 [61]	1114	3×10^{-3}	57.5

the inverse of the thermal time constant to follow the modulation of the pump and probe fields, the spectral shifts and linewidth broadening indicated by the differential absorption spectra shown in Fig.6.4.5 cannot be due to optical heating of the $MoSe_2$ lattice.

For reference, the inverse of the thermal time constant for heat conducted along the perpendicular direction through the h-BN and NBK7 layers were estimated to be about 3 GHz and 58 Hz, respectively. These estimates suggest that while the temperature of the h-BN layer would be able to follow the modulation frequency of the pump and probe fields at about 70 MHz, the temperature of the NBK7 layer would not. In spite of the fast thermal response of the h-BN layer, the slower thermal response of the $MoSe_2$ lattice prevents its temperature from following the modulation of the pump and probe fields. Moreover, the poor thermal response of NBK7 is not expected to influence the temperature of the $MoSe_2$ lattice significantly. Therefore, the spectral red shift and linewidth broadening observed in the differential absorption spectra of Fig.6.4.5 most likely arise from excitation-induced many-body interactions. Both exciton and electron-hole plasma effects are known to produce blueshifts and resonance energy broadening [177]. However, exciton-exciton scattering can cause a spectral red shift [81].

Interestingly, the differential transmission spectra in Fig.6.4.5 also reveal a narrow resonance at zero pump and probe detuning that appears as a single point due to the relatively low resolution of the energy axis. This resonance was observed only when the pump and probe lasers were co-circularly polarized as evidenced in Fig.6.4.7. Not surprisingly, these polarization-dependent differential spectra reveal the optical selection rules supported by the

$MoSe_2$ monolayer originating from the symmetry of its band structure. Although the valleys of TMD monolayers located at the K and K' points of the first Brillouin zone in momentum space are energy degenerate, they couple to light of opposite circular polarization. Therefore, when the pump and probe lasers are co-circularly polarized, the differential absorption spectrum reveals the nonlinear optical response of excitons of the same valley whereas when the lasers are cross-circularly polarized, the differential absorption spectrum reports on the coupling between the energy degenerate K and K' valleys. The narrow resonance that appears when the pump and probe are co-circularly polarized arises due to the interference of the pump and probe fields through the excitation of the medium. This coherent process is known as population pulsation and it leads to a modulation of the exciton population at the pump-probe detuning frequency [161].

The master equation model developed in section 5.2 also predicts this narrow resonance. Specifically, one of the terms in the third order off-diagonal density matrix element given by Eq.6.2.44 has a resonant denominator at the pump-probe detuning, and the half width of the resonance is equal to the spontaneous emission rate of the MBS. The population pulsation term is dominant when the dephasing rate is much larger than the spontaneous emission rate. Under such conditions, the high resolution differential absorption spectrum is characterized by a narrow population pulsation resonance peaked at zero pump-probe detuning and on top of the many-body spectrum. Since the population pulsation resonance arises from the interference of the fields through the excitation of an exciton population, this resonance naturally follows the optical selection rules of each valley. Consequently, a population pulsation resonance only appears when both the pump and the probe fields address the same valley with identical circular polarization, and it is peaked at the pump-probe detuning as shown in Fig.6.4.8.

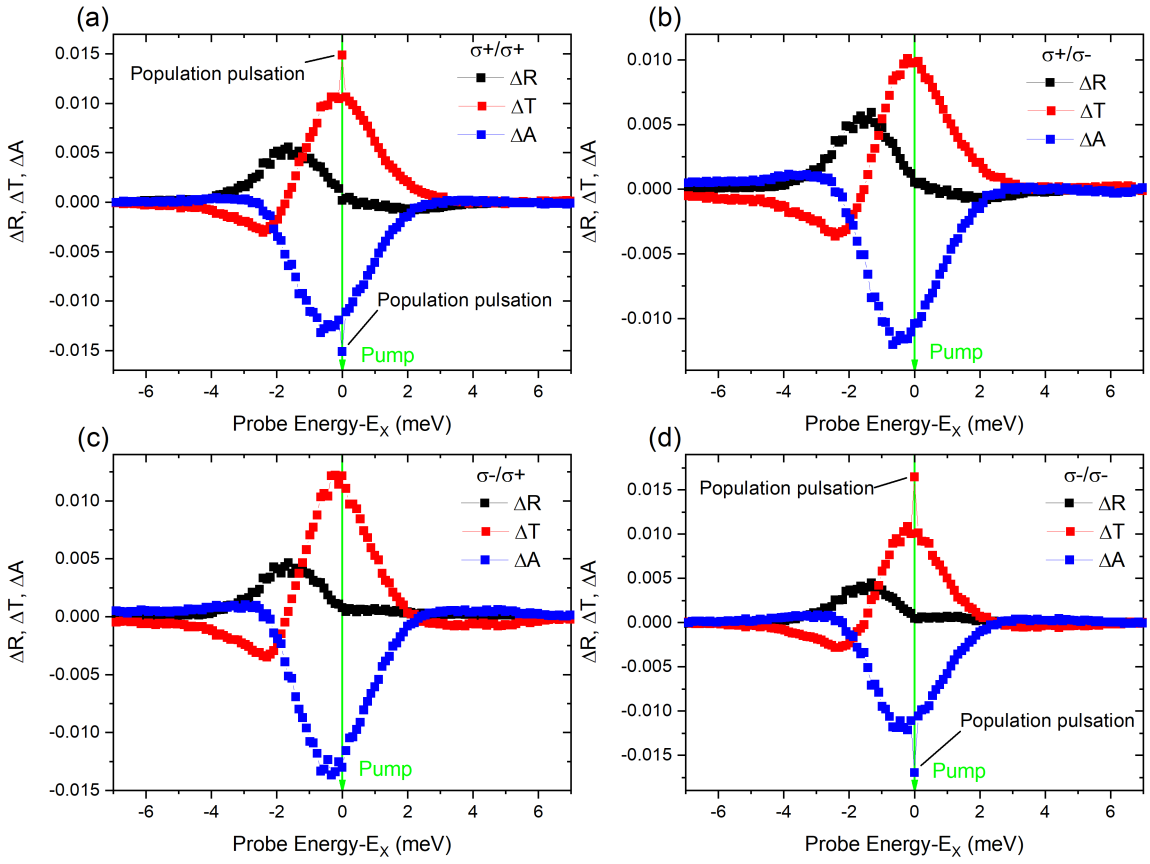

Figure 6.4.7: Absolute differential reflection, transmission, and absorption spectra of the h-BN encapsulated $MoSe_2$ monolayer for various pump-probe polarization combinations. The pump energy was fixed at the exciton resonance energy. A narrow resonance is observed when the pump and probe are co-circularly polarized. The resonance appears as a single point due to the relatively low resolution of the energy axis.

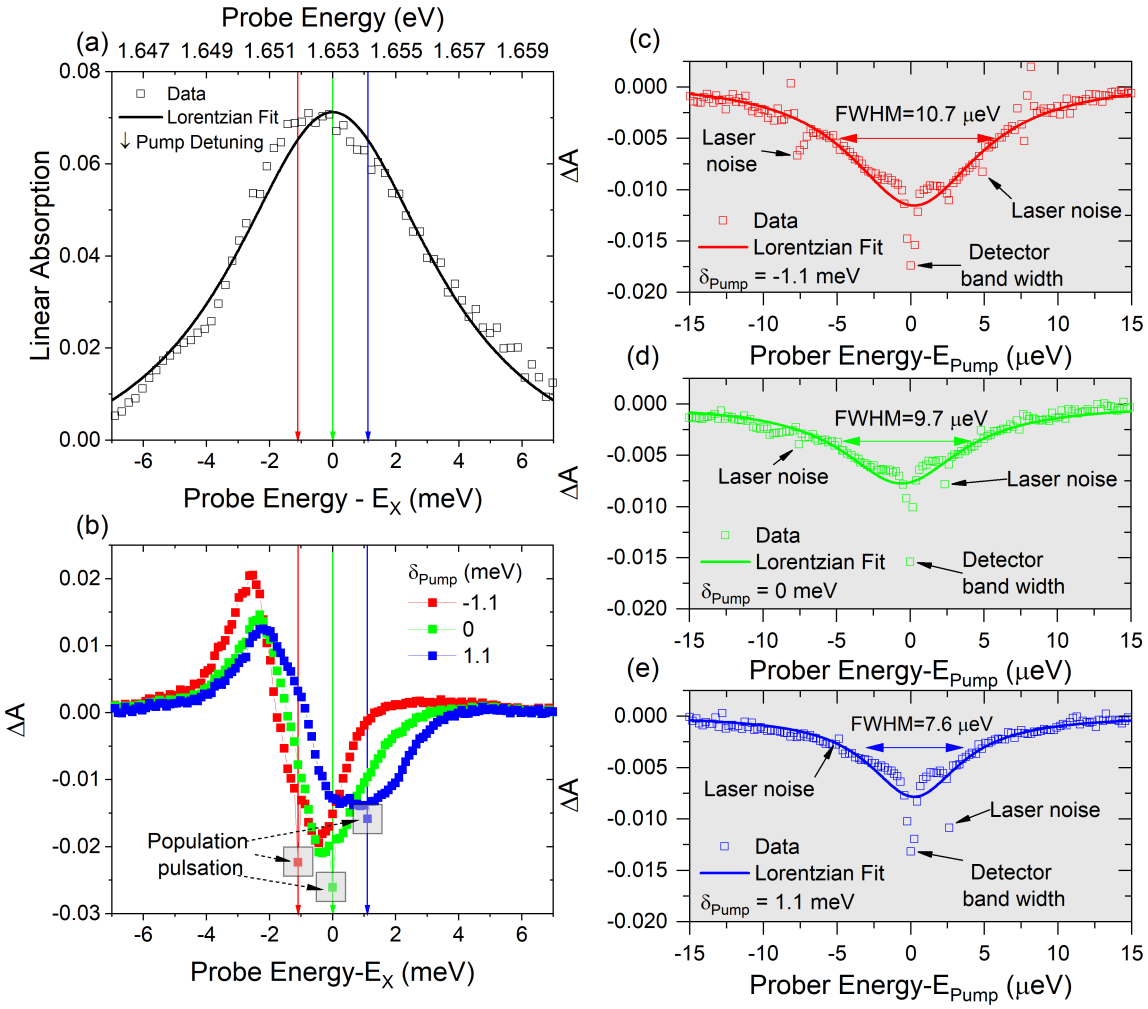

Figure 6.4.8: Absolute differential absorption of the h-BN encapsulated $MoSe_2$ monolayer for various pump energies and co-circularly polarized pump-probe fields. (a) Energy detuning of the pump with respect to the exciton resonance energy labeled on the linear absorption spectra of the monolayer with the color-coded arrows. (b) Low resolution absolute differential absorption spectrum of the $MoSe_2$ monolayer for various pump energy detuning values. The population pulsation resonances follow the pump energy. (c), (d), (e) High resolution differential absorption spectra showing the population pulsation resonances that appear at zero pump-probe detuning in (b). The sub-μeV features at zero pump-probe detuning on the high resolution spectra correspond to the electrical bandwidth of the photodetector of about 35 MHz. The additional sub-μeV features on the high resolution spectra correspond to noise coming from the laser electronics. All of these sub-μeV features are present even when the pump and probe lasers do not interact with the sample and go straight through the substrate. The pump and probe lasers were co-circularly polarized.

6.4.4 Fitting of differential absorption spectra

As previously discussed, the differential absorption spectra presented in Fig.6.4.5, Fig.6.4.7, and Fig.6.4.8 are evidence of excitation-induced, many-body spectral red shifts and dephasing. While the density matrix model developed in section 5.2 is able to qualitatively reproduce both of these features, a quantitative fit to the experimental data has not been achieved. In spite of carefully choosing the pump and power levels so that, other than the signal amplitude, all of the spectral features do not vary with power, it is possible that the differential absorption spectra contain contributions of many-body effects beyond the $\chi_e^{(3)}$ limit which are not accounted for in the model of section 5.2.

To explore the possibility of higher-order nonlinear effects, the differential absorption spectrum for zero pump detuning in Fig.6.4.7 was fitted using the difference of two Lorentzian functions (D2L) plus a correction to the nonlinear response in the absence of excitation-induced spectral shifts and linewidth broadening as

$$\begin{aligned} \Delta A_{exp} &\approx \zeta\left(\Lambda_0 + x_{pr}\right) \\ &\times \left[\frac{1+\Upsilon\rho_{22}}{\left(x_{pr}-B\rho_{22}\right)^2+\left(1+\Upsilon\rho_{22}\right)} - \frac{1}{x_{pr}^2+1} - \frac{2\rho_{22}}{x_{pr}^2+1}\right] \end{aligned} \tag{6.4.3}$$

where the first term in the brackets represents the excitation-induced shifted and broadened absorption; the second term is simply the linear absorption in the absence of the pump field; and the third term is the correction to the differential absorption arising from the third-order, nonlinear response in the absence of many-body effects. Specifically, this correction arises from the perturbation time-ordering $(j,l,m) = (P,P,pr)$ given by Eq.6.2.40. Equation (6.4.3), however, does not include the population pulsation resonance arising from the time-ordering $(j,l,m) = (pr,P,P)$ given by Eq.6.2.42. Further details of the derivation of Eq.6.4.3 can be found on appendix C. The differential absorption spectrum for zero pump detuning and excluding the population pulsation resonance was fitted and with Eq.6.4.3 and the results

are shown in Fig.6.4.9. For comparison, the fitting of the data with the density matrix model (DM) is also included.

The fact that Eq.6.4.3 fits the experimental data reasonably well suggests that there might be light-matter interaction effects beyond third order that are playing a role in the optical response of the $MoSe_2$ monolayer. Moreover, Coulomb coupling effects in TMD monolayers are prominent and play a significant role on their nonlinear optical response. The treatment of such effects, however, are beyond the scope of this work and need to be treated systematically using the semiconductor Bloch equations [81, 84, 177].

6.5 Summary and conclusion

This chapter discussed studies of the nonlinear optical response of an h-BN encapsulated $MoSe_2$ monolayer. The chapter began by motivating the study of the nonlinear optical response of TMD monolayers for applications in coherent control. Then a survey of the relevant studies of the nonlinear optical spectra of TMDs was presented. In particular, the signatures of coherent many-body effects on the differential absorption spectra of TMD monolayers, including resonance energy shifts and linewidth broadening, were mentioned. Then, a model based on the master equation for the density operator of a two-level system was developed to interpret the many-body signatures. Also, a description of the CW coherent nonlinear optical spectroscopy technique and experimental apparatus used to measure the nonlinear optical response of the sample were provided. Then, the differential absorption spectra of the h-BN encapsulated monolayer measured with various pump-probe polarization combinations were presented. The signatures of many-body effects on the differential absorption spectrum of the monolayer were included phenomenologically in the model, and a qualitative agreement with the experimental results was found. Both population pulsation resonances and many-body effects were qualitatively reproduced by the model. However, a discussion of the plausible scenarios for the quantitative disagreement between the master equation

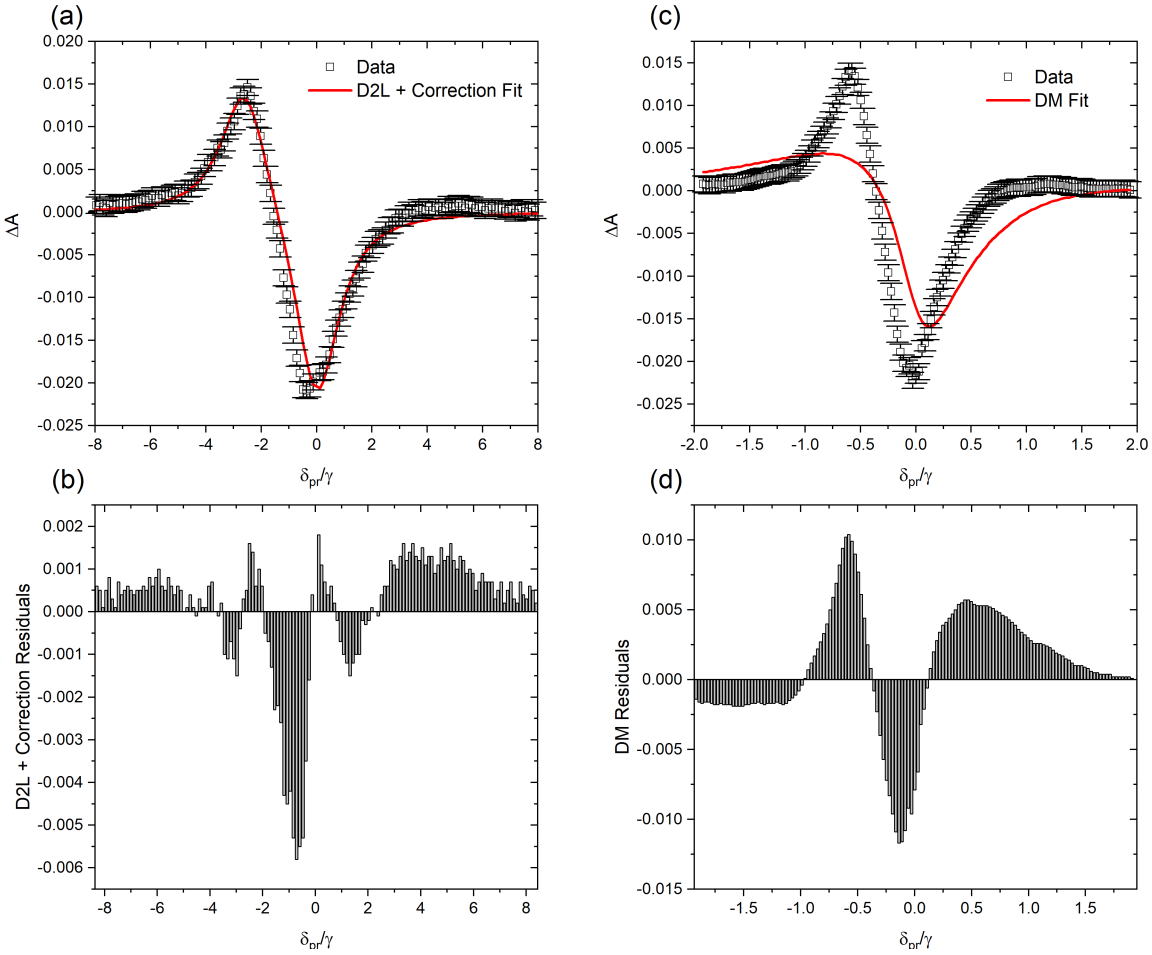

Figure 6.4.9: Fitting of the differential absorption spectrum of the h-BN encapsulated $MoSe_2$ monolayer with the difference of two Lorentzians and density matrix models. (a) Fitting of the differential absorption spectrum of the h-BN encapsulated $MoSe_2$ monolayer shown in figure 6.4.7 with the difference of two Lorentzians plus a third-order correction (D2L+Correction) for co-circularly polarized pump-probe and zero pump energy detuning. (b) Plot of the residuals from the fit of the differential absorption spectrum of the h-BN encapsulated $MoSe_2$ monolayer with the D2L+Correction model, i.e. Eq.6.4.3. The parameters extracted from the D2L+Correction fit are $\zeta = 7.3 \times 10^{-6}$, $\Lambda_0 = 2.4 \times 10^3$, $B = -16.5$, $\Upsilon = 0.524$, $\rho_{22} = 0.157$, $\gamma = 1.406 \times 10^{12} s^{-1}$. (c) Fitting of the differential absorption spectrum of the h-BN encapsulated $MoSe_2$ monolayer shown in figure 6.4.7 with the density matrix (DM) model for co-circularly polarized pump-probe and zero pump energy detuning. (d) Plot of the residuals from the fit of the differential absorption spectrum of the h-BN encapsulated $MoSe_2$ monolayer with the DM model, i.e. Eq.6.2.104. The parameters extracted from the DM fit are $\zeta = 3.42 \times 10^{-5}$, $\Lambda_0 = 413.13$, $B = -1.74 \times 10^4$, $\Upsilon = 2.17 \times 10^4$, $I_{0_P} = 3.69 \times 10^{-6}$, $S = 0.322$, $G = 0.839$, $\gamma = 6.08 \times 10^{12} s^{-1}$, $\tau_1 = \tau_2 = 0$. The population pulsation resonance was intentionally deleted from the experimental data to get a better fit with both models. The error bars are an estimate of the random error in experimental data.

based model and the experimental results was also provided. Lastly, the most likely physical mechanisms responsible for the resonance energy shifts and linewidth broadening observed in the differential absorption spectra were discussed.

Chapter 7

Summary and Future Directions

7.1 Summary and conclusion

Motivated by the need for alternatives to the increasingly energy-inefficient electronic information processing platform in the age of artificial intelligence, the work in this thesis is centered around unraveling the physical processes that impact the transport of excitons in TMD monolayers. These efforts were aimed at enabling the design of novel excitonic devices and coherent control schemes that serve as an alternative to the conventional electron-based information processing architecture as excitons are electrically neutral quasi-particles that can be manipulated with strain by leveraging the sensitivity of TMD's band structure to mechanical deformation.

The majority of exciton transport studies in this dissertation were performed via direct imaging of the PL emission of excitons using the technique described in chapter 3. With this technique, the spatial and temporal dynamics of excitons in TMD monolayers were monitored, and the data generated by these measurements was analyzed assuming that the excitons behave primarily as free particles that follow Fick's law. When deviations from this baseline behavior were observed, the fundamentals processes leading to such anomalies were investigated. Two main sources of anomalous diffusive transport were identified: the multi-

trapping-and-release of mobile excitons by traps in bare TMD monolayers, and the relaxation of excess kinetic energy of excitons in h-BN encapsulated TMD monolayers generated with a high-density, non-resonant excitation.

Another equally important part of the work in this thesis revolved around demonstrating that strain can be used to control the flow of excitons in TMD monolayers. Chapter 4 contained evidence that transferring TMD monolayers over substrates with nanoscale sharp features can generate enough strain in the monolayers to modulate their bandgap and create an effective force that drives the excitons towards the regions of highest strain. This capability was confirmed by generating excitons at a few different points near the strained region of the monolayer and every time, the excitons drifted towards the highest strain point. While the strain control of excitons has been previously demonstrated in other semiconductor materials [51], the measurements in chapter 4, to the best of our knowledge, represent the first demonstration of exciton control with strain gradients in TMD monolayers.

In addition to transport measurements of excitons, the work in this thesis included studies of the nonlinear optical response of TMD monolayers. Particularly, chapter 6 presented studies of the nonlinear optical response of a hexagonal boron nitride (h-BN) encapsulated molybdenum diselenide ($MoSe_2$) monolayer and the modeling of the resulting macroscopic optical polarization using the master equation to interpret the signatures of many-body effects. The main observation of these studies was the appearance of a unique nonlinear absorption spectrum featuring excitation-induced broadening and shifts of the exciton resonance. While modeling of the full many-body state of the system requires a higher-level theory based on the semiconductor Bloch equations [84], the main experimental observations were qualitatively reproduced with a master equation-based model. These results serve as evidence of the potential of TMD monolayers as a platform for the design of hybrid photonic-excitonic devices that leverage not only the ability to manipulate excitons but also the quantum coherent properties of these materials.

While there is a long road ahead for the field of exciton-based information processing to

reach maturity, the insights obtained from the work in this thesis undoubtedly represent a step closer to such an ambitious goal. The following section contains several future directions that this work can take to make headway in the understanding and control of the processes that impact the transport and quantum coherence of excitons in TMD monolayers.

7.2 Future directions

As discussed in chapter 3, a recurring observation in the diffusion studies of excitons in TMD monolayers is the deviation of exciton diffusion from Fick's law. While such deviation, referred to as anomalous diffusion, is a phenomenon that is observed throughout nature, its physical origin is unique to each particular system. At low excitation densities, anomalous diffusion of excitons and carriers in semiconductor materials is associated with energetic disorder caused by crystal defects that localize otherwise mobile excitons and carriers, slowing down their motion. This effect was observed in the diffusion measurements of excitons in a WSe_2 monolayer in chapter 4, and the origin of the anomaly was linked to intrinsic defects in the monolayer as well as the extrinsic defects introduced during the fabrication of the sample or hosted by the substrate. This hypothesis could be verified in future studies by performing similar exciton diffusion measurements in samples prepared in different but controlled ways to learn the effect of the fabrication process on the deviation of the exciton diffusion from Fick's law. Additional diffusion measurements could be performed on TMD monolayers transferred over different types of substrates. For example, the monolayers could be suspended over holes [172] or they could be encapsulated with hexagonal boron nitride [108] to completely isolate the monolayers from the substrates to determine the role they play in the origin of the anomalous diffusion of excitons in TMD monolayers. In addition to exciton imaging measurements, complementary absorption measurements at various lattice temperatures could be performed to map out the distribution of defect states arising from the different substrates and fabrication processes. Since the dynamics of trapping and release of

mobile excitons are largely influenced by the details of the distribution of traps in the material [195, 105], having a clear picture of such distribution would provide irrefutable evidence of the role they play in the origin of anomalous diffusion in TMD monolayers. While there are mathematical models, such as the one discussed in chapter 3, that elucidate the dynamics of multi-trapping-and-release (MTR) of excitons in energetically disordered semiconductors, a higher-level kinetic model based on the semiconductor Bloch equations that takes into account the details of the band structure of TMDs and the distribution of trap states should be developed to reconcile the experimental observations with the fundamental origin of the anomalous diffusion of excitons in these materials.

The work in chapter 5 focused on identifying yet another physical mechanism that leads to anomalous exciton diffusion in TMD monolayers. Unlike the sample studied in chapter 4, the sample in chapter 5 was encapsulated with h-BN to eliminate the influence of the substrate on the diffusion of excitons. Instead, the anomalous diffusion observed in chapter 5 was traced to the relaxation of kinetic energy and Auger scattering of hot excitons generated with a high-density, non-resonant optical excitation. While the single-valley energy relaxation model used in chapter 5 to reproduce the main signatures of the relaxation of the kinetic energy of hot excitons, additional experiments and higher-level models that take into account the band structure of TMD monolayers as well as the interaction of hot excitons with phonons should be developed. It is widely known that intervalley scattering plays a key role in the energy relaxation and recombination dynamics of excitons in TMD monolayers [16, 154, 155, 169]. Although momentum-dark excitons cannot recombine radiatively, phonon-assisted recombination is a very efficient radiative recombination channel in these materials [16, 169]. Phonon sidebands arising from the radiative recombination of momentum-dark excitons have been observed at both low and room temperature [16]. Therefore, the anomalous diffusion behavior observed in chapter 5 very likely arises from the relaxation and Auger scattering of momentum-dark excitons that emit light via phonon-assisted recombination. To confirm this hypothesis, temporally-resolved spectral measurements of the light emitted

from the material should be carried out at various temperatures and excitation densities. In addition, real and momentum space imaging of the light emitted by the TMD monolayers could be performed as the far-field spatial distribution of the emitted light should provide evidence of hot exciton relaxation [227]. These measurements will unambiguously reveal the details of the light emission process in TMD monolayers excited with a high density, non-resonant optical excitation. In conjunction with these experiments, a kinetic model based on the semiconductor Bloch equations that takes into account the band structure of TMD monolayers as well as the exciton-exciton Auger scattering and exciton-phonon scattering processes should be developed to reproduce the anomalous diffusion of hot excitons in h-BN encapsulated TMDs. Such a rigorous modeling of the exciton dynamics in these materials will shed light on other remarkable effects not discussed in this thesis, but which are routinely observed in exciton imaging experiments, including the negative diffusion of excitons at low temperature [153], the quantum interference of excitons [60], and the unconventional temperature dependence of the diffusivity of zero-kinetic energy excitons.

Beyond simply understanding the fundamental processes that give rise to the anomalous diffusion of hot excitons in h-BN encapsulated TMD monolayers, the light emission of hot excitons could be leveraged in a way similar to that in light-emitting diodes (LEDs). Conventional LEDs are known to suffer from an efficiency droop at high current densities [72]. Such limitation arises from the very efficient non-radiative Auger recombination of carriers at high current densities. Similarly, in TMD monolayers, exciton-exciton Auger scattering leads to both the non-radiative recombination of a fraction of the population of excitons and the heating of the remaining population. Much of that energy, however, is lost to lattice heating via phonon scattering. If instead, a photonic structure with a properly designed density of states that matches the momentum of these Auger-heated hot excitons is coupled to TMD monolayers, the excess energy of these excitons could be extracted in the form of light similar to the work in [31, 69]. Certainly, a TMD monolayer-based LED would require an electrical rather than an optical excitation. However, electroluminescence (EL) generation

in TMD monolayers is an active field of research, and various strategies to generate EL and leverage exciton-exciton Auger recombination are being developed [98, 202]. A thorough understanding of hot exciton dynamics in conjunction with a properly-designed photonic structure could lead to development of efficient TMD-based light emitting devices that do not suffer from efficiency droop at high current densities as conventional LEDs do.

One of the main reasons TMD monolayers are considered as one of the most promising platforms for excitonic devices is the remarkable tunability of their band structure using strain. While in chapter 4, it was shown that strain can be used to control the flow of excitons on demand, there is evidence that suggests that trions may play a bigger role in the funneling of excitons and subsequent light emission in strained TMD monolayers than previously thought [50, 63]. This unexpected complication could be circumvented by neutralizing the excess charge that give rise to the formation of trions in TMD monolayers using a substrate with electrical contacts that supply the necessary charge to create an electrically neutral environment prior to the generation of excitons in the strained monolayer. While applying non-uniform strain to TMD monolayers is an efficient strategy to control the motion of excitons in these materials by engineering energy gradients that drive the flow of excitons toward the points of highest strain, uniformly straining the monolayers to shift the relative position of both their optically bright and spin or momentum-dark energy states to favor the scattering into the optically bright states is another practical strategy. There is evidence that suggests that applying controlled amounts of bi-axial strain to TMD monolayers can shift the optically bright exciton state so that it becomes the lowest-lying energy state, increasing its occupation probability and therefore maximizing the diffusivity of bright excitons [152]. The same effect is expected to occur with the diffusivity of other optically forbidden states. However, these dark states could be out-coupled via a photonic structure that matches their momentum similar to the strategy for light extraction of hot excitons discussed above. Alternatively, side illumination and collection schemes could be employed to out-couple the light emission specifically from spin-forbidden states [54, 197].

While the control of the flow of excitons in non-uniformly strained TMD monolayers was demonstrated in chapter 4, having the capability to dynamically tune that strain would enable the control of the speed of excitons. One potential strategy to generate tunable strain in TMD monolayers is to design a sparse array of synthetic polymer fibers on top of a piezoelectric substrate. Applying a controlled voltage to the piezoelectric substrate would generate a controlled vertical deformation in the polymer fibers. Therefore, transferring TMD monolayers over these fibers would generate tunable, non-uniform strain, leading to the control of not only the direction but also the speed of excitons in the strained monolayers. This strategy is the inverse of the working principle behind gecko-inspired tactile sensors that are used to measure very small loads [124].

It is clear that non-uniform strain also increases the probability of exciton capture by defects around the areas of highest strain [15]. Defects in TMD monolayers are known to emit high-purity single photons, which is a desirable capability for hybrid quantum photonic-excitonic devices. However, strain-engineered quantum confinement in these materials still remains elusive. One of the main strategies to create quantum confinement in TMD monolayers consists of transferring them over substrates with sharp nanoscale features [133, 15]. In spite of numerous efforts across the world, there is no evidence that suggests that this type of structures create localized states with properties different from the randomly occurring defect states. Such difficulty, however, presents an opportunity for other strategies to create quantum confinement in TMD monolayers such as lattice-mismatched lateral heterostructures [143, 204], vertical heterostructures with Moiré patterns[6], or TMD nano-disks [194]. In addition, the remarkable progress in the growth of wide bandgap semiconductor monolayers [1, 212] can provide additional material platforms to develop quantum confined structures with engineered strain fields. Achieving control of not only the position but also the confinement of excitons in TMD monolayers and other monolayer semiconductors will be an important step towards the coherent control of TMD-based quantum dots and their integration with a hybrid quantum photonic-excitonic information processing architecture.

Lastly, the experimental work on coherent nonlinear optical spectroscopy of TMD monolayers discussed in chapter 6 could be expanded by exploring the population pulsation resonances observed at zero pump-probe detuning with high spectral resolution and with an intensity-stabilized tunable laser. Although these resonances were obvious in relatively low resolution nonlinear absorption spectra, the high resolution spectra presented in chapter 6 exhibited increasingly noisy features arising from instabilities in the laser intensity. These instabilities made it challenging to distinguish narrow resonances from laser noise. Because signatures of the optical response of randomly-occurring defect states in the nonlinear absorption spectrum of TMD monolayers is likely to be obscured by the laser noise, it is worth investigating the source of the noise in the laser, and devising strategies to mitigate it.

Besides providing insights into the coherent optical properties of excitons in TMD monolayers, the nonlinear optical spectroscopy technique discussed in chapter 6 could be employed to investigate the regimes of coherent and diffusive exciton transport in these materials [160]. One of the main advantages of this technique over the direct imaging of the photoluminescence of excitons is that the nonlinear spectroscopy technique employs a laser excitation that can be tuned in resonance with the exciton energy. Generating excitons resonantly will circumvent undesired processes such as the creation and relaxation of hot excitons. As a result, a clear understanding of the intrinsic transport properties of optically bright excitons in TMD monolayers could be acquired via four-wave mixing experiments.

Appendix A

Strain-Based Drift Model

In this appendix, a first-principles balance equation for the exciton density under diffusion, drift, and relaxation processes is derived. To begin, a discussion of the Boltzmann transport equation is presented.

A.1 Boltzmann transport equation

The Boltzmann transport equation is a semi-classical description of the transport of a system of particles where all the information about the state of the system is carried by its distribution function $f_{\boldsymbol{k}}(\boldsymbol{r},t)$, where $\boldsymbol{k}$, $\boldsymbol{r}$, and t denote the system's momentum, position, and time, respectively. The distribution function of a system of fermions or bosons at equilibrium are the well-known Fermi-Dirac and Bose-Einstein distributions respectively, which in the context of transport are typically denoted by the equilibrium distribution function $f^0_{\boldsymbol{k}}(\boldsymbol{r})$. There are three main processes that can affect the time-evolution of the distribution function $f_{\boldsymbol{k}}(\boldsymbol{r},t)$: diffusion, drift, and scattering. As a result, the time-evolution of a system's distribution function under the influence of these processes can be explicitly represented by

$$\frac{\partial}{\partial t} f_{\boldsymbol{k}}(\boldsymbol{r},t) = \frac{\partial}{\partial t} f_{\boldsymbol{k}}(\boldsymbol{r},t)\bigg|_{\text{Diff}} + \frac{\partial}{\partial t} f_{\boldsymbol{k}}(\boldsymbol{r},t)\bigg|_{\text{Drift}} + \frac{\partial}{\partial t} f_{\boldsymbol{k}}(\boldsymbol{r},t)\bigg|_{\text{Scatt}} \tag{A.1.1}$$

A.1.1 Diffusion-induced evolution

If a system in state $\boldsymbol{k}$, such as a Bloch wave, is moving with a group velocity $\boldsymbol{v_k} = \hbar \boldsymbol{k} \left(M\right)^{-1}$, it can be inferred that the system's distribution function at an infinitesimally-small time t and position $\boldsymbol{r}$ is $f_{\boldsymbol{k}}\left(\boldsymbol{r}, t\right)$, it will not be very different from its value at $t = 0$ and at position $\boldsymbol{r} - \boldsymbol{v_k} t$ as

$$f_{\boldsymbol{k}}\left(\boldsymbol{r}, t\right) \;=\; f_{\boldsymbol{k}}\left(\boldsymbol{r} - \boldsymbol{v_k} t, 0\right) \tag{A.1.2}$$

which can be Taylor expanded about $t = 0$ to first order yielding

$$\begin{aligned} \cancel{f_{\boldsymbol{k}}\left(\boldsymbol{r}, 0\right)} + \frac{\partial}{\partial t} f_{\boldsymbol{k}}\left(\boldsymbol{r}, 0\right) t + \mathcal{O}\left(t^2\right) \;&=\; \cancel{f_{\boldsymbol{k}}\left(\boldsymbol{r}, 0\right)} \\ &+\; \underbrace{\left[\frac{\partial}{\partial\left(\boldsymbol{r} - \boldsymbol{v_k} t\right)} f_{\boldsymbol{k}}\left(\boldsymbol{r}, 0\right)\right]}_{\nabla f_{\boldsymbol{k}}(\boldsymbol{r}, 0)} \cdot \underbrace{\left[\frac{\partial}{\partial t}\left(\boldsymbol{r} - \boldsymbol{v_k} t\right) t\right]}_{-\boldsymbol{v_k}} \\ &+\; \mathcal{O}\left(t^2\right) \end{aligned}$$

$$\left.\frac{\partial}{\partial t} f_{\boldsymbol{k}}\left(\boldsymbol{r}, 0\right)\right|_{\text{Diff}} = -\boldsymbol{v_k} \cdot \nabla f_{\boldsymbol{k}}\left(\boldsymbol{r}, 0\right) \tag{A.1.3}$$

A.1.2 Drift-induced evolution

The presence of electric or magnetic fields will cause the distribution function's momentum to evolve in time. Similarly, considering the distribution function of a system in state $\boldsymbol{k}$ at an infinitesimally small time $\boldsymbol{t}$ and position $\boldsymbol{r}$, it can also be inferred that the distribution function will not be very different from its value at time $t = 0$ and in state $\boldsymbol{k} - \dot{\boldsymbol{k}} t$ before the fields acted upon the system as

$$f_{\boldsymbol{k}}(\boldsymbol{r},t) = f_{\boldsymbol{k}-\dot{\boldsymbol{k}}t}(\boldsymbol{r},0) \tag{A.1.4}$$

which can also be Taylor expanded about $t = 0$ to obtain

$$\begin{aligned} \cancel{f_{\boldsymbol{k}}(\boldsymbol{r},0)} + \frac{\partial}{\partial t} f_{\boldsymbol{k}}(\boldsymbol{r},0)\, t + \mathcal{O}\left(t^2\right) &= \cancel{f_{\boldsymbol{k}}(\boldsymbol{r},0)} \\ &+ \underbrace{\left[\frac{\partial}{\partial\left(\boldsymbol{k}-\dot{\boldsymbol{k}}t\right)} f_{\boldsymbol{k}}(\boldsymbol{r},0)\right]}_{\nabla_{\boldsymbol{k}} f_{\boldsymbol{k}}(\boldsymbol{r},0)} \cdot \underbrace{\left[\frac{\partial}{\partial t}\left(\boldsymbol{k}-\dot{\boldsymbol{k}}t\right) t\right]}_{-\dot{\boldsymbol{k}}} \\ &+ \mathcal{O}\left(t^2\right) \end{aligned}$$

$$\frac{\partial}{\partial t} f_{\boldsymbol{k}}(\boldsymbol{r},0) = -\nabla_{\boldsymbol{k}} f_{\boldsymbol{k}}(\boldsymbol{r},0) \cdot \dot{\boldsymbol{k}} \tag{A.1.5}$$

Considering the semi-classical equation of motion given by

$$\begin{aligned} \boldsymbol{F} &= \frac{\partial \boldsymbol{p}}{\partial t} \\ &= \hbar \frac{\partial \boldsymbol{k}}{\partial t} \\ \frac{\partial \boldsymbol{k}}{\partial t} &= \frac{\boldsymbol{F}}{\hbar} \end{aligned}$$

where $\boldsymbol{F}$ is the Lorentz force, the drift-induced evolution (or drift) of the system's distribution function becomes

$$\left.\frac{\partial}{\partial t} f_{\boldsymbol{k}}(\boldsymbol{r},t)\right|_{\text{Drift}} = -\frac{1}{\hbar}\nabla_{\boldsymbol{k}} f_{\boldsymbol{k}}(\boldsymbol{r},0)\cdot\boldsymbol{F} \tag{A.1.6}$$

A.1.3 Scattering-induced evolution

Scattering can change the system's momentum (elastic scattering) and energy (inelastic scattering). If the scattering events are considered to be local and instantaneous, elastic scattering will take a particle from a state with momentum $\boldsymbol{k}'$ into a state with momentum $\boldsymbol{k}$. So, if the scattering rate is denoted by $W(\boldsymbol{k}',\boldsymbol{k})$, the time evolution of the distribution function $f_{\boldsymbol{k}}(\boldsymbol{r},t)$ due to elastic scattering is given by

$$\frac{\partial}{\partial t} f_{\boldsymbol{k}}(\boldsymbol{r},t) = \int \frac{d^3k}{(2\pi)^3}\left[f_{\boldsymbol{k}'}(1-f_{\boldsymbol{k}})W(\boldsymbol{k}',\boldsymbol{k}) - f_{\boldsymbol{k}}(1-f_{\boldsymbol{k}'})W(\boldsymbol{k},\boldsymbol{k}')\right] \tag{A.1.7}$$

where the first term in the integral represents the scattering from an occupied state $\boldsymbol{k}'$ into an empty state $\boldsymbol{k}$, and the second term is the loss from state $\boldsymbol{k}$ into state $\boldsymbol{k}'$ also due to scattering. While the transition rate $W(\boldsymbol{k},\boldsymbol{k}')$ can be calculated under certain conditions, the analysis of transport can be greatly simplified by making an assumption that is known as the relaxation time approximation or RTA[176]. This assumption considers the deviation of the distribution function $f_{\boldsymbol{k}}(\boldsymbol{r},t)$ from the equilibrium case $f^0_{\boldsymbol{k}}(\boldsymbol{r})$. Specifically, the deviation from equilibrium is denoted by

$$g_{\boldsymbol{k}}(\boldsymbol{r},t) = f_{\boldsymbol{k}}(\boldsymbol{r},t) - f^0_{\boldsymbol{k}}(\boldsymbol{r}) \tag{A.1.8}$$

and the RTA approximation describes the time-evolution of $g_{\boldsymbol{k}}(\boldsymbol{r},t)$ as a simple exponential decay

$$\frac{\partial}{\partial t} g_{\boldsymbol{k}}(\boldsymbol{r},t) = -\frac{g_{\boldsymbol{k}}(\boldsymbol{r},t)}{\tau} \tag{A.1.9}$$

which implies that

$$\begin{aligned} \frac{\partial}{\partial t}\left[f_{\boldsymbol{k}}(\boldsymbol{r},t) - f^0_{\boldsymbol{k}}(\boldsymbol{r})\right] &= -\frac{f_{\boldsymbol{k}}(\boldsymbol{r},t) - f^0_{\boldsymbol{k}}(\boldsymbol{r})}{\tau} \\ \left.\frac{\partial}{\partial t} f_{\boldsymbol{k}}(\boldsymbol{r},t)\right|_{\text{Scatt}} &= -\frac{f_{\boldsymbol{k}}(\boldsymbol{r},t) - f^0_{\boldsymbol{k}}(\boldsymbol{r})}{\tau} \end{aligned} \tag{A.1.10}$$

where $\frac{\partial}{\partial t} f^0_{\boldsymbol{k}}(\boldsymbol{r}) = 0$ by definition of thermal equilibrium, and τ represents the relaxation time constant as a result of scattering.

As a result of the three main processes that contribute to the evolution of the system's distribution function, the Boltzmann transport equation with the relaxation time approximation Eq.A.1.1 can be recast

$$\frac{\partial}{\partial t} f_{\boldsymbol{k}}(\boldsymbol{r},t) = -\boldsymbol{v}_{\boldsymbol{k}} \cdot \nabla f_{\boldsymbol{k}}(\boldsymbol{r},t) - \frac{1}{\hbar}\nabla_{\boldsymbol{k}} f_{\boldsymbol{k}}(\boldsymbol{r},t) \cdot \boldsymbol{F} - \frac{f_{\boldsymbol{k}}(\boldsymbol{r},t) - f^0_{\boldsymbol{k}}(\boldsymbol{r})}{\tau} \tag{A.1.11}$$

A.2 Balance equations

Though physically insightful, the form of the Boltzmann transport equation given by Eq.A.1.11 is not very useful to calculate transport parameters of interest. In the context of exciton transport in monolayer transition metal di-chalcogenides (TMDs), the time evolution of the exciton (or carrier) density is the quantity of interest. As a result, the Boltzmann transport equation can be used to solve the time evolution of the carrier density, and one way to do so is by the so-called method of moments[176]. In this method, the moment $\Theta(\boldsymbol{k})$ is conveniently defined to obtain a physical quantity of interest after multiplying it by the system's

distribution function and integrating them over the entire volume of interest in the relevant coordinate system. In k-space, accordingly, Eq.A.1.11 can be re-written as

$$\begin{aligned}\int \frac{d^3k}{(2\pi)^3}\Theta(\boldsymbol{k})\frac{\partial}{\partial t}f_{\boldsymbol{k}}(\boldsymbol{r},t) &= -\int \frac{d^3k}{(2\pi)^3}\Theta(\boldsymbol{k})\left[\boldsymbol{v}_{\boldsymbol{k}}\cdot\nabla f_{\boldsymbol{k}}(\boldsymbol{r},t)\right] \\ &\quad -\int \frac{d^3k}{(2\pi)^3}\Theta(\boldsymbol{k})\left[\frac{1}{\hbar}\nabla_{\boldsymbol{k}} f_{\boldsymbol{k}}(\boldsymbol{r},t)\cdot\boldsymbol{F}\right] \\ &\quad -\int \frac{d^3k}{(2\pi)^3}\Theta(\boldsymbol{k})\left[\frac{f_{\boldsymbol{k}}(\boldsymbol{r},t)-f^0_{\boldsymbol{k}}(\boldsymbol{r})}{\tau}\right] \end{aligned} \tag{A.2.1}$$

where the factor of $1/(2\pi)^3$accounts for the k-space volume occupied by each state. The left hand side of Eq.A.2.1 can be rewritten as

$$\begin{aligned}\int \frac{d^3k}{(2\pi)^3}\Theta(\boldsymbol{k})\frac{\partial}{\partial t}f_{\boldsymbol{k}}(\boldsymbol{r},t) &= \frac{\partial}{\partial t}\underbrace{\left[\int \frac{d^3k}{(2\pi)^3}\Theta(\boldsymbol{k})f_{\boldsymbol{k}}(\boldsymbol{r},t)\right]}_{\equiv n_\Theta(\boldsymbol{r},t)} \\ &= \frac{\partial}{\partial t}n_\Theta(\boldsymbol{r},t) \end{aligned} \tag{A.2.2}$$

where

$$n_\Theta(\boldsymbol{r},t) \equiv \int \frac{d^3k}{(2\pi)^3}\Theta(\boldsymbol{k})f_{\boldsymbol{k}}(\boldsymbol{r},t) \tag{A.2.3}$$

Similarly, each of the terms on the right hand side of Eq.A.2.1 can be recast as Eq.A.2.2, starting with the first term

$$\int \frac{d^3k}{(2\pi)^3}\Theta(\boldsymbol{k}) \underbrace{[\boldsymbol{v_k}\cdot\nabla f_{\boldsymbol{k}}(\boldsymbol{r},t)]}_{\nabla\cdot[f_{\boldsymbol{k}}(\boldsymbol{r},t)\boldsymbol{v_k}]-f_{\boldsymbol{k}}(\boldsymbol{r},t)\nabla\cdot\boldsymbol{v_k}} = \int \frac{d^3k}{(2\pi)^3}\Theta(\boldsymbol{k})\left\{\nabla\cdot[f_{\boldsymbol{k}}(\boldsymbol{r},t)\,\boldsymbol{v_k}]-f_{\boldsymbol{k}}(\boldsymbol{r},t)\,\nabla\cdot\boldsymbol{v_k}\right\}$$

$$= \nabla.\underbrace{\left[\int \frac{d^3k}{(2\pi)^3}\Theta(\boldsymbol{k})f_{\boldsymbol{k}}(\boldsymbol{r},t)\,\boldsymbol{v_k}\right]}_{\equiv\mathcal{F}_\Theta(\boldsymbol{r},t)} - \underbrace{\int \frac{d^3k}{(2\pi)^3}\Theta(\boldsymbol{k})f_{\boldsymbol{k}}(\boldsymbol{r},t)\,\nabla\cdot\boldsymbol{v_k}}_{\equiv S_\Theta(\boldsymbol{r},t)}$$

$$= \nabla.\mathcal{F}_\Theta(\boldsymbol{r},t) - S_\Theta(\boldsymbol{r},t) \tag{A.2.4}$$

where

$$\mathcal{F}_\Theta(\boldsymbol{r},t) \equiv \int \frac{d^3k}{(2\pi)^3}\Theta(\boldsymbol{k})f_{\boldsymbol{k}}(\boldsymbol{r},t)\,\boldsymbol{v_k} \tag{A.2.5}$$

$$S_\Theta(\boldsymbol{r},t) \equiv \int \frac{d^3k}{(2\pi)^3}\Theta(\boldsymbol{k})f_{\boldsymbol{k}}(\boldsymbol{r},t)\,\nabla\cdot\boldsymbol{v_k} \tag{A.2.6}$$

The second term in Eq.A.2.1 can be recast as

$$\int \frac{d^3k}{(2\pi)^3}\Theta(\boldsymbol{k})\left[\frac{1}{\hbar}\nabla_{\boldsymbol{k}}f_{\boldsymbol{k}}(\boldsymbol{r},t)\cdot\boldsymbol{F}\right]$$

$$= \frac{1}{\hbar}\int \frac{d^3k}{(2\pi)^3} \underbrace{\Theta(\boldsymbol{k})\left[\nabla_{\boldsymbol{k}}f_{\boldsymbol{k}}(\boldsymbol{r},t)\cdot\boldsymbol{F}\right]}_{\nabla_{\boldsymbol{k}}\cdot[f_{\boldsymbol{k}}(\boldsymbol{r},t)\Theta(\boldsymbol{k})\boldsymbol{F}]-f_{\boldsymbol{k}}(\boldsymbol{r},t)\nabla_{\boldsymbol{k}}\cdot[\Theta(\boldsymbol{k})\boldsymbol{F}]}$$

$$= \frac{1}{\hbar}\left\{\underbrace{\int \frac{d^3k}{(2\pi)^3}\nabla_{\boldsymbol{k}}\cdot[f_{\boldsymbol{k}}(\boldsymbol{r},t)\,\Theta(\boldsymbol{k})\boldsymbol{F}]}_{=0} - \int \frac{d^3k}{(2\pi)^3}f_{\boldsymbol{k}}(\boldsymbol{r},t) \underbrace{\nabla_{\boldsymbol{k}}\cdot[\Theta(\boldsymbol{k})\boldsymbol{F}]}_{\Theta(\boldsymbol{k})\nabla_{\boldsymbol{k}}\cdot\boldsymbol{F}+\boldsymbol{F}\cdot\nabla_{\boldsymbol{k}}\Theta(\boldsymbol{k})}\right\}$$

$$= -\frac{1}{\hbar}\int \frac{d^3k}{(2\pi)^3}f_{\boldsymbol{k}}(\boldsymbol{r},t)\left[\Theta(\boldsymbol{k})\nabla_{\boldsymbol{k}}\cdot\boldsymbol{F}+\boldsymbol{F}\cdot\nabla_{\boldsymbol{k}}\Theta(\boldsymbol{k})\right] \tag{A.2.7}$$

where the integral above goes to zero because the distribution function approaches zero at

a surface at infinity, i.e. $f_{\boldsymbol{k}}(\boldsymbol{r},t) \to 0$ as $|\boldsymbol{k}| \to \infty$. Notice that the external force $\boldsymbol{F}$ causing the system to drift can be rewritten in terms of the system's energy, i.e.$\boldsymbol{F} = -\nabla E_{\boldsymbol{k}}$. So, the first term in Eq.A.2.7 that contains the momentum divergence of the external force $\nabla_{\boldsymbol{k}} \cdot \boldsymbol{F}$ can be rewritten as $\nabla_{\boldsymbol{k}} \cdot \boldsymbol{F} = -\nabla_{\boldsymbol{k}} \cdot \nabla E_{\boldsymbol{k}} = -\nabla \cdot \nabla_{\boldsymbol{k}} E_{\boldsymbol{k}}$ where the order of differentiation of the energy does not matter. Notice that in the context of semiconductors, the momentum gradient of the energy is proportional to the carrier's group velocity $\boldsymbol{v_k}$ assuming that the excitons have a free-particle dispersion given by

$$\begin{aligned} E_{\boldsymbol{k}} &= \frac{\hbar^2 |\boldsymbol{k}|^2}{2M} = \frac{1}{2} M |\boldsymbol{v_k}|^2 \\ \nabla_{\boldsymbol{k}} E_{\boldsymbol{k}} &= \frac{\hbar^2}{M} \boldsymbol{k} = \frac{\hbar^2}{M} \left(\frac{M}{\hbar} \boldsymbol{v_k} \right) \\ &= \hbar \boldsymbol{v_k} \end{aligned} \tag{A.2.8}$$

where M is the translational mass, and so $\nabla_{\boldsymbol{k}} \cdot \boldsymbol{F} = -\nabla \cdot \nabla_{\boldsymbol{k}} E_{\boldsymbol{k}} = -\hbar \nabla \cdot \boldsymbol{v_k}$. Substituting this result back into Eq.A.2.7 yields

$$\begin{aligned} -\frac{1}{\hbar} \int \frac{d^3k}{(2\pi)^3} f_{\boldsymbol{k}}(\boldsymbol{r},t) \left[\Theta(\boldsymbol{k}) \nabla_{\boldsymbol{k}} \cdot \boldsymbol{F} + \boldsymbol{F} \cdot \nabla_{\boldsymbol{k}} \Theta(\boldsymbol{k}) \right] \\ = \underbrace{\int \frac{d^3k}{(2\pi)^3} f_{\boldsymbol{k}}(\boldsymbol{r},t)\, \Theta(\boldsymbol{k}) \nabla \cdot \boldsymbol{v_k}}_{=S_\Theta(\boldsymbol{r},t)} - \underbrace{\frac{1}{\hbar} \int \frac{d^3k}{(2\pi)^3} f_{\boldsymbol{k}}(\boldsymbol{r},t)\, \boldsymbol{F} \cdot \nabla_{\boldsymbol{k}} \Theta(\boldsymbol{k})}_{\equiv G_\Theta(\boldsymbol{r},t)} \\ = S_\Theta(\boldsymbol{r},t) - G_\Theta(\boldsymbol{r},t) \end{aligned} \tag{A.2.9}$$

where

$$G_\Theta(\boldsymbol{r},t) \equiv \frac{1}{\hbar} \int \frac{d^3k}{(2\pi)^3} f_{\boldsymbol{k}}(\boldsymbol{r},t)\, \boldsymbol{F} \cdot \nabla_{\boldsymbol{k}} \Theta(\boldsymbol{k}) \tag{A.2.10}$$

Lastly, the third term in Eq.A.2.1 can be recast at

$$\begin{aligned} R_{\Theta}(\boldsymbol{r},t) &= \int \frac{d^3k}{(2\pi)^3}\Theta(\boldsymbol{k})\left[\frac{f_{\boldsymbol{k}}(\boldsymbol{r},t)-f^0_{\boldsymbol{k}}(\boldsymbol{r})}{\tau}\right] \\ &= \frac{n_{\Theta}(\boldsymbol{r},t)-n^0_{\Theta}(\boldsymbol{r})}{\tau} \end{aligned} \tag{A.2.11}$$

With Eq.A.2.2-Eq.A.2.11, the Boltzmann transport equation Eq.A.1.11 can be recast as

$$\frac{\partial}{\partial t}n_{\Theta}(\boldsymbol{r},t) = \nabla.\mathcal{F}_{\Theta}(\boldsymbol{r},t)+G_{\Theta}(\boldsymbol{r},t)-R_{\Theta}(\boldsymbol{r},t) \tag{A.2.12}$$

which has the same form as the well-known balance equation with generation and recombination terms that is typically used in the analysis of optoelectronic devices [176]. Specifically, the first, second and third terms on the right hand side of Eq.A.2.12 represent the flux, generation, and recombination associated with $n_{\Theta}(\boldsymbol{r},t)$, which is explicitly defined in Eq.A.2.3.

A.2.1 Continuity equation

Using the form of the Boltzmann transport equation given by Eq.A.2.12, the moment $\Theta(\boldsymbol{k})$ can be conveniently chosen to obtain the physical quantities of interest. For example, if $\Theta(\boldsymbol{k})=1$, Eq.A.2.12 yields

$$\frac{\partial}{\partial t}n(\boldsymbol{r},t) = \nabla.\mathcal{F}(\boldsymbol{r},t)+G(\boldsymbol{r},t)-R(\boldsymbol{r},t) \tag{A.2.13}$$

where

$$
\begin{aligned}
n(\boldsymbol{r},t) &= \int \frac{d^3k}{(2\pi)^3} f_{\boldsymbol{k}}(\boldsymbol{r},t) && \text{(A.2.14)}\\
\mathcal{F}(\boldsymbol{r},t) &= \int \frac{d^3k}{(2\pi)^3} f_{\boldsymbol{k}}(\boldsymbol{r},t)\,\boldsymbol{v}_{\boldsymbol{k}} && \text{(A.2.15)}\\
G(\boldsymbol{r},t) &= \frac{1}{\hbar}\int \frac{d^3k}{(2\pi)^3} f_{\boldsymbol{k}}(\boldsymbol{r},t)\,\boldsymbol{F}\cdot\nabla_{\boldsymbol{k}}(1) = 0 && \text{(A.2.16)}\\
R(\boldsymbol{r},t) &= \frac{n(\boldsymbol{r},t) - n^0(\boldsymbol{r})}{\tau} && \text{(A.2.17)}
\end{aligned}
$$

and $n(\boldsymbol{r},t)$ and $n^0(\boldsymbol{r})$ are simply the non-equilibrium and equilibrium exciton densities, respectively. The flux term is related to the average velocity as

$$
\begin{aligned}
\mathcal{F}(\boldsymbol{r},t) &= \int \frac{d^3k}{(2\pi)^3} f_{\boldsymbol{k}}(\boldsymbol{r},t)\,\boldsymbol{v}_{\boldsymbol{k}}\\
&= n(\boldsymbol{r},t)\underbrace{\int d^3k f_{\boldsymbol{k}}(\boldsymbol{r},t)\,\boldsymbol{v}_{\boldsymbol{k}}}_{=\bar{\boldsymbol{u}}(\boldsymbol{r},t)}\\
&= n(\boldsymbol{r},t)\,\bar{\boldsymbol{u}}(\boldsymbol{r},t) && \text{(A.2.18)}
\end{aligned}
$$

Substituting this result back into the Boltzmann equation for the exciton density, and recalling that $G(\boldsymbol{r},t) = 0$ yields

$$
\frac{\partial}{\partial t} n(\boldsymbol{r},t) = \nabla.\left[n(\boldsymbol{r},t)\,\bar{\boldsymbol{u}}(\boldsymbol{r},t)\right] - \frac{n(\boldsymbol{r},t) - n^0(\boldsymbol{r})}{\tau} \qquad \text{(A.2.19)}
$$

which is the well-known continuity equation with the relaxation time approximation.

A.2.2 Drift diffusion and recombination equation

Since the time evolution of the exciton concentration under the influence of strain, fields, concentration, or temperature gradients is the quantity of interest, the Boltzmann transport

equation in the form given by Eq.A.2.12 with the moment defined as $\Theta(\boldsymbol{k}) = \boldsymbol{v_k}$ should be solved. Accordingly, the density, flux, generation, and recombination terms are respectively given by

$$
\begin{aligned}
n_{\boldsymbol{v_k}}(\boldsymbol{r},t) &= \int \frac{d^3k}{(2\pi)^3} f_{\boldsymbol{k}}(\boldsymbol{r},t)\,\boldsymbol{v_k} = n(\boldsymbol{r},t)\,\bar{\boldsymbol{u}}(\boldsymbol{r},t) && \text{(A.2.20)}\\
\mathcal{F}_{\boldsymbol{v_k}}(\boldsymbol{r},t) &= \int \frac{d^3k}{(2\pi)^3} f_{\boldsymbol{k}}(\boldsymbol{r},t)\,\boldsymbol{v_k}\boldsymbol{v_k} && \text{(A.2.21)}\\
G_{\boldsymbol{v_k}}(\boldsymbol{r},t) &= \frac{1}{\hbar}\int \frac{d^3k}{(2\pi)^3} f_{\boldsymbol{k}}(\boldsymbol{r},t)\,\boldsymbol{F}\cdot\nabla_{\boldsymbol{k}}\boldsymbol{v_k} && \text{(A.2.22)}\\
R_{\boldsymbol{v_k}}(\boldsymbol{r},t) &= \frac{n_{\boldsymbol{v_k}}(\boldsymbol{r},t) - n^0_{\boldsymbol{v_k}}(\boldsymbol{r})}{\tau} && \text{(A.2.23)}
\end{aligned}
$$

where by definition of thermal equilibrium, the average velocity $\bar{\boldsymbol{u}}^0(\boldsymbol{r})$ of a system described by the equilibrium distribution$f^0_{\boldsymbol{k}}(\boldsymbol{r})$ is zero. The product $\boldsymbol{v_k}\boldsymbol{v_k}$ is a rank-2 tensor given by the dyadic product [38]

$$\boldsymbol{v_k}\boldsymbol{v_k} = \boldsymbol{v_k}\otimes\boldsymbol{v_k} = \sum_{i,j} v_{k_i}v_{k_j}\hat{\boldsymbol{e}}_i\otimes\hat{\boldsymbol{e}}_j \qquad \text{(A.2.24)}$$

If the band is isotropic, the translational mass is a diagonal tensor with elements given by $[M^{-1}(\boldsymbol{k})]_{i,j} = (1/M)\,\delta_{i,j}$, the velocity is direction independent, i.e. $v_{k_i} = v_{k_m}\forall i$, and the product $\boldsymbol{v_k}\otimes\boldsymbol{v_k}$ simplifies to

$$\boldsymbol{v_k}\otimes\boldsymbol{v_k} = \sum_{i,j} v^2_{k_m}\delta_{i,j}\hat{\boldsymbol{e}}_i\otimes\hat{\boldsymbol{e}}_j = v^2_{k_m}\underbrace{\sum_i \hat{\boldsymbol{e}}_i\otimes\hat{\boldsymbol{e}}_i}_{\mathbb{1}} = v^2_{k_m} \qquad \text{(A.2.25)}$$

In addition, given the free-particle and isotropic translational mass assumptions, the energy is given by $E_{\boldsymbol{k}} = \frac{1}{2}M\left|\boldsymbol{v_k}\right|^2$, and $E_{k_i} = E_{k_m}\forall i$. The total energy is simply the sum of the energies along all directions, i.e. $E_{\boldsymbol{k}} = \sum_i E_{k_i} = 3E_{k_m} = \frac{3}{2}Mv^2_{k_m}$, and so $v^2_{k_m} = \frac{2}{3M}E_{\boldsymbol{k}}$,

which means that the dyadic product $\boldsymbol{v_k v_k}$ simplifies to $\boldsymbol{v_k v_k} = \frac{2E_{\boldsymbol{k}}}{3M}$, and the flux term in Eq.A.2.21 becomes

$$\begin{aligned}
\mathcal{F}_{\boldsymbol{v_k}}(\boldsymbol{r},t) &= \int \frac{d^3k}{(2\pi)^3} f_{\boldsymbol{k}}(\boldsymbol{r},t)\,\boldsymbol{v_k v_k} \\
&= \frac{2}{3M}\int \frac{d^3k}{(2\pi)^3} f_{\boldsymbol{k}}(\boldsymbol{r},t)\,E_{\boldsymbol{k}} \\
&= \frac{2}{3M} n(\boldsymbol{r},t) \underbrace{\int d^3k f_{\boldsymbol{k}}(\boldsymbol{r},t)\,E_{\boldsymbol{k}}}_{\bar{E}} \\
&= \frac{2\bar{E}}{3M} n(\boldsymbol{r},t) \qquad \text{(A.2.26)}
\end{aligned}$$

where $\bar{E}$ denotes the average energy of the excitons, which can be expressed in terms of temperature as $\bar{E} = \frac{3}{2}k_B T$. Note that the quantity of interest in the balance equation is the divergence of the flux term $\mathcal{F}(\boldsymbol{r},t)$, and so

$$\begin{aligned}
\nabla\cdot\mathcal{F}_{\boldsymbol{v_k}}(\boldsymbol{r},t) &= \frac{2}{3M}\nabla\cdot\left[\bar{E}n(\boldsymbol{r},t)\right] \\
&= \frac{k_B}{M}\nabla\cdot\left[Tn(\boldsymbol{r},t)\right] \\
&= \frac{k_B}{M}\sum_{i,j}\frac{\partial}{\partial r_i}\left[Tn(\boldsymbol{r},t)\right]\hat{\boldsymbol{e}}_i\cdot\hat{\boldsymbol{e}}_j\otimes\hat{\boldsymbol{e}}_j \\
&= \frac{k_B}{M}\nabla\left[Tn(\boldsymbol{r},t)\right] \qquad \text{(A.2.27)}
\end{aligned}$$

Similarly, the generation term in Eq.A.2.22, the term $\nabla_{\boldsymbol{k}}\boldsymbol{v_k}$ is also a second-order tensor which is given by the dyadic product (with the isotropic band assumption)

$$\begin{aligned}
\nabla_{\boldsymbol{k}}\boldsymbol{v}_{\boldsymbol{k}} &= \nabla_{\boldsymbol{k}} \otimes \boldsymbol{v}_{\boldsymbol{k}} \\
&= \sum_{i,j} \frac{\partial v_{k_i}}{\partial k_j} \hat{\boldsymbol{e}}_i \otimes \hat{\boldsymbol{e}}_j \\
&= \hbar \sum_{i,j} \left[M^{-1}\left(\boldsymbol{k}\right)\right]_{i,j} \hat{\boldsymbol{e}}_i \otimes \hat{\boldsymbol{e}}_j \\
&= \hbar \sum_{i,j} \left[1/M\right] \delta_{i,j} \hat{\boldsymbol{e}}_i \otimes \hat{\boldsymbol{e}}_j \\
&= \frac{\hbar}{M}
\end{aligned} \tag{A.2.28}$$

and the generation term becomes

$$\begin{aligned}
G_{\boldsymbol{v}_{\boldsymbol{k}}}\left(\boldsymbol{r},t\right) &= \frac{1}{\hbar}\int \frac{d^3k}{\left(2\pi\right)^3} f_{\boldsymbol{k}}\left(\boldsymbol{r},t\right) \boldsymbol{F} \cdot \nabla_{\boldsymbol{k}}\boldsymbol{v}_{\boldsymbol{k}} \\
&= \frac{\boldsymbol{F}}{M}\int \frac{d^3k}{\left(2\pi\right)^3} f_{\boldsymbol{k}}\left(\boldsymbol{r},t\right) \\
&= \frac{\boldsymbol{F}}{M} n\left(\boldsymbol{r},t\right)
\end{aligned} \tag{A.2.29}$$

As a result, substituting the density, flux, generation, and recombination terms specified by Eq.A.2.21, Eq.A.2.22, and Eq.A.2.23, respectively, back into the Boltzmann transport equation given by Eq.A.2.12 yields

$$\frac{\partial}{\partial t}\left[n\left(\boldsymbol{r},t\right)\bar{\boldsymbol{u}}\left(\boldsymbol{r},t\right)\right] = -\frac{k_B}{M}\nabla\left[Tn\left(\boldsymbol{r},t\right)\right] + \frac{\boldsymbol{F}}{M} n\left(\boldsymbol{r},t\right) - \frac{n\left(\boldsymbol{r},t\right)\bar{\boldsymbol{u}}\left(\boldsymbol{r},t\right)}{\tau} \tag{A.2.30}$$

which is a balance equation for the quantity $n\left(\boldsymbol{r},t\right)\bar{\boldsymbol{u}}\left(\boldsymbol{r},t\right)$. Note that by taking the divergence on both sides of Eq.A.2.30, the resulting continuity equation given by Eq.A.2.19 can be used as follows

$$
\begin{aligned}
\nabla \cdot \left\{ \frac{\partial}{\partial t} \left[n\left(\boldsymbol{r},t\right) \bar{\boldsymbol{u}}\left(\boldsymbol{r},t\right) \right] \right\} &= \nabla \cdot \left\{ -\frac{k_B}{M} \nabla \left[Tn\left(\boldsymbol{r},t\right) \right] + \frac{\boldsymbol{F}}{M} n\left(\boldsymbol{r},t\right) - \frac{n\left(\boldsymbol{r},t\right) \bar{\boldsymbol{u}}\left(\boldsymbol{r},t\right)}{\tau} \right\} \\
\frac{\partial}{\partial t} \left\{ \nabla \cdot \left[n\left(\boldsymbol{r},t\right) \bar{\boldsymbol{u}}\left(\boldsymbol{r},t\right) \right] \right\} &= -\frac{k_B}{M} \nabla^2 \left[Tn\left(\boldsymbol{r},t\right) \right] \\
&\quad + \frac{1}{M} \nabla \cdot \left[\boldsymbol{F} n\left(\boldsymbol{r},t\right) \right] \\
&\quad - \frac{1}{\tau} \nabla \cdot \left[n\left(\boldsymbol{r},t\right) \bar{\boldsymbol{u}}\left(\boldsymbol{r},t\right) \right] \\
\nabla \cdot \left[n\left(\boldsymbol{r},t\right) \bar{\boldsymbol{u}}\left(\boldsymbol{r},t\right) \right] &= -\tau \frac{\partial}{\partial t} \left\{ \nabla \cdot \left[n\left(\boldsymbol{r},t\right) \bar{\boldsymbol{u}}\left(\boldsymbol{r},t\right) \right] \right\} - \frac{k_B \tau}{M} \nabla^2 \left[Tn\left(\boldsymbol{r},t\right) \right] \\
&\quad + \frac{\tau}{M} \nabla \cdot \left[\boldsymbol{F} n\left(\boldsymbol{r},t\right) \right] \\
-\frac{\partial}{\partial t} n\left(\boldsymbol{r},t\right) - \frac{n\left(\boldsymbol{r},t\right) - n^0\left(\boldsymbol{r}\right)}{\tau} &= \\
\frac{\partial}{\partial t} n\left(\boldsymbol{r},t\right) &= -\frac{n\left(\boldsymbol{r},t\right) - n^0\left(\boldsymbol{r}\right)}{\tau} \\
&\quad + \tau \frac{\partial}{\partial t} \left\{ \nabla \cdot \left[n\left(\boldsymbol{r},t\right) \bar{\boldsymbol{u}}\left(\boldsymbol{r},t\right) \right] \right\} \\
&\quad + \frac{k_B \tau}{M} \nabla^2 \left[Tn\left(\boldsymbol{r},t\right) \right] \\
&\quad - \frac{\tau}{M} \nabla \cdot \left[\boldsymbol{F} n\left(\boldsymbol{r},t\right) \right]
\end{aligned}
$$

which is a drift-diffusion equation for the carrier density $n\left(\boldsymbol{r},t\right)$ that has a similar structure to that of the Boltzmann transport equation given by Eq.A.2.3, where the first term on the right hand side is the recombination term with the relaxation time approximation. The second term resembles the flux term in the Boltzmann transport equation, the third term corresponds to the diffusion of excitons, and the last term corresponds to the drift under an external force. Notice that the second term is multiplied by the relaxation time, which is typically very small, and it can be neglected to further simplify this drift-diffusion equation to yield

$$
\frac{\partial}{\partial t} n\left(\boldsymbol{r},t\right) \approx -\frac{n\left(\boldsymbol{r},t\right) - n^0\left(\boldsymbol{r}\right)}{\tau} + \frac{k_B \tau}{M} \nabla^2 \left[Tn\left(\boldsymbol{r},t\right) \right] - \frac{\tau}{M} \nabla \cdot \left[\boldsymbol{F} n\left(\boldsymbol{r},t\right) \right] \quad \text{(A.2.31)}
$$

A.2.3 Strain-based drift

The effective force caused by the strain-induced change in the band structure of TMD monolayers can be expressed as

$$F = -\nabla E_{\boldsymbol{k}} = -\frac{\partial E_{\boldsymbol{k}}}{\partial \epsilon} \nabla \epsilon \left(\boldsymbol{r} \right) \tag{A.2.32}$$

where it is clear that the excitons will move in the direction of the strain gradient given that $\partial E_k / \partial \epsilon < 0$ for the $K - K$ valley as previously discussed and illustrated in Fig.2.2.4. The transport of excitons in monolayer TMDs under strain gradients can be represented by the balance equation given by Eq.4.3.1 where the external force $\boldsymbol{F}$ is simply given by Eq.A.2.32

$$\frac{\partial}{\partial t} n \left(\boldsymbol{r}, t \right) \approx -\frac{n \left(\boldsymbol{r}, t \right) - n^0 \left(\boldsymbol{r} \right)}{\tau} + \frac{k_B \tau}{M} \nabla^2 \left[T n \left(\boldsymbol{r}, t \right) \right] + \frac{\tau}{M} \frac{\partial E_{\boldsymbol{k}}}{\partial \epsilon} \nabla \cdot \left[\nabla \epsilon \left(\boldsymbol{r} \right) n \left(\boldsymbol{r}, t \right) \right] \tag{A.2.33}$$

Note that the equilibrium exciton distribution is zero as the relaxation term implies that the excitons recombine as $t \to \infty$ and so $n^0 \left(\boldsymbol{r} \right) = 0$. Also, if there are no temperature gradients, i.e. $\nabla T = 0$, the drift-diffusion equation Eq.A.2.33 becomes

$$\frac{\partial}{\partial t} n \left(\boldsymbol{r}, t \right) \approx -\frac{n \left(\boldsymbol{r}, t \right)}{\tau} + \underbrace{\frac{k_B T \tau}{M}}_{D} \nabla^2 n \left(\boldsymbol{r}, t \right) + \underbrace{\frac{\tau}{M} \frac{\partial E_{\boldsymbol{k}}}{\partial \epsilon}}_{\mu_\epsilon} \nabla \cdot \left[\nabla \epsilon \left(\boldsymbol{r} \right) n \left(\boldsymbol{r}, t \right) \right] \tag{A.2.34}$$

where $D \equiv \frac{k_B T \tau}{M}$ and $\mu_\epsilon \equiv \frac{\tau}{M} \frac{\partial E_{\boldsymbol{k}}}{\partial \epsilon}$ are the diffusion coefficient and strain mobility, respectively.

Appendix B

Derivation of Multi-Layer Structure Transfer Matrix

The details of the derivation of the transfer matrix of the dielectric structure shown in Fig.6.2.1 are discussed on this appendix. The expressions for the transfer matrix are found by enforcing the boundary conditions Eq.6.2.68 and Eq.6.2.70 across all of the boundaries of the multi-layer structure depicted in Fig.6.2.1. Assuming that the electric and magnetic fields are parallel to the interfaces and polarized along the $\hat{x}$and $\hat{y}$ directions, respectively, these boundary conditions and the auxiliary expressions Eq.6.2.71-Eq.6.2.76 lead to

$$\begin{aligned} E_{m_x}^{(+)}\left(z_{m,m-1},t\right) &= E_{m-1_x}^{(+)}\left(z_{m,m-1},t\right) \\ \sum_{j=P,pr} E_{m_{x_j}}^{(+)}\left(z_{m,m-1},t\right) &= \sum_{j=P,pr} E_{m-1_{x_j}}^{(+)}\left(z_{m,m-1},t\right) \\ E_{m_{x_j}}^{(+)}\left(z_{m,m-1},t\right) &= E_{m-1_{x_j}}^{(+)}\left(z_{m,m-1},t\right) \end{aligned} \tag{B.0.1}$$

and

$$
\begin{aligned}
H_{m_y}^{(+)}\left(z_{m,m-1},t\right) &= H_{m-1_y}^{(+)}\left(z_{m,m-1},t\right)-K_{m,m-1} \\
\sum_{j=P,pr} H_{m_{y_j}}^{(+)}\left(z_{m,m-1},t\right) &= \sum_{j=P,pr}\left[H_{m-1_{y_j}}^{(+)}\left(z_{m,m-1},t\right)-K_{m,m-1_j}\right] \\
H_{m_{y_j}}^{(+)}\left(z_{m,m-1},t\right) &= H_{m-1_{y_j}}^{(+)}\left(z_{m,m-1},t\right)-K_{m,m-1_j} \\
-\frac{i}{\mu_0\omega_j}\frac{\partial}{\partial z}E_{m_{x_j}}^{(+)}\left(z,t\right) &= -\frac{i}{\mu_0\omega_j}\frac{\partial}{\partial z}E_{m-1_{x_j}}^{(+)}\left(z,t\right)-\frac{\partial}{\partial t}P_j^{(+)}
\end{aligned}
\tag{B.0.2}
$$

where the macroscopic polarization at the interface between the top and bottom h-BN layers is given by

$$
\begin{aligned}
P^{(+)}\left(t\right) &= N_a\rho_{21}\left(t\right)\mu_{12} \\
&= \sum_{j=P,pr} N_a\mu_{12}\left[\left(\frac{-\chi_{R_j}}{\delta_j+i\gamma}\right)_{z=0}\right. \\
&\quad +\left(\xi_{PPpr}+\xi_{prPP}\right)\left(\chi_{R_P}\chi_{R_P}^{*}\chi_{R_{pr}}\right)_{z=0}\delta_{j,pr} \\
&\quad \left.+\left(\xi_{prprP}+\xi_{Pprpr}\right)\left(\chi_{R_{pr}}\chi_{R_P}^{*}\chi_{R_P}\right)_{z=0}\delta_{j,P}\right]e^{-i\omega_j t} \\
&= \sum_{j=P,pr}\tilde{P}_j^{(+)}e^{-i\omega_j t} \\
&= \sum_{j=P,pr}P_j^{(+)}\left(t\right)
\end{aligned}
\tag{B.0.3}
$$

with

$$
\begin{aligned}
\tilde{P}_j^{(+)} &\equiv N_a \mu_{12} \left[\left(\frac{-\chi_{R_j}}{\delta_j + i\gamma} \right)_{z=0} \right. \\
&\quad + \left(\xi_{PPpr} + \xi_{prPP}\right) \left(\chi_{R_P} \chi^*_{R_P} \chi_{R_{pr}}\right)_{z=0} \delta_{j,pr} \\
&\quad \left. + \left(\xi_{prprP} + \xi_{Pprpr}\right) \left(\chi_{R_{pr}} \chi^*_{R_P} \chi_{R_P}\right)_{z=0} \delta_{j,P} \right] \\
&= N_a \mu_{12} \left[-\frac{\mu_{21}}{2\hbar\left(\delta_j + i\gamma\right)} \left(E_{1_j} + E'_{1_j} \right) + \frac{\left|\mu_{21}\right|^2}{8\hbar^3} \mu_{21} \right. \\
&\quad \left. \times \left(\xi_{PPpr} + \xi_{prPP}\right) \left(E_{1_P} + E'_{1_P}\right) \left(E_{1_P} + E'_{1_P}\right)^* \left(E_{1_{pr}} + E'_{1_{pr}}\right) \delta_{j,pr} \right] \\
&= -\frac{\zeta}{2\mu_0 c\gamma} \frac{\left(x_j - i\right)}{\left(x_j^2 + 1\right)} \\
&\quad \times \left[\left(E_{1_j} + E'_{1_j} \right) - \left(x_j + i\right) \left(\eta_{PPpr} + \eta_{prPP}\right) \Theta_P \left(E_{1_{pr}} + E'_{1_{pr}} \right) \delta_{j,pr} \right] \quad \text{(B.0.4)}
\end{aligned}
$$

The time derivative of the macroscopic polarization is generally given by

$$
\begin{aligned}
\frac{\partial}{\partial t} P^{(+)}(t) &= \frac{\partial}{\partial t} \sum_{j=P,pr} \left[P_j^{(+)}(t) \right] \\
&= \sum_{j=P,pr} \frac{\partial}{\partial t} \left[P_j^{(+)}(t) \right] \\
&= \sum_{j=P,pr} \left[-i\omega_j \tilde{P}_j^{(+)} e^{-i\omega_j t} \right] \quad \text{(B.0.5)}
\end{aligned}
$$

Therefore the time-derivative of the macroscopic polarization for the j-nth field is given by

$$
\begin{aligned}
\frac{\partial}{\partial t}P_j^{(+)}(t) &= -i\omega_j \tilde{P}_j^{(+)} e^{-i\omega_j t} \\
&= -i\omega_j \left\{ -\frac{\zeta}{2\mu_0 c\gamma} \frac{(x_j - i)}{(x_j^2+1)} \left[\left(E_{1_j} + E'_{1_j} \right) \right.\right. \\
&\quad \left.\left. - (x_j + i)\left(\eta_{PPpr} + \eta_{prPP}\right)\Theta_P \left(E_{1_{pr}} + E'_{1_{pr}} \right) \delta_{j,pr} \right] \right\} e^{-i\omega_j t} \\
&= \frac{i}{2\mu_0 c} y_j (x_j - i) \left[\left(E_{1_j} + E'_{1_j} \right) \right. \\
&\quad \left. - (x_j + i)\left(\eta_{PPpr} + \eta_{prPP}\right)\Theta_P \left(E_{1_{pr}} + E'_{1_{pr}} \right) \delta_{j,pr} \right] e^{-i\omega_j t} \qquad \text{(B.0.6)}
\end{aligned}
$$

For the interface between vacuum and top h-BN (layers 0 and 1) at $z = -t_1$, the boundary conditions Eq.B.0.1 and Eq.B.0.2 lead to

$$
\begin{aligned}
E_{1_j}^{(+)}(-t_1, t) &= E_{0_j}^{(+)}(-t_1, t) \\
\frac{1}{2}\left(E_{1_j} e^{ik_{1_j} z - i\omega_j t} + E'_{1_j} e^{-ik_{1_j} z - i\omega_j t} \right)_{z=-t_1} &= \frac{1}{2}\left[E_{0_j} e^{ik_{0_j}(z+t_1) - i\omega_j t} \right. \\
&\quad \left. + E'_{0_j} e^{-ik_{0_j}(z+t_1) - i\omega_j t} \right]_{z=-t_1} \\
E_{1_j} e^{-ik_{1_j} t_1} + E'_{1_j} e^{ik_{1_j} t_1} &= E_{0_j} + E'_{0_j} \qquad \text{(B.0.7)}
\end{aligned}
$$

and

$$
\begin{aligned}
H_{1_j}^{(+)}(-t_1, t) &= H_{0_j}^{(+)}(-t_1, t) \\
-\frac{i}{\mu_0 \omega_j}\frac{\partial}{\partial z} E_{1_j}^{(+)}(z,t)\Big|_{z=-t_1} &= -\frac{i}{\mu_0 \omega_j}\frac{\partial}{\partial z} E_{0_j}^{(+)}(z,t)\Big|_{z=-t_1} \\
\frac{k_{1_j}}{2\mu_0 \omega_j}\left(E_{1_j} e^{-ik_{1_j} t_1} - E'_{1_j} e^{ik_{1_j} t_1} \right) &= \frac{k_{0_j}}{2\mu_0 \omega_j}\left(E_{0_j} - E'_{0_j} \right) \\
\left(\frac{n_1}{n_0} e^{-ik_{1_j} t_1} \right) E_{1_j} - \left(\frac{n_1}{n_0} e^{ik_{1_j} t_1} \right) E'_{1_j} &= E_{0_j} - E'_{0_j} \qquad \text{(B.0.8)}
\end{aligned}
$$

Adding and subtracting Eq.B.0.7 and Eq.B.0.8 leads to the matrix expression

$$\frac{1}{2}\begin{bmatrix} e^{-ik_{1_j}t_1}\left(1+\frac{n_1}{n_0}\right) & e^{ik_{1_j}t_1}\left(1-\frac{n_1}{n_0}\right) \\ e^{-ik_{1_j}t_1}\left(1-\frac{n_1}{n_0}\right) & e^{ik_{1_j}t_1}\left(1+\frac{n_1}{n_0}\right) \end{bmatrix}\begin{bmatrix} E_{1_j} \\ E'_{1_j} \end{bmatrix} = \begin{bmatrix} E_{0_j} \\ E'_{0_j} \end{bmatrix}$$

$$\begin{bmatrix} E_{1_j} \\ E'_{1_j} \end{bmatrix} = \left(\frac{1}{2}\begin{bmatrix} e^{-ik_{1_j}t_1}\left(1+\frac{n_1}{n_0}\right) & e^{ik_{1_j}t_1}\left(1-\frac{n_1}{n_0}\right) \\ e^{-ik_{1_j}t_1}\left(1-\frac{n_1}{n_0}\right) & e^{ik_{1_j}t_1}\left(1+\frac{n_1}{n_0}\right) \end{bmatrix}\right)^{-1} \times \begin{bmatrix} E_{0_j} \\ E'_{0_j} \end{bmatrix} \tag{B.0.9}$$

Similarly, for the interface between top hBN and bottom hBN (layers 1 and 2) at $z = 0$, the boundary conditions Eq.B.0.1 and Eq.B.0.2 along with Eq.B.0.6 lead to

$$\begin{aligned} E^{(+)}_{2_j}(0,t) &= E^{(+)}_{1_j}(0,t) \\ \frac{1}{2}\left(E_{2_j}e^{ik_{2_j}z-i\omega_j t}+E'_{2_j}e^{-ik_{2_j}z-i\omega_j t}\right)_{z=0} &= \frac{1}{2}\left(E_{1_j}e^{ik_{1_j}z-i\omega_j t}\right. \\ &\quad \left.+E'_{1_j}e^{-ik_{1_j}z-i\omega_j t}\right)_{z=0} \qquad \text{(B.0.10)} \\ E_{2_j}+E'_{2_j} &= E_{1_j}+E'_{1_j} \qquad \text{(B.0.11)} \end{aligned}$$

and

$$
\begin{aligned}
H_{2_j}^{(+)}(0,t) &= H_{1_j}^{(+)}(0,t) - K_{m,m-1_j} \\
-\frac{i}{\mu_0\omega_j}\frac{\partial}{\partial z}\, E_{2_j}^{(+)}(z,t)\Big|_{z=0} &= -\frac{i}{\mu_0\omega_j}\frac{\partial}{\partial z}\, E_{1_j}^{(+)}(z,t)\Big|_{z=0} - \frac{\partial}{\partial t}P_j^{(+)} \\
\frac{k_{2_j}}{2\mu_0\omega_j}e^{-i\omega_j t}\left(E_{2_j} - E'_{2_j}\right) &= \frac{k_{1_j}}{2\mu_0\omega_j}e^{-i\omega_j t}\left(E_{1_j} - E'_{1_j}\right) \\
&\quad -\frac{i}{2\mu_0 c}y_j(x_j - i)\left[\left(E_{1_j} + E'_{1_j}\right)\right. \\
&\quad \left. -(x_j + i)\left(\eta_{PPpr} + \eta_{prPP}\right)\Theta_P\left(E_{1_{pr}} + E'_{1_{pr}}\right)\delta_{j,pr}\right] e^{i\omega_j t} \qquad \text{(B.0.12)} \\
E_{2_j} - E'_{2_j} &= \frac{n_1}{n_2}\left(E_{1_j} - E'_{1_j}\right) \\
&\quad -iy_{2_j}(x_j - i)\left[\left(E_{1_j} + E'_{1_j}\right)\right. \\
&\quad \left. -(x_j + i)\left(\eta_{PPpr} + \eta_{prPP}\right)\Theta_P\left(E_{1_{pr}} + E'_{1_{pr}}\right)\delta_{j,pr}\right] \qquad \text{(B.0.13)}
\end{aligned}
$$

where

$$
\begin{aligned}
\Theta_P &= |\psi|^2\left(E_{1_P} + E'_{1_P}\right)\left(E_{1_P} + E'_{1_P}\right)^* \\
&= \left\{M_1(1,1)_P + M_1(2,1)_P + \left[M_1(1,2)_P + M_1(2,2)_P\right] r_P\right\} \\
&\times \left\{M_1(1,1)_P + M_1(2,1)_P + \left[M_1(1,2)_P + M_1(2,2)_P\right] r_P\right\}^* |\psi|^2 \left|E_{0_P}\right|^2 \\
&\equiv f_P f_P^* I_{0_P} \qquad \text{(B.0.14)}
\end{aligned}
$$

Adding and subtracting Eq.B.0.11 and Eq.B.0.13 leads to the matrix expressions

$$\begin{aligned}
\begin{bmatrix} E_{2_j} \\ E'_{2_j} \end{bmatrix} &= \frac{1}{2}\begin{bmatrix} 1+\frac{n_1}{n_2}-iy_{2_j}\left(x_j-i\right) & 1-\frac{n_1}{n_2}-iy_{2_j}\left(x_j-i\right) \\ 1-\frac{n_1}{n_2}+iy_{2_j}\left(x_j-i\right) & 1+\frac{n_1}{n_2}+iy_{2_j}\left(x_j-i\right) \end{bmatrix}\begin{bmatrix} E_{1_j} \\ E'_{1_j} \end{bmatrix} \\
&\quad +\frac{i}{2}y_{2_{pr}}\left(x_{pr}^2+1\right)\left(\eta_{PPpr}+\eta_{prPP}\right)f_P f_P^* I_{0_P}\mathbf{g}\delta_{j,pr}\begin{bmatrix} E_{1_j} \\ E'_{1_j} \end{bmatrix} \\
&= \left[\mathbf{M_{2_A}}_{j}+\mathbf{M_{2_B}}_{pr}\,\delta_{j,pr}\right]\begin{bmatrix} E_{1_j} \\ E'_{1_j} \end{bmatrix} \qquad \text{(B.0.15)}
\end{aligned}$$

Similarly, for the interface between bottom h-BN and NBK7 glass substrate (layers 2 and 3) at $z=t_2$, the boundary conditions Eq.B.0.1 and Eq.B.0.2 lead to

$$\begin{aligned}
E_{3_j}^{(+)}\left(t_2,t\right) &= E_{2_j}^{(+)}\left(t_2,t\right) \\
\frac{1}{2}\left[E_{3_j}e^{ik_{3_j}(z-t_2)-i\omega_j t}+E'_{3_j}e^{-ik_{3_j}(z-t_2)-i\omega_j t}\right]_{z=t_2} &= \frac{1}{2}\Big(E_{2_j}e^{ik_{2_j}z-i\omega_j t} \\
&\quad +E'_{2_j}e^{-ik_{2_j}z-i\omega_j t}\Big)_{z=t_2} \qquad \text{(B.0.16)} \\
E_{3_j}+E'_{3_j} &= E_{2_j}e^{ik_{2_j}t_2}+E'_{2_j}e^{-ik_{2_j}t_2} \qquad \text{(B.0.17)}
\end{aligned}$$

and

$$\begin{aligned}
H_{3_j}^{(+)}\left(t_2,t\right) &= H_{2_j}^{(+)}\left(t_2,t\right) \\
-\frac{i}{\mu_0\omega_j}\frac{\partial}{\partial z}E_{3_j}^{(+)}\left(z,t\right)\Big|_{z=t_2} &= -\frac{i}{\mu_0\omega_j}\frac{\partial}{\partial z}E_{2_j}^{(+)}\left(z,t\right)\Big|_{z=t_2} \\
\frac{n_3}{2\mu_0 c}\left(E_{3_j}-E'_{3_j}\right) &= \frac{n_2}{2\mu_0 c}\left(E_{2_j}e^{ik_{2_j}t_2}-E'_{2_j}e^{-ik_{2_j}t_2}\right) \\
E_{3_j}-E'_{3_j} &= \left(\frac{n_2}{n_3}e^{ik_{2_j}t_2}\right)E_{2_j} \\
&\quad -\left(\frac{n_2}{n_3}e^{-ik_{2_j}t_2}\right)E'_{2_j} \qquad \text{(B.0.18)}
\end{aligned}$$

Adding and subtracting Eq.B.0.17 and Eq.B.0.18 leads to the matrix expression

$$\begin{bmatrix} E_{3_j} \\ E'_{3_j} \end{bmatrix} = \frac{1}{2} \begin{bmatrix} e^{ik_{2_j}t_2}\left(1+\frac{n_2}{n_3}\right) & e^{-ik_{2_j}t_2}\left(1-\frac{n_2}{n_3}\right) \\ e^{ik_{2_j}t_2}\left(1-\frac{n_2}{n_3}\right) & e^{-ik_{2_j}t_2}\left(1+\frac{n_2}{n_3}\right) \end{bmatrix} \times \begin{bmatrix} E_{2_j} \\ E'_{2_j} \end{bmatrix} \tag{B.0.19}$$

Lastly, for the interface between NBK7 glass substrate and vacuum (layers 3 and 4) at $z = t_2 + t_3$, the boundary conditions Eq.B.0.1 and Eq.B.0.2 lead to

$$\begin{aligned} E^{(+)}_{4_j}(t_2+t_3,t) &= E^{(+)}_{3_j}(t_2+t_3,t) \\ \left[\frac{1}{2}E_{4_j}e^{ik_{4_j}(z-t_2-t_3)-i\omega_j t}\right]_{z=t_2+t_3} &= \frac{1}{2}\Big[E_{3_j}e^{ik_{3_j}(z-t_2)-i\omega_j t} \\ &\quad + E'_{3_j}e^{-ik_{3_j}(z-t_2)-i\omega_j t}\Big]_{z=t_2+t_3} \qquad \text{(B.0.20)} \\ E_{4_j} &= E_{3_j}e^{ik_{3_j}t_3} + E'_{3_j}e^{-ik_{3_j}t_3} \qquad \text{(B.0.21)} \end{aligned}$$

and

$$\begin{aligned} H^{(+)}_{4_j}(t_2,t) &= H^{(+)}_{3_j}(t_2,t) \\ -\frac{i}{\mu_0\omega_j}\frac{\partial}{\partial z}E^{(+)}_{4_j}(z,t)\Big|_{z=t_2+t_3} &= -\frac{i}{\mu_0\omega_j}\frac{\partial}{\partial z}E^{(+)}_{3_j}(z,t)\Big|_{z=t_2+t_3} \\ \frac{n_4}{2\mu_0 c}E_{4_j} &= \frac{n_3}{2\mu_0 c}\left(E_{3_j}e^{ik_{3_j}t_3} - E'_{3_j}e^{-ik_{3_j}t_3}\right) \\ E_{4_j} &= \frac{n_3}{n_4}\left(E_{3_j}e^{ik_{3_j}t_3} - E'_{3_j}e^{-ik_{3_j}t_3}\right) \qquad \text{(B.0.22)} \end{aligned}$$

Adding and subtracting Eq.B.0.21 and Eq.B.0.22 leads to the matrix expression

$$\begin{bmatrix} E_{4_j} \\ 0 \end{bmatrix} = \frac{1}{2} \begin{bmatrix} e^{ik_{3_j}t_3}\left(1+\frac{n_3}{n_4}\right) & e^{-ik_{3_j}t_3}\left(1-\frac{n_3}{n_4}\right) \\ e^{ik_{3_j}t_3}\left(1-\frac{n_3}{n_4}\right) & e^{-ik_{3_j}t_3}\left(1+\frac{n_3}{n_4}\right) \end{bmatrix} \times \begin{bmatrix} E_{3_j} \\ E'_{3_j} \end{bmatrix} \tag{B.0.23}$$

Carrying out the matrix multiplication using Eqs.B.0.9, B.0.15, B.0.19 and B.0.23 leads to the transfer matrix for the entire multi-layer structure given by Eq.6.2.78.

Appendix C

Difference of Two Lorentzians

This appendix provides a detailed derivation of Eq.6.4.3 on chapter 5. The goal is to show that the differential absorption estimated as the difference of two Lorentzian functions is equivalent to the differential absorption expression calculated from the third-order, off-diagonal density matrix element, but only for the perturbation field sequence $(j, l, m) = (P, P, pr)$.

For a two-dimensional system, the pump-induced change in the sample's absorption of the probe is assumed to be

$$\Delta A_{DM} = 2\frac{\omega}{c}\chi_e^{I,(3)} |E_P|^2 \tag{C.0.1}$$

where the imaginary component of the third-order optical susceptibility $\chi_e^{I,(3)}$ is obtained by comparing the series expansion of the macroscopic polarization with the macroscopic polarization calculated from the density matrix as

$$\begin{aligned} \tilde{P}_{Series}^{(3)} &= \tilde{P}_{DM}^{(3)} \\ \epsilon_0 \chi^{(3)} |E_P|^2 E_{pr} &= N_a \tilde{\rho}_{21}^{(3)} \mu_{12} \end{aligned}$$

After substituting the third-order, off-diagonal density matrix element given by Eq. 6.2.40, the third-order optical susceptibility becomes

$$\chi_e^{(3)} = \frac{N_a}{\epsilon_0}\left[\frac{\gamma}{\gamma_{sp}}\frac{1}{\delta_{pr}+i\gamma}\left(2-\frac{\beta-i\alpha}{\delta_{pr}+i\gamma}\right)\frac{1}{\delta_P^2+\gamma^2}\frac{|\mu_{12}|^4}{4\hbar^3}\right] \tag{C.0.2}$$

and its imaginary component is explicitly given by

$$\begin{aligned}\chi_e^{I,(3)} &= \frac{N_a}{\epsilon_0}\frac{\gamma}{\gamma_{sp}}\frac{1}{\left(\delta_{pr}^2+\gamma^2\right)^2}\left[2\delta_{pr}\beta\gamma+\alpha\left(\delta_{pr}^2-\gamma^2\right)-2\gamma\left(\delta_{pr}^2+\gamma^2\right)\right] \\ &\quad\times\frac{1}{\delta_P^2+\gamma^2}\frac{|\mu_{12}|^4}{4\hbar^3}\end{aligned} \tag{C.0.3}$$

As a result, the differential absorption becomes

$$\begin{aligned}\Delta A_{DM} &= \zeta\omega\frac{|\mu_{12}|^2}{2\hbar^2\left(\delta_P^2+\gamma^2\right)}\frac{\gamma}{\gamma_{sp}}|E_P|^2 \\ &\quad\times\left[\frac{\alpha\left(\delta_{pr}^2-\gamma^2\right)+2\beta\gamma\delta_{pr}}{\left(\delta_{pr}^2+\gamma^2\right)^2}-\frac{2\gamma}{\left(\delta_{pr}^2+\gamma^2\right)}\right]\end{aligned} \tag{C.0.4}$$

On the other hand, the differential absorption approximated as the difference of two Lorentzians is

$$\begin{aligned}\Delta A_{D2L} &= \zeta\omega\left[\frac{(\gamma+\alpha\rho_{22})}{\left(\delta_{pr}-\beta\rho_{22}\right)^2+\left(\gamma+\alpha\rho_{22}\right)^2}-\frac{\gamma}{\delta_{pr}^2+\gamma^2}\right] \\ &\approx \zeta\omega\left[\frac{\gamma}{\delta_{pr}^2+\gamma^2}+\frac{\alpha\left(\delta_{pr}^2-\gamma^2\right)+2\beta\gamma\delta_{pr}}{\left(\delta_{pr}^2+\gamma^2\right)^2}\rho_{22}-\frac{\gamma}{\delta_{pr}^2+\gamma^2}\right] \\ &\approx \zeta\omega\left[\frac{\alpha\left(\delta_{pr}^2-\gamma^2\right)+2\beta\gamma\delta_{pr}}{\left(\delta_{pr}^2+\gamma^2\right)^2}\right]\rho_{22}\end{aligned} \tag{C.0.5}$$

where the diagonal density matrix element for a single (pump) field to lowest order in the intensity is

$$\begin{aligned}
\rho_{22}^{(2)}(t) &= \sum_{j,l=1}^{N} \tilde{\rho}_{22_{j,l}}^{(2)} e^{i(\mathbf{k}_j-\mathbf{k}_l)\cdot\mathbf{R}-i(\omega_j-\omega_l)t} \\
&= \tilde{\rho}_{22_{P,P}}^{(2)} \\
&= \frac{|\chi_P|^2}{(\delta_P^2+\gamma^2)}\left(1+\frac{2\Gamma}{\gamma_{sp}}\right) \\
&= \frac{|\mu_{12}|^2}{2\hbar^2(\delta_P^2+\gamma^2)}\frac{\gamma}{\gamma_{sp}}|E_P|^2
\end{aligned} \tag{C.0.6}$$

Therefore, to lowest order in the pump intensity, the difference of two Lorentzians becomes

$$\Delta A_{D2L} = \zeta\omega\frac{|\mu_{12}|^2}{2\hbar^2(\delta_P^2+\gamma^2)}\frac{\gamma}{\gamma_{sp}}|E_P|^2\left[\frac{\alpha\left(\delta_{pr}^2-\gamma^2\right)+2\beta\gamma\delta_{pr}}{\left(\delta_{pr}^2+\gamma^2\right)^2}\right] \tag{C.0.7}$$

Comparing Eq.C.0.4 and Eq.C.0.7, it becomes clear that the differential absorption calculated from the master equation is approximately equal to the difference of two Lorentzians up to a population dependent correction as

$$\begin{aligned}
\Delta A_{DM} &= \zeta\omega\tilde{\rho}_{22_{P,P}}^{(2)}\left[\frac{\alpha\left(\delta_{pr}^2-\gamma^2\right)+2\beta\gamma\delta_{pr}}{\left(\delta_{pr}^2+\gamma^2\right)^2}-\frac{2\gamma}{\left(\delta_{pr}^2+\gamma^2\right)}\right] \\
&= \zeta\omega\tilde{\rho}_{22_{P,P}}^{(2)}\left[\frac{\alpha\left(\delta_{pr}^2-\gamma^2\right)+2\beta\gamma\delta_{pr}}{\left(\delta_{pr}^2+\gamma^2\right)^2}\right]-\zeta\omega\tilde{\rho}_{22_{P,P}}^{(2)}\left[\frac{2\gamma}{\left(\delta_{pr}^2+\gamma^2\right)}\right] \\
&= \Delta A_{D2L}-\zeta\omega\tilde{\rho}_{22_{P,P}}^{(2)}\left[\frac{2\gamma}{\left(\delta_{pr}^2+\gamma^2\right)}\right] \\
&= \Delta A_{D2L}-\zeta\omega\rho_{22}\left[\frac{2\gamma}{\left(\delta_{pr}^2+\gamma^2\right)}\right]
\end{aligned} \tag{C.0.8}$$

This means that Eq.C.0.4 predicts a third-order response even in the absence of excitation-

induced resonance energy shifts and linewidth broadening. To estimate many-body contributions to the differential absorption beyond first order in the pump field intensity, all of the terms in the series expansion of ΔA_{D2L} could be kept and that the experimental differential absorption can be estimated as

$$\begin{aligned}
\Delta A_{exp} &\approx \zeta\omega\left[\frac{(\gamma+\alpha\rho_{22})}{(\delta_{pr}-\beta\rho_{22})^2+(\gamma+\alpha\rho_{22})^2}-\frac{\gamma}{\delta_{pr}^2+\gamma^2}\right]-\zeta\omega\rho_{22}\left[\frac{2\gamma}{\left(\delta_{pr}^2+\gamma^2\right)}\right] \\
&\approx \zeta\omega\left[\frac{(\gamma+\alpha\rho_{22})}{(\delta_{pr}-\beta\rho_{22})^2+(\gamma+\alpha\rho_{22})^2}-\frac{\gamma\,(1+2\rho_{22})}{\delta_{pr}^2+\gamma^2}\right] \\
&\approx \zeta\,(x_{pr}+\Lambda_0)\left[\frac{(1+\Upsilon\rho_{22})}{(x_{pr}-B\rho_{22})^2+(1+\Upsilon\rho_{22})^2}-\frac{(1+2\rho_{22})}{x_{pr}^2+1}\right] \qquad \text{(C.0.9)}
\end{aligned}$$

Equation C.0.9 was used to fit the data shown in Fig.6.4.9.

Bibliography

[1] Anthony Aiello, Yuanpeng Wu, Ayush Pandey, Ping Wang, Woncheol Lee, Dylan Bayerl, Nocona Sanders, Zihao Deng, Jiseok Gim, Kai Sun, Robert Hovden, Emmanouil Kioupakis, Zetian Mi, and Pallab Bhattacharya. Deep Ultraviolet Luminescence Due to Extreme Confinement in Monolayer GaN/Al(Ga)N Nanowire and Planar Heterostructures. *Nano Letters*, 19(11):7852–7858, nov 2019.

[2] Gleb M. Akselrod, Parag B. Deotare, Nicholas J. Thompson, Jiye Lee, William A. Tisdale, Marc A. Baldo, Vinod M. Menon, and Vladimir Bulović. Visualization of exciton transport in ordered and disordered molecular solids. *Nature Communications*, 5(1):3646, may 2014.

[3] Anders Andrae and Tomas Edler. On Global Electricity Usage of Communication Technology: Trends to 2030. *Challenges*, 6(1):117–157, apr 2015.

[4] H K Avetissian, G F Mkrtchian, and K Z Hatsagortsyan. Many-body effects for excitonic high-order wave mixing in monolayer transition metal dichalcogenides. *Physical Review Research*, 2(2):023072, apr 2020.

[5] David Awschalom, Karl K Berggren, Hannes Bernien, Sunil Bhave, Lincoln D Carr, Paul Davids, Sophia E Economou, Dirk Englund, Andrei Faraon, Martin Fejer, Saikat Guha, Martin V Gustafsson, Evelyn Hu, Liang Jiang, Jungsang Kim, Boris Korzh, Prem Kumar, Paul G Kwiat, Marko Lončar, Mikhail D Lukin, David A.B. Miller, Christopher Monroe, Sae Woo Nam, Prineha Narang, Jason S. Orcutt, Michael G. Raymer, Amir H. Safavi-Naeini, Maria Spiropulu, Kartik Srinivasan, Shuo Sun, Jelena Vučković, Edo Waks, Ronald Walsworth, Andrew M Weiner, and Zheshen Zhang. Development of Quantum Interconnects (QuICs) for Next-Generation Information Technologies. *PRX Quantum*, 2(1):017002, feb 2021.

[6] Yusong Bai, Lin Zhou, Jue Wang, Wenjing Wu, Leo J. McGilly, Dorri Halbertal, Chiu Fan Bowen Lo, Fang Liu, Jenny Ardelean, Pasqual Rivera, Nathan R. Finney, Xu-Chen Yang, D. N. Basov, Wang Yao, Xiaodong Xu, James Hone, Abhay N. Pasupathy, and X.-Y. Zhu. Excitons in strain-induced one-dimensional moiré potentials at transition metal dichalcogenide heterojunctions. *Nature Materials*, 19(10):1068–1073, oct 2020.

[7] Marc Baldo and Vladimir Stojanović. Excitonic interconnects. *Nature Photonics*, 3(10):558–560, oct 2009.

[8] Britton W. H. Baugher, Hugh O. H. Churchill, Yafang Yang, and Pablo Jarillo-Herrero. Optoelectronic devices based on electrically tunable p-n diodes in a monolayer dichalcogenide. *Nature Nanotechnology*, 9(4):262–267, apr 2014.

[9] S. Ben-Tabou de Leon and B. Laikhtman. Exciton-exciton interactions in quantum wells: Optical properties and energy and spin relaxation. *Physical Review B*, 63(12):125306, mar 2001.

[10] Paul R. Berman and Vladimir S. Malinovsky. *Principles of Laser Spectroscopy and Quantum Optics*. Princeton University Press, 2011.

[11] Boston Electronics. B and H What is Time Correlated Single Photon Counting REV 8-16. Technical report, 2012.

[12] Jean-Philippe Bouchaud and Antoine Georges. Anomalous diffusion in disordered media: Statistical mechanisms, models and physical applications. *Physics Reports*, 195(4-5):127–293, nov 1990.

[13] Robert W. Boyd. *Nonlinear Optics*. Academic Press, New York, 3rd edition, 2008.

[14] P. Bozsoki, M. Kira, W. Hoyer, T. Meier, I. Varga, P. Thomas, and S. W. Koch. Microscopic modeling of photoluminescence of strongly disordered semiconductors. *Journal of Luminescence*, 124(1):99–112, may 2007.

[15] Artur Branny, Santosh Kumar, Raphaël Proux, and Brian D Gerardot. Deterministic strain-induced arrays of quantum emitters in a two-dimensional semiconductor. *Nature Communications*, 8(1):15053, aug 2017.

[16] Samuel Brem, August Ekman, Dominik Christiansen, Florian Katsch, Malte Selig, Cedric Robert, Xavier Marie, Bernhard Urbaszek, Andreas Knorr, and Ermin Malic. Phonon-Assisted Photoluminescence from Indirect Excitons in Monolayers of Transition-Metal Dichalcogenides. *Nano Letters*, 20(4):2849–2856, apr 2020.

[17] Samuel Brem, Malte Selig, Gunnar Berghaeuser, and Ermin Malic. Exciton Relaxation Cascade in two-dimensional Transition Metal Dichalcogenides. *Scientific Reports*, 8(1):8238, dec 2018.

[18] Kevin F. Brennan. *The Physics of Semiconductors with applications to optoelectronic devices*. Cambridge University Press, Cambridge, 1999.

[19] Michele Buscema, Gary A. Steele, Herre S J van der Zant, and Andres Castellanos-Gomez. The effect of the substrate on the Raman and photoluminescence emission of single-layer MoS2. *Nano Research*, 7(4):1–11, apr 2014.

[20] L.V. Butov. Excitonic devices. *Superlattices and Microstructures*, 108:2–26, aug 2017.

[21] F. Cadiz, E. Courtade, C. Robert, G. Wang, Y. Shen, H. Cai, T. Taniguchi, K. Watanabe, H. Carrere, D. Lagarde, M. Manca, T. Amand, P. Renucci, S. Tongay, X. Marie, and B. Urbaszek. Excitonic Linewidth Approaching the Homogeneous Limit in MoS2-Based van der Waals Heterostructures. *Physical Review X*, 7(2):021026, may 2017.

[22] F. Cadiz, C. Robert, E. Courtade, M. Manca, L. Martinelli, T. Taniguchi, K. Watanabe, T. Amand, A. C. H. Rowe, D. Paget, B. Urbaszek, and X. Marie. Exciton diffusion in WSe2 monolayers embedded in a van der Waals heterostructure. *Applied Physics Letters*, 112(15):152106, apr 2018.

[23] Felix Carrascoso, Hao Li, Riccardo Frisenda, and Andres Castellanos-Gomez. Strain engineering in single-, bi- and tri-layer MoS2, MoSe2, WS2 and WSe2. *Nano Research*, 14(6):1698–1703, jun 2021.

[24] Andres Castellanos-Gomez, Michele Buscema, Rianda Molenaar, Vibhor Singh, Laurens Janssen, Herre S J van der Zant, and Gary A. Steele. Deterministic transfer of two-dimensional materials by all-dry viscoelastic stamping. *2D Materials*, 1(1):011002, apr 2014.

[25] A. H. Castro Neto, F. Guinea, N. M.R. Peres, K. S. Novoselov, and A. K. Geim. The electronic properties of graphene. *Reviews of Modern Physics*, 81(1):109–162, jan 2009.

[26] Frank Ceballos, Qiannan Cui, Matthew Z Bellus, and Hui Zhao. Exciton formation in monolayer transition metal dichalcogenides. *Nanoscale*, 8(22):11681–11688, 2016.

[27] Woo Hyun Chae, Jeffrey D. Cain, Eve D. Hanson, Akshay A. Murthy, and Vinayak P. Dravid. Substrate-induced strain and charge doping in CVD-grown monolayer MoS2. *Applied Physics Letters*, 111(14):143106, oct 2017.

[28] Chung Huai Chang, Xiaofeng Fan, Shi Hsin Lin, and Jer Lai Kuo. Orbital analysis of electronic structure and phonon dispersion in MoS2, MoSe2, WS2, and WSe2 monolayers under strain. *Physical Review B - Condensed Matter and Materials Physics*, 88(19):195420, nov 2013.

[29] A. Chaves, J. G. Azadani, Hussain Alsalman, D. R. da Costa, R. Frisenda, A. J. Chaves, Seung Hyun Song, Y. D. Kim, Daowei He, Jiadong Zhou, A. Castellanos-Gomez, F. M. Peeters, Zheng Liu, C. L. Hinkle, Sang-Hyun Oh, Peide D. Ye, Steven J. Koester, Young Hee Lee, Ph Avouris, Xinran Wang, and Tony Low. Bandgap engineering of two-dimensional semiconductor materials. *npj 2D Materials and Applications*, 4(1):29, dec 2020.

[30] Manish Chhowalla, Hyeon Suk Shin, Goki Eda, Lain Jong Li, Kian Ping Loh, and Hua Zhang. The chemistry of two-dimensional layered transition metal dichalcogenide nanosheets, apr 2013.

[31] Chang-Hee Cho, Carlos O. Aspetti, Michael E. Turk, James M. Kikkawa, Sung-Wook Nam, and Ritesh Agarwal. Tailoring hot-exciton emission and lifetimes in semiconducting nanowires via whispering-gallery nanocavity plasmons. *Nature Materials*, 10(9):669–675, sep 2011.

[32] Hiram J. Conley, Bin Wang, Jed I. Ziegler, Richard F. Haglund, Sokrates T. Pantelides, and Kirill I. Bolotin. Bandgap Engineering of Strained Monolayer and Bilayer MoS2. *Nano Letters*, 13(8):3626–3630, aug 2013.

[33] Darwin F. Cordovilla Leon, Zidong Li, Sung Woon Jang, Che-Hsuan Cheng, and Parag B Deotare. Exciton transport in strained monolayer WSe2. *Applied Physics Letters*, 113(25):252101, dec 2018.

[34] Darwin F. Cordovilla Leon, Zidong Li, Sung Woon Jang, and Parag B. Deotare. Hot exciton transport in WSe2 monolayers. *Physical Review B*, 100(24):241401, dec 2019.

[35] Zhaohe Dai, Luqi Liu, and Zhong Zhang. Strain Engineering of 2D Materials: Issues and Opportunities at the Interface. *Advanced Materials*, 31(45):1805417, nov 2019.

[36] B. Dal Don, Hui Zhao, G. Schwartz, and H. Kalt. Spatial breathing of the exciton distribution in ZnSe quantum wells. *physica status solidi (b)*, 241(3):579–582, mar 2004.

[37] Thomas P. Darlington, Christian Carmesin, Matthias Florian, Emanuil Yanev, Obafunso Ajayi, Jenny Ardelean, Daniel A. Rhodes, Augusto Ghiotto, Andrey Krayev, Kenji Watanabe, Takashi Taniguchi, Jeffrey W. Kysar, Abhay N. Pasupathy, James C. Hone, Frank Jahnke, Nicholas J. Borys, and P. James Schuck. Imaging strain-localized excitons in nanoscale bubbles of monolayer WSe2 at room temperature. *Nature Nanotechnology*, 15(10):854–860, oct 2020.

[38] Emil de Souza Sánchez Filho. *Tensor Calculus for Engineers and Physicists*. Springer International Publishing, Cham, 2016.

[39] C. R. Dean, A. F. Young, I. Meric, C. Lee, L. Wang, S. Sorgenfrei, K. Watanabe, T. Taniguchi, P. Kim, K. L. Shepard, and J. Hone. Boron nitride substrates for high-quality graphene electronics. *Nature Nanotechnology*, 5(10):722–726, oct 2010.

[40] C. L. Degen, F Reinhard, and P Cappellaro. Quantum sensing. *Reviews of Modern Physics*, 89(3):035002, jul 2017.

[41] Sujay B Desai, Surabhi R Madhvapathy, Angada B Sachid, Juan Pablo Llinas, Qingxiao Wang, Geun Ho Ahn, Gregory Pitner, Moon J Kim, Jeffrey Bokor, Chenming Hu, H.-S. P. Wong, and Ali Javey. MoS2 transistors with 1-nanometer gate lengths. *Science*, 354(6308):99–102, oct 2016.

[42] Sujay B. Desai, Gyungseon Seol, Jeong Seuk Kang, Hui Fang, Corsin Battaglia, Rehan Kapadia, Joel W. Ager, Jing Guo, and Ali Javey. Strain-Induced Indirect to Direct Bandgap Transition in Multilayer WSe 2. *Nano Letters*, 14(8):4592–4597, aug 2014.

[43] S. R. Dhariwal and B. M. Deoraj. Theory of dispersive relaxation in amorphous semiconductors. *Solid State Communications*, 79(6):521–524, aug 1991.

[44] Liang Dong, Raju R. Namburu, Terrance P. O'Regan, Madan Dubey, and Avinash M. Dongare. Theoretical study on strain-induced variations in electronic properties of monolayer MoS2. *Journal of Materials Science*, 49(19):6762–6771, oct 2014.

[45] John D. Dow and David Redfield. Toward a unified theory of Urbach's rule and exponential absorption edges. *Physical Review B*, 5(2):594–610, jan 1972.

[46] Daniel Erkensten, Samuel Brem, and Ermin Malic. Exciton-exciton interaction in transition metal dichalcogenide monolayers and van der Waals heterostructures. *Physical Review B*, 103(4):045426, jan 2021.

[47] H. H. Fang, B Han, C Robert, M. A. Semina, D Lagarde, E Courtade, T Taniguchi, K Watanabe, T Amand, B Urbaszek, M. M. Glazov, and X Marie. Control of the Exciton Radiative Lifetime in van der Waals Heterostructures. *Physical Review Letters*, 123(6):067401, aug 2019.

[48] Maja Feierabend, Alexandre Morlet, Gunnar Berghäuser, and Ermin Malic. Impact of strain on the optical fingerprint of monolayer transition-metal dichalcogenides. *Physical Review B*, 96(4):045425, jul 2017.

[49] Ji Feng, Xiaofeng Qian, Cheng-Wei Wei Huang, and Ju Li. Strain-engineered artificial atom as a broad-spectrum solar energy funnel. *Nature Photonics*, 6(12):866–872, nov 2012.

[50] Riccardo Frisenda and Andres Castellanos-Gomez. Strain creates a trion factory. *Nature Photonics*, 14(5):269–270, may 2020.

[51] Xuewen Fu, Gwenole Jacopin, Mehran Shahmohammadi, Ren Liu, Malik Benameur, Jean-Daniel Ganière, Ji Feng, Wanlin Guo, Zhi-Min Liao, Benoit Deveaud, and Dapeng Yu. Exciton Drift in Semiconductors under Uniform Strain Gradients: Application to Bent ZnO Microwires. *ACS Nano*, 8(4):3412–3420, apr 2014.

[52] Ilya Fushman, Dirk Englund, Andrei Faraon, Nick Stoltz, Pierre Petroff, and Jelena Vučković. Controlled phase shifts with a single quantum dot. *Science*, 320(5877):769–772, may 2008.

[53] A. K. Geim and K. S. Novoselov. The rise of graphene. In *Nanoscience and Technology: A Collection of Reviews from Nature Journals*, pages 11–19. World Scientific Publishing Co., jan 2009.

[54] Ryan J Gelly, Dylan Renaud, Xing Liao, Benjamin Pingault, Stefan Bogdanovic, Giovanni Scuri, Kenji Watanabe, Takashi Taniguchi, Bernhard Urbaszek, Hongkun Park, and Marko Lončar. Probing dark exciton navigation through a local strain landscape in a WSe2 monolayer. *ArXiv*, mar 2021.

[55] Ed Gerstner. Nobel Prize 2010: Andre Geim and Konstantin Novoselov. *Nature Physics*, 6(11):836–836, nov 2010.

[56] Subhamoy Ghatak, Atindra Nath Pal, and Arindam Ghosh. Nature of electronic states in atomically thin MoS2 field-effect transistors. *ACS Nano*, 5(10):7707–7712, oct 2011.

[57] Areg Ghazaryan, Mohammad Hafezi, and Pouyan Ghaemi. Anisotropic exciton transport in transition-metal dichalcogenides. *Physical Review B*, 97(24):245411, jun 2018.

[58] Dave Gilliam. Initial Value Problem for the Heat Equation, 2008.

[59] M. M. Glazov. Phonon wind and drag of excitons in monolayer semiconductors. *Physical Review B*, 100(4):045426, jul 2019.

[60] M. M. Glazov. Quantum Interference Effect on Exciton Transport in Monolayer Semiconductors. *Physical Review Letters*, 124(16):166802, apr 2020.

[61] Prazisions Glas GmbH and Optik. N-BK7 Optical borosilicate-crown glass.

[62] Robert J. Gordon and Stuart A. Rice. Active control of the dynamics of atoms and molecules. *Annual Review of Physical Chemistry*, 48(1):601–641, oct 1997.

[63] Moshe G. Harats, Jan N. Kirchhof, Mengxiong Qiao, Kyrylo Greben, and Kirill I. Bolotin. Dynamics and efficient conversion of excitons to trions in non-uniformly strained monolayer WS2. *Nature Photonics*, 14(5):324–329, may 2020.

[64] Shlomo Havlin and Daniel Ben-Avraham. Diffusion in disordered media. *Advances in Physics*, 36(6):695–798, jan 1987.

[65] Keliang He, Nardeep Kumar, Liang Zhao, Zefang Wang, Kin Fai Mak, Hui Zhao, and Jie Shan. Tightly Bound Excitons in Monolayer WSe2. *Physical Review Letters*, 113(2):026803, jul 2014.

[66] Yu-Ming He, Genevieve Clark, John R. Schaibley, Yu-Ming He, Ming-Cheng Chen, Yu-Jia Wei, Xing Ding, Qiang Zhang, Wang Yao, Xiaodong Xu, Chao-Yang Lu, and Jian-Wei Pan. Single quantum emitters in monolayer semiconductors. *Nature Nanotechnology*, 10(6):497–502, jun 2015.

[67] Eugene Hecht. *Optics*. Addison-Wesley, 4 edition, 2002.

[68] Jinhua Hong, Zhixin Hu, Matt Probert, Kun Li, Danhui Lv, Xinan Yang, Lin Gu, Nannan Mao, Qingliang Feng, Liming Xie, Jin Zhang, Dianzhong Wu, Zhiyong Zhang, Chuanhong Jin, Wei Ji, Xixiang Zhang, Jun Yuan, and Ze Zhang. Exploring atomic defects in molybdenum disulphide monolayers. *Nature Communications*, 6(1):6293, dec 2015.

[69] Jason Horng, Eric W. Martin, Yu-Hsun Chou, Emmanuel Courtade, Tsu-chi Chang, Chu-Yuan Hsu, Michael-Henr Wentzel, Hanna G. Ruth, Tien-Chang Lu, Steven T. Cundiff, Feng Wang, and Hui Deng. Perfect Absorption by an Atomically Thin Crystal. *Physical Review Applied*, 14(2):024009, aug 2020.

[70] Yusuke Hoshi, Takashi Kuroda, Mitsuhiro Okada, Rai Moriya, Satoru Masubuchi, Kenji Watanabe, Takashi Taniguchi, Ryo Kitaura, and Tomoki Machida. Suppression of exciton-exciton annihilation in tungsten disulfide monolayers encapsulated by hexagonal boron nitrides. *Physical Review B*, 95(24):241403, jun 2017.

[71] J. Hwang, M. Pototschnig, R. Lettow, G. Zumofen, A. Renn, S. Götzinger, and V. Sandoghdar. A single-molecule optical transistor. *Nature*, 460(7251):76–80, jul 2009.

[72] Justin Iveland, James S. Speck, Lucio Martinelli, Jacques Peretti, and Claude Weisbuch. Auger effect identified as main cause of efficiency droop in LEDs. *SPIE Newsroom*, jun 2014.

[73] John David Jackson. *Classical Electrodynamics*. John Wiley and Sons, Inc, 3 edition, 1998.

[74] Andreas Jakobs and Klaus W Kehr. Theory and simulation of multiple-trapping transport through a finite slab. *Physical Review B*, 48(12):8780–8789, sep 1993.

[75] Zhenghe Jin, Xiaodong Li, Jeffrey T. Mullen, and Ki Wook Kim. Intrinsic transport properties of electrons and holes in monolayer transition-metal dichalcogenides. *Physical Review B*, 90(4):045422, jul 2014.

[76] Priya Johari and Vivek B. Shenoy. Tuning the electronic properties of semiconducting transition metal dichalcogenides by applying mechanical strains. *ACS Nano*, 6(6):5449–5456, jun 2012.

[77] Nicola Jones. How to stop data centres from gobbling up the world's electricity. *Nature*, 561(7722):163–166, sep 2018.

[78] Toshiaki Kato and Toshiro Kaneko. Transport Dynamics of Neutral Excitons and Trions in Monolayer WS2. *ACS Nano*, 10(10):9687–9694, oct 2016.

[79] Florian Katsch and Andreas Knorr. Optical Preparation and Coherent Control of Ultrafast Nonlinear Quantum Superpositions in Exciton Gases: A Case Study for Atomically Thin Semiconductors. *Physical Review X*, 10(4):041039, nov 2020.

[80] Florian Katsch, Malte Selig, Alexander Carmele, and Andreas Knorr. Theory of Exciton-Exciton Interactions in Monolayer Transition Metal Dichalcogenides. *Physica Status Solidi (B) Basic Research*, 255(12):1800185, dec 2018.

[81] Florian Katsch, Malte Selig, and Andreas Knorr. Exciton-Scattering-Induced Dephasing in Two-Dimensional Semiconductors. *Physical Review Letters*, 124(25), 2020.

[82] G. M. Kavoulakis, Gordon Baym, and J. P. Wolfe. Quantum saturation and condensation of excitons in CuO2: A theoretical study. *Physical Review B*, 53(11):7227–7243, mar 1996.

[83] Ahmed Raza Khan, Teng Lu, Wendi Ma, Yuerui Lu, and Yun Liu. Tunable Optoelectronic Properties of WS2 by Local Strain Engineering and Folding. *Advanced Electronic Materials*, 6(4):1901381, apr 2020.

[84] M. Kira and S.W. Koch. Many-body correlations and excitonic effects in semiconductor spectroscopy. *Progress in Quantum Electronics*, 30(5):155–296, 2006.

[85] Mackillo (University of Michigan) Kira and Stephan W. (Philipps-Universitat Marburg) Koch. *Semiconductor Quantum Optics*. Cambridge University Press, Cambridge, 2012.

[86] J. Klein, A. Hötger, M. Florian, A. Steinhoff, A. Delhomme, T. Taniguchi, K. Watanabe, F. Jahnke, A. W. Holleitner, M. Potemski, C. Faugeras, J. J. Finley, and A. V. Stier. Controlling exciton many-body states by the electric-field effect in monolayer MoS2. *Physical Review Research*, 3(2):L022009, apr 2021.

[87] Alexander V. Kolobov and Junji Tominaga. *Two-Dimensional Transition-Metal Dichalcogenides*, volume 239 of *Springer Series in Materials Science*. Springer International Publishing, Cham, 2016.

[88] Hannu Pekka Komsa, Jani Kotakoski, Simon Kurasch, Ossi Lehtinen, Ute Kaiser, and Arkady V. Krasheninnikov. Two-dimensional transition metal dichalcogenides under electron irradiation: Defect production and doping. *Physical Review Letters*, 109(3):035503, jul 2012.

[89] Yeonjeong Koo, Yongchul Kim, Soo Ho Choi, Hyeongwoo Lee, Jinseong Choi, Dong Yun Lee, Mingu Kang, Hyun Seok Lee, Ki Kang Kim, Geunsik Lee, and Kyoung-Duck Park. Tip-Induced Nano-Engineering of Strain, Bandgap, and Exciton Funneling in 2D Semiconductors. *Advanced Materials*, 33(17):2008234, apr 2021.

[90] Marvin Kulig, Jonas Zipfel, Philipp Nagler, Sofia Blanter, Christian Schüller, Tobias Korn, Nicola Paradiso, Mikhail M. Glazov, and Alexey Chernikov. Exciton Diffusion and Halo Effects in Monolayer Semiconductors. *Physical Review Letters*, 120(20):207401, may 2018.

[91] Nardeep Kumar, Qiannan Cui, Frank Ceballos, Dawei He, Yongsheng Wang, and Hui Zhao. Exciton diffusion in monolayer and bulk MoSe2. *Nanoscale*, 6(9):4915–4919, apr 2014.

[92] Nardeep Kumar, Qiannan Cui, Frank Ceballos, Dawei He, Yongsheng Wang, and Hui Zhao. Exciton-exciton annihilation in MoSe2 monolayers. *Physical Review B*, 89(12):125427, mar 2014.

[93] B. Laikhtman and R. Rapaport. Exciton correlations in coupled quantum wells and their luminescence blue shift. *Physical Review B*, 80(19):195313, nov 2009.

[94] Akash Laturia, Maarten L. Van de Put, and William G. Vandenberghe. Dielectric properties of hexagonal boron nitride and transition metal dichalcogenides: from monolayer to bulk. *npj 2D Materials and Applications*, 2(1):6, dec 2018.

[95] Song Lin Li, Katsunori Wakabayashi, Yong Xu, Shu Nakaharai, Katsuyoshi Komatsu, Wen Wu Li, Yen Fu Lin, Alex Aparecido-Ferreira, and Kazuhito Tsukagoshi. Thickness-dependent interfacial coulomb scattering in atomically thin field-effect transistors. *Nano Letters*, 13(8):3546–3552, aug 2013.

[96] Yilei Li, Alexey Chernikov, Xian Zhang, Albert Rigosi, Heather M Hill, Arend M van der Zande, Daniel A Chenet, En-Min Shih, James Hone, and Tony F Heinz. Measurement of the optical dielectric function of monolayer transition-metal dichalcogenides: MoS2, MoSe2, WS2, and WSe2. *Physical Review B*, 90(20):205422, nov 2014.

[97] Zidong Li, Darwin Cordovilla Leon, Sung Woon Jang, and Parag Deotare. Excitation Density-Dependent Exciton Transport in a h-BN Encapsulated WSe2 Monolayer. *Bulletin of the American Physical Society*, Volume 64,, 2019.

[98] Eric Linardy, Dinesh Yadav, Daniele Vella, Ivan A Verzhbitskiy, Kenji Watanabe, Takashi Taniguchi, Fabian Pauly, Maxim Trushin, and Goki Eda. Harnessing Exciton-Exciton Annihilation in Two-Dimensional Semiconductors. *Nano Letters*, 20(3):1647–1653, mar 2020.

[99] Xuefeng Liu, Hongyi Yu, Qingqing Ji, Zhihan Gao, Shaofeng Ge, Jun Qiu, Zhongfan Liu, Yanfeng Zhang, and Dong Sun. An ultrafast terahertz probe of the transient evolution of the charged and neutral phase of photo-excited electron-hole gas in a monolayer semiconductor. *2D Materials*, 3(1):014001, jan 2016.

[100] Hoi-Kwong Lo, Marcos Curty, and Kiyoshi Tamaki. Secure quantum key distribution. *Nature Photonics*, 8(8):595–604, aug 2014.

[101] Oriol Lopez-Sanchez, Dominik Lembke, Metin Kayci, Aleksandra Radenovic, and Andras Kis. Ultrasensitive photodetectors based on monolayer MoS2. *Nature Nanotechnology*, 8(7):497–501, jul 2013.

[102] Peng Lu, Xiaojun Wu, Wanlin Guo, and Xiao Cheng Zeng. Strain-dependent electronic and magnetic properties of MoS2 monolayer, bilayer, nanoribbons and nanotubes. *Physical Chemistry Chemical Physics*, 14(37):13035, aug 2012.

[103] Nan Ma and Debdeep Jena. Charge scattering and mobility in atomically thin semiconductors. *Physical Review X*, 4(1):011043, mar 2014.

[104] Hideo Mabuchi. Cavity-QED models of switches for attojoule-scale nanophotonic logic. *Physical Review A - Atomic, Molecular, and Optical Physics*, 80(4):045802, oct 2009.

[105] F Mady, J M Reboul, and R Renoud. Formal analogy between multiple-trapping and polarization models: a physical picture for the Cole-Cole formula. *Journal of Physics D: Applied Physics*, 38(13):2271–2275, jul 2005.

[106] Kin Fai Mak and Jie Shan. Photonics and optoelectronics of 2D semiconductor transition metal dichalcogenides. *Nature Photonics*, 10(4):216–226, mar 2016.

[107] Ermin Malic, Malte Selig, Maja Feierabend, Samuel Brem, Dominik Christiansen, Florian Wendler, Andreas Knorr, and Gunnar Berghäuser. Dark excitons in transition metal dichalcogenides. *Physical Review Materials*, 2(1):014002, jan 2018.

[108] Michael K. L. Man, Skylar Deckoff-Jones, Andrew Winchester, Guangsha Shi, Gautam Gupta, Aditya D. Mohite, Swastik Kar, Emmanouil Kioupakis, Saikat Talapatra, and Keshav M. Dani. Protecting the properties of monolayer MoS2 on silicon based substrates with an atomically thin buffer. *Scientific Reports*, 6(1):20890, aug 2016.

[109] Aristea E. Maniadaki, Georgios Kopidakis, and Ioannis N. Remediakis. Strain engineering of electronic properties of transition metal dichalcogenide monolayers. *Solid State Communications*, 227:33–39, feb 2016.

[110] Eric W. Martin, Jason Horng, Hanna G. Ruth, Eunice Paik, Michael-Henr Wentzel, Hui Deng, and Steven T. Cundiff. Encapsulation Narrows and Preserves the Excitonic Homogeneous Linewidth of Exfoliated Monolayer MoSe2. *Physical Review Applied*, 14(2):021002, aug 2020.

[111] Ralf Metzler and Joseph Klafter. The random walk's guide to anomalous diffusion: a fractional dynamics approach. *Physics Reports*, 339(1):1–77, dec 2000.

[112] Ralf Metzler and Joseph Klafter. The restaurant at the end of the random walk: recent developments in the description of anomalous transport by fractional dynamics. *Journal of Physics A: Mathematical and General*, 37(31):R161–R208, aug 2004.

[113] S. Michaelis de Vasconcellos, S. Gordon, M. Bichler, T. Meier, and A. Zrenner. Coherent control of a single exciton qubit by optoelectronic manipulation. *Nature Photonics*, 4(8):545–548, aug 2010.

[114] D. Miller. Device Requirements for Optical Interconnects to Silicon Chips. *Proceedings of the IEEE*, 97(7):1166–1185, jul 2009.

[115] David A. B. Miller. Are optical transistors the logical next step? *Nature Photonics*, 4(1):3–5, jan 2010.

[116] Galan Moody. Two-Dimensional Coherent Spectroscopy of Transition Metal Dichalcogenides. *Encyclopedia of Modern Optics*, pages 52–62, jan 2018.

[117] Galan Moody, Chandriker Kavir Dass, Kai Hao, Chang-Hsiao Chen, Lain-Jong Li, Akshay Singh, Kha Tran, Genevieve Clark, Xiaodong Xu, Gunnar Berghäuser, Ermin Malic, Andreas Knorr, and Xiaoqin Li. Intrinsic homogeneous linewidth and broadening mechanisms of excitons in monolayer transition metal dichalcogenides. *Nature Communications*, 6(1):8315, nov 2015.

[118] Galan Moody, John Schaibley, and Xiaodong Xu. Exciton dynamics in monolayer transition metal dichalcogenides. *Journal of the Optical Society of America B*, 33(7):C39, jul 2016.

[119] Hyowon Moon, Gabriele Grosso, Chitraleema Chakraborty, Cheng Peng, Takashi Taniguchi, Kenji Watanabe, and Dirk Englund. Dynamic Exciton Funneling by Local Strain Control in a Monolayer Semiconductor. *Nano Letters*, 20(9):6791–6797, sep 2020.

[120] Nicolas Morell, Slaven Tepsic, Antoine Reserbat-Plantey, Andrea Cepellotti, Marco Manca, Itai Epstein, Andreas Isacsson, Xavier Marie, Francesco Mauri, and Adrian Bachtold. Optomechanical Measurement of Thermal Transport in Two-Dimensional MoSe 2 Lattices. *Nano Letters*, 19(5):3143–3150, may 2019.

[121] Shinichiro Mouri, Yuhei Miyauchi, Minglin Toh, Weijie Zhao, Goki Eda, and Kazunari Matsuda. Nonlinear photoluminescence in atomically thin layered WSe2 arising from diffusion-assisted exciton-exciton annihilation. *Physical Review B*, 90(15):155449, oct 2014.

[122] B. Movaghar, M. Grunewald, B. Pohlmann, D. Wurtz, and W. Schirmacher. Theory of hopping and multiple-trapping transport in disordered systems. *Journal of Statistical Physics*, 30(2):315–334, feb 1983.

[123] B. Movaghar, M. Grünewald, B. Ries, H. Bassler, and D. Würtz. Diffusion and relaxation of energy in disordered organic and inorganic materials. *Physical Review B*, 33(8):5545–5554, apr 1986.

[124] Ä°lker Murat Koç and Emre Akça. Design of a piezoelectric based tactile sensor with bio-inspired micro/nano-pillars. *Tribology International*, 59:321–331, mar 2013.

[125] Ebrahim Najafi, Vsevolod Ivanov, Ahmed Zewail, and Marco Bernardi. Super-diffusion of excited carriers in semiconductors. *Nature Communications*, 8(1):15177, aug 2017.

[126] Cameron Nelson. *Coherent Nonlinear Optical Spectroscopy of InGaN Disks in GaN Nanowires*. PhD thesis, University of Michigan, 2016.

[127] K S Novoselov, D Jiang, F Schedin, T J Booth, V V Khotkevich, S V Morozov, and A K Geim. Two-dimensional atomic crystals. *Proceedings of the National Academy of Sciences*, 102(30):10451–10453, jul 2005.

[128] Desmond V. O'Connor and David Phillips. Basic Principles of the Single Photon Counting Lifetime Measurement. *Time-Correlated Single Photon Counting*, pages 36–54, 1984.

[129] K. E. O'Hara, J. R. Gullingsrud, and J. P. Wolfe. Auger decay of excitons in CuO2. *Physical Review B*, 60(15):10872–10885, oct 1999.

[130] K. E. O'Hara and J P Wolfe. Relaxation kinetics of excitons in cuprous oxide. *Physical Review B - Condensed Matter and Materials Physics*, 62(19):12909–12922, 2000.

[131] K. Ohsawa, Y. Hayashi, R. Hasunuma, and K. Yamabe. Roughness increase on surface and interface of SiO2grown on atomically flat Si (111) terrace. *Journal of Physics: Conference Series*, 191(1):012031, nov 2009.

[132] Joseph Orenstein and Marc Kastner. Photocurrent Transient Spectroscopy: Measurement of the Density of Localized States in a-As2Se3. *Physical Review Letters*, 46(21):1421–1424, may 1981.

[133] Carmen Palacios-Berraquero, Dhiren M. Kara, Alejandro R.-P. Montblanch, Matteo Barbone, Pawel Latawiec, Duhee Yoon, Anna K. Ott, Marko Loncar, Andrea C. Ferrari, and Mete Atatüre. Large-scale quantum-emitter arrays in atomically thin semiconductors. *Nature Communications*, 8:15093, may 2017.

[134] Raül Perea-Causín, Samuel Brem, Roberto Rosati, Roland Jago, Marvin Kulig, Jonas D Ziegler, Jonas Zipfel, Alexey Chernikov, and Ermin Malic. Exciton Propagation and Halo Formation in Two-Dimensional Materials. *Nano Letters*, 19(10):7317–7323, oct 2019.

[135] S. Permogorov. Hot excitons in semiconductors. *physica status solidi (b)*, 68(1):9–42, mar 1975.

[136] G. Pfister and H. Scher. Time-dependent electrical transport in amorphous solids: As2Se3. *Physical Review B*, 15(4):2062–2083, feb 1977.

[137] G. Pfister and H. Scher. Dispersive (non-Gaussian) transient transport in disordered solids. *Advances in Physics*, 27(5):747–798, sep 1978.

[138] A. Piryatinska, A.I. Saichev, and W.A. Woyczynski. Models of anomalous diffusion: the subdiffusive case. *Physica A: Statistical Mechanics and its Applications*, 349(3-4):375–420, apr 2005.

[139] V. Podzorov, M. E. Gershenson, Ch. Kloc, R. Zeis, and E. Bucher. High-mobility field-effect transistors based on transition metal dichalcogenides. *Applied Physics Letters*, 84(17):3301–3303, apr 2004.

[140] Evgeniy Ponomarev, Árpád Pásztor, Adrien Waelchli, Alessandro Scarfato, Nicolas Ubrig, Christoph Renner, and Alberto F. Morpurgo. Hole Transport in Exfoliated Monolayer MoS2. *ACS Nano*, 12(3):2669–2676, mar 2018.

[141] Andreas Pospischil, Marco M. Furchi, and Thomas Mueller. Solar-energy conversion and light emission in an atomic monolayer p-n diode. *Nature Nanotechnology*, 9(4):257–261, apr 2014.

[142] David Press, Thaddeus D. Ladd, Bingyang Zhang, and Yoshihisa Yamamoto. Complete quantum control of a single quantum dot spin using ultrafast optical pulses. *Nature*, 456(7219):218–221, nov 2008.

[143] Christopher C Price, Nathan C Frey, Deep Jariwala, and Vivek B Shenoy. Engineering Zero-Dimensional Quantum Confinement in Transition-Metal Dichalcogenide Heterostructures. *ACS Nano*, 13(7):8303–8311, jul 2019.

[144] Diana Y. Qiu, Felipe H. da Jornada, and Steven G. Louie. Optical Spectrum of MoS2: Many-Body Effects and Diversity of Exciton States. *Physical Review Letters*, 111(21):216805, nov 2013.

[145] Hao Qiu, Tao Xu, Zilu Wang, Wei Ren, Haiyan Nan, Zhenhua Ni, Qian Chen, Shijun Yuan, Feng Miao, Fengqi Song, Gen Long, Yi Shi, Litao Sun, Jinlan Wang, and Xinran Wang. Hopping transport through defect-induced localized states in molybdenum disulphide. *Nature Communications*, 4(1):2642, dec 2013.

[146] Gabriel Ramos-Fernández, José L Mateos, Octavio Miramontes, Germinal Cocho, Hernán Larralde, and Bárbara Ayala-Orozco. Lévy walk patterns in the foraging movements of spider monkeys (Ateles geoffroyi). *Behavioral Ecology and Sociobiology*, 55(3):223–230, jan 2004.

[147] Shuliang Ren, Qinghai Tan, and Jun Zhang. Review on the quantum emitters in two-dimensional materials. *Journal of Semiconductors*, 40(7):071903, jul 2019.

[148] B. K. Ridley. *Quantum processes in semiconductors*. Clarendon Press, Oxford, 4th ed. edition, 1999.

[149] Ken Ritchie, Xiao-Yuan Shan, Junko Kondo, Kokoro Iwasawa, Takahiro Fujiwara, and Akihiro Kusumi. Detection of Non-Brownian Diffusion in the Cell Membrane in Single Molecule Tracking. *Biophysical Journal*, 88(3):2266–2277, mar 2005.

[150] Christopher Rogers, Dodd Gray, Nathan Bogdanowicz, Takashi Taniguchi, Kenji Watanabe, and Hideo Mabuchi. Coherent feedback control of two-dimensional excitons. *Physical Review Research*, 2(1):012029, jan 2020.

[151] Rafael Roldán, Andrés Castellanos-Gomez, Emmanuele Cappelluti, and Francisco Guinea. Strain engineering in semiconducting two-dimensional crystals. *Journal of Physics: Condensed Matter*, 27(31):313201, aug 2015.

[152] Roberto Rosati, Samuel Brem, Raül Perea-Causín, Robert Schmidt, Iris Niehues, Steffen Michaelis de Vasconcellos, Rudolf Bratschitsch, and Ermin Malic. Strain-dependent exciton diffusion in transition metal dichalcogenides. *2D Materials*, 8(1):015030, dec 2020.

[153] Roberto Rosati, Raül Perea-Causín, Samuel Brem, and Ermin Malic. Negative effective excitonic diffusion in monolayer transition metal dichalcogenides. *Nanoscale*, 12(1):356–363, aug 2020.

[154] Roberto Rosati, Koloman Wagner, Samuel Brem, Raül Perea-Causín, Edith Wietek, Jonas Zipfel, Jonas D. Ziegler, Malte Selig, Takashi Taniguchi, Kenji Watanabe, Andreas Knorr, Alexey Chernikov, and Ermin Malic. Temporal Evolution of Low-Temperature Phonon Sidebands in Transition Metal Dichalcogenides. *ACS Photonics*, 7(10):2756–2764, oct 2020.

[155] Roberto Rosati, Koloman Wagner, Samuel Brem, Raül Perea-Causín, Jonas D Ziegler, Jonas Zipfel, Takashi Taniguchi, Kenji Watanabe, Alexey Chernikov, and Ermin Malic. Non-equilibrium diffusion of dark excitons in atomically thin semiconductors. *ArXiv*, may 2021.

[156] Matthew R Rosenberger, Hsun-Jen Chuang, Kathleen M. McCreary, Aubrey T Hanbicki, Saujan V Sivaram, and Berend T Jonker. Nano-Squeegee for the Creation of Clean 2D Material Interfaces. *ACS Applied Materials and Interfaces*, 10(12):10379–10387, mar 2018.

[157] Aaron M. Ross. *Optical Spectroscopy of Dynamic Nuclear Spin Polarization in Single InAs Quantum Dots*. PhD thesis, University of Michigan, 2019.

[158] Jason S. Ross, Philip Klement, Aaron M. Jones, Nirmal J. Ghimire, Jiaqiang Yan, D. G. Mandrus, Takashi Taniguchi, Kenji Watanabe, Kenji Kitamura, Wang Yao, David H. Cobden, and Xiaodong Xu. Electrically tunable excitonic light-emitting diodes based on monolayer WSe2 p-n junctions. *Nature Nanotechnology*, 9(4):268–272, 2014.

[159] Avinash Rustagi and Alexander F. Kemper. Theoretical Phase Diagram for the Room-Temperature Electron-Hole Liquid in Photoexcited Quasi-Two-Dimensional Monolayer MoS2. *Nano Letters*, 18(1):455–459, jan 2018.

[160] A. C Schaefer, J. Erland, and D. G Steel. Nondiffusive excitonic transport in GaAs and the effects of momentum scattering. *Physical Review B*, 54(16):R11046–R11049, oct 1996.

[161] John R. Schaibley, Todd Karin, Hongyi Yu, Jason S. Ross, Pasqual Rivera, Aaron M. Jones, Marie E. Scott, Jiaqiang Yan, D. G. Mandrus, Wang Yao, Kai Mei Fu, and Xiaodong Xu. Population pulsation resonances of excitons in monolayer MoSe2 with Sub-microeV linewidths. *Physical Review Letters*, 114(13):1–6, 2015.

[162] John R. Schaibley, Hongyi Yu, Genevieve Clark, Pasqual Rivera, Jason S. Ross, Kyle L. Seyler, Wang Yao, and Xiaodong Xu. Valleytronics in 2D materials. *Nature Reviews Materials*, 1(11):16055, nov 2016.

[163] Harvey Scher and Elliott W. Montroll. Anomalous transit-time dispersion in amorphous solids. *Physical Review B*, 12(6):2455–2477, sep 1975.

[164] Christoph Schindler and Roland Zimmermann. Analysis of the exciton-exciton interaction in semiconductor quantum wells. *Physical Review B*, 78(4):045313, jul 2008.

[165] Robert Schmidt, Gunnar Berghäuser, Robert Schneider, Malte Selig, Philipp Tonndorf, Ermin Malić, Andreas Knorr, Steffen Michaelis De Vasconcellos, and Rudolf Bratschitsch. Ultrafast Coulomb-Induced Intervalley Coupling in Atomically Thin WS2. *Nano Letters*, 16(5):2945–2950, 2016.

[166] H. Schnörer, D Haarer, and A Blumen. Crossover from dispersive to nondispersive transport in a trap-controlled hopping model. *Physical Review B*, 38(12):8097–8101, oct 1988.

[167] Reinhard Schwarz. Dispersive transport in disordered semiconductors. *Journal of Non-Crystalline Solids*, 227-230(PART 1):148–152, may 1998.

[168] Klaus Schwidtal. SiO2surface defect centers studied by AES. *Surface Science*, 77(3):523–536, nov 1978.

[169] Malte Selig, Gunnar Berghäuser, Marten Richter, Rudolf Bratschitsch, Andreas Knorr, and Ermin Malic. Dark and bright exciton formation, thermalization, and photoluminescence in monolayer transition metal dichalcogenides. *2D Materials*, 5(3):035017, may 2018.

[170] V Shahnazaryan, I Iorsh, I A Shelykh, and O Kyriienko. Exciton-exciton interaction in transition-metal dichalcogenide monolayers. *Physical Review B*, 96(11):115409, 2017.

[171] Moshe Shapiro and Paul Brumer. Coherent Control of Atomic, Molecular, and Electronic Processes. In *Advances in Atomic, Molecular and Optical Physics*, volume 42, pages 287–345. Academic Press, jan 2000.

[172] Hongyan Shi, Rusen Yan, Simone Bertolazzi, Jacopo Brivio, Bo Gao, Andras Kis, Debdeep Jena, Huili Grace Xing, and Libai Huang. Exciton Dynamics in Suspended Monolayer and Few-Layer MoS 2 2D Crystals. *ACS Nano*, 7(2):1072–1080, feb 2013.

[173] S. Shree, M. Semina, C. Robert, B. Han, T. Amand, A. Balocchi, M. Manca, E. Courtade, X. Marie, T. Taniguchi, K. Watanabe, M. M. Glazov, and B. Urbaszek. Observation of exciton-phonon coupling in MoSe2 monolayers. *Physical Review B*, 98(3):035302, jul 2018.

[174] E K Sichel, R E Miller, M S Abrahams, and C J Buiocchi. Heat capacity and thermal conductivity of hexagonal pyrolytic boron nitride. *Physical Review B*, 13(10):4607–4611, may 1976.

[175] Edbert J Sie, Alex J Frenzel, Yi-Hsien Lee, Jing Kong, and Nuh Gedik. Intervalley biexcitons and many-body effects in monolayer MoS2. *Physical Review B*, 92(12):125417, sep 2015.

[176] Jasprit. Singh. *Electronic and optoelectronic properties of semiconductor structures*. Cambridge University Press, 2003.

[177] R P Smith, J K Wahlstrand, A C Funk, R P Mirin, S T Cundiff, J T Steiner, M Schafer, M Kira, and S W Koch. Extraction of Many-Body Configurations from Nonlinear Absorption in Semiconductor Quantum Wells. *Physical Review Letters*, 104(24):247401, jun 2010.

[178] Duncan G. Steel. Laser Spectroscopy and Quantum Optics in GaAs and InAs Semiconductor Quantum Dots. In *Advances in Atomic, Molecular and Optical Physics*, volume 64, pages 181–222. Elsevier Inc., 1 edition, 2015.

[179] Duncan G Steel. *Introduction to Quantum Nanotechnology*. Oxford University Press, 2021.

[180] Philipp Steinleitner, Philipp Merkl, Philipp Nagler, Joshua Mornhinweg, Christian Schüller, Tobias Korn, Alexey Chernikov, and Rupert Huber. Direct Observation of Ultrafast Exciton Formation in a Monolayer of WSe 2. *Nano Letters*, 17(3):1455–1460, mar 2017.

[181] T H Stievater, Xiaoqin Li, D G Steel, D Gammon, D S Katzer, D Park, C Piermarocchi, and L J Sham. Rabi Oscillations of Excitons in Single Quantum Dots. *Physical Review Letters*, 87(13):133603, sep 2001.

[182] Dezheng Sun, Yi Rao, Georg A. Reider, Gugang Chen, Yumeng You, Louis Brézin, Avetik R. Harutyunyan, and Tony F. Heinz. Observation of Rapid Exciton-Exciton Annihilation in Monolayer Molybdenum Disulfide. *Nano Letters*, 14(10):5625–5629, oct 2014.

[183] M. Tahir. Electrical and optical transport properties of single layer WSe 2. *Physica E: Low-dimensional Systems and Nanostructures*, 97:184–190, mar 2018.

[184] Roel Tempelaar and Timothy C. Berkelbach. Many-body simulation of two-dimensional electronic spectroscopy of excitons and trions in monolayer transition metal dichalcogenides. *Nature Communications*, 10(1):3419, dec 2019.

[185] T. Tiedje and A. Rose. A physical interpretation of dispersive transport in disordered semiconductors. *Solid State Communications*, 37(1):49–52, jan 1981.

[186] Philipp Tonndorf, Robert Schmidt, Robert Schneider, Johannes Kern, Michele Buscema, Gary A. Steele, Andres Castellanos-Gomez, Herre S. J. van der Zant, Steffen Michaelis de Vasconcellos, and Rudolf Bratschitsch. Single-photon emission from localized excitons in an atomically thin semiconductor. *Optica*, 2(4):347, apr 2015.

[187] Milos Toth and Igor Aharonovich. Single Photon Sources in Atomically Thin Materials. *Annual Review of Physical Chemistry*, 70(1):123–142, jun 2019.

[188] Meng-Lin Tsai, Sheng-Han Su, Jan-Kai Chang, Dung-Sheng Tsai, Chang-Hsiao Chen, Chih-I Wu, Lain-Jong Li, Lih-Juann Chen, and Jr-Hau He. Monolayer MoS 2 Heterojunction Solar Cells. *ACS Nano*, 8(8):8317–8322, aug 2014.

[189] Miguel M. Ugeda, Aaron J. Bradley, Su-Fei Shi, Felipe H. da Jornada, Yi Zhang, Diana Y. Qiu, Wei Ruan, Sung-Kwan Mo, Zahid Hussain, Zhi-Xun Shen, Feng Wang, Steven G. Louie, and Michael F. Crommie. Giant bandgap renormalization and excitonic effects in a monolayer transition metal dichalcogenide semiconductor. *Nature Materials*, 13(12):1091–1095, dec 2014.

[190] Dmitrii Unuchek, Alberto Ciarrocchi, Ahmet Avsar, Kenji Watanabe, Takashi Taniguchi, and Andras Kis. Room-temperature electrical control of exciton flux in a van der Waals heterostructure. *Nature*, 560(7718):340–344, aug 2018.

[191] Franz Urbach. The Long-Wavelength Edge of Photographic Sensitivity and of the Electronic Absorption of Solids. *Physical Review*, 92(5):1324–1324, dec 1953.

[192] Dinh Van Tuan, Benedikt Scharf, Zefang Wang, Jie Shan, Kin Fai Mak, Igor Žutić, and Hanan Dery. Probing many-body interactions in monolayer transition-metal dichalcogenides. *Physical Review B*, 99(8):085301, feb 2019.

[193] M. Veldhorst, J. C. C. Hwang, C. H. Yang, A. W. Leenstra, B. de Ronde, J. P. Dehollain, J. T. Muhonen, F. E. Hudson, K. M. Itoh, A. Morello, and A. S. Dzurak. An addressable quantum dot qubit with fault-tolerant control-fidelity. *Nature Nanotechnology*, 9(12):981–985, dec 2014.

[194] Ruggero Verre, Denis G. Baranov, Battulga Munkhbat, Jorge Cuadra, Mikael Käll, and Timur Shegai. Transition metal dichalcogenide nanodisks as high-index dielectric Mie nanoresonators. *Nature Nanotechnology*, 14(7):679–683, jul 2019.

[195] S. M. Vlaming, V. A. Malyshev, A. Eisfeld, and J. Knoester. Subdiffusive exciton motion in systems with heavy-tailed disorder. *The Journal of Chemical Physics*, 138(21):214316, jun 2013.

[196] Michael Wahl. Time-Correlated Single Photon Counting The Principle of Time-Correlated. Technical report, 2014.

[197] G. Wang, C. Robert, M. M. Glazov, F. Cadiz, E. Courtade, T. Amand, D. Lagarde, T. Taniguchi, K. Watanabe, B. Urbaszek, and X. Marie. In-Plane Propagation of Light in Transition Metal Dichalcogenide Monolayers: Optical Selection Rules. *Physical Review Letters*, 119(4):047401, jul 2017.

[198] Gang Wang, Alexey Chernikov, Mikhail M. Glazov, Tony F. Heinz, Xavier Marie, Thierry Amand, and Bernhard Urbaszek. Colloquium : Excitons in atomically thin transition metal dichalcogenides. *Reviews of Modern Physics*, 90(2):021001, apr 2018.

[199] H. Wang, K. B. Ferrio, D. G. Steel, P R Herman, Y. Z. Hu, R. Binder, S. W. Koch, P. R. Berman, Y. Z. Hu, R. Binder, and S. W. Koch. Transient four-wave-mixing line shapes: Effects of excitation-induced dephasing. *Physical Review A*, 49(3):R1551–R1554, mar 1994.

[200] Haining Wang, Jared H Strait, Changjian Zhang, Weimin Chan, Christina Manolatou, Sandip Tiwari, and Farhan Rana. Fast exciton annihilation by capture of electrons or holes by defects via Auger scattering in monolayer metal dichalcogenides. *Physical Review B*, 91(16):165411, apr 2015.

[201] Haining Wang, Changjian Zhang, and Farhan Rana. Ultrafast Dynamics of Defect-Assisted Electron-Hole Recombination in Monolayer MoS2. *Nano Letters*, 15(1):339–345, jan 2015.

[202] Junyong Wang, Ivan Verzhbitskiy, and Goki Eda. Electroluminescent Devices Based on 2D Semiconducting Transition Metal Dichalcogenides. *Advanced Materials*, 30(47):1802687, nov 2018.

[203] Ke Wang, Kristiaan De Greve, Luis A. Jauregui, Andrey Sushko, Alexander High, You Zhou, Giovanni Scuri, Takashi Taniguchi, Kenji Watanabe, Mikhail D. Lukin, Hongkun Park, and Philip Kim. Electrical control of charged carriers and excitons in atomically thin materials. *Nature Nanotechnology*, 13(2):128–132, feb 2018.

[204] Ziqian Wang, Ruichun Luo, Isaac Johnson, Hamzeh Kashani, and Mingwei Chen. Inlaid ReS2 Quantum Dots in Monolayer MoS2. *ACS Nano*, 14(1):899–906, jan 2020.

[205] J. T. Warren, K. E. O'Hara, and J. P. Wolfe. Two-body decay of thermalized excitons in CuO2. *Physical Review B*, 61(12):8215–8223, mar 2000.

[206] Warren S. Warren, Herschel Rabitz, and Mohammed Dahleh. Coherent control of quantum dynamics: The dream is alive. *Science*, 259(5101):1581–1589, mar 1993.

[207] Stephanie Wehner, David Elkouss, and Ronald Hanson. Quantum internet: A vision for the road ahead. *Science*, 362(6412):eaam9288, oct 2018.

[208] Eric W. Weisstein. Convolution, 2021.

[209] F. Withers, O. Del Pozo-Zamudio, A. Mishchenko, A. P. Rooney, A. Gholinia, K. Watanabe, T. Taniguchi, S. J. Haigh, A. K. Geim, A. I. Tartakovskii, and K. S. Novoselov. Light-emitting diodes by band-structure engineering in van der Waals heterostructures. *Nat Mater*, 14(3):301–306, mar 2015.

[210] James P. Wolfe. Thermodynamics of excitons in semiconductors. *Physics Today*, 35(17):2463–2346, mar 1982.

[211] Jianrong Wu and Keith M. Berland. Propagators and Time-Dependent Diffusion Coefficients for Anomalous Diffusion. *Biophysical Journal*, 95(4):2049–2052, aug 2008.

[212] Y. Wu, X. Liu, P. Wang, D. A. Laleyan, K. Sun, Y. Sun, C. Ahn, M. Kira, E. Kioupakis, and Z. Mi. Monolayer GaN excitonic deep ultraviolet light emitting diodes. *Applied Physics Letters*, 116(1):013101, jan 2020.

[213] Zongyou Yin, Hai Li, Hong Li, Lin Jiang, Yumeng Shi, Yinghui Sun, Gang Lu, Qing Zhang, Xiaodong Chen, and Hua Zhang. Single-Layer MoS2 Phototransistors. *ACS Nano*, 6(1):74–80, jan 2012.

[214] Jun Yoneda, Kenta Takeda, Tomohiro Otsuka, Takashi Nakajima, Matthieu R. Delbecq, Giles Allison, Takumu Honda, Tetsuo Kodera, Shunri Oda, Yusuke Hoshi, Noritaka Usami, Kohei M. Itoh, and Seigo Tarucha. A quantum-dot spin qubit with coherence limited by charge noise and fidelity higher than 99.9 *Nature Nanotechnology*, 13(2):102–106, feb 2018.

[215] H. W. Yoon, D. R. Wake, J. P. Wolfe, and H. Morkoç. In-plane transport of photoexcited carriers in GaAs quantum wells. *Physical Review B*, 46(20):13461–13470, nov 1992.

[216] Peter Y. Yu and Manuel Cardona. *Fundamentals of Semiconductors*. Graduate Texts in Physics. Springer Berlin Heidelberg, Berlin, Heidelberg, 2010.

[217] Yiling Yu, Yifei Yu, Chao Xu, Andy Barrette, Kenan Gundogdu, and Linyou Cao. Fundamental limits of exciton-exciton annihilation for light emission in transition metal dichalcogenide monolayers. *Physical Review B*, 93(20):201111, may 2016.

[218] Long Yuan, Ti Wang, Tong Zhu, Mingwei Zhou, and Libai Huang. Exciton Dynamics, Transport, and Annihilation in Atomically Thin Two-Dimensional Semiconductors. *The Journal of Physical Chemistry Letters*, 8(14):3371–3379, jul 2017.

[219] S Zaynobidinov, R G Ikramov, and R M Jalalov. Urbach energy and the tails of the density of states in amorphous semiconductors. *Journal of Applied Spectroscopy*, 78(2):223–227, may 2011.

[220] Chendong Zhang, Amber Johnson, Chang Lung Hsu, Lain Jong Li, and Chih Kang Shih. Direct imaging of band profile in single layer MoS2 on graphite: Quasiparticle energy gap, metallic edge states, and edge band bending. *Nano Letters*, 14(5):2443–2447, may 2014.

[221] Xiao-Xiao Xiao Zhang, Yumeng You, Shu Yang Frank Zhao, and Tony F. Heinz. Experimental Evidence for Dark Excitons in Monolayer WSe2. *Physical Review Letters*, 115(25):257403, dec 2015.

[222] Y. J. Zhang, T. Oka, R. Suzuki, J. T. Ye, and Y. Iwasa. Electrically Switchable Chiral Light-Emitting Transistor. *Science*, 344(6185):725–728, may 2014.

[223] Hui Zhao, B. Dal Don, S. Moehl, and H. Kalt. Non-classical excitonic transport in quantum wells. *physica status solidi (b)*, 238(3):529–532, aug 2003.

[224] Hui Zhao, B. Dal Don, S. Moehl, H. Kalt, K. Ohkawa, and D. Hommel. Spatiotemporal dynamics of quantum-well excitons. *Physical Review B*, 67(3):035306, jan 2003.

[225] Hui Zhao, Benedicte Dal Don, Gregor Schwartz, and Heinz Kalt. Ultrafast Breathinglike Oscillation in the Exciton Density of ZnSe Quantum Wells. *Physical Review Letters*, 94(13):137402, apr 2005.

[226] Hui Zhao, Heinz Kalt, and M. Hetterich. *Optics of Semiconductors and Their Nanostructures*, volume 146 of *Springer Series in Solid-State Sciences*. Springer Berlin Heidelberg, Berlin, Heidelberg, first edit edition, 2004.

[227] Hui Zhao, Sebastian Moehl, and Heinz Kalt. Coherence Length of Excitons in a Semiconductor Quantum Well. *Physical Review Letters*, 89(9), 2002.

[228] Hui Zhao, Sebastian Moehl, and Heinz Kalt. Energy relaxation during hot-exciton transport in quantum wells: Direct observation by spatially resolved phonon-sideband spectroscopy. *Applied Physics Letters*, 81(15):2794–2796, oct 2002.

[229] G. Zumofen, J. Klafter, and A. Blumen. Trapping aspects in enhanced diffusion. *Journal of Statistical Physics*, 65(5-6):991–1013, dec 1991.